

**Topics in the Emergence of Cooperation in
Competing Populations and Optical
Properties of Patterned Metallic Films**
競爭群體中合作的產生及具規則結構之金屬
薄膜的光學性質

YIN, Haiping

尹海平

A Thesis Submitted in Partial Fulfillment
of the Requirements for the Degree of
Doctor of Philosophy
in
Physics

The Chinese University of Hong Kong

March 2010

UMI Number: 3445943

All rights reserved

INFORMATION TO ALL USERS

The quality of this reproduction is dependent upon the quality of the copy submitted.

In the unlikely event that the author did not send a complete manuscript and there are missing pages, these will be noted. Also, if material had to be removed, a note will indicate the deletion.



UMI 3445943

Copyright 2011 by ProQuest LLC.

All rights reserved. This edition of the work is protected against unauthorized copying under Title 17, United States Code.



ProQuest LLC
789 East Eisenhower Parkway
P.O. Box 1346
Ann Arbor, MI 48106-1346

Thesis/Assessment Committee

Professor CHU, Ming Chung (Chair)

Professor HUI, Pak Ming (Thesis Supervisor)

Professor ONG, Hock Chun Daniel (Committee Member)

Professor WANG, Binghong (External Examiner)

Abstract of thesis entitled:

Topics in the Emergence of Cooperation in Competing Populations and Optical Properties of Patterned Metallic Films

Submitted by YIN, Haiping

for the degree of Doctor of Philosophy

at The Chinese University of Hong Kong in March 2010

The thesis consists of two independent parts. Part I focuses on evolutionary games in networked entities and Part II focuses on calculations on optical properties of metallic gratings.

Part I focuses on studying the extent of cooperation in networked entities, within the context of the Prisoner's Dilemma (PD) and the Snowdrift Game (SG). The iterated prisoner's dilemma (IPD) is studied in the full payoff space spanned by two parameters β and γ . A theoretical study on two-strategy IPD is presented. We then numerically study the IPD in the full payoff space, with four different initial configurations. It is found that including the Tit-for-tat-like (E_{TFT}) and Always-defecting-like (E_{AUD}) strategies as initial strategies can maximize the dominating area of generous strategies in the payoff space at equilibrium. The roles played by E_{TFT} and E_{AUD} are further studied on the diagonal and anti-diagonal lines of the payoff space.

The Snowdrift Game is regarded as an important alternative to PD in studying the emergence of cooperation in competing populations. The phase transitions in spatial snowdrift games are introduced. By studying the relative alignments of the payoffs of C and D nodes, the phase transitions are analytically explained. As an extension to the standard two-person SG, an N -person Snowdrift Game (NPSG) is proposed to include generic multi-person interactions. NPSG in a well-mixed population is studied analytically by using the replicator dynamics. A simulation algorithm is developed. We also study NPSG on lattices and find a suppressed cooperation frequency, when compared with the well-mixed case. For NPSG played on 1D chain, the problem

can be solved analytically. We further extend our work to study co-evolving dynamics. We propose and study a model in which the connections are driven to evolve by the dynamics of SG. Compared with played on static network, the cooperation frequency is promoted. A semi-analytic theory is proposed, with the results qualitatively agree with simulation results.

Part II focuses mainly on studying the optical properties of grating within the Rigorous Coupled-Wave Analysis (RCWA) method. The surface plasmon (SP) dispersion relation in a system consisting of a thin metallic film sandwiched between a linear dielectric and nonlinear dielectric of arbitrary non-linearity is derived, based on a generalized "first integral" approach. The SP dispersion relation in a system consisting of a thin metallic film sandwiched in a symmetric nonlinear dielectric environment is then derived. The changes in SP dispersion relations on film thicknesses are discussed for both cases.

The optical properties of two samples of one-dimensional metallic reflection gratings are studied. The numerical results of the zeroth order reflectance are in good agreement with experimental data. The Wood's anomaly occurs when a particular diffraction order emerges or disappears, thus inducing a change in the efficiency of other diffraction orders. This phenomenon is studied by calculating and measuring the efficiencies of all allowed diffraction orders. Numerical results of the near field patterns show a coupling between the waveguide and SP modes. We also study the controllable enhanced transmission in a semiconductor grating. The dielectric constant of a semiconductor becomes a tensor in the presence of a static magnetic field parallel to the slit. Numerical results based on RCWA reveal that the zeroth order transmission peaks at normal incidence can be shifted to longer wavelengths and the peak values of transmission can largely be enhanced when a moderate magnetic field is applied. A single-mode theory incorporating anisotropy is developed. The analytic results are in quantitative agreement with RCWA, indicating that the tunability in the transmission stems from the waveguide mode.

摘要

本論文包含兩個獨立的部分。第一部分是對網絡上的演化博弈的探討。第二部分則是對金屬光柵之光學性質的計算。

論文的第一部分主要研究網絡結構上的囚徒困境 (Prisoner's Dilemma) 及雪堆博弈 (Snowdrift Game)。我們在整個收益空間 (payoff space) 中對反覆囚徒困境 (Iterated Prisoner's Dilemma) 進行了研究。先是對系統只包含兩個策略 (strategy) 的情況進行了理論分析。然後，我們對系統中初始有 100 個策略的情形進行了數值模擬。模擬涵蓋了整個收益空間，並採用了四個不同的初始條件。結果顯示，當系統初始同時包含下列兩種策略時，以慷慨策略主導的平衡態會在收益空間中占據最大面積。這兩種重要策略分別是“以牙還牙” (Tit-for-tat) 和“永不合作” (Always-defecting)。通過對收益空間的對角線和反對角線的研究，我們對該兩種策略所起的作用做了更為仔細的探討。

在囚徒困境之外，雪堆博弈也被廣泛的用於研究競爭性群體中的合作現象。前人研究發現晶格上的雪堆博弈中存在相變現象。我們通過對合作者和不合作者的收益進行比較和排序，解析的解釋了此類相變產生的原因及相變點的位置。經典的雪堆博弈是一個雙人博弈，但在現實中多人博弈的情況屢見不鮮。所以我們將其推廣至多人博弈，提出了一個多人雪堆博弈模型 (N -Person Snowdrift Game)。我們首先研究了該模型在全接觸人群 (well-mixed population) 中的表現，並用“複製子動力學” (replicator dynamics) 對結果進了解析分析。我們亦發展了一套算法來對該模型進行數值模擬。對晶格上的多人博弈的研究揭示其平衡態合作率 (the equilibrium frequency of cooperation) 顯著低於在全接觸人群中的表現。在一維鏈條上的多人雪堆博弈可以進行解析分析。我們也研究了博弈與網絡結構的共同演化。在所構造的模型中，網絡的結構會因其上進行的雪堆博弈的動力學而改變。與網絡結構固定的情況相比，該模型的平衡態合作率顯著提升。我們提出了一個半近似理論，理論與數值結果具有定性的一致性。

論文的第二部分主要是對金屬光柵光學性質的探討。主要的數值計算方法是嚴格耦合波分析 (Rigorous Coupled-Wave Analysis)。我們首先推導出了

下面兩個系統的表面等離子體模 (Surface Plasmon) 的色散關係。第一個系統包含一層金屬薄膜，其一邊是非線性介質，另一邊則為線性介質。在第二個系統中，金屬薄膜處于對稱的非線性介質中。我們對一種叫做“首次積分” (first integral) 的技巧進行了推廣，使得我們可以處理任意的非線性介質。我們還討論了金屬膜厚度對色散關係的影響。

之後我們研究了兩個一維金屬反射光柵樣品的光學性質。我們採用嚴格耦合波分析計算得到的反射率，跟實驗測量的結果吻合的很好。當光柵的某一級衍射波產生或者消失的時候，會伴隨著其他級衍射波衍射率的突然改變，該效應被稱為伍德奇異性 (Wood's Anomaly)。我們對各容許衍射級的衍射率進行了計算和測量，兩者都證明了伍德奇異性的發生對應于衍射率的突變。我們也通過計算，繪出了光柵及其附近範圍內磁場的分佈。通過對特定波長和入射角度對應的近場分佈進行分析，我們發現狹縫中的波導模 (waveguide mode) 和光柵表面的表面等離子模存在著耦合。

我們亦對一維半導體光柵的可調控增強透射 (enhanced transmission) 進行了探討。當沿平行于光柵縫隙的方向施加一個磁場時，半導體的介電常數會由一個數值變為跟磁場強度相關聯的張量。通過改變磁場強度，我們可以改變介電常數張量，進而控制光柵的透射率。在數值計算方面，我們採用嚴格耦合波分析計算了垂直入射時的 0 級透射率。計算結果顯示與沒有磁場的情況相比，在施加了適當強度的磁場之後，透射峰所在的波長會向長波方向移動，移動幅度可達 15% 之多。相應的，透射率也會顯著增大，甚至倍增。在理論方面，我們發展了一個單模理論 (single-mode theory)，該理論建基于光柵狹縫中只有一個主導本征模的假設之上。應用此單模理論得到的解析結果跟 RCWA 的數值結果相當一致，證明了增強透射是由狹縫中的波導模引致。

Acknowledgments

First and foremost I would like to express my sincerest gratitude to my supervisor, Professor Hui Pak Ming, for his warm encouragement, remarkable patience and thoughtful guidance throughout my Ph.D. studying period. Also, his strict working attitude sets a very good example for me. It is my great honor to work with him these years.

I thank Prof. Zheng Da-Fang for his original proposal of the N -person snowdrift game (NPSG). I also thank Prof. Xu Chen for the collaborations on the Iterated Prisoner's Dilemma (IPD) and on studying the surface plasmon modes. I have learned a lot from the cooperation with them.

Thank for all members of the research group, including Mr. Chan Chun Him, Mr. Fong King Yan, Mr. Oliver Gräser, Mr. Lee Kwan Ho, and Miss Li Pingping. In particular, I thank Chan Chun Him for the collaborations on IPD and NPSG. I also thank Fong King Yan, for his help on implementation of the Rigorous Coupled-Wave Analysis, and his valuable discussions on the optical properties of gratings.

Chapter 8 of this thesis is based on a collaboration work with Prof. Ong's experimental group. I am very thankful to the support from the experimental group, including Prof. Daniel H. C. Ong, Mr. Luk Wai Chun, Mr. Li Jia, and Mr. Sham Chun Hong.

I would also like to thank members in Room 224 and friends in the physics department, for providing a happy environment in which to learn and grow.

Lastly, I am forever indebted to my parents for their support and encouragement whenever I need. I also wish to express my love to my wife Zhang Ling, for her unselfish dedication and persistent confidence in me.

Part of the work in this thesis was supported in part by research grants from the Research Grants Council of the Hong Kong SAR Government under grant number CUHK-401005 and CUHK-401109.

Publications

Journal Publications

1. D. F. Zheng, **H. P. Yin**, C. H. Chan, and P. M. Hui, Cooperative behavior in a model of evolutionary snowdrift games with N -person interactions. *Europhysics Letters*, 80: 18002, 2007.
2. Chun-Him Chan, **Haiping Yin**, P. M. Hui, and Da-Fang Zheng, Evolution of cooperation in well-mixed N -person snowdrift games. *Physica A*, 387: 2919, 2008.
3. **Haiping Yin**, C. Xu, and P. M. Hui, Exact surface plasmon dispersion relations in a linear-metal-nonlinear dielectric structure of arbitrary nonlinearity. *Applied Physics Letters*, 94: 221102, 2009.
4. **Haiping Yin**, Zhihai Rong, Gang Yan, Development of friendship network among young scientists in an international Summer School. *Physica A*, 388: 3636, 2009.
5. **Haiping Yin** and P. M. Hui, Controlling enhanced transmission through semiconductor gratings with subwavelength slits by a magnetic field: Numerical and analytical results. *Applied Physics Letters*, 95: 011115, 2009.

Conference Presentations

1. W.-C. Luk, **H.-P. Yin**, J. Li, P. M. Hui, and H. C. Ong. Theoretical and experimental studies of the optical properties of one-dimensional metallic gratings. Oral presentation in *Progress In Electromagnetics Research Symposium*, Hangzhou, China, March 2008.

Contents

Abstract	i
Acknowledgments	v
Publications	vi
0 Overview	1
1 Review on evolutionary games and networks	6
1.1 The prisoner's dilemma and the snowdrift game	6
1.1.1 Two-strategy games	7
1.1.2 The prisoner's dilemma	10
1.1.3 The snowdrift game	11
1.2 Review on networks	12
1.2.1 Basic properties	13
1.2.2 Random Graph	14
1.2.3 Barabási-Albert Network	15
1.3 Conclusion	18
2 The Iterated Prisoner's Dilemma	19
2.1 Review of previous works on IPD	19
2.2 Two-strategy IPD Game	24
2.2.1 Determine the sign of $K(E_i, E_j)$	25

2.2.2	The invasion problem	27
2.3	Two-parameter IPD	29
2.3.1	Diagonal line	34
2.3.2	Anti-diagonal line	39
2.3.3	Analytical calculations of $\langle p_{win} \rangle$ and $\langle q_{win} \rangle$	44
2.4	Conclusion	50
3	Phase transitions in spatial snowdrift game	52
3.1	Introduction	52
3.2	The spatial snowdrift game	54
3.2.1	One-parameter payoff matrix	54
3.2.2	Snowdrift game on lattices	54
3.3	Theoretical investigations on phase transitions in spatial SG	57
3.3.1	Phase transition between AllC and mixed phases	58
3.3.2	Phase transition between mixed and AllD phases	61
3.4	Discussion	65
4	The N-Person Snowdrift Game	66
4.1	Motivation and set up of the game	66
4.2	NPSG in well-mixed population	68
4.2.1	Analytical approach: the replicator dynamics	69
4.2.2	Simulation algorithm	71
4.2.3	Time evolution of cooperation	72
4.3	NPSG on lattices	76
4.3.1	Simulation algorithm and numerical results	76
4.3.2	Analytic study on 1D chain	78
4.3.3	Analytic theory for 2D lattices	81
4.4	Conclusion	83
5	Snowdrift game on adaptive network	85

5.1	Model and numerical results	86
5.1.1	Numerical results	87
5.1.2	The steady state	88
5.2	Semi-analytic approach	91
5.3	Conclusion	96
6	Surface plasmon excitations	98
6.1	Basic concepts	99
6.1.1	Maxwell's Equations	99
6.1.2	TE and TM polarizations	100
6.1.3	Dielectric constants of metals	101
6.2	Surface plasmon at metal/linear dielectric interface	102
6.2.1	Semi-infinite metal/linear system	103
6.2.2	Metallic film between two linear dielectrics	106
6.3	Surface plasmon of nonlinear/metal system	111
6.3.1	Nonlinear-metal-linear structure	112
6.3.2	Symmetric nonlinear/metal/nonlinear structure	118
6.4	Conclusion	120
7	The Rigorous Coupled-Wave Analysis	122
7.1	Introduction	122
7.2	RCWA for 1D periodic structures	123
7.2.1	TM polarization	123
7.2.2	TE polarization	126
7.2.3	Fourier factorization rule	127
7.2.4	Matching boundary conditions	128
7.3	Sample calculations	132
7.3.1	Total internal reflection at glass-air interface	132
7.3.2	Enhanced transmission in a silver grating	132
7.4	Summary	135

8	Optical properties of metallic reflection gratings	136
8.1	Sample preparation	136
8.2	The zeroth order reflectance	140
8.3	Effects of the Wood's anomaly	142
8.4	Coupling between waveguide mode and SP mode	145
8.5	Summary	149
9	Controlling enhanced transmission through semiconductor gratings with subwavelength slits by a magnetic field	151
9.1	Introduction	152
9.2	The system and numerical results	154
9.3	Single mode approximation	157
9.3.1	The propagating mode inside the slits	157
9.3.2	The zeroth order transmittance	160
9.4	Summary	165
10	Summary	166
A	Development of Friendship Network Among Young Scientists in an International Summer School	169
A.1	Introduction	170
A.2	The surveyed group in Santa Fe CSSS2008	171
A.3	Basic properties of the networks	173
A.4	Correlation between reciprocal evaluations	175
A.5	Community-like structures in friendship networks	179
A.6	Summary	183
	Bibliography	185

List of Figures

1.1	The degree distribution of a random graph of size $N = 1001$ and probability $p = 0.05$ obtained by numerical simulations (symbols). The theoretical result given by Eq.(1.18) is shown for comparison (line). Each data point is an average over 100 realizations.	15
1.2	The degree distribution $P(k)$ of BA networks of size $N = 10^6$ with $m_0 = m = 3$ and $m_0 = m = 5$. The linear fit of the $m_0 = 3$ case (blue line) gives a slope of -2.92 . Each data point is an average over 10 realizations.	17
1.3	The clustering coefficient C versus N for BA networks with $m_0 = m = 3$. The simulation results (black crosses) and results given by Eq.(1.22) (red dots) are shown. Each simulation data point is an average over 10 realizations.	18
2.1	The sign of $c_i - s_j$ for an arbitrary strategy E_i , given a strategy $E_j = (p_j, q_j)$	26
2.2	The sign of $B(E_i)$ of an arbitrary strategy E_i under the condition that $\beta + \gamma = 1$	26
2.3	For a given β under the condition that $\beta + \gamma = 1$, a strategy (p_1, q_1) in Region I can invade any strategy in IB. Meanwhile, it can be invaded by any strategy in IA.	28

2.4	For a given β under the condition that $\beta + \gamma = 1$, a strategy (p_1, q_1) in Region II can invade any strategy in IIA. Meanwhile, it can be invaded by any strategy in IIB.	28
2.5	$\langle p \rangle$ and $\langle q \rangle$ for systems with initial configuration T0 in the β - γ space. Results are obtained by averaging over 100 realizations.	30
2.6	$\langle p \rangle$ and $\langle q \rangle$ for systems with initial configuration T1 in the β - γ space. Results are obtained by averaging over 100 realizations.	31
2.7	$\langle p \rangle$ and $\langle q \rangle$ for systems with initial configuration T2 in the β - γ space. Results are obtained by averaging over 100 realizations.	31
2.8	$\langle p \rangle$ and $\langle q \rangle$ for systems with initial configuration T3 in the β - γ space. Results are obtained by averaging over 100 realizations.	32
2.9	The coverage of the three regions in the payoff space for the four types of initial configurations. White color for AllD-like region, green for TFT-like region, and red for AllC-like region.	33
2.10	(a) $\langle p \rangle$ and (b) $\langle q \rangle$ as a function of β along the diagonal line $\gamma = \beta$ in the β - γ space for the four initial configurations. Each data point is an average over 500 realizations. The inset of (b) is a zoom-in picture for $\beta < 0.45$	35
2.11	Contour plot of $G(E, E_{AUD})$ for any strategy $E = (p, q)$ at $\beta = 0.1$. White color for $G(E, E_{AUD}) = 1$, green color for $G(E, E_{AUD}) = 0$ and red color for $G(E, E_{AUD}) = -1$	36
2.12	The winning strategies (black cross) and the strategy with minimum $l = q/(1 - p)$ value (dot) in 500 realizations. $\beta = 0.1$, initial configurations are T3 and T0.	38
2.13	The threshold frequency x_c of E_{TFT} when playing against E_{AUD} as a function of β along the diagonal line of the β - γ space. The inset is a zoom-in picture at large β	39

2.14	Contour plot of (a) $G(E, E_{AUD})$ and (b) $G(E, E_{TFT})$ at $\beta = 0.95$. White color for $G(E, E_{AUD}) = 1$, green color for $G(E, E_{AUD}) = 0$ and red color for $G(E, E_{AUD}) = -1$. The winning strategies of 1000 realizations with initial configuration T3 are also shown in (b) as blue dots.	40
2.15	(Left) $\langle p \rangle$ and (Right) $\langle q \rangle$ as a function of β along the anti-diagonal line $\gamma = 1 - \beta$ in the β - γ space for the four initial configurations. Each data point is an average over 500 realizations.	41
2.16	The threshold frequency x_c of E_{TFT} when playing against E_{AUD} as a function of β along the anti-diagonal line of the β - γ space. The inset is a zoom-in picture at small β	42
2.17	A typical evolution process for system with initial configuration T3 at $\beta = 0.1$	42
2.18	The winning strategies obtained by simulations (black crosses) and the strategy with maximum $l = q/(1 - p)$ value in Region I for 500 realizations (dots). $\beta = 1 - \gamma = 0.1$, with initial configurations T0 and T1.	44
2.19	The winning strategies obtained by simulations (black cross) and the strategy with minimum $l = q/(1 - p)$ value in Region II (dots) for 500 realizations. $\beta = 0.7$, with initial configurations T0 and T2.	45
2.20	Schematic diagrams of the relative positions of strategies discussed in Sec. 2.3.3 for calculating $\langle p_{win} \rangle$ and $\langle q_{win} \rangle$ at small β	46
2.21	Schematic diagrams of the relative positions of strategies discussed in Sec. 2.3.3 for calculating $\langle p_{win} \rangle$ and $\langle q_{win} \rangle$ at large β	49

3.1	Different types of 2D lattices. From Left to right: Hexagonal ($k = 3$), Square ($k = 4$), Triangle ($k = 6$) and Square lattice with nearest and next nearest neighbors connected ($k = 8$).	55
3.2	The frequency of cooperation f_C as a function of the cost-to-benefit ratio r for SG played on lattices of different geometries (symbols). f_C of the well-mixed case is shown for comparison (line).	56
3.3	Schematic diagram showing the phase transition between AllC and mixed phases.	59
3.4	The simulation results of f_C versus r for systems with initial condition $x_C(t = 0) = 0.5$ (symbols). The analytically predicted phase transition points r_C and r_{C1} are shown as the vertical bars.	60
3.5	Schematic diagram showing the phase transition between AllC and mixed phases for square lattice with one defector initially.	61
3.6	The simulation results of f_C versus r for systems with one D -node initially, i.e., the invasion problem. The critical points of the phase transition between the AllC and mixed phase shifts from $1/(k + 1)$ to $1/k$ (black vertical bars).	62
3.7	Schematic diagram showing the phase transition between mixed phase and AllD phase in systems with a small fraction of cooperators initially.	63
3.8	The simulation results of f_C versus r for systems with initial condition $x_C(t = 0) = 0.003$. The transition into an AllD phase is predicted to occur at $\frac{k-1}{k+1}$ (vertical bars).	64
3.9	The simulation results of f_C versus r in a hexagonal lattice ($k = 3$) with initial condition $x_C(t = 0) = 0.5$. The critical point of phase transition between mixed phase and AllD phase is estimated to be $2/3$ (green vertical bar).	65

- 4.1 The equilibrium frequency of cooperation as a function of r , for $N = 2, 3, 5$, and 10 in a well-mixed population. The analytic results (lines) obtained by solving Eq.(4.15) and the simulation results (symbols) are in good agreement. The simulation parameters are $N_{all} = 2000$, initial fraction of cooperators $x(t = 0) = 0.5$, and 10^5 time steps. Each data point is an average over 100 realizations. 71
- 4.2 A log-log plot of the equilibrium frequency of cooperation as a function of N for $r = 0.2, 0.5$, and 0.8 in a well-mixed population. The analytic results (lines) from Eq.(4.15) and the simulation results (symbols) are in good agreement. The simulation parameters are $N_{all} = 5000$, $x(t = 0) = 0.5$, and 10^7 time steps. Every data point is an average over 10 realizations. A dotted line of slope -1 is shown to guide the eye. 72
- 4.3 The simulation (symbols) and analytic results (lines) of the time evolution of $x(t)$ for 2-person ($N = 2$) and 3-person ($N = 3$) snowdrift game. The parameters are $r = 1/7$, $x(t = 0) = 1/2$, and $N_{all} = 5000$. The simulation results are obtained by one single run. The analytic results are obtained by Eq.(4.28) and Eq.(4.31). The equilibrium frequency of cooperation $x_{N=2}^* = 12/13$ and $x_{N=3}^* = 3/4$ (dotted lines) are shown to guide the eye. 77
- 4.4 The frequency of cooperation as a function of r for different lattices. Numerical results (symbols) of 1D chain with $k = 2$, 2D lattice with $k = 3, 4, 6$, and 8 are shown. The simulation parameters are $N_{all} = 10^4$, $x(t = 0) = 0.5$, and 10^6 time steps. Each data point is an average over 50 runs. For comparison, the lines show the results in the well-mixed case with the same values of $N = k + 1$. The presence of an underlying lattice structure suppresses the frequency of cooperation significantly. 78

4.5	The frequency of cooperation as a function of r in a 1D chain (symbols). In simulations, we used $N_{all} = 10^4$, $x(t = 0) = 0.5$ and 10^6 time steps. Each data point is an average over 50 realizations. The analytic results obtained by Eq.(4.40) (line) are shown for comparison, and good agreement is found.	82
4.6	The frequency of cooperation as a function of r in 2D lattices with $k = 4, 6$ and 8 (symbols). In simulations, we used $N_{all} = 10^4$, $x(t = 0) = 0.5$ and 10^6 time steps. Each data point is an average over 50 realizations. The analytic results proposed in Eq.(4.45) (lines) are shown for comparison.	83
5.1	The equilibrium frequency of cooperation f_C as a function of r (symbols) for random rewiring (upper panel) and opinion rewiring (lower panel). The initial network structures are 2D lattices with $\langle k \rangle = 3$ and 4 . The simulation parameters are $N = 10^4$, initial fraction of cooperators $x_0 = 0.5$, and 5×10^5 time steps. Each data point is an average over 100 realizations. The standard deviation of f_C is shown as error bar. For comparison, f_C as a function of r for SG on static lattices are also shown (dotted lines).	89
5.2	Schematic diagrams show the two different scenarios of the system at equilibrium for $r > r_C$. (a) Two big clusters of opposite characters. (b) One cluster with C and D nodes.	91
5.3	Schematic diagrams show the change of the key quantities of the four evolutionary processes.	95

5.4	The analytic (lines) and simulation results (symbols) of the equilibrium frequency of cooperation f_C as a function of r , for both $\langle k \rangle = 3$ (Left) and 4 (Right) cases. The initial frequency of cooperation are taken to be $x_0 = 0.3, 0.5$ and 0.7 . The simulation parameters are $N = 10^4$ and 5×10^5 time steps. Each data point is an average over 100 realizations:	96
6.1	The SP dispersion relation at semi-infinite metal/linear interface. The metal is assumed to be lossless.	105
6.2	Schematic diagram shows the structure of a linear-metal-linear system.	106
6.3	The SP dispersion relations for a metallic film in air. The thickness of the metallic film is taken to be $d = 20$ nm, 30 nm and 100 nm. Two points with the same k_x and d values are chosen for which the H_y field distributions are shown in Fig. 6.4.	110
6.4	The H_y field distribution for Points 1 and 2 in Fig. 6.3. Points 1 and 2 have the same k_x and thickness d , with $k_x = 4.53 \times 10^7 \text{ m}^{-1}$ and $d = 30$ nm.	110
6.5	Schematic diagram showing the structure of a nonlinear-metal-linear system.	112
6.6	The dispersion relation of SP modes in a MBBA/silver/air system typical of thick ($d = 200$ nm) and thin ($d = 20$ nm) metallic films are shown.	115
6.7	The limiting value $\omega_{sp}^{(m,n\ell)}$ as a function of $ \alpha E_0^\beta$ for both $\alpha < 0$ and $\alpha > 0$ and different values of β in the thick film limit. The metal takes a Drude form dielectric constant ϵ_m and the linear part of the nonlinear medium takes on $\epsilon = 2$	117

6.8	The dispersion relations at a metal/Kerr medium interface for different nonlinearities in the thick film limit. The metal takes a Drude form dielectric constant ϵ_m and the linear part of the nonlinear medium takes on $\epsilon = 2$	117
6.9	The dispersion relations of SP modes in a MBBA/metal/MBBA system. The thicknesses of the metallic film are taken to be $d = 20$ nm, 30 nm and 100 nm.	121
7.1	Schematic diagram showing a 1D structure with period L along the x direction.	123
7.2	The transmittance T_0 and reflectance R_0 as a function of the incident angle θ_I , for a TE polarized EM wave incident from glass to air. Analytic results (solid lines) and results by RCWA (symbols) are shown.	133
7.3	Schematic diagram showing a silver grating of period $L = 900$ nm, thickness $d = 60$ nm, and slit width $w = 36$ nm. One side of the grating is air and the slits are filled with air of dielectric constant $\epsilon_a = 1$, and another side of the grating is glass with dielectric constant $\epsilon_g = 2$. A TM polarized wave is incident upon the grating from air with an angle θ	134
7.4	(a) The zeroth order transmission at normal incidence for the system shown in Fig. 7.3. (b) Symbols show the positions of the transmission peaks. Lines show the folded dispersion curves of SP modes excited at metal-air interface (dashed lines) and metal-glass interface (solid lines), respectively.	135
8.1	Schematic diagram showing the sample preparation process. . .	138
8.2	The SEM pictures of Sample 1 (left panel) and Sample 2 (right panel).	139

8.3	Schematic diagram showing the topological structures of Sample 1 (left panel) and Sample 2 (right panel). The parameters are measured by SEM.	139
8.4	Schematic diagram showing the experimental set up for measuring the zeroth order reflectance.	140
8.5	The zeroth order reflectance of Sample 1. Both experimental results (left panel) and results by RCWA (right panel) are shown.	141
8.6	The zeroth order reflectance of Sample 2. Both experimental results (left panel) and results by RCWA (right panel) are shown.	142
8.7	RCWA results of the zeroth order reflectance of Sample 2. The x axis is the incident angle and the y axis is the wavelength. Colors indicate the reflectance, with red for large reflectance and blue for low reflectance. The folded dispersion relations of the Wood's anomaly (dashed lines) and SP (solid lines) are shown. Four points, Point 1 – Point 4, are marked for studying the low reflectance flat bands.	143
8.8	The efficiency of the 0th, +1, -1, and -2 diffraction orders for Sample 2, as a function of the incident angle. The incident wave has a wavelength of 633 nm, corresponding to a He-Ne laser. The left panel shows the experimental results, and the right panel shows the numerical results obtained by RCWA. The occurrences of the Wood's anomaly are marked by dashed vertical lines.	145
8.9	(a) The near field pattern of H_y at Point 2 in Fig. 8.7. (b) The upper panel shows the direction of the incident wave. The lower panel illustrates the sinusoidal pattern of the field inside the slit.	146
8.10	Near field pattern of H_y at Point 1 in Fig. 8.7.	148
8.11	Near field pattern of H_y at Point 3 (left panel) and Point 4 (right panel) in Fig. 8.7.	149

8.12	Near field pattern of H_y for Sample 1, at an incident angle of 38° and a wavelength of 721 nm.	150
9.1	Schematic diagram showing a semiconductor grating of period L , thickness d , and slit width w . The tensorial dielectric constant is due to an external magnetic field $B_0\hat{y}$ applied in the direction parallel to the slits. The slits are filled with a medium with a scalar dielectric constant ϵ_1 and the media on both sides have scalar dielectric constants ϵ_h . Here, θ is the angle of incidence of a TM polarized electromagnetic wave.	154
9.2	The zeroth order transmission at normal incidence as a function of incident wavelength for three different values of the magnetic field $B_0 = 0, 0.20$ T and 0.33 T. Results obtained by RCWA (solid lines) and single-mode theory (Eq.(9.45)) (dashed lines) are shown for comparison.	156
9.3	A zoom-in picture of a slit. Regions I and III are semiconductor. The two regions are separated by a slit (Region II) that occupies $-w/2 < x < w/2$	157
9.4	Real and imaginary parts of the propagation constant γ for incident wavelengths from 3 mm to 20 mm and $B_0 = 0, 0.20$ T and 0.33 T. Results obtained by RCWA (solid lines) and single-mode theory (Eq.(9.23)) (dashed lines) are shown for comparison.	161
A.1	Topology of the friendship networks, Network 1, 2 and 3 (from left to right), formed at different times of the workshop. ●: Non-Chinese females, ○: Non-Chinese males, ◆: Chinese females and ▲: Chinese males. Pajek is used to create the visualizations.	174

A.2	Degree distributions $P(k)$ of the friendship networks, Network 1, 2 and 3, obtained at different times. The lines are just drawn to guide the eye.	174
A.3	The Pearson's correlation coefficient of all informants in the second survey. The participants are labeled by a number and grouped as NCF (Non-Chinese female), NCM (Non-Chinese male), CF (Chinese female), and CM (Chinese male). The dash line shows the average value of the correlation coefficient over all participants.	177
A.4	Values of $\Delta r(i, \text{group } G')$ as defined in Eq.(A.2) for every participant i against different groups $G' =$ (a) Non-Chinese females, (b) Non-Chinese males, (c) Chinese females, and (d) Chinese males. The values are shown for data collected in the second survey. The values for G' in the own group of the participant i are shown in red (squares), which are always positive.	178
A.5	The k -clique components in networks constructed from data in the (a) first and (b) second survey. A link is drawn between two participants only when they ranked each other "very familiar". Vertices connected by links with the same color (grey scale) belong to the same clique percolation component. Red vertices are shared by two CPCs or above.	180
A.6	The community structures in Activity Network 2 (upper) and 3 (lower). Symbols of different shapes (colors) are the nodes belonging to different groups. ●: Non-Chinese females, ○: Non-Chinese males, ◆: Chinese females and ▲: Chinese males. Pajek is used to create the visualizations.	182

List of Tables

1.1	The network size N , mean degree $\langle k \rangle$, exponent γ , mean shortest path length ℓ , and clustering coefficient C of some real networks that show a power-law degree distribution. This table is reproduced from part of table II of Ref. [1]. (γ exponent of in/out degree)	16
2.1	$\langle p_{win} \rangle$ and $\langle q_{win} \rangle$ values obtained by simulations and analytic calculations for the four initial configurations at $\beta = 1 - \gamma = 0.06$.	48
2.2	$\langle p_{win} \rangle$ and $\langle q_{win} \rangle$ values obtained by simulations and analytic calculations for the four initial configurations at $\beta = 1 - \gamma = 0.81$.	51
4.1	Classification of local configurations in a 1D chain with nearest neighboring connections.	79
5.1	The size, frequency of cooperation x_{Cs} and the mean degree $\langle k_s \rangle$ of the two largest clusters for the system in the steady state. $\tau = 0.3, 0.7$ and 0.8 . The system size is $N = 10^4$, each set of data is obtained by one realization.	90

A.1 Basic properties of friendship networks and randomized networks at different times of the workshop. These properties include the clustering coefficient C , the average shortest path length L , the diameter D , the modularity Q and the average degree $\langle k \rangle$. Properties of randomized networks are averaged over 10 realizations. 175

Chapter 0

Overview

Half of the 2009 Nobel Prize in Physics has been awarded to Prof. Charles K. Kao, for his “groundbreaking achievements concerning the transmission of light in fibers for optical communication” [2]. Since the development of the first generation optical fiber communication system in 1976, the worldwide communication system based on optical fibers has greatly changed our life [3]. The internet is probably the biggest change that optical fibers has brought us, and using the internet has become a part of our daily life. The World Wide Web, which is a collection of all webpages on the internet, is a huge network consists of billions of webpages that are connected by hyperlinks. The topological structure of the World Wide Web has been studied, by taking the webpages as nodes and the hyperlinks between them as edges between the nodes [4]. In fact, the research on the structure of networks has a much longer history than the history of the internet. As early as 1960s, Milgram studied on social networks and revealed the famous “Six Degrees of Separation” [5]. In recently years, with the availability of large databases, the structures of many real networks have been studied [1], e.g., the citation network [6], the protein network [7], and the mobile communication networks [8]. Alongside the studies on the network structures, researchers have been interested in dealing with effects of the structural properties of networks on dynamical processes in

networks. Such dynamical processes can be opinion formation [9, 10], decision making [11], spread of epidemics [12, 13], etc. The first part of the thesis is on the emergence of cooperation in networked entities, within the context of the prisoner's dilemma (PD) and the snowdrift game (SG). These two games are the most-studied games in game theory. This part includes Chapters 1–5 of the thesis.

Chapter 1 gives a brief review on evolutionary games and networks. For evolutionary games, the general properties of the prisoner's dilemma and the snowdrift game are introduced. For networks, several important properties of networks are introduced. The random graph and the Barabási-Albert network are then reviewed. Chapter 1 provides the background information for Chapters 2–5.

Chapter 2 gives the results on the iterated prisoner's dilemma (IPD). A theoretical study on two-strategy IPD is presented in the full payoff space spanned by two parameters β and γ . The IPD game is then numerically studied on the full payoff space. The roles played by the Tit-for-tat-like (E_{TFT}) and Always-defecting-like (E_{AUD}) strategies are investigated in detail.

Chapters 3–5 deal with the evolutionary snowdrift game. In Chapter 3, we introduce the spatial snowdrift game. By invoking the idea of comparing the payoffs to cooperators and to defectors in the last surviving patterns, we explain the phase transitions in the spatial snowdrift game. The idea can further be extended in future studies on the emergent behavior in other games.

In Chapter 4, we propose and study a multi-person version of the standard two-person snowdrift game: The N -person Snowdrift Game (NPSG). The NPSG in a well-mixed population is studied analytically and numerically. The numerical results are in good agreement with analytic results. The time evolution of cooperation is also studied analytically. Besides the well-mixed case, the NPSG is also studied on 1D chain and 2D lattices. Compared with the well-mixed case, the frequency of cooperation is suppressed by the underlying

network structure. The equilibrium frequency of cooperation is analytically worked out for the case of a 1D chain.

In Chapter 5, we study the snowdrift game on adaptive networks. The evolution of the network structure is driven by the game dynamics. Two rewiring mechanisms, the random rewiring and opinion rewiring, are imposed. By carrying out numerical simulations, it is found that the frequency of cooperation f_C is promoted in both cases. The network structure at equilibrium is examined for opinion rewiring. A semi-analytic approach is proposed to find the equilibrium f_C . The results are in qualitative agreement with simulation results.

Now, back to our story on the internet. Over the last few years, optical fibers are being laid from the operator's switching equipment all the way to our homes [3]. However, signals are still transmitted by electronic circuits inside the computers. To connect our computer to the internet, we still need an optical/electrical converter. If the electronic circuits can be replaced by photonic devices someday, it will be another revolution. However, the size and performance of the photonic devices are constrained by the diffraction limit. For chip-based optical signals that most likely to employ wavelengths of about 1500 nm, the minimum width of the optical wire is much larger than the smallest circuit width in microprocessors [14]. In recently years, studies on the surface plasmon (SP) polaritons suggest a possible way for reducing the size of photonic devices. Surface plasmon is a surface electromagnetic (EM) wave that is localized and propagating along a metal/dielectric interface. By properly designing the metal/dielectric interfaces, SP can be excited by EM wave from outside. The excited SP mode has the same frequency as the outside EM wave, but has a much shorter wavelength. Thus, SP could travel along nanoscale wires to carry information in photonic devices. Surface plasmon cannot be directly excited by light incident from the dielectric. A common method to excite surface plasmon is to use a grating. It was found

that for optically thick metallic films with patterned subwavelength holes, the SP excited on one side can be tunneled to another side and results in a much larger transmittance than predicted by classical theory. This phenomenon is referred to as enhanced transmission or extraordinary transmission, which has attracted much attention since its discovery by Ebbesen et al. in 1998 [15]. Besides the possible applications in photonic devices, SP has a wide range of exciting applications, such as enhanced spectrum [16], high efficiency lighting [17], biological sensing [18], etc. The discipline that studies the surface plasmons has been termed as plasmonics [19]. The second part of the thesis focuses on surface plasmon excitations and the optical properties of metallic gratings.

In Chapter 6, we introduce the dispersion relation of SP modes in a semi-infinite metal/linear dielectric system, and in a linear/metal/linear system. By invoking a "first integral" technique, the SP dispersion relation of a nonlinear/metal/linear system is analytically studied, where the nonlinear medium can take on arbitrary nonlinearity. For this case, the dispersion relation can be modified by tuning the electric field at the nonlinear/metal interface. The SP modes in a symmetric nonlinear/metal/nonlinear system are also discussed.

Chapter 7 introduces the formalism of the Rigorous Couple-Wave Analysis (RCWA), which is a grating theory that is commonly used to study the optical properties of periodic structures. Techniques to improve the numerical stabilities and the convergence rate are introduced. Two sample calculations are carried out to verify that the computer code that we set up is valid.

Chapter 8 discusses the optical properties of two samples of one-dimensional metallic reflection gratings. The samples are fabricated at CUHK and their reflectance are measured. Numerical calculations are carried out based on RCWA. The numerical results agree well with measured results. The phenomenon of Wood's anomaly is studied by measuring and calculating the

efficiencies of diffraction orders, and the coupling between waveguide and SP modes are examined.

Chapter 9 studies a semiconductor grating with a static magnetic field applied parallel to the slits. The dielectric constant of semiconductors becomes a tensor under a non-zero magnetic field. The numerical results based on RCWA reveal that the zeroth-order transmission peaks can be shifted and the transmittance can be enhanced by applying a moderate magnetic field. A single-mode theory is developed and results are in quantitative agreement with RCWA.

Chapters 1, Sections 6.1 and 6.2 of Chapter 6, and Chapter 7 are reviews. Other parts contain original results. All numerical results, unless stated otherwise, are obtained by the author himself. Part of the results in Chapters 4, 6, and 9 have been published in physics journals. Results in Chapter 8 have been presented in a conference. The titles of the journal articles and the conference paper are included as references. Appendix A gives the results of the development of a friendship network in an international summer school, which has been published.

Chapter 1

Review on evolutionary games and networks

This chapter gives a brief review on the properties of evolutionary games and networks. For evolutionary games, some basic properties such as the fitness, Nash equilibrium and evolutionarily stable strategy are introduced. The prisoner's dilemma and the snowdrift game are also discussed. For networks, several important properties are introduced, including the degree distribution, the clustering coefficient and the shortest path length. The random graph and the Barabási-Albert scale-free growing network are also reviewed.

1.1 The prisoner's dilemma and the snowdrift game

Game theory is a branch of mathematics that studies the behavior in strategic situations [20]. It was developed by John von Neumann and Oskar Morgenstern in the 1940s [21]. In general, the games studied in game theory consist of a number of players and a set of strategies. Traditional game theory is mainly focused on the case of two players, while evolutionary game theory typically considers a population of players instead of just two. The number of strategies can be two or more, but the two-strategy games, e.g., the prisoner's dilemma

and the snowdrift game, are the most studied cases.

1.1.1 Two-strategy games

Before we discuss the prisoner's dilemma (PD) and the snowdrift game (SG), we first discuss two-strategy games in general. Both PD and SG are special cases of the general scenario. Our discussion here mainly follows Chapter 4 of Ref. [20].

Consider two strategies A and B and a game described by a payoff matrix

$$\begin{array}{cc} & \begin{array}{cc} A & B \end{array} \\ \begin{array}{c} A \\ B \end{array} & \begin{pmatrix} a & b \\ c & d \end{pmatrix} \end{array} \quad (1.1)$$

This payoff matrix should be read as follows: A gets a payoff a when playing with A , and a payoff b when playing with B ; while B gets a payoff c when playing with A , and a payoff d when playing with B .

Consider a population of size N . Each of them can hold either strategy A or B . $x_A N$ of them are holding strategy A . Here, x_A is the frequency of strategy A . The frequency of B is then $x_B = 1 - x$. The fitness f_A and f_B are defined by

$$f_A(x) = xa + (1 - x)b, \quad (1.2)$$

$$f_B(x) = xc + (1 - x)d. \quad (1.3)$$

The evolution of x_i ($i = A$ or B) is governed by the replicator equation:

$$\dot{x}_i = x_i[f_i(x) - \Phi]. \quad (1.4)$$

where Φ is the mean fitness given by

$$\Phi = xf_A(x) + (1 - x)f_B(x). \quad (1.5)$$

From Eq.(1.4), the frequency of strategy i increases (decreases), if the fitness f_i of strategy i is larger (smaller) than the mean fitness Φ .

For the frequency of strategy A

$$\dot{x} = x(1-x)[f_A(x) - f_B(x)] . \quad (1.6)$$

The equilibria of this equation can be obtained by setting the right hand side to zero. The solutions are 0, 1, and any x between 0 and 1 that satisfies $f_A(x) = f_B(x)$.

Dominating strategy at equilibrium

By Eqs. (1.2) and (1.3),

$$f_A(x) - f_B(x) = x(a-c) + (1-x)(b-d) . \quad (1.7)$$

By determining the sign of $f_A(x) - f_B(x)$ and thus the sign of \dot{x} , the dominating strategy at equilibrium can be found as follows:

- If $a > c$ and $b > d$, A dominates.
- If $a < c$ and $b < d$, B dominates.
- If $a > c$ and $b < d$, there is an unstable equilibrium $x^* = (d-b)/(a-c+d-b)$ between 0 and 1. For $0 < x < x^*$, $\dot{x} < 0$, $x \rightarrow 0$. For $x^* < x < 1$, $\dot{x} > 0$, $x \rightarrow 1$.
- If $a < c$ and $b > d$, there is a stable equilibrium $x^* = (d-b)/(a-c+d-b)$ between 0 and 1, and two unstable equilibria: $x = 0$ and 1. For both $0 < x < x^*$ and $x^* < x < 1$, $x \rightarrow x^*$. The strategies A and B coexist at equilibrium.

Nash equilibrium

The Nash equilibrium was proposed by the Nobel laureate John Forbes Nash. The concept of Nash equilibrium for a two-strategy game is explained as follows: If two players are holding the same strategy that is a Nash equilibrium,

then neither of them can be benefited (increase the payoff) by changing his strategy. The Nash equilibrium can be divided into two categories, weak and strict. For the two-strategy game discussed before, considering two players both holding strategy A . If $a = c$, one player can switch to strategy B without changing its payoff. Under this condition, A is called a *weak Nash equilibrium*. If $a > c$, the payoff will be lowered if one switches to B , thus A is called a *strict Nash equilibrium*. Similarly, for the two-strategy game we discussed before, B is a weak Nash equilibrium if $d = b$, and a strict Nash equilibrium if $d > b$.

Evolutionarily stable strategy

The evolutionarily stable strategy (ESS), proposed by John Maynard Smith, is a Nash equilibrium that is “evolutionarily” stable [22]. It means that the selection dynamics automatically oppose other strategies to invade an ESS. If a strategy A can be taken over by a tiny portion of another strategy B , then we call that B can invade strategy A . In our case, for strategy A to be an ESS, either of the following conditions should be satisfied:

1. $a > c$,
2. $a = c$ and $b > d$.

Proof: Consider the case that the frequency of B is an infinitesimally small number ϵ , thus the frequency of A is $1 - \epsilon$. For A not to be invaded by B , Eq.(1.6) implies that $f_A(x)$ should be greater than $f_B(x)$, leading to

$$(1 - \epsilon)(a - c) > \epsilon(d - b) . \quad (1.8)$$

Since d and b are finite and ϵ is infinitesimal small, for $a \neq c$, $\epsilon(d - b)$ can be neglected and Eq.(1.8) requires $a > c$. For $a = c$, $b > d$ is required.

Similarly, for strategy B to be an ESS, either $d > b$ or $d = b$ and $c > a$ should be satisfied.

1.1.2 The prisoner's dilemma

The most extensively studied two-strategy game is the prisoner's dilemma (PD). The classical scenario of the prisoner's dilemma is as follows: The police arrested two suspects of a crime, without sufficient evidence for a conviction. The two prisoners are separated and cannot communicate with each other. The police offer each of them the same deal, i.e., to confess the crime so as to avoid a severe sentence. If one confesses (defects to the other) while the other remains silent (cooperates with the other), the defector will go free immediately while the cooperator will receive a 10-year sentence. If both confess, each of them will receive a 5-year sentence. If both remain silent, then both will be free after six months due to insufficient evidence. The payoff matrix of this story is

$$\begin{array}{cc}
 & \begin{array}{cc} \text{Remains silent } (C) & \text{Confesses } (D) \end{array} \\
 \begin{array}{c} \text{Remains silent } (C) \\ \text{Confesses } (D) \end{array} & \left(\begin{array}{cc} 6 \text{ months} & 10 \text{ years} \\ \text{goes free} & 5 \text{ years} \end{array} \right)
 \end{array} \quad (1.9)$$

A generalized form of the above payoff matrix is

$$\begin{array}{cc}
 & \begin{array}{cc} C & D \end{array} \\
 \begin{array}{c} C \\ D \end{array} & \left(\begin{array}{cc} R & S \\ T & P \end{array} \right)
 \end{array}, \quad (1.10)$$

where T stands for temptation to defect, P for punishment, R for reward and S for sucker's payoff. The ranking of the payoffs in Eq.(1.10) requires $T > R > P > S$. For repeated games, i.e., the same two players play for more than one round, an additional constraint $2R > (T + S)$ should be satisfied, since the payoff of full cooperation should be higher than alternating between cooperation and defection.

Based on the discussion on the general two-strategy game in Sec. 1.1.1, the strategy D is both a strict Nash equilibrium and an ESS. It is also the

dominating strategy at equilibrium in a well-mixed population, in which every agent can interact with all other agents.

For the convenience of both theoretical and numerical treatments, it is common to fix the values of two payoffs, and then use two variables to represent the payoffs. For example, we can fix $R = 1$ and $S = 0$, then let $T = 1 + \beta$ and $P = 1 - \gamma$. The two constraints $T > R > P > S$ and $2R > (T + S)$ can be satisfied when $0 < \beta < 1$ and $0 < \gamma < 1$. The ranges of β and γ cover the whole payoff space of the PD game.

1.1.3 The snowdrift game

The snowdrift game (SG), also called the Hawk-Dove game, is an alternate to the PD game. Consider two drivers driving home in opposite directions blocked by a snowdrift. Each driver can take one of the two actions, to get out to shovel the snowdrift (cooperate) or stay in the car (defect, or not-to-cooperate). If both start shoveling, they can share the total labor cost c for the work and enjoy the benefit b of getting home. However, if only one shovels the snowdrift, both of them can still get home, but the defector avoids the labor cost. If both of them choose to stay in the car, they have to wait for the snow to melt and receive no benefit at all.

Based on this scenario, the payoff matrix of SG can be written as

$$\begin{array}{cc} & \begin{array}{cc} C & D \end{array} \\ \begin{array}{c} C \\ D \end{array} & \left(\begin{array}{cc} R = b - c/2 & S = b - c \\ T = b & P = 0 \end{array} \right), \end{array} \quad (1.11)$$

with $b > c > 0$. Thus, the ranking of the payoff values is $T > R > S > P$. The main difference between SG and PD is the ordering of S and P , with $P > S$ for PD and $S > P$ for SG. For SG, neither C nor D is a Nash equilibrium or an ESS.

Let x_C be the frequency of cooperators. A stable equilibrium x_C^* exists in

a well-mixed population, since $T > R$ and $P < S$. The value of x_C^* is given by

$$x_C^* = \frac{S - P}{T - R + S - P} = 1 - \frac{c}{2b - c} \quad (1.12)$$

By introducing $r = c/(2b - c)$, $f_C = 1 - r$, which is a line that connecting $(1, 0)$ and $(0, 1)$ in the (r, x_C) plain. Another common treatment in dealing with SG is to define $r_1 = c/b$. In terms of r_1 , $x_C^* = 1 - 2r_1/(2 - r_1)$.

1.2 Review on networks

A network or a graph is composed of a set of vertices (nodes) with a number of edges (links) connecting them. The study of graph, called graph theory in mathematics and computer science, has a long history starting from Euler's study on the *Seven Bridges of Königsberg* in 1735. Many systems take the form of networks [1]. A few examples are the internet, the social networks of acquaintances, the collaboration networks of scientists, the air traffic networks, and neural networks. Networks with directed links are called directed networks. An example is the air traffic network, in which the nodes are the airports and the links are the airlines connecting them. A flight from airport A to airport B is a directed link initiated at A and pointing towards B . Accordingly, networks with undirected links are called undirected networks. Links can carry weights, with the weights representing costs, distances or capacities etc., depending on the system. Taking again the air traffic network as an example, the weights can be the number of flights between two airports. The number of flights from Hong Kong to Shanghai is 32 per day, while it is only 18 for flights to Beijing. Taking the weight of the link between Hong Kong and Beijing to be 1, then the link between Hong Kong and Shanghai has a weight of $32/18 = 1.78$.

1.2.1 Basic properties

Degree

For an undirected network, the degree k of a node is the number of edges that connects to the node. For a directed network, the degree is divided into two types, the indegree and the outdegree. The indegree (outdegree) of a node is the number of edges directed into (from) the node. The spread in the degrees of the nodes in a network is described by the degree distribution $P(k)$.

Clustering coefficient

In social networks, the friends of your friend have a good chance to also be your friends. The clustering coefficient (CC) is used to quantify this tendency. For a node i , if its k_i neighbors are fully connected, the total number of edges between them would be $k_i(k_i - 1)/2$. The clustering coefficient of node i is defined as the ratio between the number E_i of edges that really exist between the k_i neighbors of the node i and $k_i(k_i - 1)/2$ [23],

$$C_i = \frac{2E_i}{k_i(k_i - 1)} \quad (1.13)$$

The clustering coefficient of a network of size N is the average of C_i over all nodes,

$$C = \frac{1}{N} \sum_{i=1}^N C_i \quad (1.14)$$

Shortest path length

The shortest path between two nodes i and j is the path that connects nodes i and j with the sum of the weights of the constituting edges being minimized. This definition is also applicable to unweighted networks by assigning each edge the same weight. The sum of the weights ℓ_{ij} is called the length of the path. Many algorithms, such as the Dijkstra's algorithm, have been developed for finding the shortest path and ℓ_{ij} .

The mean shortest path length of a network of size N is the average of ℓ_{ij} over all the $\frac{N(N-1)}{2}$ i - j pairs,

$$\ell = \frac{1}{N(N-1)/2} \sum_i \sum_{j>i} \ell_{ij}. \quad (1.15)$$

This definition becomes problematic if the networks is disconnected [1]. An alternative way is to define $1/\ell$ as the average of reciprocals $1/\ell_{ij}$,

$$\frac{1}{\ell} = \frac{1}{N(N-1)/2} \sum_i \sum_{j>i} \frac{1}{\ell_{ij}}. \quad (1.16)$$

The **diameter** D of a network is the largest ℓ_{ij} among all pairs of nodes in the network.

1.2.2 Random Graph

The random graph is the most studied model in graph theory. It was introduced by Paul Erdős and Alfréd Rényi [24]. A random graph of N nodes and n edges is constructed by randomly choosing n edges from the $N(N-1)/2$ possible edges. An alternative definition is the binomial model: For the N nodes, each pair of nodes is connected with probability p . The expectation value of the total number of links is $p[N(N-1)/2]$. Under the condition that $n = p[N(N-1)/2]$, the two definitions give the same result.

For a random graph of size N and probability p , the average degree $\langle k \rangle = p(N-1) \simeq pN$. The degree distribution follows a binomial distribution

$$P(k_i = k) = \binom{N-1}{k} p^k (1-p)^{N-1-k}. \quad (1.17)$$

For large N , it can be approximated by a Poisson distribution

$$P(k) \simeq e^{-\langle k \rangle} \frac{\langle k \rangle^k}{k!}. \quad (1.18)$$

Figure 1.1 shows the degree distribution of a random graph obtained by numerical simulations for systems of size $N = 1001$ and probability $p = 0.05$. The results agree well with Eq.(1.18).

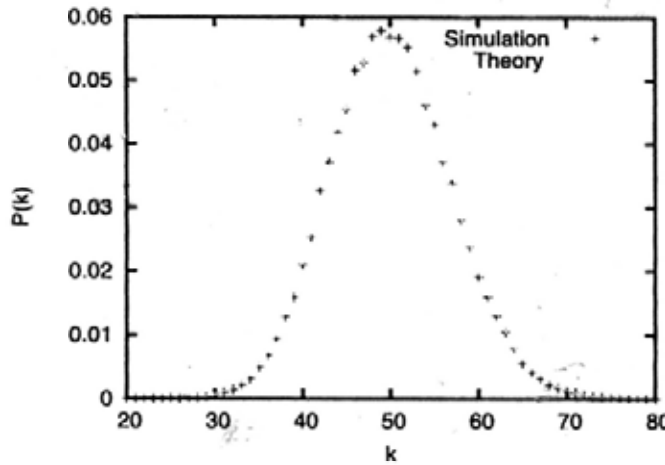


Figure 1.1: The degree distribution of a random graph of size $N = 1001$ and probability $p = 0.05$ obtained by numerical simulations (symbols). The theoretical result given by Eq.(1.18) is shown for comparison (line). Each data point is an average over 100 realizations.

By definition, the connecting probability of two neighbors of an arbitrary node i in a random graph is equal to the connecting probability of two randomly selected nodes, which is p . So the clustering coefficient of a random graph is

$$C_{rand} = p = \frac{\langle k \rangle}{N}. \quad (1.19)$$

For fixed $\langle k \rangle$, $C_{rand} \propto N^{-1}$.

The average path length of a random graph follows $\ell_{rand} \sim \frac{\ln(N)}{\ln(\langle k \rangle)}$ [23], which means that a random graph has the small-world effect. A network is said to show the small-world effect if ℓ scales with or slower than $\ln(N)$ for fixed $\langle k \rangle$ [1].

1.2.3 Barabási-Albert Network

In recently years, studies on real networks reveal that many of them are scale free, i.e, the degree distribution follows a power law at large k , $P(k) \sim k^{-\gamma}$

network	N	$\langle k \rangle$	γ	ℓ	C
film actors [26, 27]	449, 913	113.43	2.3	3.48	0.2
WWW Altavista [28]	203, 549, 046	10.46	2.1/2.7 ¹	16.18	-
citation network [6]	783, 339	8.57	3	-	-
Internet [29, 30]	10, 697	5.98	2.5	3.31	0.035
metabolic network [31]	765	9.64	2.2	2.56	0.09
protein interactions [7]	2, 115	2.12	2.4	6.80	0.072

Table 1.1: The network size N , mean degree $\langle k \rangle$, exponent γ , mean shortest path length ℓ , and clustering coefficient C of some real networks that show a power-law degree distribution. This table is reproduced from part of table II of Ref. [1]. (¹exponent of in/out degree)

[23, 1]. Table 1.1 lists the power law exponents and some other properties for a collection of real networks. The power-law degree distribution of these real networks is quite different from that of the classical random graph, for which the degree distribution follows a Poisson distribution. Inspired by this fact, Barabási and Albert [25] proposed the so called Barabási-Albert (BA) model, which gives a possible origin of the power-law degree distribution. The key ideas are *growing network* and *preferential attachment*.

The growth of a BA network starts with m_0 nodes, with the degree of each of them be greater or equal to m . Here $m \leq m_0$ is an integer. At every time step, a new node is added, with m links to be established with m different existing nodes. The probability p that a new node will be connected to an existing node j depends on the degree k_j of node j :

$$p(k_j) = \frac{k_j}{\sum_{i=0}^N k_i} \quad (1.20)$$

This mechanism of establishing new links is called *preferential attachment*.

The degree distribution of BA networks has been derived theoretically by

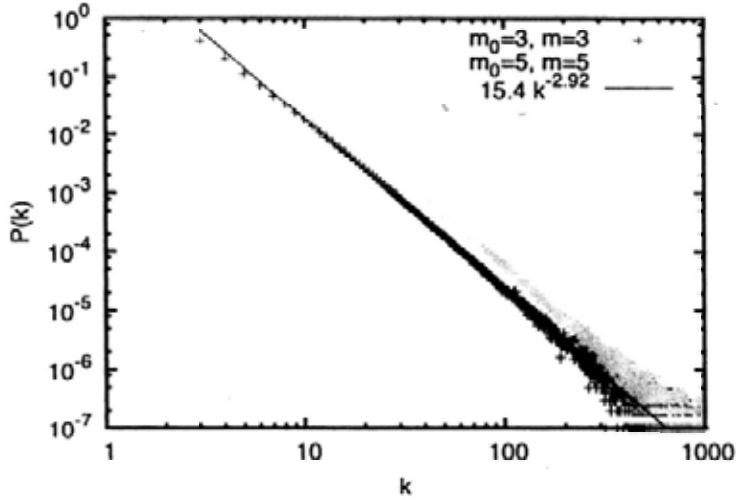


Figure 1.2: The degree distribution $P(k)$ of BA networks of size $N = 10^6$ with $m_0 = m = 3$ and $m_0 = m = 5$. The linear fit of the $m_0 = 3$ case (blue line) gives a slope of -2.92 . Each data point is an average over 10 realizations.

different methods [25, 32, 33]. Here we just give the result

$$P(k) \sim k^{-\gamma} = k^{-3}, \quad (1.21)$$

which is independent of m . Figure 1.2 shows the degree distribution of BA networks with $m_0 = m = 3$ and $m_0 = m = 5$ obtained by numerical simulations. The best fit in the $m = 3$ case gives an exponent $\gamma = 2.92$, which is very close to the theoretical prediction of $\gamma = 3$.

The clustering coefficient of a BA network can be expressed as [34]

$$C = \frac{m^2(m+1)^2}{4(m-1)} \left[\ln\left(\frac{m+1}{m}\right) - \frac{1}{m+1} \right] \frac{[\ln(N)]^2}{N}. \quad (1.22)$$

A comparison between Eq.(1.22) and simulation results is shown in Fig. 1.3, and good agreement is obtained. The mean shortest path length of a BA network is given by $\ell \sim \ln(N)/\ln \ln(N)$ for $m \geq 2$, and $\ell \sim \ln(N)$ for $m = 1$ [35].

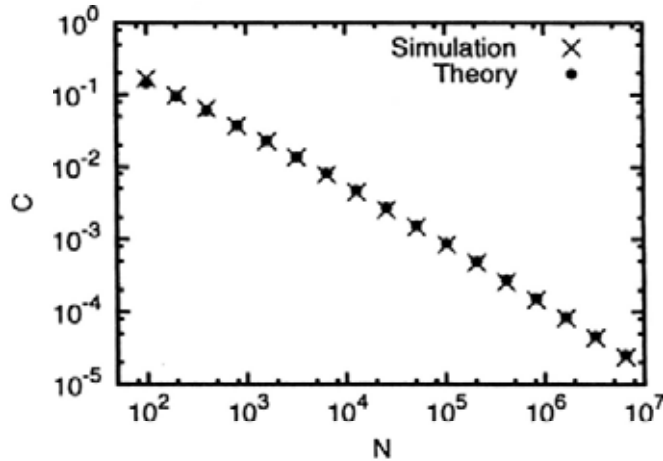


Figure 1.3: The clustering coefficient C versus N for BA networks with $m_0 = m = 3$. The simulation results (black crosses) and results given by Eq.(1.22) (red dots) are shown. Each simulation data point is an average over 10 realizations.

1.3 Conclusion

In this chapter, we reviewed the properties of evolutionary games and networks. For evolutionary games, we introduced some basic properties and discussed the prisoner's dilemma and the snowdrift game. For networks, we introduced several basic properties, such as the degree distribution and the clustering coefficient. The random graph and the BA network are also reviewed. The concepts we discussed in this chapter will be used in Chapters 2–5 and Appendix A.

Chapter 2

The Iterated Prisoner's Dilemma

In this chapter, we first give a review on previous studies on the iterated prisoner's dilemma (IPD) game, including Axelrod's famous experiment and related works. The two-strategy IPD game is then analytically investigated. The IPD game is studied in the full payoff-space spanned by β and γ , using four types of initially configurations. Both numerical and analytical investigations are carried out. It is found that for systems with the two strategies E_{TFT} and E_{AUD} added initially, the dominating area of generous strategies in the payoff space is the largest among the four initial configurations. The roles played by E_{TFT} and E_{AUD} are further studied on the diagonal and anti-diagonal lines of the payoff space. The winning strategies for small and large β values along the anti-diagonal line are analytically predicted.

2.1 Review of previous works on IPD

It is well known that evolution is based on fierce competitions. Thus only selfish behavior should be rewarded [36]. Yet cooperation exists everywhere and it is an essential element of our society. Why and how can cooperation emerge in a group of egoists? Studies on iterated games, such as the IPD, provide a possible answer.

We begin the story by introducing a famous experiment conducted by Robert Axelrod around 1980 [37]. In the experiment, Axelrod invited experts in game theory to submit computer programs to play the IPD game with the payoff matrix

$$\begin{array}{cc} & \begin{array}{cc} C & D \end{array} \\ \begin{array}{c} C \\ D \end{array} & \left(\begin{array}{cc} R = 3 & S = 0 \\ T = 5 & P = 1 \end{array} \right) \end{array} \quad (2.1)$$

For the first tournament, fourteen strategies were submitted. The lengths of the strategies ranged from 4 lines to 77 lines in Fortran. A random strategy, which randomly chooses to cooperate or defect with equal probability, was also introduced. Thus there were fifteen strategies in total. Each strategy competes with itself and every other strategy in one move, with a total of two hundred moves. Surprisingly, the winner was found to be the strategy with the shortest length, named the Tit-for-tat (TFT) strategy, submitted by Anatol Rapoport at the University of Toronto. The TFT strategy cooperates in the first move, and then repeats the opponent's action in the previous move. To further investigate the role of TFT, Axelrod conducted the second tournament. The strategy pool of the second tournament was much larger than the first one, including 62 strategies plus a random strategy. Instead of repeating exactly 200 moves, a continuing probability $w = 0.99654$ was introduced. With probability w , the same two players will play for another move. Once again, TFT won the second tournament. By comparing the behavior and payoffs of different strategies, Axelrod concluded that the robust success of TFT came from "its combination of being nice, retaliatory, forgiving, and clear." [37]

Nowak and Sigmund studied the role played by TFT in heterogeneous populations [38]. They used a triplet (y, p, q) to represent a strategy, where y is the probability to cooperate at the first round, p (q) is the conditional probability to cooperate given that the opponent's last action is C (D). It is obvious that $0 \leq p \leq 1$ and $0 \leq q \leq 1$. This set up covers several key

strategies, including TFT (1, 1, 0), always defecting (AllD) (0, 0, 0), and always cooperating (AllC) (1, 1, 1).

They studied the infinitely IPD ($w = 1$) of a total of 100 strategies. In this case, the final outcome is independent of the action in the first round, and the two parameters (p, q) are sufficient to represent a strategy. Among the 100 strategies, 99 were placed randomly on the p - q space, and one TFT-like strategy (0.99, 0.01) was added by hand. For Axelrod's payoff values in Eq.(2.1), they found that the presence of a tiny portion of TFT-like strategy at the beginning could lead to the dominance of generous Tit-for-tat (GTFT) strategies in the long run. A GTFT strategy refers to one with a large p and a non-zero but small q . Thus, they concluded that TFT strategy serves as the pivot that leads the evolution toward cooperation.

In a noisy environment, the performance of TFT strategy becomes worse. Here, noise means that a player will occasionally take the action that contradicts to the prediction of its strategy by mistake. Consider two players both using TFT, they will always cooperate in a noise-free environment. Once noise is introduced, e.g., one player chooses to defect after a C action of the other player by mistake, then they begin to punish each other in the long run, which largely reduces the total payoff of the system. Some other strategies, such as GTFT [39] and the Pavlov strategy [40], were found to be more robust than TFT, when playing in a noisy environment. A holder of GTFT has a nonzero probability q to cooperate when the opponent defected in the previous round. This generosity makes GTFT more robust than TFT when playing in a noisy environment. A player of the Pavlov strategy repeats its previous action if it received a high payoff, i.e., R or T , in the previous round, but switches its action if it received a punishing payoff P or S in the previous round. This strategy cannot be represented in the (p, q) space. However, it can be defined by introducing a vector (p_1, p_2, p_3, p_4), where p_1, p_2, p_3 , and p_4 are the conditional probabilities to cooperate after receiving a payoff of R, S, T , and P in

the previous round. The Povlov strategy is $(1, 0, 0, 1)$, while TFT is $(1, 0, 1, 0)$ in this representation.

Motivated by the work of Nowak and Sigmund [38], we study the infinitely IPD game beyond the Axelrod's payoff values, including the *whole* payoff space of PD game. We intend to investigate the role played by TFT for payoff values other than Axelrod's, and understand the evolution process analytically. To cover the whole payoff space of the PD game, we set $R = 1$ and $S = 0$. The values of P and T are related to R and S using two variables β and γ . The payoff matrix is

$$\begin{array}{cc} & \begin{array}{cc} C & D \end{array} \\ \begin{array}{c} C \\ D \end{array} & \left(\begin{array}{cc} 1 & 0 \\ 1 + \beta & 1 - \gamma \end{array} \right), \end{array} \quad (2.2)$$

with $0 < \beta < 1$ and $0 < \gamma < 1$. The β - γ space covers all possible payoff values. Axelrod's payoff values correspond to a single point with coordinate $(\frac{2}{3}, \frac{2}{3})$ in the payoff space.

The system we considered contains n reactive strategies of the type $E_i = (p_i, q_i)$. The frequency of strategy E_i at time t is denoted by $x_i(t)$, with $\sum_i^n x_i(t) = 1$. For infinitely IPD, the payoff obtained by a strategy E_i when playing against E_j is [41]

$$A(E_i, E_j) = c_i c_j (R - S - T + P) + c_i (S - P) + c_j (T - P) + P, \quad (2.3)$$

where the parameters c_i and c_j are given by

$$c_i = \frac{q_i + d_i q_j}{1 - d_i d_j} \quad (2.4)$$

$$c_j = \frac{q_j + d_j q_i}{1 - d_i d_j} \quad (2.5)$$

with $d_i = p_i - q_i$. For a strategy E_i playing against itself, c_i can be simplified to the form denoted by

$$s_i = \frac{q_i}{1 - d_i}. \quad (2.6)$$

For the payoff values given by Eq.(2.2), c_i , c_j and $A(E_i, E_j)$ are positive for all possible combinations of E_i and E_j .

The fitness of strategy E_i at time t is defined as

$$f_i(t) = \sum_{j=1}^n x_j(t) A(E_i, E_j) , \quad (2.7)$$

which is the mean payoff E_i obtained when competing with all strategies. The mean fitness is

$$\begin{aligned} \Phi(t) &= \sum_{i=1}^n x_i(t) f_i(t) \\ &= \sum_{i=1}^n \sum_{j=1}^n x_i(t) x_j(t) A(E_i, E_j) . \end{aligned} \quad (2.8)$$

The evolutionary dynamics of x_i follows the replicator equation

$$x_i(t+1) = x_i(t) f_i(t) / \Phi(t) . \quad (2.9)$$

Strategies with a fitness higher (lower) than the mean fitness have their frequencies increased (decreased) in the next time step. Equation (2.9) keeps the normalization of frequencies.

Li extended the work of Nowak and Sigmund to the case of $\gamma = \beta$ [42], i.e., the diagonal line in the β - γ space. It was found that GTFT strategies only dominate in an intermediate range along this line. For β values outside this range, the system is dominated by defecting strategies that have small (p, q) values. The diagonal line is later studied by Chan et al. [43], with a slightly-modified initial condition. In addition to the TFT-like strategy $E_{TFT} = (0.99, 0.01)$ added into the system by hand initially, they also included an AllD-like strategy $E_{AUD} = (0.01, 0.01)$. Surprisingly, the emergence of GTFT strategies becomes very robust in the large β region. They went on to explain this effect by analytically studying a two-strategy game with the strategies E_{TFT} and E_{AUD} . Chan [44] studied IPD in the whole payoff space, with fixed strategies that form a lattice in the p - q space.

Here we study the IPD in the whole payoff space in a more detailed way. Our work is motivated by the following questions.

- What are the behavior of the dominating strategies of any payoff value in the whole payoff space?
- What are the roles played by E_{TFT} and E_{AUD} for payoff values other than those on the diagonal line?
- How the winning strategies emerge from a collection of strategies with equal initial fraction?
- Can the results be understood analytically?

2.2 Two-strategy IPD Game

Before introducing the numerical results, we give a theoretical study on the two-strategy IPD game, which will be very useful for our later discussions. We study analytically the simplest case of IPD in a system consisting only of two strategies $E_1 = (p_1, q_1)$ and $E_2 = (p_2, q_2)$. The frequencies of E_1 and E_2 are x and $1 - x$, respectively. According to Eq.(2.7), the fitness of E_1 and E_2 are

$$f_1 = xA(E_1, E_1) + (1 - x)A(E_1, E_2), \quad (2.10)$$

$$f_2 = (1 - x)A(E_2, E_2) + xA(E_2, E_1). \quad (2.11)$$

The mean fitness is $\Phi = xf_1 + (1 - x)f_2$. The evolution of x is governed by the replicator equation

$$\dot{x} = x f_1 / \Phi. \quad (2.12)$$

Both f_1 and Φ are positive, so whether x will grow or drop is determined by whether $f_1 > \Phi$ or $f_1 < \Phi$ and thus the sign of $f_1 - \Phi$. We note that

$$\begin{aligned} (f_1 - \Phi) &= (1 - x)(f_1 - f_2) \\ &= (1 - x)[x(A(E_1, E_1) - A(E_2, E_1)) + (1 - x)(A(E_1, E_2) - A(E_2, E_2))] . \end{aligned} \quad (2.13)$$

Defining

$$K(E_i, E_j) = A(E_i, E_j) - A(E_j, E_j) , \quad (2.14)$$

Equation (2.13) becomes

$$(f_1 - \Phi) = (1 - x)[(1 - x)K(E_1, E_2) - xK(E_2, E_1)] . \quad (2.15)$$

Since both x and $1 - x$ are positive, so the following conclusions can be drawn:

- If $K(E_1, E_2)$ and $K(E_2, E_1)$ have opposite signs, then $[(1 - x)K(E_1, E_2) - xK(E_2, E_1)]$ and $K(E_1, E_2)$ have the same sign. If $K(E_1, E_2) > 0$, $\dot{x} > 0$, strategy E_1 will replace E_2 definitely. If $K(E_1, E_2) < 0$, E_2 will replace E_1 .
- If $K(E_1, E_2)$ and $K(E_2, E_1)$ have the same sign, then the sign of \dot{x} will be related to their relative frequencies.

2.2.1 Determine the sign of $K(E_i, E_j)$

By Eqs. (2.3) and (2.14),

$$\begin{aligned} K(E_i, E_j) &= A(E_i, E_j) - A(E_j, E_j) \\ &= (c_i c_j - s_i s_j)(R - S - T + P) + (c_i - s_j)(S - P) + (c_j - s_j)(T - P) \\ &= (1 - \beta - \gamma)[d_j c_i^2 - d_j s_j c_i + c_i s_j - s_j^2] + (c_i - s_j)[\gamma - 1 + d_j(\beta + \gamma)] \\ &= (c_i - s_j)B(E_i, E_j) , \end{aligned} \quad (2.16)$$

where $B(E_i, E_j) = [(1 - \beta - \gamma)(d_j c_i + s_j) + \gamma - 1 + d_j(\beta + \gamma)]$. So the sign of $K(E_i, E_j)$ is related to the signs of $(c_i - s_j)$ and $B(E_i, E_j)$.

It can be proved that $c_i - c_j$, $c_i - s_j$, and $s_i - s_j$ always share the same sign [41]. So the sign of $c_i - s_j$ can be obtained once we know the sign of $s_i - s_j$, which can be determined readily. Consider the strategy $E_j = (p_j, q_j)$, q_j can

be written as a function of s_j using Eq.(2.6):

$$q_j = \frac{1}{\frac{1}{s_j} - 1}(1 - p_j), \tag{2.17}$$

which is a line that connects (p_j, q_j) to the TFT corner $(1, 0)$ in the p - q space with a slope $-\frac{1}{1/s_j - 1}$. The absolute value of the slope is

$$l_j = \frac{1}{\frac{1}{s_j} - 1} = \frac{q_j}{1 - p_j}. \tag{2.18}$$

If $E_i = (p_i, q_i)$ lies along this line, $c_i - s_j = 0$, thus $K(E_i, E_j) = K(E_j, E_i) = 0$. When E_i plays against E_j , it does as well as E_j does against itself. This line divides the p - q space into two regions. We call the area above the line Region A, and the area below the line Region B (see Fig. 2.1). For a strategy E_i lies in Region A, $l_i > l_j$, so $s_i - s_j < 0$ and thus $c_i - s_j < 0$. Following a similar consideration, for E_i in Region B, $c_i - s_j > 0$. The sign of $c_i - s_j$ for a given strategy E_j and an arbitrary E_i is shown in Fig. 2.1 schematically.

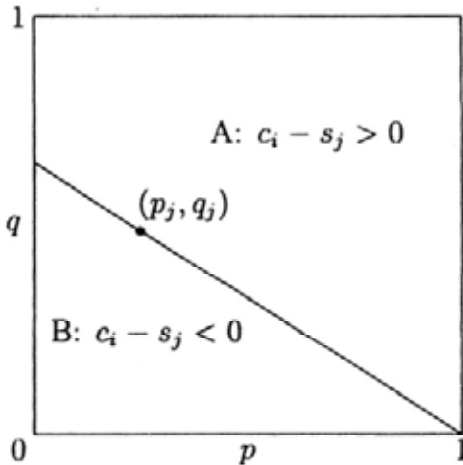


Figure 2.1: The sign of $c_i - s_j$ for an arbitrary strategy E_i , given a strategy $E_j = (p_j, q_j)$.

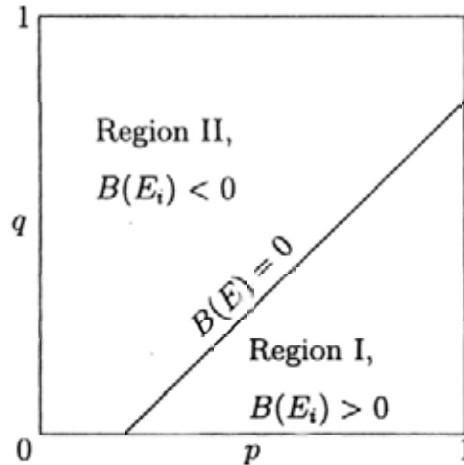


Figure 2.2: The sign of $B(E_i)$ of an arbitrary strategy E_i under the condition that $\beta + \gamma = 1$.

The sign of $B(E_i, E_j)$, which is related to both E_i and E_j , is difficult to determine in general. However, under the condition that $\beta + \gamma = 1$, $B(E_i, E_j)$

becomes a function of E_j only, with $B(E_i, E_j) = B(E_j) = p_j - q_j - \beta$. The sign of $B(E_j)$ can then be determined easily[41]. For a given β , $B(E) = p - q - \beta = 0$ is a line in the p - q space. The whole p - q space is divided into two regions by this line. For a strategy E_i that lies in the region towards the southeast corner of this line (Region I), $B(E_i) > 0$. For E_i that lies in the other region (Region II), $B(E_i) < 0$ (see Fig. 2.2).

2.2.2 The invasion problem

Based on our previous discussions, the winner of the two-strategy game between E_1 and E_2 can be determined when $\beta + \gamma = 1$. For a given β value, if E_1 lies in Region I (see Fig. 2.3):

- E_2 in IA: $c_2 - s_1 > 0$, $B(E_2, E_1) > 0$ and $B(E_1, E_2) > 0$, so $K(E_2, E_1) > 0$ and $K(E_1, E_2) < 0$. E_2 can invade E_1 .
- E_2 in IB: $c_2 - s_1 < 0$, $B(E_2, E_1) > 0$ and $B(E_1, E_2) > 0$, so $K(E_2, E_1) < 0$ and $K(E_1, E_2) > 0$. E_1 can invade E_2 .
- E_2 in IIA and IIB: $B(E_2, E_1) > 0$ and $B(E_1, E_2) < 0$, thus $K(E_2, E_1)$ and $K(E_1, E_2)$ always share the same sign. The invasion relation depends on their frequencies.

If E_1 lies in Region II (see Fig. 2.4):

- E_2 in IA and IB: $B(E_2, E_1) < 0$ and $B(E_1, E_2) > 0$. $K(E_2, E_1)$ and $K(E_1, E_2)$ always share the same sign. The invasion relation depends on their frequencies.
- E_2 in IIA: $c_2 - s_1 > 0$, $B(E_2, E_1) < 0$ and $B(E_1, E_2) < 0$, so that $K(E_2, E_1) < 0$ and $K(E_1, E_2) > 0$. E_2 can be invaded by E_1 .
- E_2 in IIB: $c_2 - s_1 < 0$, $B(E_2, E_1) < 0$ and $B(E_1, E_2) < 0$, so that $K(E_2, E_1) > 0$ and $K(E_1, E_2) < 0$. E_2 can invade E_1 .

For general cases of arbitrary β and γ and arbitrary E_2, E_1 , once we determined the sign of $B(E_2, E_1)$, the previous arguments still hold.

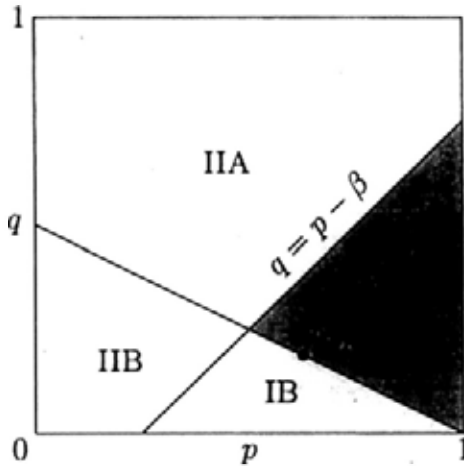


Figure 2.3: For a given β under the condition that $\beta + \gamma = 1$, a strategy (p_1, q_1) in Region I can invade any strategy in IB. Meanwhile, it can be invaded by any strategy in IA.

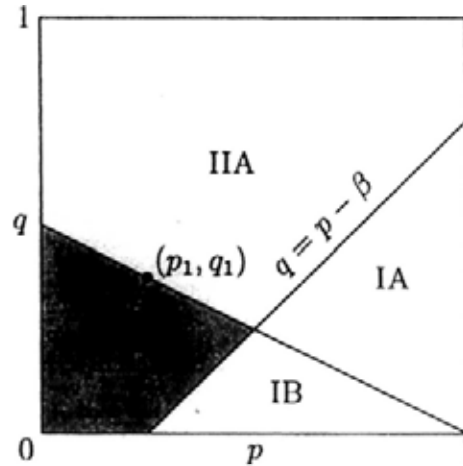


Figure 2.4: For a given β under the condition that $\beta + \gamma = 1$, a strategy (p_1, q_1) in Region II can invade any strategy in IIA. Meanwhile, it can be invaded by any strategy in IIB.

To sum up, if $B(E_1, E_2)$ shares the same sign as $B(E_2, E_1)$, then one strategy can definitely invade another strategy. If $B(E_1, E_2)$ and $B(E_2, E_1)$ have different signs, then the competitiveness of the two strategies depends on their relative frequencies.

Threshold frequency x_c

For later discussions, it is useful to define a threshold frequency x_c for strategy E_1 . For $x > x_c$, strategy E_1 can take over the whole population of strategy E_2 when playing a two-strategy game against E_2 . Under the condition that $B(E_1, E_2)$ and $B(E_2, E_1)$ share the same sign, $x_c = 0$ or 1 , depending on whether E_1 can invade E_2 or not.

When $B(E_1, E_2)$ and $B(E_2, E_1)$ have different signs, $0 < x_c < 1$. Here we derive the expression of x_c . For E_1 to replace E_2 , the fitness f_1 of E_1 should be greater than the fitness f_2 of E_2 . By Eq.(2.7), we have

$$xA(E_1, E_1) + (1-x)A(E_1, E_2) > (1-x)A(E_2, E_2) + xA(E_2, E_1). \quad (2.19)$$

Thus we can obtain an inequality,

$$x > \frac{A(E_2, E_2) - A(E_1, E_2)}{A(E_1, E_1) - A(E_1, E_2) + A(E_2, E_2) - A(E_2, E_1)} \equiv x_{th}. \quad (2.20)$$

Noticing that $0 \leq x_c \leq 1$, x_c can be defined as

$$x_c = \begin{cases} 0, & x_{th} \leq 0, \\ x_{th}, & 0 < x_{th} < 1, \\ 1, & x_{th} \geq 1. \end{cases} \quad (2.21)$$

2.3 Two-parameter IPD

Here, we study the IPD game in the whole payoff space. The system we studied consists of 100 strategies, each of them has the same initial frequency $x_{init} = 0.01$. Four types of initial configurations are studied:

- Type 0 (T0) — 100 stochastic strategies.
- Type 1 (T1) — A TFT-like strategy $E_{TFT} = (0.99, 0.01)$ and 99 stochastic strategies.
- Type 2 (T2) — An AllD-like strategy $E_{AUD} = (0.01, 0.01)$ and 99 stochastic strategies.
- Type 3 (T3) — E_{TFT} , E_{AUD} , together with 98 stochastic strategies.

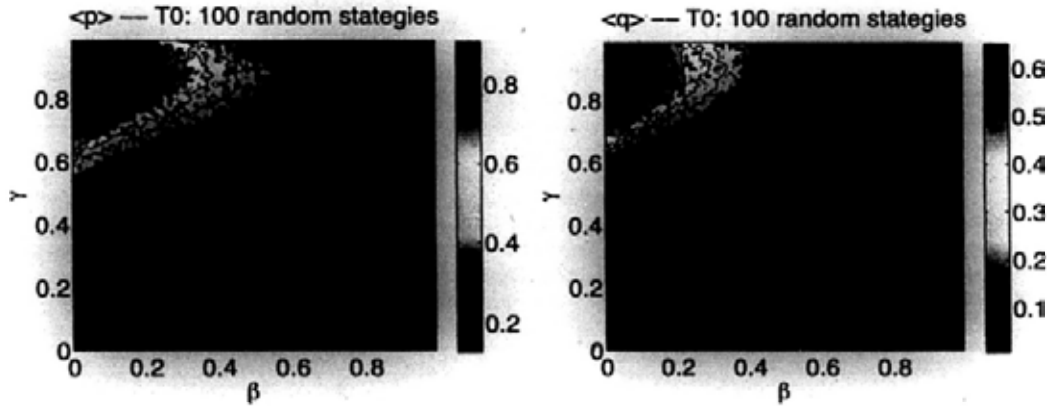


Figure 2.5: $\langle p \rangle$ and $\langle q \rangle$ for systems with initial configuration T0 in the β - γ space. Results are obtained by averaging over 100 realizations.

A cutoff frequency $x_{\min} = 10^{-10}$ is introduced in our simulations to model a system with finite population [43]. If the frequency of a strategy drops below x_{\min} , the strategy will be removed. In a single run, IPD is played for 10^6 time steps, and it is found to be sufficiently long for the system to reach the steady state for most cases. At the end of each run, the mean values of p and q of the surviving strategies are calculated:

$$p_{\text{mean}} = \sum_{i=1}^{100} x_i p_i, \quad q_{\text{mean}} = \sum_{i=1}^{100} x_i q_i. \quad (2.22)$$

Note that $x_i = 0$ for extinct strategies. In most realizations, there is only one surviving strategy $E_s \leftarrow (p_s, q_s)$ at equilibrium. For these cases, $(p_{\text{mean}}, q_{\text{mean}}) = (p_s, q_s)$.

For each type of initial configuration, M realizations is run for a certain payoff value. The average values of p_{mean} and q_{mean} over these M realizations are

$$\langle p \rangle = \frac{1}{M} \sum p_{\text{mean}}, \quad \langle q \rangle = \frac{1}{M} \sum q_{\text{mean}}. \quad (2.23)$$

$\langle p \rangle$ and $\langle q \rangle$ reflects the behavior of the dominating strategies of the steady state. The values of $\langle p \rangle$ and $\langle q \rangle$ for the four types of initial configurations are shown as contour plots in Figs. 2.5–2.8.

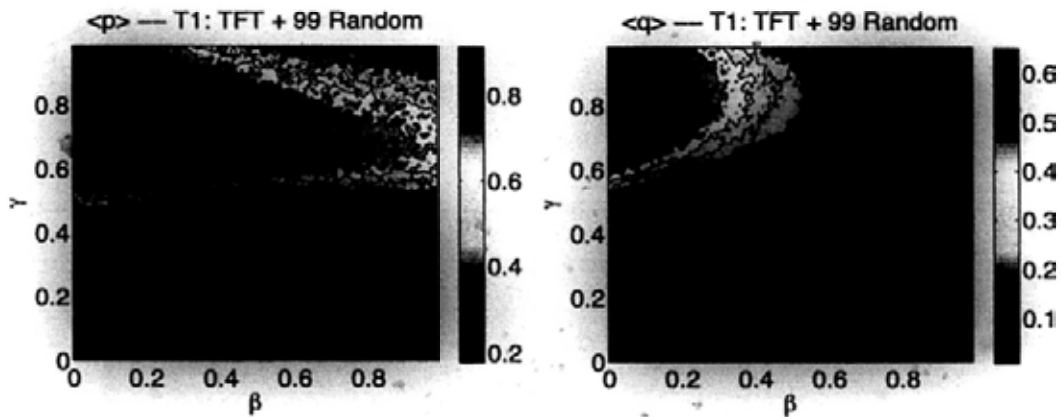


Figure 2.6: $\langle p \rangle$ and $\langle q \rangle$ for systems with initial configuration T1 in the β - γ space. Results are obtained by averaging over 100 realizations.

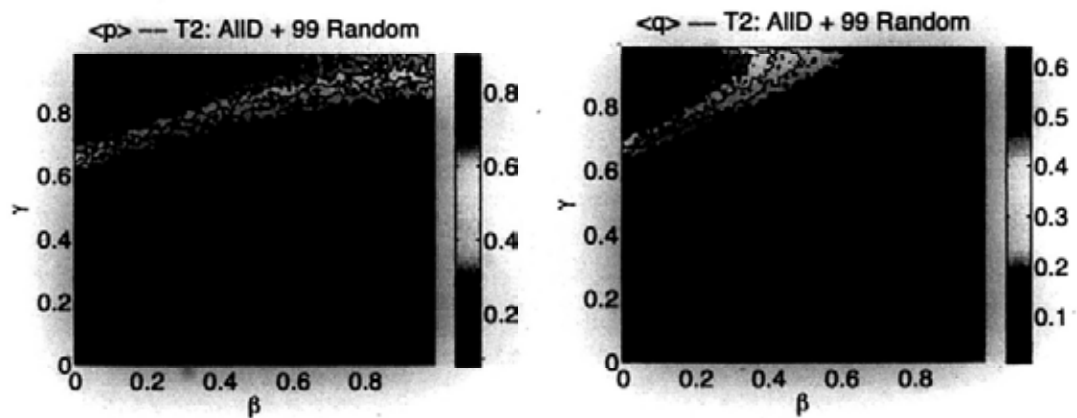


Figure 2.7: $\langle p \rangle$ and $\langle q \rangle$ for systems with initial configuration T2 in the β - γ space. Results are obtained by averaging over 100 realizations.

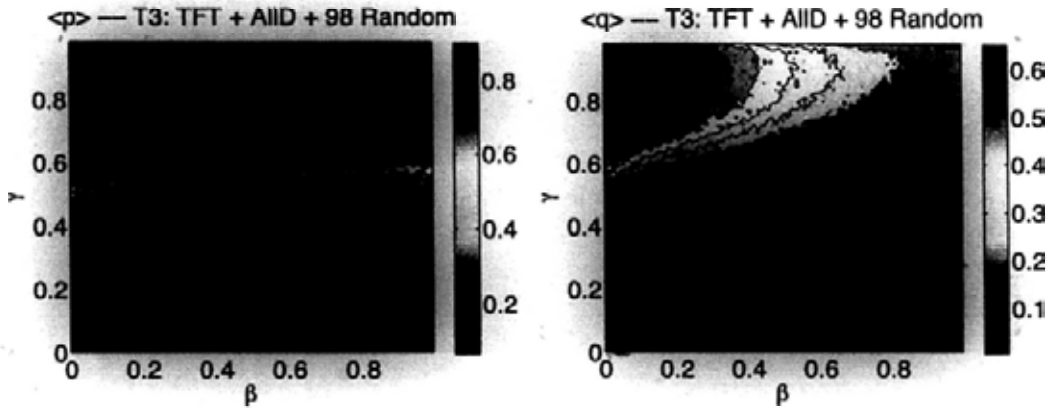


Figure 2.8: $\langle p \rangle$ and $\langle q \rangle$ for systems with initial configuration T3 in the β - γ space. Results are obtained by averaging over 100 realizations.

For all four initial configurations, the lower half part ($\gamma < 0.5$) of the β - γ space is occupied by blue and deep blue colors, corresponding to the dominance of defecting strategies that have small $\langle p \rangle$ and $\langle q \rangle$ values. The upper left-hand corner of β - γ space is the cooperative region that has large $\langle p \rangle$ and $\langle q \rangle$ values (in deep red and red colors). The area of this region is smallest for the initial configuration T0, and increases as the initial configuration changes to T2, T1 and T3. For initial configuration T3, the whole upper half plane is dominated by large $\langle p \rangle$ values, with $\langle q \rangle$ decreasing as β increases. Thus the dominance of cooperative strategies gradually changes into TFT-like strategies (large $\langle p \rangle$ and small $\langle q \rangle$) as β increases. To see the effect of different initial configurations more clearly, we divide the payoff space into three regions, according to the values of $\langle p \rangle$ and $\langle q \rangle$:

- AllD-like Region: $\langle p \rangle \leq 0.5$ and $\langle q \rangle \leq 0.5$.
- TFT-like Region: $\langle p \rangle > 0.5$ and $\langle q \rangle < 0.5$.
- AllC-like Region: $\langle p \rangle > 0.5$ and $\langle q \rangle > 0.5$.

Figure 2.9 shows the results in Figs. 2.5–2.8 in terms of these three regions. We intend to call AllC-like and TFT-like strategies generous strategies,

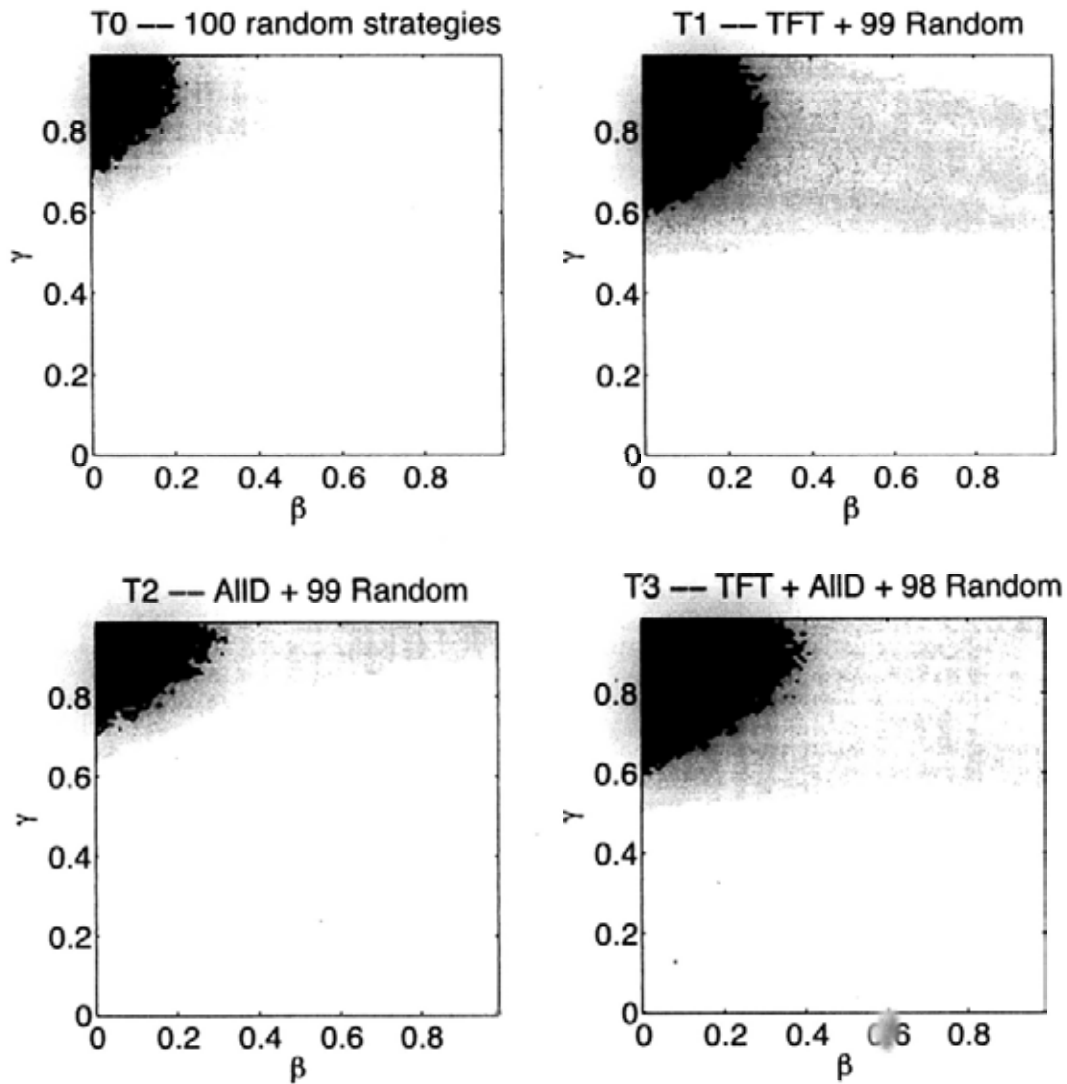


Figure 2.9: The coverage of the three regions in the payoff space for the four types of initial configurations. White color for AllD-like region, green for TFT-like region, and red for AllC-like region.

since they are likely to cooperate with cooperating opponents. While AllD-like strategies intend to always defect, thus we call them egotistic strategies. In Fig. 2.9, the dominating area of generous strategies of T2 is larger than T0, which means that a system with a small portion of E_{TFT} added initially can do better than a system consisting of only random strategies. By adding both E_{AllD} and E_{TFT} initially, the area of generous strategies is the largest among the four initial configurations. The results indicate that a small fraction of very egotistic strategy E_{AllD} added initially can help E_{TFT} to extend the dominating area of generous strategies. This result is rather surprising. To further investigate the roles played by E_{AllD} and E_{TFT} in the evolution process, we study the IPD game along the diagonal and anti-diagonal lines of the β - γ space in detail. The diagonal line has been studied by Li and Chan et al. previously, here we continue on their works. The anti-diagonal line is chosen because it crosses the three regions for all four initial configurations and it can be treated theoretically.

2.3.1 Diagonal line

By setting $\gamma = \beta$ and varying the value of β , we get the dominating strategies along the diagonal line in the payoff space. Figure 2.10 shows $\langle p \rangle$ and $\langle q \rangle$ as a function of β for the four types of initial configurations.

For $\beta < 0.45$, the curves of both $\langle p \rangle$ and $\langle q \rangle$ are nearly parallel to the x axis and they can be divided into two categories. The first category consists of T0 and T1, with $\langle p \rangle \sim 0.33$ and $\langle q \rangle > 0.01$. The second category consists of T2 and T3, with $\langle p \rangle < 0.2$ and $\langle q \rangle < 0.01$. The main difference between these two categories is that E_{AllD} is added initially in the second category. Thus we can conclude that E_{AllD} plays a key role in reducing $\langle p \rangle$ and $\langle q \rangle$ values at small β region.

For $\beta > 0.5$, T2 has larger $\langle p \rangle$ and $\langle q \rangle$ values compared with T0, with

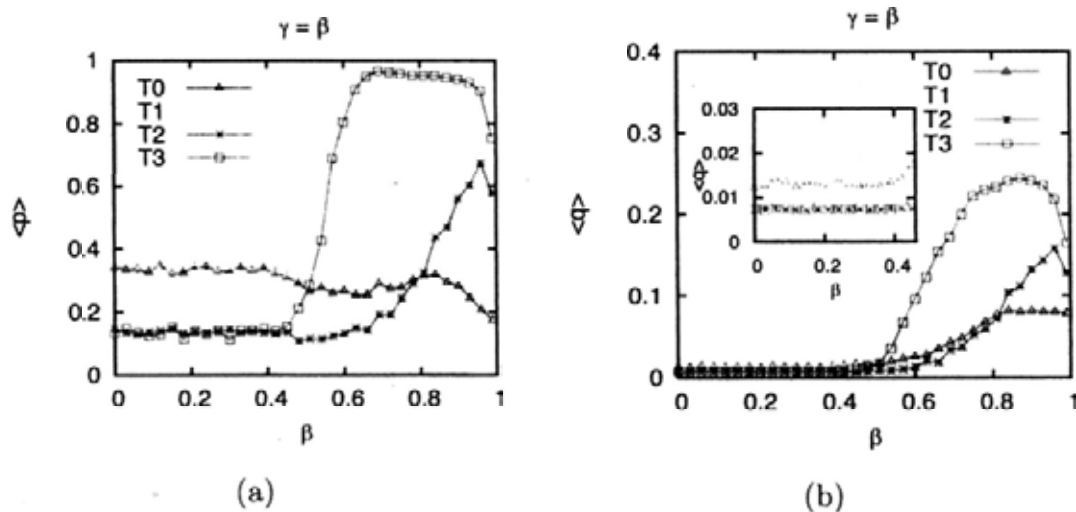


Figure 2.10: (a) $\langle p \rangle$ and (b) $\langle q \rangle$ as a function of β along the diagonal line $\gamma = \beta$ in the β - γ space for the four initial configurations. Each data point is an average over 500 realizations. The inset of (b) is a zoom-in picture for $\beta < 0.45$.

their values first increase and then decrease as β increases. T3 has even larger $\langle p \rangle$ and $\langle q \rangle$ values, showing the dominance of the generous TFT-like strategies at large β region. So the existence of E_{TFT} at the beginning can bring the system towards cooperation when β is large, and E_{AUD} makes this effect more stable.

To have a better understanding of the roles played by E_{AUD} and E_{TFT} , we carry out analytical studies based on our previous discussions on two-strategy game.

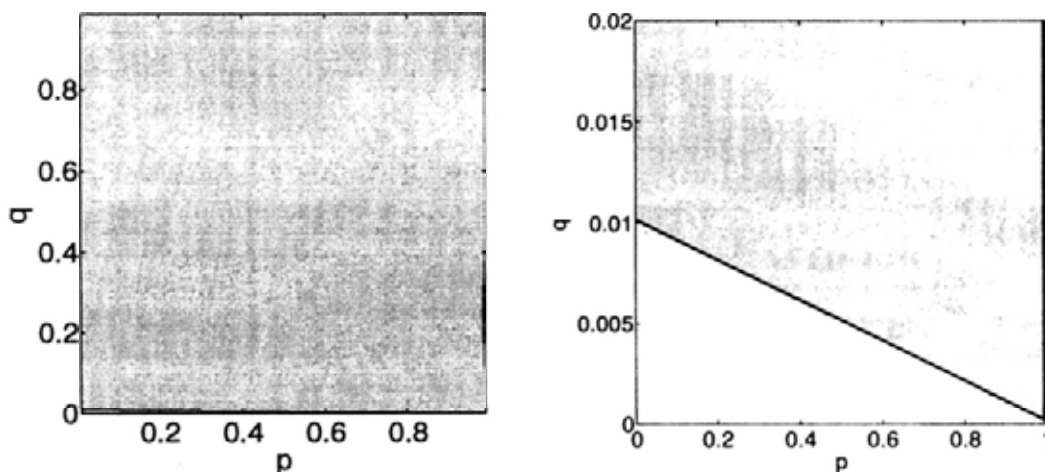
Dominating strategies at small β region

The small β region is dominated by AllD-like strategies. To facilitate our analytical discussions, we define

$$G(E_1, E_2) = \begin{cases} 1, & K(E_1, E_2) > 0 \text{ and } K(E_2, E_1) < 0 \\ 0, & K(E_1, E_2) < 0 \text{ and } K(E_2, E_1) > 0, \\ -1, & \text{sgn}(K(E_1, E_2)) = \text{sgn}(K(E_2, E_1)) \end{cases} \quad (2.24)$$

where $\text{sgn}(x)$ extracts the sign of x . The meaning of the different values of $G(E_1, E_2)$ is

$$G(E_1, E_2) = \begin{cases} 1, & E_1 \text{ can always invade } E_2, \\ 0, & E_2 \text{ can always invade } E_1, \\ -1, & \text{invasion depends on their frequencies.} \end{cases} \quad (2.25)$$



(a) The whole (p, q) space.

(b) Zoom-in picture for $q < 0.02$.

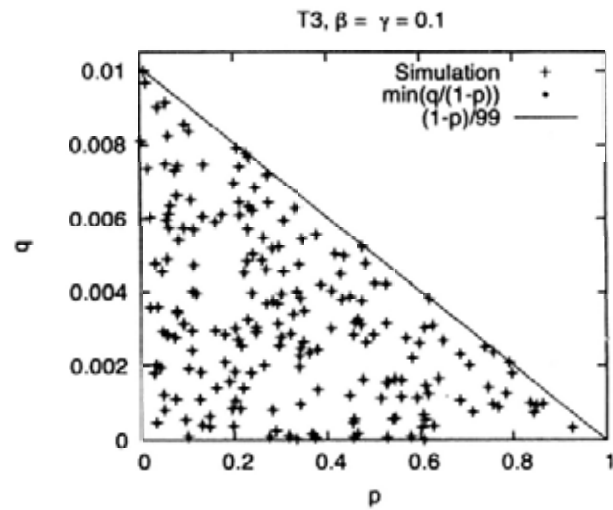
Figure 2.11: Contour plot of $G(E, E_{AUD})$ for any strategy $E = (p, q)$ at $\beta = 0.1$. White color for $G(E, E_{AUD}) = 1$, green color for $G(E, E_{AUD}) = 0$ and red color for $G(E, E_{AUD}) = -1$.

The value of $G(E, E_{AUD})$ for arbitrary $E = (p, q)$ at $\beta = 0.1$ is shown in Fig. 2.11(a). We use white, green and red colors for $G(E, E_{AUD}) = 1, 0$ and -1 ,

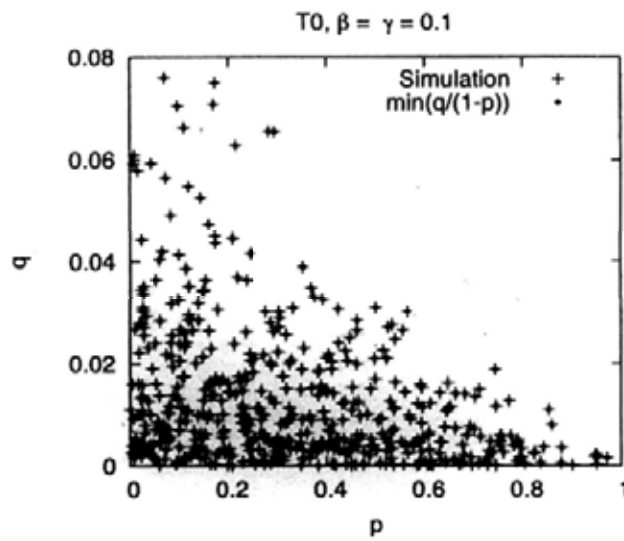
respectively. The dominating color is green, implying that E_{AUD} can replace most strategies when playing a two-strategy game against them. The areas of white and red colors are tiny. An enlarged picture for $q < 0.02$ is shown in Fig. 2.11(b), which is divided into two parts by the blue line that connects E_{AUD} to the TFT corner (1,0). The area under this line is colored white. Thus E_{AUD} can be taken over by any strategy that lies below this line when playing a two-strategy game. Recall our previous discussions on two-strategy game in Sec. 2.2, here our case only has a tiny area of Region I (red color area), which we can ignore and assume all strategies are in Region II. As defined before, $l = q/(1-p)$ is the absolute value of the line that connects strategy $E = (p, q)$ to the TFT corner (1,0). For strategies in Region II, the smaller l value a strategy has, the more competitive it is. So the winning strategy should be the one with the smallest l value. A winning strategy of a single run is the strategy that has the largest frequency in the steady state of that run. Figure 2.12 shows the winning strategy (black cross) of every single run, for a total of 500 runs using initial configuration T3. The strategy with the minimum l of that single run is also shown (red dot). Our predictions coincide well with simulation results. Due to the competitiveness of strategies with small l value at small β , even without E_{AUD} added initially, the winning strategy of one realization is still the strategy of the minimum l value in that realization (Fig. 2.12 (b)) .

Dominating strategies at large β region

Figure 2.13 shows the threshold frequency x_c of E_{TFT} when playing a two-strategy game against E_{AUD} . For $x_{TFT} > x_c$, E_{AUD} can be taken over by E_{TFT} . For large β , a small portion of E_{TFT} can easily take over a large portion of E_{AUD} . However, E_{AUD} can still be able to invade a large area of strategies. Figure 2.14(a) shows $G(E, E_{AUD})$ at $\beta = 0.95$. Strategies in the area of green color can be replaced by E_{AUD} when playing a two-strategy game. In a system



(a): initial configuration T3.



(b): initial configuration T0.

Figure 2.12: The winning strategies (black cross) and the strategy with minimum $l = q/(1-p)$ value (dot) in 500 realizations. $\beta = 0.1$, initial configurations are T3 and T0.

with 100 strategies, E_{AUD} is still able to replace strategies in the green area, which can then be replaced by TFT-like strategies, such as E_{TFT} . These TFT-like strategies are then replaced by generous TFT strategies. Figure 2.14(b) shows $G(E, E_{TFT})$ at $\beta = 0.95$. The winning strategies of 1000 runs are also shown (blue dots). Most of them are inside the white area, indicating the winning strategies have a large chance to be those that can invade E_{TFT} .

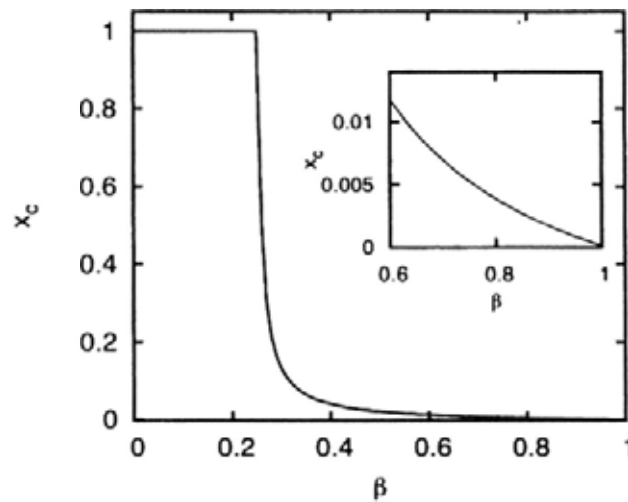


Figure 2.13: The threshold frequency x_c of E_{TFT} when playing against E_{AUD} as a function of β along the diagonal line of the β - γ space. The inset is a zoom-in picture at large β .

2.3.2 Anti-diagonal line

Figure 2.15 shows $\langle p \rangle$ and $\langle q \rangle$ as a function of β for the four types of initial configurations along the anti-diagonal line. Both $\langle p \rangle$ and $\langle q \rangle$ are very large when β is small, showing the dominance of cooperative behavior. For $\beta > 0.6$, $\langle p \rangle$ and $\langle q \rangle$ become small, the systems become dominated by egotistic strategies. T0 and T2 have similar $\langle p \rangle$ and $\langle q \rangle$ behavior when β is small, so are T1 and T3. The difference between the two groups is that for T0 and T2, $\langle p \rangle$ and $\langle q \rangle$ begin to drop at a smaller β . So the initially added E_{TFT} in

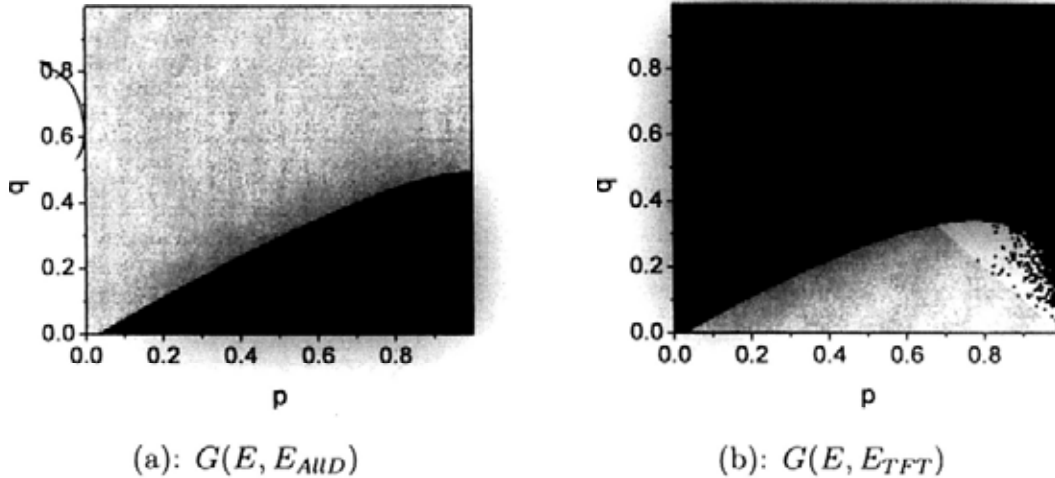


Figure 2.14: Contour plot of (a) $G(E, E_{AUD})$ and (b) $G(E, E_{TFT})$ at $\beta = 0.95$. White color for $G(E, E_{AUD}) = 1$, green color for $G(E, E_{AUD}) = 0$ and red color for $G(E, E_{AUD}) = -1$. The winning strategies of 1000 realizations with initial configuration T3 are also shown in (b) as blue dots.

T1 and T3 can keep a large $\langle p \rangle$ and large $\langle q \rangle$ for a larger range of β values. In other words, the dominance of cooperative behavior becomes more stable with the existence of E_{TFT} at the beginning. For $\beta > 0.6$, T0 and T1 make up one group. T2 and T3 make up another group, which has smaller $\langle p \rangle$ and $\langle q \rangle$ values. Each group have similar $\langle p \rangle$ and $\langle q \rangle$ behavior. Thus, the initially added E_{AUD} in T2 and T3 can lower the values of $\langle p \rangle$ and $\langle q \rangle$ at large β region. To conclude, the dominating strategies in small and large β regions can be changed separately by the initially added E_{TFT} and E_{AUD} . We shall study the origin of this in what follows.

Two-strategy game of E_{TFT} and E_{AUD}

Figure 2.16 shows the threshold frequency x_c of E_{TFT} when playing a two-strategy game against E_{AUD} . For $x > x_c$, E_{AUD} can be replaced by E_{TFT} . When β is small, a tiny portion of E_{TFT} can eventually replace a large population of E_{AUD} . So, AllD-like strategies are very weak when competing with TFT-like

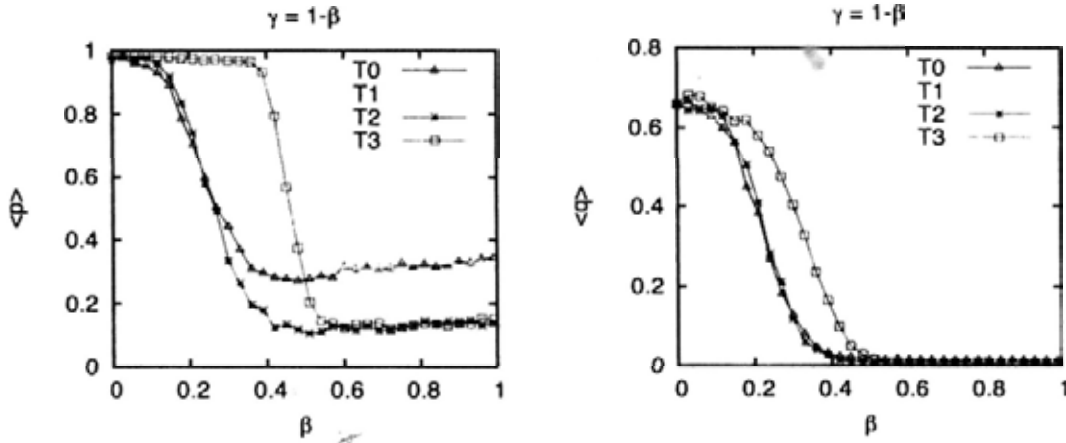


Figure 2.15: (Left) $\langle p \rangle$ and (Right) $\langle q \rangle$ as a function of β along the anti-diagonal line $\gamma = 1 - \beta$ in the β - γ space for the four initial configurations. Each data point is an average over 500 realizations.

strategies at small β region. This explains why $\langle p \rangle$ and $\langle q \rangle$ of systems with initial configuration T2, which has E_{AUD} added initially, have similar behavior with systems consisting of 100 random strategies (with initial configuration T0) at the small β region. When β becomes larger, E_{TFT} becomes less competitive when facing E_{AUD} . The dominating strategies change to AllD-like.

Dominating strategies at small β

For β is small, E_{TFT} and other TFT-like strategies have advantages when playing with E_{AUD} and other AllD-like strategies. Recall our discussion on the invasion problem in two-strategy games. For a given β with $\beta + \gamma = 1$, the p - q space is divided into Region I and II by the line $q = p - \beta$ (Fig. 2.2). E_{AUD} is always in Region II for any $\beta > 0$, and E_{TFT} is in Region I for $\beta < 0.98$. For a strategy in Region II, a line connecting this strategy to the TFT corner $(1, 0)$ can be drawn. The absolute value of the slope of this line is $l = q/(1 - p)$. Strategies below this line can definitely replace strategies on or above this line when playing a two-strategy game. Thus, AllD-like strategies, which has small l values, are able to replace most of the strategies in Region II. These AllD-like

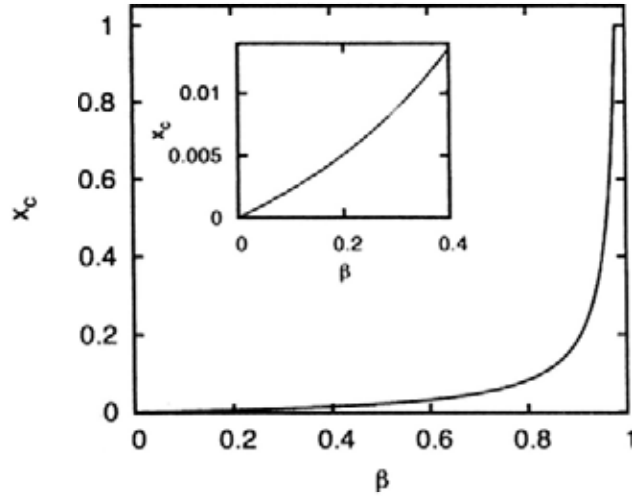


Figure 2.16: The threshold frequency x_c of E_{TFT} when playing against E_{AUD} as a function of β along the anti-diagonal line of the β - γ space. The inset is a zoom-in picture at small β .

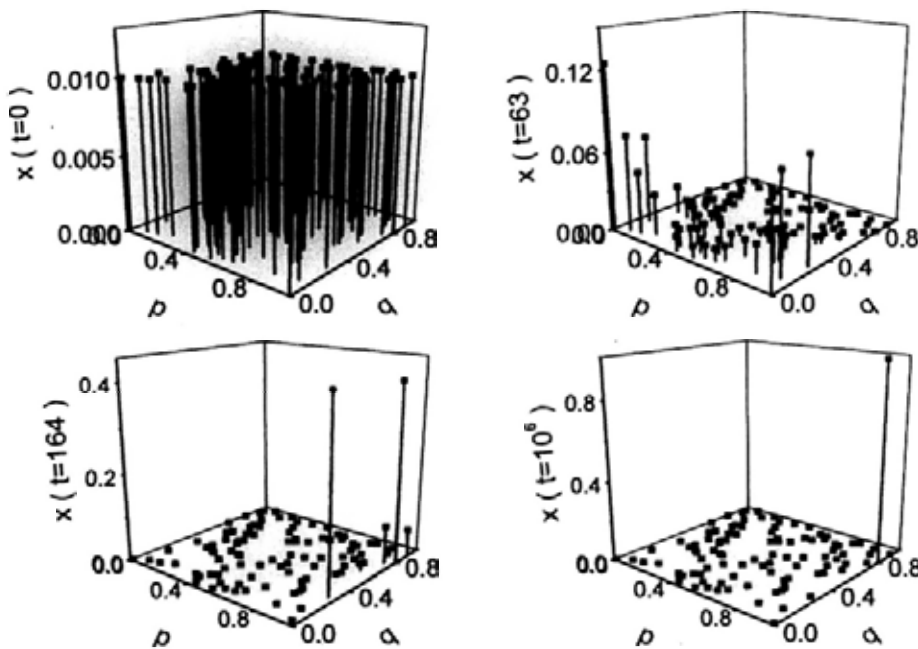


Figure 2.17: A typical evolution process for system with initial configuration T3 at $\beta = 0.1$.

strategies can then be taken over by TFT-like strategies in Region I. For a strategy in Region I, it can be invaded by any other strategy in Region I that has a larger l value. AllC-like strategies, which have both large p and large q values, have larger l than TFT-like strategies. So they are able to invade TFT-like strategies. Based on our discussion, we imagine that strategies with small l values in Region II would have advantages at the early stage of the evolution, and then TFT-like strategies begin to grow. TFT-like strategies are then replaced by AllC-like strategies, with the winning strategy being the one with the largest l value.

Figure 2.17 shows a typical evolution process at $\beta = 0.1$ for system with initial configuration T3. At $t = 0$, all the 100 strategies have the same frequency $x_{init} = 0.01$. As t increases, AllD-like strategies begin to take the largest percentage at $t = 63$. When $t = 163$, these AllD-like strategies are replaced by a TFT-like strategy and three AllC-like strategies. Eventually, there is only one AllC-like strategy survived at $t = 10^6$. So the evolution process we predicted is verified by the simulation results in Fig. 2.17. In Fig. 2.18, we show the winning strategies (black cross) of 500 realizations for systems with initial configurations T0 and T1, together with the strategy that has the largest l value in Region I of every run (red dot). Good agreements between simulation results and our predictions are obtained.

Dominating strategies at large β

For very large β , strategies in Region I become very weak when competing with AllD-like strategies in Region II. Strategies in Region II with large l values can also be invaded by AllD-like strategies. So the system is dominated by strategies that have small l values in Region II. The winning strategy in a single run should be the particular strategy that has the smallest l value. In Fig. 2.19, the simulation results well agree with our predictions.

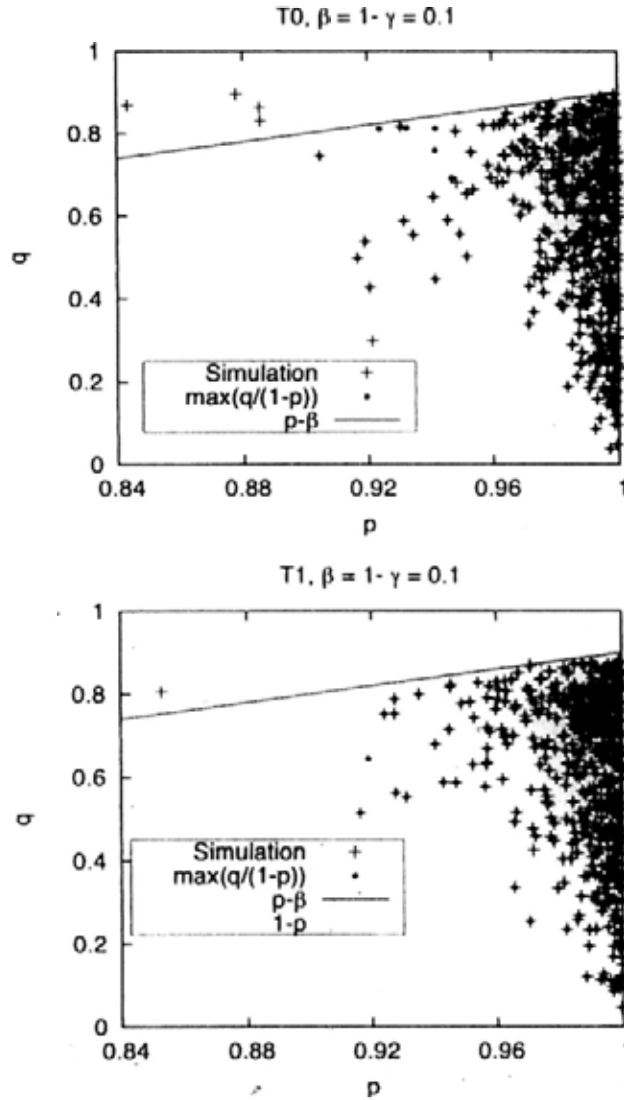


Figure 2.18: The winning strategies obtained by simulations (black crosses) and the strategy with maximum $l = q/(1 - p)$ value in Region I for 500 realizations (dots). $\beta = 1 - \gamma = 0.1$, with initial configurations T0 and T1.

2.3.3 Analytical calculations of $\langle p_{win} \rangle$ and $\langle q_{win} \rangle$

Since we can predict the winning strategy $E_{win} = (p_{win}, q_{win})$ of a single run for very small and very large β values for the anti-diagonal line, we should be able to calculate the mean values of p_{win} and q_{win} analytically. Chan [44] has calculated $\langle p_{win} \rangle$ and $\langle q_{win} \rangle$ for small β values along the diagonal line. Here

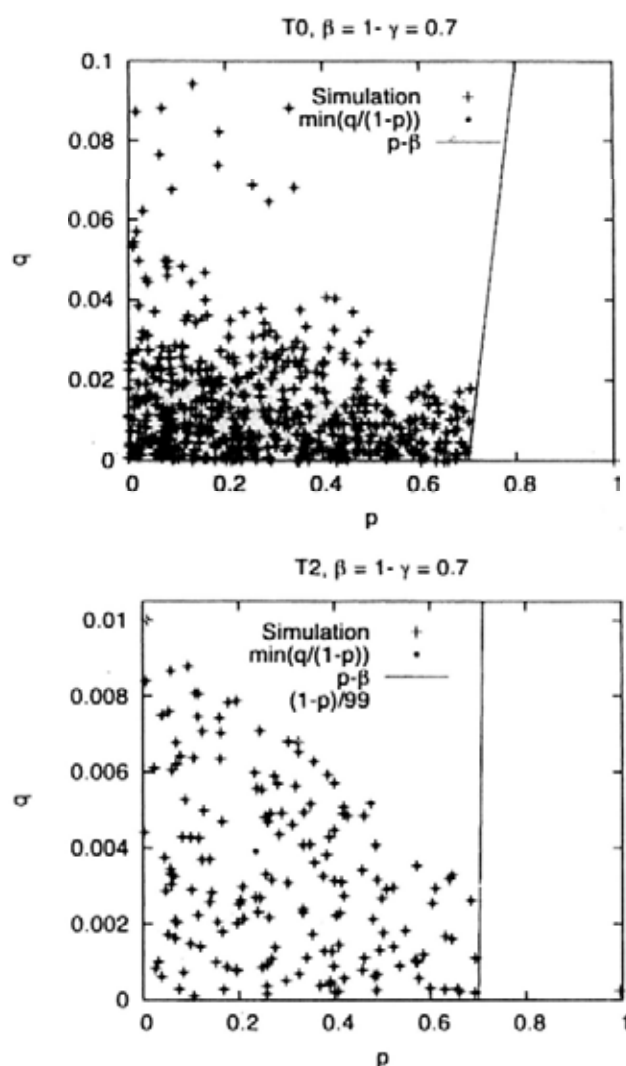


Figure 2.19: The winning strategies obtained by simulations (black cross) and the strategy with minimum $l = q/(1 - p)$ value in Region II (dots) for 500 realizations. $\beta = 0.7$, with initial configurations T0 and T2

we calculate $\langle p_{win} \rangle$ and $\langle q_{win} \rangle$ along the anti-diagonal line.

$\langle p_{win} \rangle$ and $\langle q_{win} \rangle$ at small β

Take m to be the number of stochastic strategies of the system, $100 - m$ is the number of intentionally inserted strategies. $m = 100, 99, 99$, and 98 for systems with initial configuration T0, T1, T2 and T3, respectively. For small

β , the winning strategy has the maximum $l = q/(1 - p)$ value among all strategies that lie below the line $q = p - \beta$ (Region I).

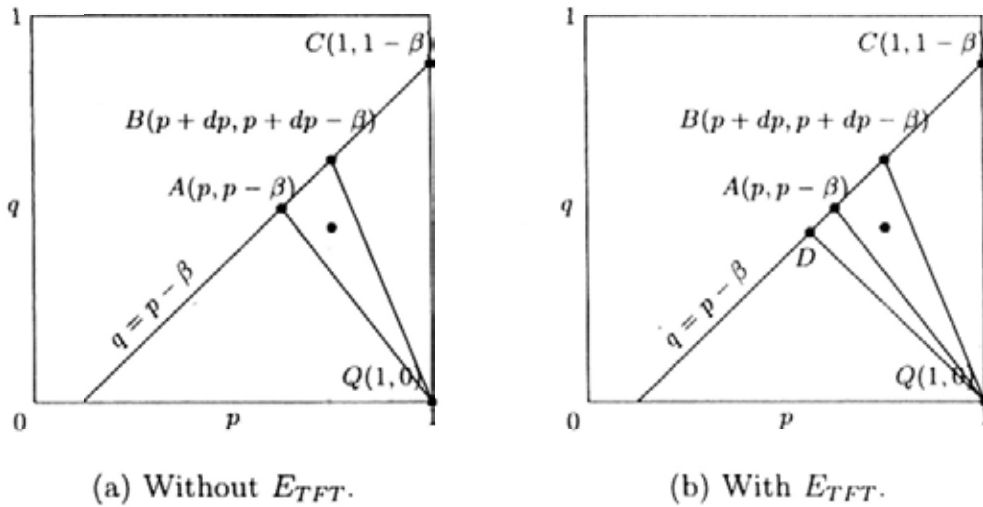


Figure 2.20: Schematic diagrams of the relative positions of strategies discussed in Sec. 2.3.3 for calculating $\langle p_{win} \rangle$ and $\langle q_{win} \rangle$ at small β .

Define the points Q and C to be the TFT corner $(1, 0)$ and the point of intersection of the two lines $q = p - \beta$ and $p = 1$, respectively (see Fig. 2.20). We construct the triangle ΔQAB in the p - q space, where $A = (p, p - \beta)$ and $B = (p + dp, p + dp - \beta)$ are two points on the line $q = p - \beta$. Figure 2.20(a) shows the relative positions of these points schematically. For the m random strategies, if there is one strategy in ΔQAB and no strategy in ΔQBC , then the winning strategy will be the strategy in ΔQAB . The probability for this to happen is

$$\begin{aligned}
 Pr &= m \times S_{\Delta QAB} \times (1 - S_{\Delta QBC})^{m-1} \\
 &= m \times \frac{(1 - \beta)dp}{2} \times \left(1 - \frac{(1 - \beta)(1 - p)}{2}\right)^{m-1} \\
 &\equiv Fdp,
 \end{aligned}$$

where $S_{\Delta QAB}$ is the area of ΔQAB . We neglected the dp term in calculating $S_{\Delta QBC}$. A strategy can be anywhere inside ΔQAB . The averaged p, q values

of strategies in ΔQAB for many runs is the coordinate of the centroid of ΔQAB , which is $\left(\frac{2p+1}{3}, \frac{2(p-\beta)}{3}\right)$ after neglecting the dp terms. The values of $\langle p_{win} \rangle$ and $\langle q_{win} \rangle$ can be calculated by integrating over p .

For systems with initial configurations T0 and T2 that do not contain E_{TFT} , p ranges from β to 1. Thus,

$$\begin{aligned}\langle p_{win} \rangle &= \int_{\beta}^1 F \times \frac{2p+1}{3} dp, \\ \langle q_{win} \rangle &= \int_{\beta}^1 F \times \frac{2(p-\beta)}{3} dp.\end{aligned}\tag{2.26}$$

For systems with E_{TFT} added initially, we define $D = \left(\frac{1+\beta}{2}, \frac{1-\beta}{2}\right)$, which is the point of intersection of lines $q = p - \beta$ and $q = 1 - p$ (see Fig. 2.20(b)). With probability $P_{TFT} = (1 - S_{\Delta QCD})^{100-m}$, there is no strategy in ΔQCD . Under this condition, the winner is E_{TFT} . With probability $1 - P_{TFT}$, there is one or more strategies in ΔQCD , the winning strategy is the one with largest l value in ΔQCD . $\langle p_{win} \rangle$ and $\langle q_{win} \rangle$ can then be calculated as

$$\begin{aligned}\langle p_{win} \rangle &= P_{TFT} \times 0.99 + (1 - P_{TFT}) \times \int_{\frac{\beta+1}{2}}^1 F \times \frac{2p+1}{3} dp, \\ \langle q_{win} \rangle &= P_{TFT} \times 0.01 + (1 - P_{TFT}) \times \int_{\frac{\beta+1}{2}}^1 F \times \frac{2(p-\beta)}{3} dp.\end{aligned}\tag{2.27}$$

Table 2.1 shows the simulation and analytic results of $\langle p_{win} \rangle$ and $\langle q_{win} \rangle$ for the four initial configurations at $\beta = 0.06$. The analytic results agree well with the simulation results.

$\langle p_{win} \rangle$ and $\langle q_{win} \rangle$ at large β

When β is large, the winning strategy has the minimum $l = \frac{q}{1-p}$ value among all strategies that lie to the west of the line $q = p - \beta$ (Region II). The line $q = p - \beta$ intersects with lines $q = 0$ and $p = 1$ at points $G = (\beta, 0)$ and $H = (1, 1 - \beta)$. Point Q is the TFT corner $(1, 0)$ (see Fig. 2.21). Since the presence of a small fraction of E_{AUD} initially can affect the winning strategies,

Table 2.1: $\langle p_{win} \rangle$ and $\langle q_{win} \rangle$ values obtained by simulations and analytic calculations for the four initial configurations at $\beta = 1 - \gamma = 0.06$.

$\langle p_{win} \rangle$	T0	T1	T2	T3
Simulation	0.953	0.974	0.982	0.985
Analytic	0.986	0.986	0.986	0.986

$\langle q_{win} \rangle$	T0	T1	T2	T3
Simulation	0.631	0.653	0.656	0.670
Analytic	0.613	0.612	0.612	0.612

we divide our discuss into two parts, depending on whether the system has E_{AUD} added initially or not.

For systems with E_{AUD} added initially, we use point A to denote E_{AUD} in the p - q space. Line AQ intersects with line GH at point $C = (0.99\beta + 0.01, 0.01(1 - \beta))$. Figure 2.21(a) shows the relative positions of these points schematically. With probability $P_{AUD} = (1 - S_{\square ACGO})^{100-m}$, there is no strategy in the quadrilateral $\square ACGO$, the winner is E_{AUD} . With probability $(1 - P_{AUD})$, there is at least one strategy in $\square ACGO$, the winning strategy is inside $\square ACGO$. The probability that there are two or more strategies in $\square ACGO$ is tiny, thus we can simplify assume that there is only one strategy inside $\square ACGO$, which is the winner. The average value $(\langle p_{win} \rangle, \langle q_{win} \rangle)$ of winning strategies inside $\square ACGO$ for multiple runs corresponds to the centroid (p_C, q_C) of $\square ACGO$, which is given by

$$p_C = \frac{p_1 \times S_{\triangle QAO} - p_2 \times S_{\triangle QCG}}{S_{\square ACGO}}, \quad (2.28)$$

$$q_C = \frac{q_1 \times S_{\triangle QAO} - q_2 \times S_{\triangle QCG}}{S_{\square ACGO}}, \quad (2.29)$$

where $(p_1 = \frac{1}{3}, q_1 = \frac{1}{3 \times 99})$ and $(p_2 = \frac{1.99\beta + 1.01}{3}, q_2 = \frac{0.01(1-\beta)}{3})$ are the centroids of $\triangle QAO$ and $\triangle QCG$, respectively, $S_{\triangle QAO} = \frac{1}{198}$, $S_{\triangle QCG} = \frac{(1-\beta)^2}{200}$ and $S_{\square ACGO} = S_{\triangle QAO} - S_{\triangle QCG}$.

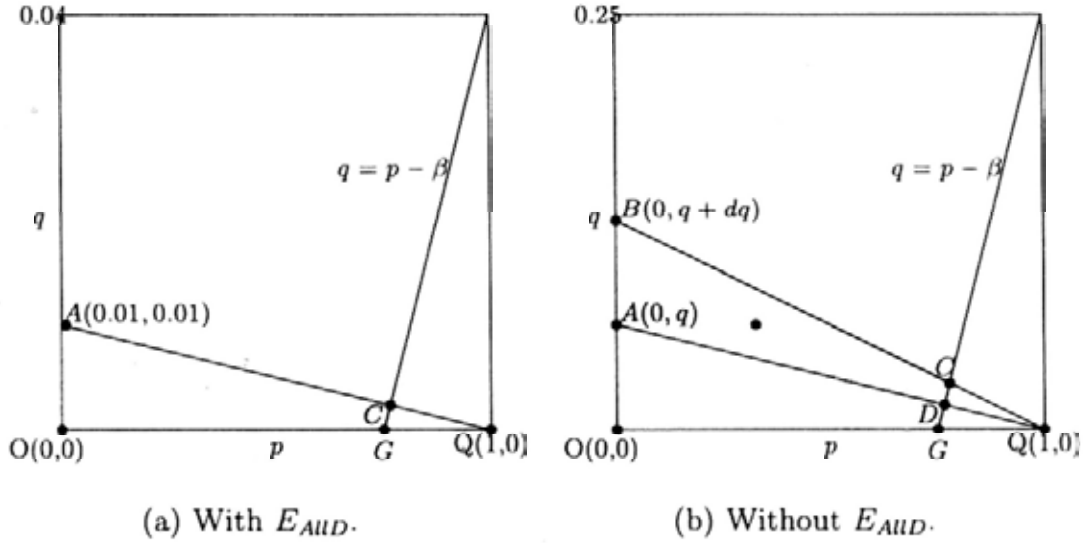


Figure 2.21: Schematic diagrams of the relative positions of strategies discussed in Sec. 2.3.3 for calculating $\langle p_{win} \rangle$ and $\langle q_{win} \rangle$ at large β .

$\langle p_{win} \rangle$ and $\langle q_{win} \rangle$ can be calculated in terms of P_{AUD} , p_C and q_C :

$$\begin{aligned} \langle p_{win} \rangle &= P_{AUD} \times 0.01 + (1 - P_{AUD}) \times q_C, \\ \langle q_{win} \rangle &= P_{AUD} \times 0.01 + (1 - P_{AUD}) \times p_C. \end{aligned} \quad (2.30)$$

For systems without E_{AUD} added initially, it is more involved to calculate $\langle p_{win} \rangle$ and $\langle q_{win} \rangle$. Consider two points $A = (0, q)$ and $B = (0, q + dq)$ in the p - q space (see Fig. 2.21(b)). A triangle $\triangle QAB$ is formed by connecting points A and B to the TFT corner $Q = (1, 0)$. The area of $\triangle QAB$ is $S_{\triangle QAB} = dq/2$. The two lines QA and QB intersect with the line $q = p - \beta$ at points $C = \left(\frac{q+\beta}{1+q}, \frac{(1-\beta)q}{1+q} \right)$ and $D = \left(\frac{q+dq+\beta}{1+q+dq}, \frac{(1-\beta)(q+dq)}{1+q+dq} \right)$. So $S_{\triangle QCD} = (1 + q - \beta)(1 - \beta)dq/(2(1 + q)^2)$. A quadrilateral $\square ABCD$ is constructed by connecting the points A , B , C , and D . Figure 2.21(b) illustrates the set up. For a system with m stochastic strategies, if there is one strategy in $\square ABCD$ and no strategy in $\square OADG$, the winning strategy will be the one inside $\square ABCD$.

The probability for this to happen is

$$\begin{aligned}
 Pr &= m \times S_{\square ABCD} \times (1 - S_{\square OADG})^{m-1} \\
 &= m \times \left(\frac{dq}{2} - \frac{(1+q-\beta)(1-\beta)dq}{2(1+q)^2} \right) \times \left(\frac{q}{2} - \frac{(1-\beta)^2 q}{1+q} \right)^{m-1} \\
 &\equiv Fdq .
 \end{aligned} \tag{2.31}$$

The averaged p , q values of strategies in $\square ABCD$ for many runs are the coordinates (p_C, q_C) of the centroid of $\square ABCD$.

$$p_C = \frac{p_1 \times S_{\triangle QAB} - p_2 \times S_{\triangle QCD}}{S_{\square ABCD}} , \tag{2.32}$$

$$q_C = \frac{q_1 \times S_{\triangle QAB} - q_2 \times S_{\triangle QCD}}{S_{\square ABCD}} , \tag{2.33}$$

where $(p_1 = \frac{1}{3}, q_1 = \frac{2q}{3})$ and $(p_2 = \frac{1+2q+\beta}{3+3q}, q_2 = \frac{2q(1-\beta)}{3+3q})$ are the centroid of $\triangle QAB$ and $\triangle QCD$, respectively. We have neglected the dq terms.

The values of $\langle p_{win} \rangle$ and $\langle q_{win} \rangle$ can then be calculated by

$$\begin{aligned}
 \langle p_{win} \rangle &= \int_0^1 F \times p_C dq , \\
 \langle q_{win} \rangle &= \int_0^1 F \times q_C dq .
 \end{aligned} \tag{2.34}$$

Table 2.2 shows the simulation and analytic results of $\langle p_{win} \rangle$ and $\langle q_{win} \rangle$ given by Eqs. (2.30) and (2.34) for the four initial configurations at $\beta = 0.81$. Good agreement is obtained between the simulation results and the analytic results.

2.4 Conclusion

This chapter gives a detailed study on the iterated prisoner's dilemma. We reviewed previous studies on IPD, in which the main focus was the role played by the TFT strategy. Then we analytically studied the two-strategy IPD in the whole payoff space spanned by β and γ . We focused on the $\beta = 1 - \gamma$ case, which can be treated analytically. We numerically studied the IPD game in

Table 2.2: $\langle p_{win} \rangle$ and $\langle q_{win} \rangle$ values obtained by simulations and analytic calculations for the four initial configurations at $\beta = 1 - \gamma = 0.81$.

$\langle p_{win} \rangle$	T0	T1	T2	T3
Simulation	0.323	0.339	0.129	0.147
Analytic	0.311	0.311	0.126	0.125

$\langle q_{win} \rangle$	T0	T1	T2	T3
Simulation	0.0135	0.0134	0.00744	0.00697
Analytic	0.0140	0.0142	0.00750	0.00752

the whole payoff space, using four types of initial configurations. It was found that for systems with both E_{TFT} and E_{AUD} added initially, the dominating area of AllC and GTFT strategies in the payoff space is the largest among the four initial configurations. The roles played by E_{TFT} and E_{AUD} were further studied by working on the diagonal and anti-diagonal lines of the payoff space. It was found that E_{AUD} could replace many strategies for any payoff value. For payoff values with large β , E_{TFT} can easily take over E_{AUD} , which was then replaced by more generous strategies. This process leads to the dominance of generous strategies at large β . Based on the analysis on the two-strategy game, we analytically predicted the winning strategies for small and large β values along the anti-diagonal line. The average p and q values of these winning strategies were also calculated. The results agree well with the simulation results.

Chapter 3

Phase transitions in spatial snowdrift game

In this chapter, we first review previous studies on the spatial prisoner's dilemma game and spatial snowdrift games. We then study the behaviors of phase transitions in the spatial snowdrift game. By studying the relative alignments of the payoffs of C and D nodes, we explain the phase transitions analytically.

3.1 Introduction

Evolutionary game theory has been used in studying the emergence of cooperation. The prisoner's dilemma (PD) and the snowdrift game (SG) are the mostly studied two-person evolutionary games. Both of them are two-strategy games in which the players have two options: to cooperate (C) or defect (D). A basic introduction of the two games has been given in Sec. 1.1.

The behavior of these two games in a well-mixed population can be investigated theoretically. For PD, the D -character is always the dominating strategy in the steady state. For SG, both C and D can coexist at equilibrium, with the fraction of cooperators $f_C = 1 - \frac{c}{2b-c}$ (Eq.(1.12)). Besides

the well-mixed case, both games have been studied in structured populations, in which an agent is connected only to a group of other agents rather than the whole population. It was found that the emergence of cooperation can be affected by the underlying network structure [45, 46]. Among the network structures, the spatial structure is the most studied structure [45]. The iterated PD game was first studied on grid by Axelrod [37]. Later, Nowak and May studied the one-round PD game on lattices [47]. In their set up, each player competes with all neighbors and obtain a payoff at each time step. By comparing the payoff with that of the neighbors, a player will follow the strategy of the neighbor with the highest payoff. Their observation is that C and D coexist at equilibrium for a substantial subset of the payoff space and for most initial conditions, which means that lattice structure promotes cooperation in PD game. The effect of lattice structure is verified by many later works [45, 48, 49, 50]. The reason why spatial structure can promote cooperation is that cooperators can form clusters. By gaining benefit from mutual cooperation within the clusters, agents at the cluster boundaries are able to resist the invasion from the surrounding defectors. Following the studies of PD game on spatial structures, the SG was played on lattices by Hauert and Doebeli [51]. Contrasted to the spatial PD game, they found that spatial structure often inhibits cooperation for SG.

In this chapter, we will first review the work by Hauert and Doebeli, and then analytically explain the behavior of the phase transitions in spatial snowdrift game.

3.2 The spatial snowdrift game

3.2.1 One-parameter payoff matrix

The payoff matrix of SG has been given in Eq.(1.11) as

$$\begin{array}{c} C \\ D \end{array} \begin{array}{cc} C & D \\ \left(\begin{array}{cc} R = b - c/2 & S = b - c \\ T = b & P = 0 \end{array} \right) \end{array} \quad (3.1)$$

For convenience of both numerical and theoretical discussions, we normalize the payoff values by dividing them with R , thus $R = 1$ and $P = 0$. The values of T and S are

$$T = \frac{b}{b - c/2} = 1 + r, \quad (3.2)$$

$$S = \frac{b - c}{b - c/2} = 1 - r, \quad (3.3)$$

where $r = c/(2b - c)$ is the cost-to-benefit ratio. $f_C = 1 - r$ is the equilibrium frequency of cooperation of the well-mixed case. The payoff matrix of SG after normalization is:

$$\begin{array}{c} C \\ D \end{array} \begin{array}{cc} C & D \\ \left(\begin{array}{cc} R = 1 & S = 1 - r \\ T = 1 + r & P = 0 \end{array} \right) \end{array} \quad (3.4)$$

3.2.2 Snowdrift game on lattices

Hauert and Doebeli [51] played the snowdrift game on 2D lattices with periodic boundary conditions. The size of the lattices are 100×100 , with the number of neighbors takes on $k = 3$ (hexagonal lattice), 4 (square lattice), 6 (triangle lattice) and 8 (square lattice with nearest and next nearest neighbors connected). Figure 3.1 illustrates the geometrical structures of these lattices.

Let $x_C(t)$ be the frequency of cooperation at time t . An initial condition $x_C(t = 0) = 0.5$ was used in their simulations, i.e., half of the agents take

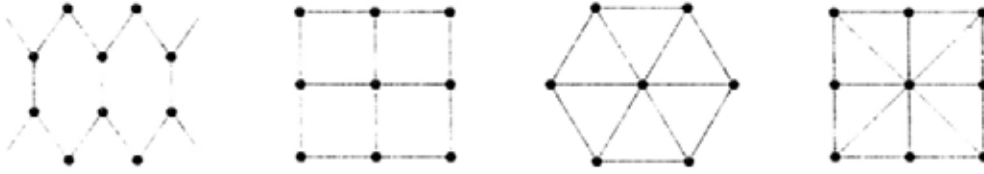


Figure 3.1: Different types of 2D lattices. From Left to right: Hexagonal ($k = 3$), Square ($k = 4$), Triangle ($k = 6$) and Square lattice with nearest and next nearest neighbors connected ($k = 8$).

on the C character initially. The updating process could be synchronous or asynchronous. For synchronous updating, every node i plays SG with all its k neighbors and obtain an accumulated payoff P_i at each time step. Every node i then randomly chooses a neighbor j as reference for updating. If $P_j > P_i$, then with probability $f(P_j - P_i)$ agent i will adapt j 's strategy, and with probability $1 - f(P_j - P_i)$ agent i keeps its character. For asynchronous updating, only one node i is randomly selected for possible updating at each time step. By comparing its payoff P_i and the payoff P_j of a randomly selected neighbor j , node i will follow j 's strategy with probability $f(P_j - P_i)$ if $P_j > P_i$. The updating process may be interpreted as reproduction, i.e., strategies with higher payoffs have more offspring. The probability function $f(P_j - P_i)$ can take one of the following two forms [51]:

- Form 1:

$$f(P_j - P_i) = \frac{P_j - P_i}{kT} = \frac{P_j - P_i}{k(1+r)}, \quad (3.5)$$

where $k(1+r)$ normalizes the probability. By taking this form, the probability f is proportional to the payoff difference between nodes j and i .

- Form 2:

$$f(P_j - P_i) = \frac{1}{1 + \exp\left(\frac{P_i - P_j}{k(1+r)\kappa}\right)}, \quad (3.6)$$

where κ represents a noise parameter. This form is similar to the Fermi-distribution in physics.

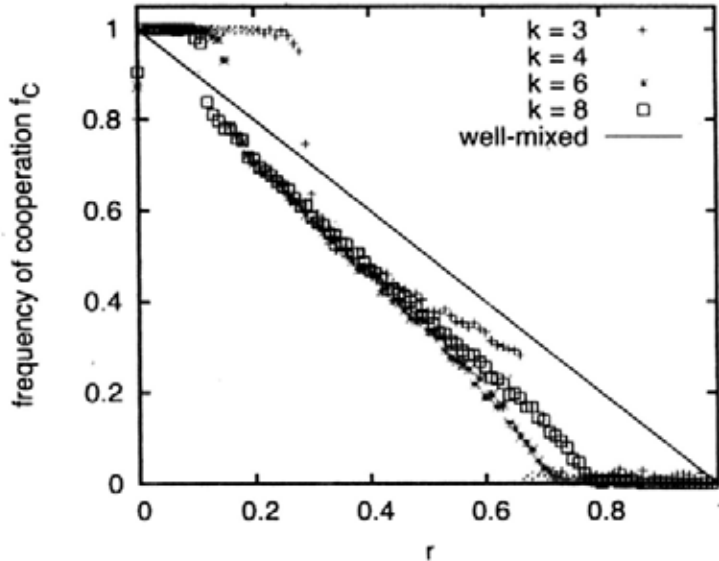


Figure 3.2: The frequency of cooperation f_C as a function of the cost-to-benefit ratio r for SG played on lattices of different geometries (symbols). f_C of the well-mixed case is shown for comparison (line).

We use Form 1 in the following discussion.

Figure 3.2 shows the steady state frequency of cooperation f_C as a function of the cost-to-benefit ratio r for SG played on 2D lattices (symbols). The asynchronous updating process is used. The key features of f_C are:

- For small r , $f_C \sim 1$, the system is in an AllC phase dominated by C character.
- For r larger than a critical value r_C , the system changes from an AllC phase to a mixed phase that contains both C and D characters.
- For $r > r_D$, $f_C \sim 0$, the system evolves into an AllD phase, C character becomes extinct.

Compared with the well-mixed case, cooperation is promoted by the lattice structure for $r < r_C$, and suppressed for $r > r_C$. Except for the small range of $r < r_C$, spatial structure is found to inhibit cooperation for SG for a large

range of r values. Using a technique called pair approximation [52, 51], f_C can be estimated analytically. The analytic results agree well with the numerical results at intermediate r , but fails at high and low r [51]. Here we explain the phase transitions and predict the values of r_C and r_D by comparing the payoffs of neighboring C and D nodes.

3.3 Theoretical investigations on phase transitions in spatial SG

To understand the origin of the phase transitions and analytically predict the transition points, it is useful to study the case when cooperators and defectors have the same payoff.

The payoff of an agent that plays SG with its neighbors can be expressed as a function of its degree k (thus the number of neighbors) and the number of D -neighbors. For a C -agent with y D -neighbors,

$$\begin{aligned} P_C(k, y) &= (k - y)R + yS \\ &= k - yr . \end{aligned} \tag{3.7}$$

For a D -agent with z D -neighbors,

$$\begin{aligned} P_D(k, z) &= (k - z)T + zP \\ &= (k - z)(1 + r) . \end{aligned} \tag{3.8}$$

When a C -agent has the same payoff with one D -neighbor, $P_C(k, y) = P_D(k, z)$. In this case, r can be expressed as a function of k , y , and z ,

$$r = \frac{z}{k - z + y} . \tag{3.9}$$

3.3.1 Phase transition between AllC and mixed phases

When r is small, the system is in the AllC phase that is dominated by C -character, with only a tiny fraction of isolated D -nodes. An isolated D node that is surrounded by C nodes cannot be replaced by C , since its payoff is higher than any C node.

Many defectors initially

For systems with many defectors initially, consider a C -agent with two D -neighbors ($y = 2$) competing with one of its D neighbors that has one D -neighbor ($z = 1$). Figure 3.3(a) illustrates this pattern on a square lattice. The payoffs of the C and D nodes are:

$$\begin{aligned} P_C(k, 2) &= k - 2r, \\ P_D(k, 1) &= k + (k - 1)r - 1. \end{aligned} \quad (3.10)$$

The payoff difference between the C and D nodes is

$$P_C(k, 2) - P_D(k, 1) = 1 - (k + 1)r. \quad (3.11)$$

For r is very small, $P_C(k, 2) > P_D(k, 1)$, D nodes with one D -neighbor can be replaced by C -character, when competing with C nodes with two or less D neighbors. Only isolated D nodes left, so the system involves into an AllC phase (Fig. 3.3(b)). Thus the pattern shown in Fig. 3.3(a) is the last surviving pattern before the system transits into an AllC state. For r becomes larger than a critical value r_C , $P_C(k, 2) < P_D(k, 1)$, C can be replaced by D . The number of D nodes tends to increase, and the steady state contains both C and D nodes. The critical value r_C separates the AllC phase and the mixed phase with both C and D nodes. By Eq.(3.9),

$$r_C = \frac{1}{k + 1}. \quad (3.12)$$

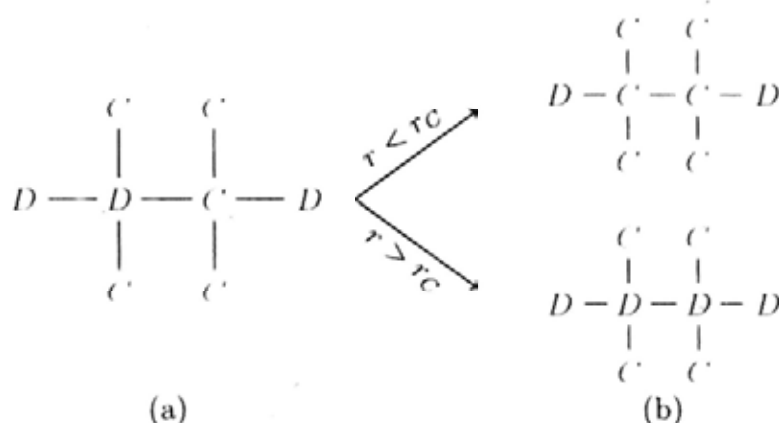


Figure 3.3: Schematic diagram showing the phase transition between AllC and mixed phases.

Figure 3.4 shows a comparison between the simulation results (symbols) of f_C versus r and the critical points predicted by Eq.(3.12) (vertical bars). The transition points are very well predicted by the theoretical analysis.

For r slightly larger than r_C , f_C drops sharply with a dropping rate $\frac{df_C}{dr}$. A second discontinuity of $\frac{df_C}{dr}$ occurs at a slightly larger value r_{C1} . f_C drops slower for $r > r_{C1}$, indicating another phase transition behavior. This transition can be explained as follows: When r becomes slightly larger than r_C , C nodes with two D -neighbors can be replaced by D -character, thus f_C drops sharply. However, C nodes with only one D -neighbor ($y = 1$) can still replace D nodes with one or more D -neighbors ($z = 1$ or above). When r becomes larger than a critical value r_{C1} , $P_C(k, 1) < P_D(k, 1)$, and C nodes with one D -neighbor are taken over by D nodes. By setting $P_C(k, 1) = P_D(k, 1)$, we obtain the critical point

$$r_{C1} = \frac{1}{k}. \quad (3.13)$$

The values of r_{C1} given by Eq.(3.13) are shown in Fig. 3.4 (vertical black bars), which coincide with the slope discontinuity points in the simulation results.

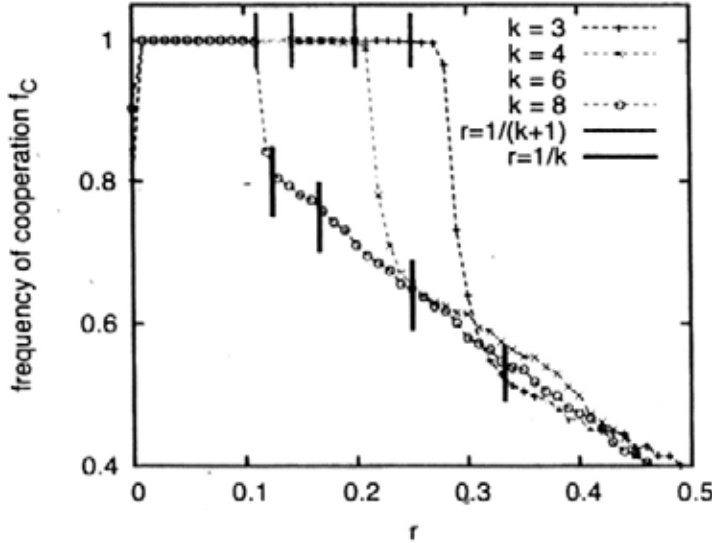


Figure 3.4: The simulation results of f_C versus r for systems with initial condition $x_C(t=0) = 0.5$ (symbols). The analytically predicted phase transition points r_C and r_{C1} are shown as the vertical bars.

Invasion problem: one defector initially

As mentioned, an isolated D character has the largest payoff value, which can replace one of its C neighbors and form a D - D pair. It is interesting to study the spread of the D character in systems with only one D node initially. This is called the invasion problem.

Consider a D - D pair surrounded by C nodes. Each of the two D nodes has $(k-1)$ C -neighbors. Thus they have the same payoff value

$$P_D(k, 1) = (k-1)(1+r). \quad (3.14)$$

The surrounding C nodes are also sharing the same payoff value

$$P_C(k, 1) = k - r. \quad (3.15)$$

$P_C(k, 1) > P_D(k, 1)$ at small r , one D in the D - D pair can be replaced by C , which leaves an isolated D node. The D pattern switches between an isolated

D node and a D - D pair. The D -character cannot spread and the system is in an AllC state. When r becomes large enough so that $P_C(k, 1) < P_D(k, 1)$, the D - D pair can grow, e.g. into D - D - D or other structures, the D -character can spread and the system involves into a mixed phase. The phase transition thus occurs at $P_C(k, 1) = P_D(k, 1)$, with the critical value

$$r_{C1} = \frac{1}{k}. \quad (3.16)$$

Figure 3.5 illustrates the phase transition schematically. The simulation results of f_C as a function of r for systems with one defector initially are shown in Fig. 3.6. Compared with systems with many defectors initially, the transition shifts from $1/(k+1)$ to $1/k$ (vertical bars), in agreement with the theoretical predictions in Eq.(3.16).

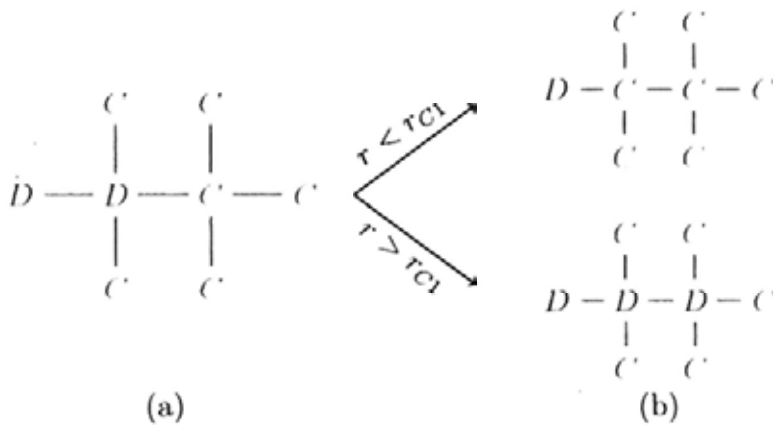


Figure 3.5: Schematic diagram showing the phase transition between AllC and mixed phases for square lattice with one defector initially.

3.3.2 Phase transition between mixed and AllD phases

As r increases, C nodes become less and less competitive. For r becomes larger than a critical value r_D , C node becomes almost extinct and the system changes from a phase containing both C and D characters to an AllD phase.

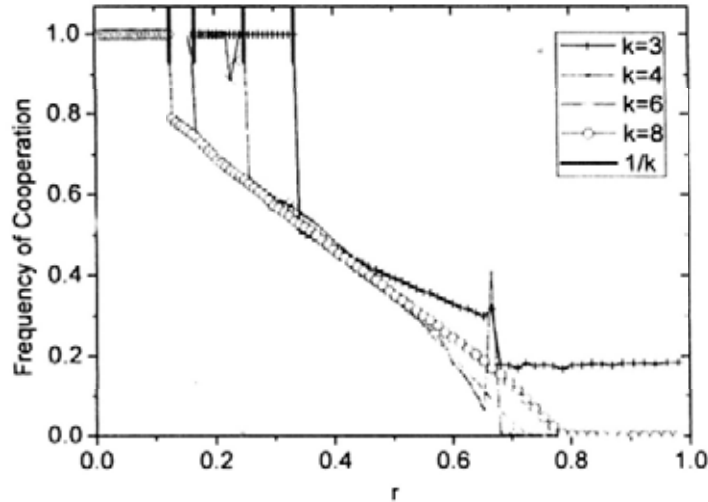


Figure 3.6: The simulation results of f_C versus r for systems with one D -node initially, i.e., the invasion problem. The critical points of the phase transition between the AllC and mixed phase shifts from $1/(k+1)$ to $1/k$ (black vertical bars).

This transition can also be explained by comparing the payoffs of C and D nodes.

Small fraction of cooperators initially

When the fraction of cooperators is initially small, it is difficult for C nodes to form big clusters. The last surviving pattern should be a C node surrounded by D nodes. If this C node is replaced by D , then C node extincts and the system evolves into an AllD phase (see Fig. 3.7).

The payoff of an isolated C node is

$$P_C(k, k) = k - kr, \quad (3.17)$$

Since we are considering the last surviving pattern, it is reasonable to assume this C node is the only C -neighbor of all its D -neighbors. The payoff value of

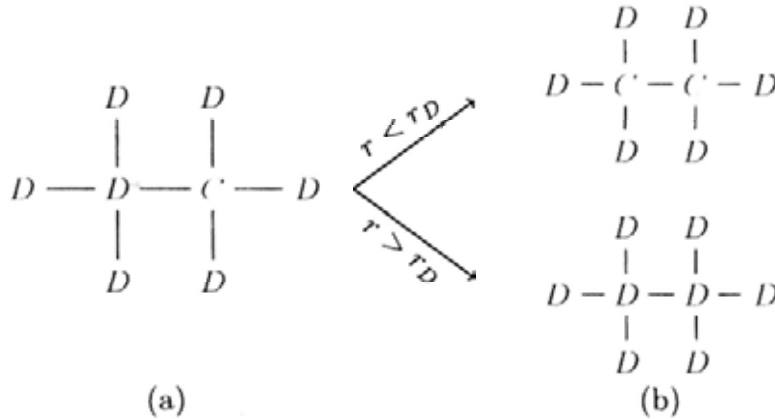


Figure 3.7: Schematic diagram showing the phase transition between mixed phase and AllD phase in systems with a small fraction of cooperators initially.

its D -neighbors are identical and given by

$$P_D(k, k-1) = 1 + r. \quad (3.18)$$

Let $P_C(k, k) = P_D(k, k-1)$, we obtain the critical value

$$r_D = \frac{k-1}{k+1}. \quad (3.19)$$

For $r > r_D$, the system evolves into an AllD phase. Figure 3.8 shows f_C as a function of r with initial condition $x_C(t=0) = 0.003$ for all four types of lattice structures. Equation (3.19) predicted the phase transition points r_D very well for all types of lattices.

Many cooperators initially

For systems with a large fraction of cooperators initially, Eq.(3.19) fails to predict r_D for the cases of $k = 3$ and 4. The reason is that C nodes with one or more C neighbors are able to resist the invasion from a D neighbor who has no other C -neighbors for $r = r_D$. For systems with a large fraction of cooperators initially, C - C pairs are common. Thus the phase transition point shifts from r_D to a larger value for $k = 3$ and 4. Here we explain the transition behavior of the $k = 3$ case.

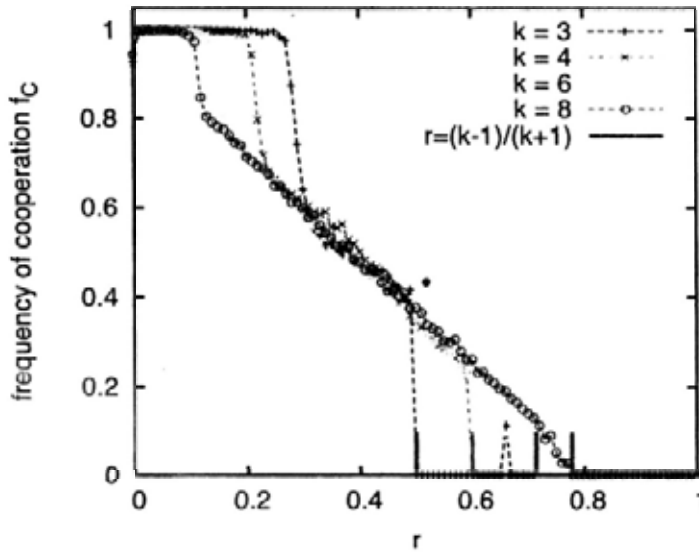


Figure 3.8: The simulation results of f_C versus r for systems with initial condition $x_C(t=0) = 0.003$. The transition into an AllD phase is predicted to occur at $\frac{k-1}{k+1}$ (vertical bars).

The surviving pattern critical to the extinction of C nodes in the $k=3$ case is a $C-C$ pair surrounded by D nodes for system with many cooperators initially, instead of an isolated C node. After this pattern breaks, an isolated C node can be replaced by D node, the system evolves into an AllD phase. The payoff to the C node is

$$P_C(3,2) = 3 - 2r. \quad (3.20)$$

The payoff to the surrounding D neighbors is

$$P_D(3,2) = 1 + r. \quad (3.21)$$

Phase transition occurs when $P_C(3,2) = P_D(3,2)$, so the transition point is

$$r_{D2} = \frac{2}{3}, \quad (k=3). \quad (3.22)$$

The r_{D2} value is shown in Fig. 3.9, which agrees with the simulation result.

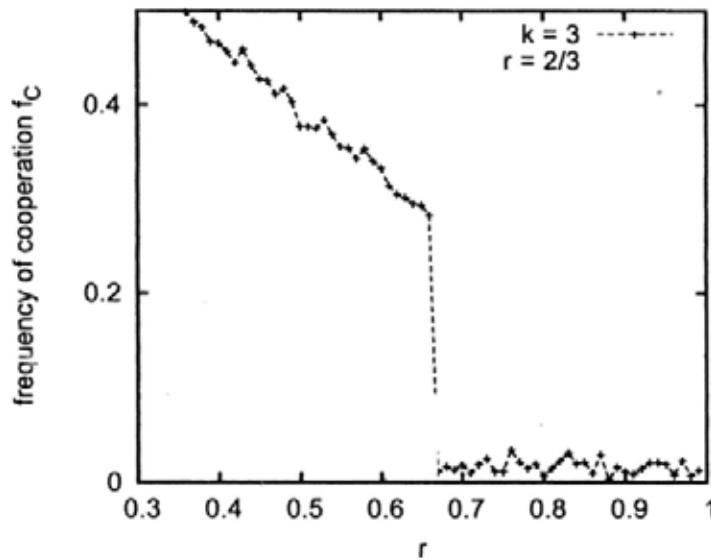


Figure 3.9: The simulation results of f_C versus r in a hexagonal lattice ($k = 3$) with initial condition $x_C(t = 0) = 0.5$. The critical point of phase transition between mixed phase and AllD phase is estimated to be $2/3$ (green vertical bar).

3.4 Discussion

In this chapter, we explained the phase transitions in the spatial snowdrift game by involving the idea of comparing the payoffs to C and D nodes in the last surviving patterns. This theory successfully explains the phase transition between AllC phase and mixed phase, and the transition between mixed phase and AllD phase. In other models of complex systems, similar ideas have been applied to explain the success rate in the Binary-Agent-Resource(BAR) game [53] and the critical phenomena of SG played on networks [54, 55]. This idea can further be extended in future studies on the emergent behavior in other games, such as the Public Good Game [56] and the N -person snowdrift game [57].

Chapter 4

The N -Person Snowdrift Game

In this chapter, we propose and study the multi-person version of the standard two-person Snowdrift game: The N -person Snowdrift Game (NPSG). The NPSG in a well-mixed population is studied analytically using the replicator dynamics. A numerical algorithm is proposed to simulate the game, with results in good agreement with the analytic result. The time evolution of cooperation is analytically studied. Besides the well-mixed case, the NPSG is also studied on 1D chain and 2D lattices. Compared with the well-mixed case, the fraction of cooperators is suppressed by the underlying structure in the population. By considering the 3-site local configurations in a 1D chain, we worked out analytically the equilibrium frequency of cooperation. Approximate solutions are then given for 2D lattices. Part of the results reported in this chapter can be found in Refs. [57, 58].

4.1 Motivation and set up of the game

The study of two-person games, such as the Prisoner's Dilemma and the snowdrift game, have been the main theme of evolutionary game theory. However, multi-person interactions are abundant in reality, which should better be described by multi-person games. A representative multi-person interacting game

is the Public Goods Game (PGG) [56, 59]. The PGG considers N interacting agents, each of them can choose to contribute an amount c to the public good or not. With n contributors (cooperators), the total contribution is nc , which is then multiplied by a factor \mathcal{R} ($\mathcal{R} < N$) and equally distributed to all N members. Thus a cooperator can obtain a benefit $\mathcal{R}nc/N - c$ and a defector (non-cooperator) can get $\mathcal{R}nc/N$. For $N = 2$, PGG reduces to the standard PD game. Thus, PGG is an N -person generalization of PD game. As in PD, cooperative behavior extinct for PGG played in a well-mixed population. In a spatial structured population, cooperators and defectors coexist [60, 61].

Here we propose a multi-person version of the snowdrift game, namely the N -person snowdrift game (NPSG)[57]. Consider a system consisting of N_{all} agents. A group of N agents are chosen to complete a task with cost c . If the task is completed, each member in the group gets a reward b . Each agent has two options: to share the labor to complete the task (cooperate), or to do nothing and wait for others to complete the task (defect). If there are n ($n \geq 1$) cooperators among the N agents, each of the N agent obtains a benefit b , with the cost shared by the n cooperators. However, if there is no cooperator ($n = 0$), then the N defectors get nothing. The payoffs to cooperators and defectors can then be written as

$$\bar{P}_C(n) = b - \frac{c}{n}, \quad \text{for } n \in [1, N], \quad (4.1)$$

$$\bar{P}_D(n) = \begin{cases} 0 & n = 0 \\ b & n \in [1, N - 1] \end{cases}, \quad (4.2)$$

where n is the number of cooperators in the group of N agents.

We can normalize the payoffs by introducing the cost-to-benefit ratio $r = c/b$. In terms of r , the payoffs can be written as

$$P_C(n) = 1 - \frac{r}{n}, \quad \text{for } n \in [1, N], \quad (4.3)$$

$$P_D(n) = \begin{cases} 0 & n = 0 \\ 1 & n \in [1, N - 1] \end{cases} \quad (4.4)$$

There are many real-life situations that can be modeled by the N -person snowdrift game, here we give a few examples:

- **Traffic blocked by snowdrift.** Consider an intersection of roads blocked by a snowdrift, cars from N directions are blocked. If the snowdrift is shoveled with a cost c , everyone can pass through the junction.
- **Group project.** Students in a course are often required to do a group project. Usually, the job is not evenly shared by the group members. Some students participate heavily, someone just wait for others to do the job. But everyone earns the some credit from the project as long as the active members finish the task [44].
- **Public construction.** For a public construction, such as a bridge or a road that serves a small community, if someone choose to contribute and share the cost, then everyone will be benefited from their contribution.
- **Clean up common areas.** Some common areas, such as a classroom or a dormitory, need to be cleaned up regularly with a cost c , so that everyone can be benefited from the cleanliness.

NPSG can be studied in a well-mixed population or on a network structure. The well-mixed and structured population in lattices will be studied in this chapter.

4.2 NPSG in well-mixed population

In this section, we study NPSG in a well-mixed population both analytically and numerically. This section is based on Ref. [57] and [58].

4.2.1 Analytical approach: the replicator dynamics

Consider a well-mixed population consists of N_{all} agents, the number of cooperators at time t is denoted by $N_C(t)$. The frequency of cooperation $x(t) = N_C/N_{\text{all}}$. The evolution of $x(t)$ is governed by the replicator dynamics [57]:

$$\dot{x} = x(f_C - \bar{f}), \quad (4.5)$$

where f_C (\bar{f}) is the instantaneous average fitness of cooperators (the whole population). Here,

$$\bar{f} = x f_C + (1 - x) f_D, \quad (4.6)$$

with f_D being the instantaneous average fitness of defectors. Substituting Eq.(4.6) into Eq.(4.5), we get

$$\dot{x} = x(1 - x)(f_C - f_D). \quad (4.7)$$

In a well-mixed population, the N agents forming a group are randomly chosen in every time step. The number of cooperators among the N agents follows a binomial distribution. f_C is then given by

$$f_C = \sum_{j=0}^{N-1} \binom{N-1}{j} x^j (1-x)^{N-1-j} P_C(j+1), \quad (4.8)$$

with the first three factors giving the probability of having $(j+1)$ cooperators in a group of N agents. Similarly,

$$f_D = \sum_{j=0}^{N-1} \binom{N-1}{j} x^j (1-x)^{N-1-j} P_D(j). \quad (4.9)$$

We first focus on the steady state of $x(t)$. In the steady state, $\dot{x} = 0$. By Eq.(4.7), it implies that the equilibrium frequency of cooperation x^* satisfies

$$f_C(x^*) = f_D(x^*). \quad (4.10)$$

Substituting Eqs. (4.3) and (4.4) into Eqs. (4.8) and (4.9), f_C and f_D can be expressed in terms of N and r . Equation (4.10) then becomes

$$\sum_{j=1}^{N-1} \frac{1}{j+1} \binom{N-1}{j} \left(\frac{x^*}{1-x^*} \right)^j = \frac{1-r}{r}. \quad (4.11)$$

The summation over j can be treated analytically by using the binomial expansion

$$(1 + y)^N = \sum_{i=0}^N \binom{N}{i} y^i. \quad (4.12)$$

Integrating both sides of Eq.(4.12) with respect to y ,

$$\begin{aligned} \int_0^x (1 + y)^N dy &= \frac{1}{N + 1} (1 + y)^{N+1} \Big|_0^x \\ &= \sum_{i=0}^N \binom{N}{i} \frac{y^{i+1}}{i + 1} \Big|_0^x, \end{aligned} \quad (4.13)$$

which results in an identity

$$\sum_{i=0}^N \binom{N}{i} \frac{x^{i+1}}{i + 1} = \frac{1}{N + 1} [(1 + x)^{N+1} - 1]. \quad (4.14)$$

Substituting Eq.(4.14) into Eq.(4.11), we obtain an N -th-order equation for x^* ,

$$r(1 - x^*)^N + Nx^*(1 - x^*)^{N-1} - r = 0. \quad (4.15)$$

Note that the population size N_{all} does not enter, as the analysis assumes an infinite population following the mean-field spirit. Among the N roots of Eq.(4.15), only the one between 0 and 1 is physically acceptable. For $N \leq 4$, Eq.(4.15) can be solved in closed form. For $N = 2$, the solution is $x^* = \frac{b-c}{b-c/2}$, which recovers the result of the standard two-person evolutionary snowdrift game in a well-mixed population (Eq.(1.12)). Figure 4.1 shows $x^*(r)$ for $N = 2, 3, 5$, and 10. $x^*(r)$ decreases as r increases for arbitrary N . For a given r , x^* is lower for larger N . This indicates that as the cost and group size increase, the incentives for being a cooperator drops, and agents tend to wait for others to complete the task and enjoy the benefit. The dependences of x^* on N for $r = 0.2, 0.5$ and 0.8 are shown in Fig. 4.2. x^* decreases as N increases, with a power law of exponent -1 . Analytically, by considering the small x^* limit of Eq.(4.15) we find

$$x^* = \frac{2(1 - r)}{(N - 1)(2 - r)}, \quad (4.16)$$

thus $x^* \sim 1/N$ for large N follows.

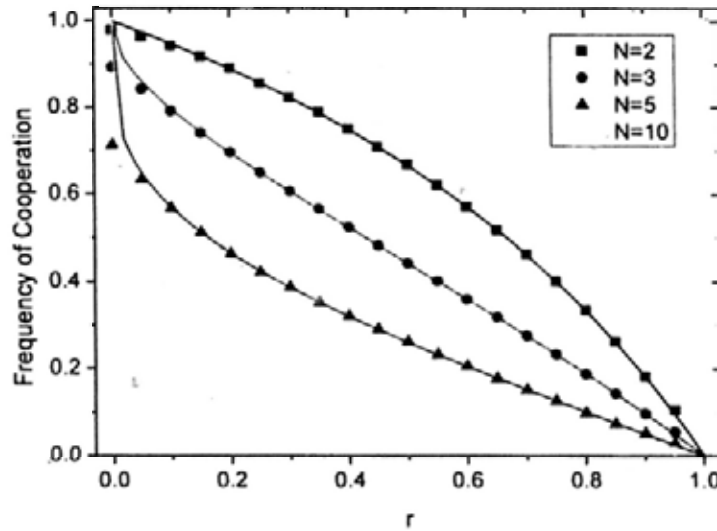


Figure 4.1: The equilibrium frequency of cooperation as a function of r , for $N = 2, 3, 5$, and 10 in a well-mixed population. The analytic results (lines) obtained by solving Eq.(4.15) and the simulation results (symbols) are in good agreement. The simulation parameters are $N_{all} = 2000$, initial fraction of cooperators $x(t = 0) = 0.5$, and 10^5 time steps. Each data point is an average over 100 realizations.

4.2.2 Simulation algorithm

To verify the analytic results of replicator dynamics, we perform numerical simulations on NPSG using the following algorithm: Consider a large population of N_{all} agents, every one can take on either the C -character or the D -character initially. At each time step, an agent i is randomly chosen, which competes with a group of $N - 1$ agents that are randomly chosen among the $N_{all} - 1$ agents. Depending on the character of agent i , its payoff P_i is evaluated according to Eq.(4.3) or Eq.(4.4). For evolution to happen, another agent j is randomly chosen. Agent j competes with a group of randomly chosen $N - 1$ agents and obtain a payoff P_j . If $P_i < P_j$, agent i will follow the character

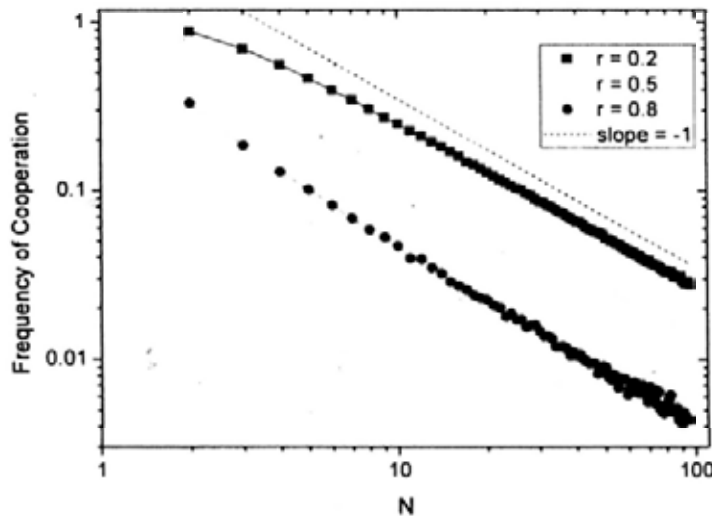


Figure 4.2: A log-log plot of the equilibrium frequency of cooperation as a function of N for $r = 0.2, 0.5,$ and 0.8 in a well-mixed population. The analytic results (lines) from Eq.(4.15) and the simulation results (symbols) are in good agreement. The simulation parameters are $N_{all} = 5000$, $x(t = 0) = 0.5$, and 10^7 time steps. Every data point is an average over 10 realizations. A dotted line of slope -1 is shown to guide the eye.

of agent j with probability $(P_j - P_i)$. If $P_i \geq P_j$, the character of agent i remains unchanged. The results obtained from numerical simulations (symbols in Figs. 4.1 and 4.2) agree well with the analytic results based on the replicator dynamics, showing that the simulation algorithm is constructed properly. The construction of a proper simulation algorithm will be useful in studying variations of the model in which analytical approaches fail.

4.2.3 Time evolution of cooperation

The time evolution of cooperation based on the above algorithm can also be studied analytically. To proceed, it is useful to focus on the *effective* time step. In carrying out numerical simulations, evolution (i.e., change in character or strategy) cannot happen if agents i and j are sharing the same character.

The effective time steps are those in which a possible strategy switching may happen, i.e., agents i takes C and j takes D or vice versa. For a system with the fraction of cooperators being x , the probability for a time step to be effective is $2x(1-x)$.

Competing factors in evolutionary dynamics

Among the effective time steps, the probability that agent i holds C and agent j holds D is $1/2$. Under this condition, $P_j > P_i$ holds, except for the case that agent j faces a group of $N-1$ defectors. The probability for this situation to happen is $(1-x)^{N-1}$. With probability $1 - (1-x)^{N-1}$, $P_j = 1 > P_i$, and agent i will adapt the character of agent j with probability $(1-P_i)$. For agent i , the number of cooperators among its all $N-1$ neighbors follows a binomial distribution. The probability $\text{Prob}(C \rightarrow D)$ that agent i switches from C to D in an effective time step is given by

$$\text{Prob}(C \rightarrow D) = \frac{1}{2} \times [1 - (1-x)^{N-1}] \times \sum_{n=0}^{N-1} \left[\frac{r}{n+1} \binom{N-1}{n} x^n (1-x)^{N-1-n} \right]. \quad (4.17)$$

Following similar arguments, the probability that agent i switches from D to C in an effective time step is

$$\text{Prob}(D \rightarrow C) = \frac{1}{2} \times (1-x)^{N-1} \times \sum_{n=0}^{N-1} \left[\left(1 - \frac{r}{n+1}\right) \binom{N-1}{n} x^n (1-x)^{N-1-n} \right]. \quad (4.18)$$

It is useful to define two coefficients P_{\downarrow} and Q_{\uparrow} :

$$\begin{aligned} P_{\downarrow}(r, x; N) &= \sum_{n=0}^{N-1} \frac{r}{n+1} \binom{N-1}{n} x^n (1-x)^{N-1-n} \\ &= \frac{r}{Nx} [1 - (1-x)^N], \end{aligned} \quad (4.19)$$

and

$$Q_{\uparrow}(x; N) = (1-x)^{N-1}. \quad (4.20)$$

P_{\downarrow} is the average deviation of the cooperator's payoff from the maximum payoff value 1, and Q_{\uparrow} is the probability that the $N - 1$ random neighbors are all defectors. In terms of P_{\downarrow} and Q_{\uparrow} , Eqs. (4.17) and (4.18) can be written as

$$F_{\downarrow} \equiv \text{Prob}(C \rightarrow D) = \frac{1}{2}P_{\downarrow}(1 - Q_{\uparrow}), \quad (4.21)$$

$$F_{\uparrow} \equiv \text{Prob}(D \rightarrow C) = \frac{1}{2}Q_{\uparrow}(1 - P_{\downarrow}). \quad (4.22)$$

By introducing F_{\downarrow} and F_{\uparrow} , we change our viewpoint from the switching of character of individual players, to the change in the global fraction of cooperators in the whole population. F_{\downarrow} (F_{\uparrow}) is a "force" that acts on the population to suppress (promote) cooperation.

For a system at the steady state with cooperators take a fraction x^* , $\text{Prob}(C \rightarrow D) = \text{Prob}(D \rightarrow C)$, which implies

$$P_{\downarrow}(r, x^*; N) = Q_{\uparrow}(x^*; N). \quad (4.23)$$

Substituting Eqs. (4.19) and (4.20) into Eq.(4.23), we recover the N -th-order equation Eq.(4.15) that obtained by replicator dynamics.

Time evolution of the frequency of cooperation

The two quantities $P_{\downarrow}(r, x; N)$ and $Q_{\uparrow}(x; N)$ are time dependent as they depend on the instantaneous frequency of cooperation $x(t)$. Therefore, F_{\downarrow} and F_{\uparrow} are also time dependent. Thus our analysis can be applied to study the time evolution of $x(t)$. Consider a system of size N_{all} . $N_C(t)$ is the number of cooperators at time t and the frequency of cooperation $x(t) = N_C(t)/N_{\text{all}}$. With probability F_{\uparrow} , the system has one more cooperator in an effective time step, and F_{\downarrow} is the probability to lose one cooperator. Let $\langle N_C(t) \rangle$ be the expected value of N_C at time step t , the expected value for N_C in the next

time step $\langle N_C(t+1) \rangle$ is

$$\begin{aligned} \langle N_C(t+1) \rangle &= \langle N_C(t) \rangle \times (1 - F_\uparrow - F_\downarrow) + (\langle N_C(t) \rangle + 1) \times F_\uparrow \\ &\quad + (\langle N_C(t) \rangle - 1) \times F_\downarrow \\ &= \langle N_C(t) \rangle + \frac{1}{2}(Q_\uparrow - P_\downarrow). \end{aligned} \quad (4.24)$$

By Eq.(4.24), we get a difference equation of $\langle x(t) \rangle$:

$$\langle x(t+1) \rangle - \langle x(t) \rangle = \frac{1}{2N_{all}}(Q_\uparrow - P_\downarrow). \quad (4.25)$$

Substituting Eqs. (4.19) and (4.20) into Eq.(4.25) and taking time as a continuous variable, we obtain a differential equation of $\langle x(t) \rangle$:

$$\frac{d\langle x \rangle}{dt} = \frac{1}{2N_{all}} \left[(1 - \langle x \rangle)^{N-1} + \frac{r}{N\langle x \rangle} ((1 - \langle x \rangle)^N - 1) \right]. \quad (4.26)$$

Equation (4.26) is a differential equation for the time evolution of $\langle x(t) \rangle$, starting from its initial value $x(t=0)$ to the equilibrium value x^* . It is possible to solve $\langle x(t) \rangle$ analytically for $N=2$ and 3. For $N \geq 4$, Eq.(4.26) can be solved numerically.

When $N=2$, the NPSG recovers the standard two-person SG, the analytic solution for Eq.(4.26) is simple. For $N=2$, Eq.(4.26) becomes

$$\frac{d\langle x \rangle}{dt} = \frac{1}{2N_{all}} \left[\left(\frac{r}{2} - 1 \right) \langle x \rangle + (1 - r) \right], \quad (4.27)$$

which gives the time evolution of $\langle x(t) \rangle$,

$$\begin{aligned} \langle x(t) \rangle &= \frac{2-2r}{2-r} + \left(x_0 - \frac{2-2r}{2-r} \right) e^{-\frac{2-r}{2N_{all}}t} \\ &= x_{N=2}^* + (x_0 - x_{N=2}^*)e^{-\beta t}. \end{aligned} \quad (4.28)$$

The long time limits gives $x_{N=2}^* = \frac{2-2r}{2-r}$, which agrees with the equilibrium x^* obtained by replicator dynamics (Eq.(1.12)).

For $N=3$, Eq.(4.26) becomes

$$\frac{d\langle x \rangle}{dt} = \frac{1}{2N_{all}} \left[\left(1 - \frac{r}{3} \right) \langle x \rangle^2 - (2-r)\langle x \rangle + (1-r) \right]. \quad (4.29)$$

Depending on the comparison between the values of x_0 and x^* , there are two solutions. If $x_0 \geq x^*$,

$$x(t) = \frac{6-3r}{6-2r} - \frac{\sqrt{3r(4-r)}}{6-2r} \tanh \left[\frac{\sqrt{3r(4-r)}}{12N_{all}} t + \tanh^{-1} \left(\frac{(6-3r) - (6-2r)x_0}{\sqrt{3r(4-r)}} \right) \right] \quad (4.30)$$

For $x_0 < x^*$, the solution is

$$x(t) = \frac{6-3r}{6-2r} - \frac{\sqrt{3r(4-r)}}{6-2r} \coth \left[\frac{\sqrt{3r(4-r)}}{12N_{all}} t + \coth^{-1} \left(\frac{(6-3r) - (6-2r)x_0}{\sqrt{3r(4-r)}} \right) \right] \quad (4.31)$$

Both solutions give the same long time limit of $x_{N=3}^* = \frac{6-3r-\sqrt{3r(4-r)}}{6-2r}$, which agrees with $x_{N=3}^*$ obtained by Eq.(4.15). As an illustration of how the frequency of cooperation $x(t)$ evolves, Figure 4.3 shows the typical evolutionary trends of $x(t)$ for $N = 2$ and 3 obtained by numerical simulations, together with analytic results given by Eq.(4.28) and Eq.(4.31). Good agreement between analytic results and simulation data is found.

4.3 NPSG on lattices

In addition to the well-mixed case, we study NPSG in structured population in chain and 2D lattices. An simulation algorithm is proposed to obtain numerical results. Besides the numerical results, analytic results are given for NPSG on 1D chain.

4.3.1 Simulation algorithm and numerical results

The simulation algorithm is similar to that of the well-mixed case. In each time step, a node i is randomly picked to play a $(k+1)$ -person game with its k neighbors in a lattice. Depending on the character of agent i , its payoff P_i is evaluated according to Eq.(4.3) or Eq.(4.4). Another agent j is then randomly picked and its payoff P_j is found by competing with its k neighbors. If P_i is

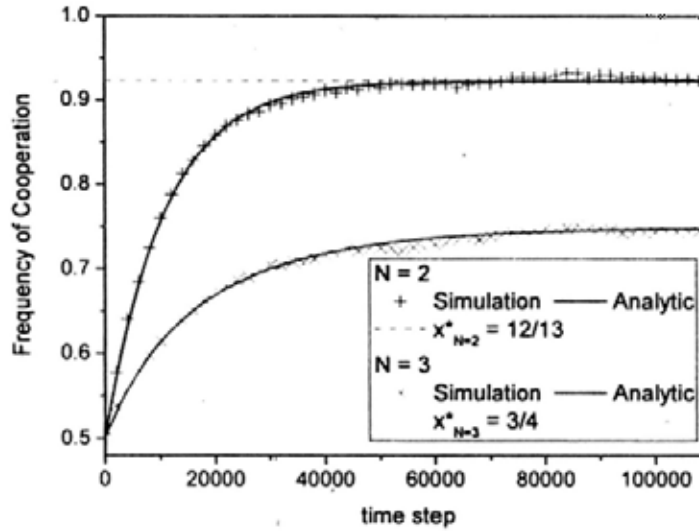


Figure 4.3: The simulation (symbols) and analytic results (lines) of the time evolution of $x(t)$ for 2-person ($N = 2$) and 3-person ($N = 3$) snowdrift game. The parameters are $r = 1/7$, $x(t = 0) = 1/2$, and $N_{all} = 5000$. The simulation results are obtained by one single run. The analytic results are obtained by Eq.(4.28) and Eq.(4.31). The equilibrium frequency of cooperation $x_{N=2}^* = 12/13$ and $x_{N=3}^* = 3/4$ (dotted lines) are shown to guide the eye.

less than P_j , the character of agent i will be replaced by that of agent j with probability $(P_j - P_i)$. If $P_i \geq P_j$, agent i keeps its own character.

We play NPSG on the following lattices: 1D chain with two nearest neighbors ($k = 2$), 2D hexagonal lattice ($k = 3$), 2D square lattice ($k = 4$), 2D triangle lattice ($k = 6$), and 2D square lattice with connections to the nearest and next nearest neighbors ($k = 8$). We use a typical size of lattice $N_{all} = 10^4$ nodes. The periodic boundary condition is imposed to mimic an infinite population. Numerical results are shown in Fig. 4.4 (symbols), together with the corresponding analytic results of the well-mixed case with the same group size $N = k + 1$ (lines). Comparing with the well-mixed case with the same N , the frequency of cooperation x^* is suppressed in the presence of an underlying lattice structure. This result is consistent with that in the spatial two-person

snowdrift game (Chapter 3).

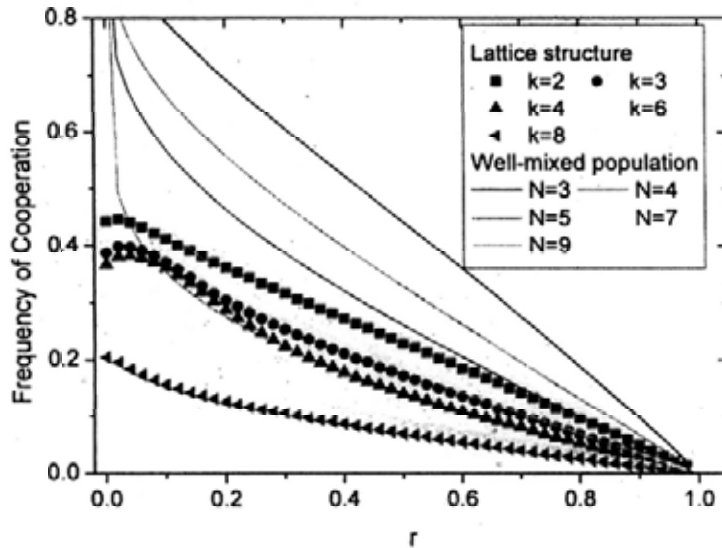


Figure 4.4: The frequency of cooperation as a function of r for different lattices. Numerical results (symbols) of 1D chain with $k = 2$, 2D lattice with $k = 3, 4, 6$, and 8 are shown. The simulation parameters are $N_{all} = 10^4$, $x(t = 0) = 0.5$, and 10^6 time steps. Each data point is an average over 50 runs. For comparison, the lines show the results in the well-mixed case with the same values of $N = k + 1$. The presence of an underlying lattice structure suppresses the frequency of cooperation significantly.

4.3.2 Analytic study on 1D chain

Here, we derive an analytic solution for NPSG in a 1D chain by considering the transitions between different local configurations. In a 1D chain, we observed that two connected C -nodes do not exist in the steady state. This is because such a C - C pair is unstable. One C node in this C - C pair will try to switch its character when it compares its payoff with a D node that has a C neighbor. After switching, this defected C node has no interest to switch back to C again, since it gets the highest payoff when competing with the adjacent C neighbor.

Local configuration	Type	Payoff of central site
DCD	$C1$	$1 - r$
CDC	$D1$	1
CDD	$D2$	1
DDC	$D2$	1
DDD	$D3$	0

Table 4.1: Classification of local configurations in a 1D chain with nearest neighboring connections.

As a result, only isolated C nodes exist at equilibrium.

For NPSG on a 1D chain, every node plays a 3-person game with its two neighbors. Consider the possible local configurations involving three neighboring nodes. There are eight possible local configurations in principle. Since two C nodes cannot be adjacent, we only need to consider five out of the eight configurations at equilibrium: DDD , CDD , DDC , CDC , and DCD . Due to the left-right symmetry, the two configurations CDD and DDC can be further classified to belong to one type, which left us four types. These configurations are listed in Table 4.1.

Let N_{C1} , N_{D1} , N_{D2} , N_{D3} be the number of the four types of local configurations. At any time, these numbers add up to

$$N_{C1} + N_{D1} + N_{D2} + N_{D3} = N_{all} . \quad (4.32)$$

For every C -agent in the central site (type $C1$), it also appears twice in the peripheral sites (types $D1$ and $D2$). The balance between the sum of C -agents in the central and peripheral sites lead to

$$2N_{D1} + N_{D2} = 2N_{C1} . \quad (4.33)$$

Next we consider the probabilities of making a transition from one configuration to another, as the system evolves. In doing so, it is convenient to consider

the effective time steps, in which there is an attempt in a change of the character of a chosen node [58]. For a chosen agent i comparing its payoff with another agent j , the agents i and j must hold different characters for a possible change to occur. Taking the central site as the one for evolution, there will be transitions between types $C1$ and $D3$. For transition from $C1$ to $D3$, we select a type $C1$ agent as node i , and a type $D1$ or $D2$ agent as node j . The payoff difference is $P_j - P_i = r$. The probability for the transition to happen is

$$\text{Prob}(C1 \rightarrow D3) = 1 \times \frac{N_{D1} + N_{D2}}{N_{D1} + N_{D2} + N_{D3}} \times r. \quad (4.34)$$

Similarly, the probability that a type $D3$ configuration becomes type $C1$ is

$$\text{Prob}(D3 \rightarrow C1) = \frac{N_{D3}}{N_{D1} + N_{D2} + N_{D3}} \times 1 \times (1 - r). \quad (4.35)$$

In dynamical equilibrium, these two probabilities are equal and we have

$$\frac{N_{D3}}{N_{D1} + N_{D2}} = \frac{r}{1 - r}. \quad (4.36)$$

One more equation can be obtained by considering the transition between types $D1$ and $D2$. When the central agent changes its character, the neighboring sites can notice this change in their peripheral sites. Two peripheral C sites are removed for a C -agent switches to D . The neighboring sites of that C -agent may change from type $D1$ to $D2$, or from type $D2$ to $D3$. In a mean field approach, the two peripheral C sites are randomly removed from all configurations that have one or more peripheral C sites. Thus, the probability that type $D1$ loses a peripheral C site is twice as of that for type $D2$. Therefore, the probability for a transition from type $D1$ to type $D2$ is

$$\text{Prob}(D1 \rightarrow D2) = 2 \times \frac{2N_{D1}}{2N_{D1} + N_{D2}}. \quad (4.37)$$

The same analysis when applied to the transition from type $D2$ to type $D1$ gives

$$\text{Prob}(D2 \rightarrow D1) = 2 \times \frac{N_{D2}}{2N_{D3} + N_{D2}}. \quad (4.38)$$

Dynamical equilibrium implies $\text{Prob}(D1 \rightarrow D2) = \text{Prob}(D2 \rightarrow D1)$, and thus

$$\frac{2N_{D1}}{2N_{D1} + N_{D2}} = \frac{N_{D2}}{2N_{D3} + N_{D2}}. \quad (4.39)$$

The ratio $\frac{N_{type}^*}{N_{all}}$ of the four types of configuration can be obtained by solving the set of four equations Eqs. (4.32), (4.33), (4.36), and (4.39). The results are

$$\frac{N_{C1}^*}{N_{all}} = \frac{1 - \sqrt{r}}{2 - \sqrt{r}}, \quad (4.40)$$

$$\frac{N_{D1}^*}{N_{all}} = \frac{(1 - \sqrt{r})^2}{2 - \sqrt{r}}, \quad (4.41)$$

$$\frac{N_{D2}^*}{N_{all}} = \frac{2\sqrt{r} - 2r}{2 - \sqrt{r}}, \quad (4.42)$$

$$\frac{N_{D3}^*}{N_{all}} = \frac{r}{2 - \sqrt{r}}. \quad (4.43)$$

The equilibrium frequency of cooperation $x^* = \frac{N_{C1}^*}{N_{all}}$ is given by Eq.(4.40). A comparison between the simulation results and Eq.(4.40) is shown in Fig. 4.5, and good agreement is found. Therefore, it is sufficient to consider local configurations consisting of 3 neighboring sites for a 1D chain, and there is no need to consider local configurations longer than 3 sites.

4.3.3 Analytic theory for 2D lattices

Chan [44] extended the analysis to NPSG on a 2D square lattice ($k = 4$) by considering local configurations of 5 sites: the central site and its four nearest neighbors. The analytic result of the frequency of cooperation is found to be

$$x_C^*(k = 4) = \frac{1 - r^{1/4}}{2 - r^{1/4}}. \quad (4.44)$$

Comparing Eq.(4.44) with simulation results of x_C^* , the analytic result of x_C^* works well only for large r , and discrepancies are found at small r (see Fig. 4.6). Examining the spatial patterns of C and D nodes, it was found that checkerboard-like structures exist at small r , showing a correlation between an agent

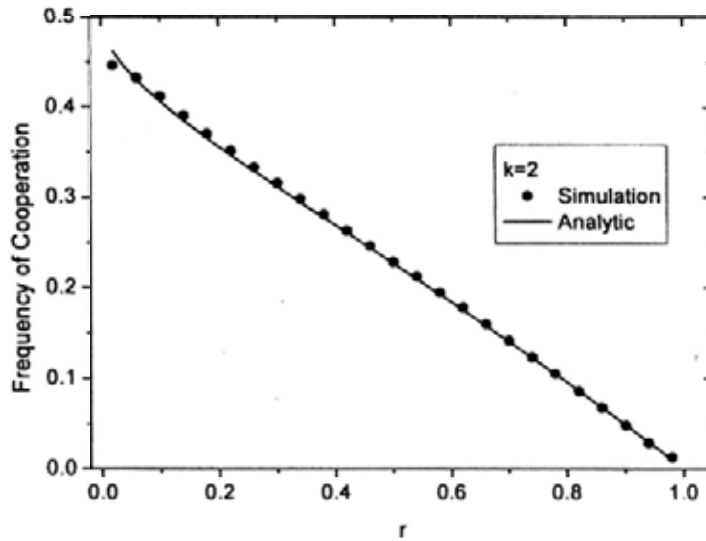


Figure 4.5: The frequency of cooperation as a function of r in a 1D chain (symbols). In simulations, we used $N_{all} = 10^4$, $x(t = 0) = 0.5$ and 10^6 time steps. Each data point is an average over 50 realizations. The analytic results obtained by Eq.(4.40) (line) are shown for comparison, and good agreement is found.

and its *diagonal* neighbors (next nearest neighbors). This is the reason why the analytic result obtained by considering only 5-site configurations fails at small r .

For lattices with larger values of k , it is difficult to obtain an analytic solution for x_C^* . Inspired by the analytic results of 1D chain and 2D square lattice, we propose a form for the equilibrium frequency of cooperation for large k values:

$$x_C^*(k) = \frac{1 - r^{1/k}}{2 - r^{1/k}}. \quad (4.45)$$

When $k = 2$ and 4, Eq.(4.45) recovers x_C^* in 1D chain and 2D square lattice. Figure 4.6 shows the results given by Eq.(4.45) (lines) and the simulation results (symbols) for the 2D triangle lattice ($k = 6$) and 2D square lattice with nearest and next nearest neighbors connected ($k = 8$). The proposed form

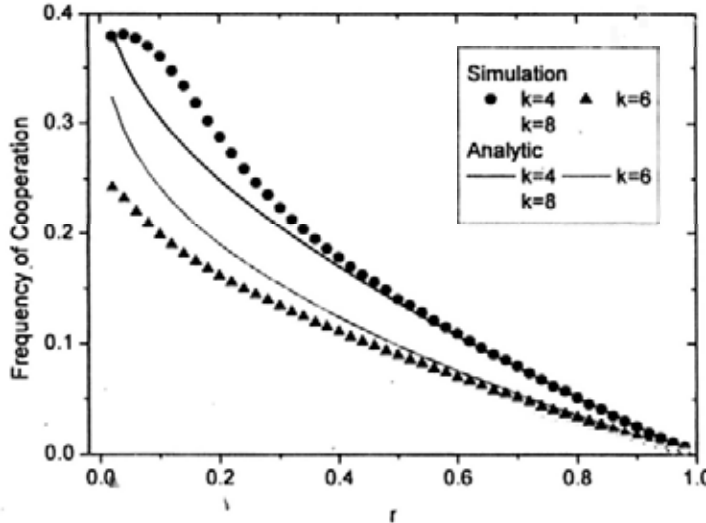


Figure 4.6: The frequency of cooperation as a function of r in 2D lattices with $k = 4, 6$ and 8 (symbols). In simulations, we used $N_{all} = 10^4$, $x(t = 0) = 0.5$ and 10^6 time steps. Each data point is an average over 50 realizations. The analytic results proposed in Eq.(4.45) (lines) are shown for comparison.

works well at large r , when compared with simulation results.

4.4 Conclusion

In this chapter, we proposed and studied the N -person snowdrift game. The model is a generalization of the snowdrift game to include N -person interactions. The game was studied both analytically and numerically in a well-mixed population. It was found that the frequency of cooperation decreases as r and N increases. The time evolution of cooperation was studied analytically by considering the two opposite forces that promote (F_{\uparrow}) and suppress (F_{\downarrow}) the cooperation. The simulation results verified the results of the $N = 2$ and 3 cases.

In addition to the well-mixed case, NPSG was numerically studied on lattice structures. Compared with the well-mixed case, cooperation is suppressed

by the underlying lattices. Analytic theories were developed by focusing on the local configurations consisting of a central site and its nearest neighbors. The theory works successfully in 1D chain. In 2D lattices, the theory works at large r and discrepancies are found at small r , suggesting that a theory that includes larger spatial correlation is needed in the small- r region.

Chapter 5

Snowdrift game on adaptive network

In Chapters 3 and 4, we studied the dynamics of games on static lattices, in which the network structure does not change as the game evolves. However, in many real world systems, the relation between agents (thus the structure of the network) often co-evolves with the interactions between them (thus the dynamics of the game). Examples are abundant. In the spread of an epidemic, such as SARS or H1N1, it is useful to isolate infected patients from healthy people so as to slow down the spread. In the language of Susceptible-Infected-Recovered (SIR) model [62] on networks, it means that the links between an agent and others will be broken if the character of the agent changes from susceptible to infected. Another example is that before an election, voters like to communicate with people that share the same opinion, and the social network is thus influenced by the opinion of the voters.

The co-evolution of dynamical processes and network structures is now an important problem in complex networks and complex systems. Gross et al. studied epidemic dynamics on an adaptive network [63]. Besides the normal Susceptible-Infected-Susceptible (SIS) process, a susceptible agent breaks the

link and rewire to another randomly chosen susceptible agent with a probability w for every SI link. The rewiring process can change the degree correlations, the fraction of infected agents, and other properties of the systems. For the Voter Model [64], rewiring can lead to a phase transition between a connected and a fragmented network [65]. In the connected condition, the dependence of the consensus time on the network size can either be logarithm (direct Voter Model) or exponential (reverse Voter Model) [66]. For two-person games, the Prisoner's Dilemma has been studied on an adaptive network by Zimmermann et al. [67].

In this chapter, we propose and study a model of an adaptive network of agents competing in the Snowdrift game.

5.1 Model and numerical results

The Snowdrift game has been introduced in Sec. 1.1.3. The normalized payoff matrix of SG has been given in Eq.(3.4) as

$$\begin{array}{cc} & \begin{array}{cc} C & D \end{array} \\ \begin{array}{c} C \\ D \end{array} & \left(\begin{array}{cc} R = 1 & S = 1 - r \\ T = 1 + r & P = 0 \end{array} \right), \end{array}$$

with the cost-to-benefit ratio $r \in (0, 1)$.

Consider a system consisting of N agents connected by a network structure. An agent can take on one of the two characters, either cooperate (C) or non-cooperate/defect (D). The average degree $\langle k \rangle$ is kept fixed as the network evolves.

At each time step, a pair of C - D link connecting nodes i and j of opposite characters is randomly picked. Agents i and j then play the Snowdrift game with each of their neighboring agents and obtain an accumulative payoff Pa_i and Pa_j , respectively. The per link payoffs P_i and P_j are obtained by dividing

Pa_i and Pa_j by their degrees, i.e.,

$$P_i = \frac{Pa_i}{k_i} \quad \text{and} \quad P_j = \frac{Pa_j}{k_j},$$

where k_i and k_j are the instantaneous degrees of nodes i and j . Evolution takes place if $P_i \neq P_j$. Here we call the agent with the lower payoff the *loser*, and the agent with the higher payoff the *winner*. The loser tries to do better by either changing his character or his neighborhood. With probability $f(P_i, P_j)$, the loser switches his character to follow the winner's character. With probability $1 - f(P_i, P_j)$, the loser will break the link that connected to the winner and rewire to another agent m . The probability function $f(P_i, P_j)$ takes the form of

$$f(P_i, P_j) = \left| \frac{P_i - P_j}{1 + r} \right|, \quad (5.1)$$

where $(1 + r)$ is a normalization factor. Two mechanisms are imposed to find the target agent m :

- *Random Rewiring*: m is randomly chosen from all agents, except those who are the current neighbors of the loser.
- *Opinion Rewiring*: m is randomly chosen from the agents that share the same character as the loser.

Compared with previous studies on the Snowdrift game on static networks (see Chapter 3), the new element is the rewiring process driven by the dynamics of the game.

5.1.1 Numerical results

We carried out numerical simulations of the model. The 2D hexagonal ($\langle k \rangle = 3$) and square ($\langle k \rangle = 4$) lattices are chosen to be the initial underlying networks. With the rewiring process, the network structure evolves with time. Initially, a fraction x_0 of agents are randomly assigned the C character and

other agents take on the D character. The equilibrium frequency of cooperation f_C as a function of the cost-to-benefit ratio r are shown in Fig. 5.1 for the two rewiring mechanisms. We compare the results with that of the snowdrift game on static lattices discussed in Chapter 3 (dotted lines). By introducing the rewiring process, f_C is promoted in a large range of r for both random rewiring and opinion rewiring. In both cases, there is a critical point r_C , above which f_C decreases sharply. The results of opinion rewiring (lower panel) are more interesting. When $r < r_C$, $f_C = 1$ corresponding to a homogeneous AllC phase. As r becomes larger than r_C , f_C decreases and the system is in a mixed phase with both C and D agents. We will focus on the case of opinion rewiring in the following discussion.

5.1.2 The steady state

The network structure is changed by the rewiring process. It is found that the system often breaks into clusters in the steady state. Table 5.1 shows some key properties of the system for several values of r , including the size of the two biggest clusters, the fraction of cooperators, and the mean degree of these clusters. When $r < r_c$, the system is dominated by one big cluster containing only C nodes, together with a few isolated nodes and small clusters. When $r > r_C$, except for some particular values, the system has two big clusters generally: one cluster is AllC and the other is AllD (see Fig. 5.2(a)). For some particular values of r , such as the $r = 0.8$ case in Table 5.1, the system is dominated by one cluster containing both C and D nodes.

What is happening at these values of r ? Why does the system not break into pieces of opposite characters? To answer these questions, we examine the remaining C - D pairs at equilibrium. It turns out that the payoffs of the connected C and D nodes are equal, i.e., $f(P_C, P_D) = 0$, and evolution stops. For most cases, the number of C - D links L_{CD} amounts only to a small fraction

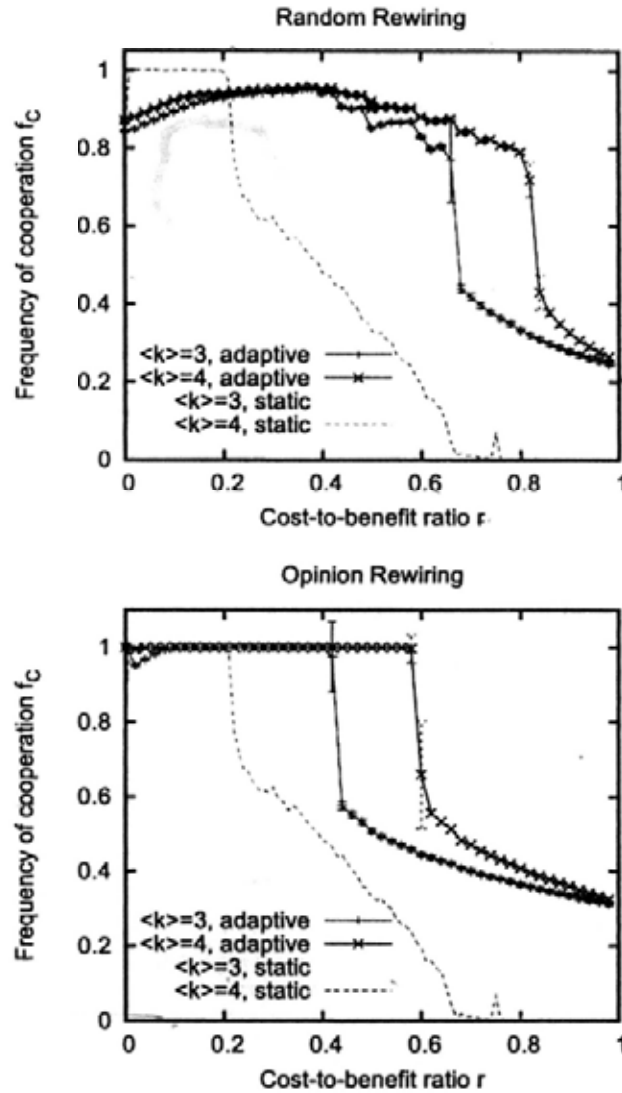


Figure 5.1: The equilibrium frequency of cooperation f_C as a function of r (symbols) for random rewiring (upper panel) and opinion rewiring (lower panel). The initial network structures are 2D lattices with $\langle k \rangle = 3$ and 4. The simulation parameters are $N = 10^4$, initial fraction of cooperators $x_0 = 0.5$, and 5×10^5 time steps. Each data point is an average over 100 realizations. The standard deviation of f_C is shown as error bar. For comparison, f_C as a function of r for SG on static lattices are also shown (dotted lines).

Table 5.1: The size, frequency of cooperation x_{Cs} and the mean degree $\langle k_s \rangle$ of the two largest clusters for the system in the steady state. $r = 0.3, 0.7$ and 0.8 . The system size is $N = 10^4$, each set of data is obtained by one realization.

$\langle k \rangle = 3, x_C = 0.4$			$\langle k \rangle = 4, x_C = 0.58$		
Cluster Size	x_{Cs}	$\langle k_s \rangle$	Cluster Size	x_{Cs}	$\langle k_s \rangle$
$r = 0.3, f_C = 0.9999$			$r = 0.3, f_C = 0.9999$		
9957	1	3.012	9986	1	4.005
4	1	1.5	2	1	1
$r = 0.7, f_C = 0.3965$			$r = 0.7, f_C = 0.4737$		
3965	1	3.390	4737	1	3.811
5877	0	2.794	5229	0	4.194
$r = 0.8, f_C = 0.3556$			$r = 0.8, f_C = 0.4041$		
9900	0.359	3.02	9972	0.4052	4.009
3	0	1.333	2	0	1

of the total number of links L . So the largest cluster has the form of a C cluster connected to a D cluster by a number of C - D links, as shown in Fig. 5.2(b) schematically.

It is possible to explain the existence of these particular values of r analytically. Recall that in Sec. 3.3, we express the payoff of a C or D node as a function of its degree and the number of D -neighbors. Here we follow the idea. For a node of degree k that has y D -neighbors, its payoff can be written as

$$P_C(k, y) = \frac{(k-y)R + yS}{k} = 1 - \frac{y}{k}r \quad (5.2)$$

if it is of C character, and

$$P_D(k, y) = \frac{(k-y)T + zP}{k} = \frac{(k-y)(1+r)}{k} \quad (5.3)$$

if it is of D character. For the two nodes at the two ends of a C - D link when

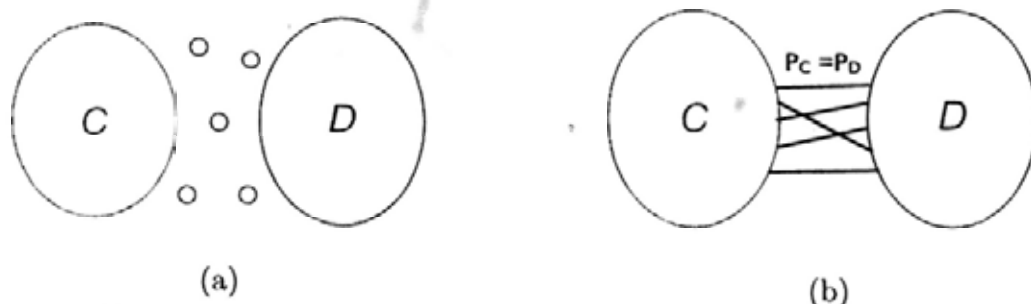


Figure 5.2: Schematic diagrams show the two different scenarios of the system at equilibrium for $r > r_C$. (a) Two big clusters of opposite characters. (b) One cluster with C and D nodes.

evolution stopped, they should have the same payoff. It implies that

$$P_C(k_C, y_C) = P_D(k_D, y_D), \quad (5.4)$$

where k_C (k_D) and y_C (y_D) are the degree and number of D -neighbors of the C (D) node, respectively. Substituting Eqs. (5.2) and (5.3) into Eq.(5.4), we obtain an equality

$$r = \frac{k_C y_D}{k_D y_C + k_C (k_D - y_D)}. \quad (5.5)$$

Since k_C , k_D , y_C and y_D are all integers and they satisfy the conditions that $y_C \leq k_C$ and $y_D \leq (k_D - 1)$, this equality only holds for some particular values of r . For other values of r , Eq.(5.5) cannot be satisfied and the system breaks into two large pieces.

5.2 Semi-analytic approach

It is not easy to develop an analytic solution for f_C . The main difficulty is to express the probability function $f(P_i, P_j)$, and thus the switching and rewiring probabilities, analytically. Here we use numerical simulations as a guide to develop a semi-analytic theory. To proceed, it is necessary to define some quantities. The number of C and D nodes are denoted by N_C and N_D , respectively. Since evolution happens on C - D links, these links are called

active links. The C (D) nodes that have C - D links are *active* C (D) nodes. N_{aC} (N_{aD}) be the number of active C (D) nodes. The nodes that have no C - D links are called *inactive* nodes. Thus, the nodes are divided into four types: the active C (D) nodes and inactive C (D) nodes. The number of C - D links is denoted by L_{CD} . k_{aC} is the mean degree of active C nodes and k_{aD} is the mean degree of active D nodes. The mean number of C neighbors of active C (active D) node is defined as ν_{aC} (ν_{aD}).

To carry out a mean-field approach, several assumptions are made:

- Nodes of the same type are *identical*.
- *Inactive* C and D nodes share the same degree k_{ia} .
- The fraction of *active* C nodes among all the C neighbors of a C node is $\frac{N_{aC}}{N_C}$. The fraction of *active* D nodes among all the D neighbors of a D node is $\frac{N_{aD}}{N_D}$.

By making these assumptions, we have neglected the degree distribution and the distribution in the number of C neighbors among all neighbors.

The calculation is carried out as follows: Consider N agents that are located on a lattice structure and a fraction of x_0 agents are assigned as cooperators initially. The values of the quantities discussed above are calculated. At each time step, the following tasks are carried out.

1. The average payoffs of active C nodes P_{aC} and active D nodes P_{aD} are calculated according to

$$P_{aC} = \frac{\nu_{aC} + (k_{aC} - \nu_{aC})(1 - r)}{k_{aC}}, \quad (5.6)$$

$$P_{aD} = \frac{\nu_{aD}(1 + r)}{k_{aD}}. \quad (5.7)$$

2. A random number $i \in [0, 1]$ is generated.
3. If $i < f(P_{aC}, P_{aD})$, the node with lower payoff will follow winner's strategy.

4. Otherwise, the node with lower payoff will “rewire” to another node that has the same character.
5. The new values of the quantities are calculated.

Figure 5.3 shows the change of the quantities in one time step schematically. The evolution process stops if one of the following conditions is satisfied.

- $N_C = N$ or $N_D = N$.
- $k_{aC} \leq 1$ or $k_{aD} \leq 1$.
- $\nu_{aC} \leq 0$ or $\nu_{aD} \leq 1$.

Here we use the switching process $C \rightarrow D$ to show the change of the quantities in one time step. The change of the quantities for other processes can be calculated in a similar manner. Consider a convincing process of $C \rightarrow D$ happens in time step t . The number of active and inactive C neighbors of the C node are

$$n_{aC}(t) = \frac{N_{aC}(t)}{N_C(t)} \nu_{aC}(t) , \quad (5.8)$$

and

$$n_{iaC}(t) = \nu_{aC}(t) - n_{aC}(t) . \quad (5.9)$$

For a C node switching to D , the C - C links between this node and its neighbors become C - D links. Meanwhile, the C - D links become D - D links, thus the change of L_{CD} is $\nu_{aC}(t) - (k_{aC}(t) - \nu_{aC}(t))$, i.e.,

$$L_{cd}(t+1) = L_{cd}(t) + 2\nu_{aC}(t) - k_{aC}(t) . \quad (5.10)$$

After switching, the C node becomes active D node, and its $n_{iaC}(t)$ inactive C neighbors become active, so that

$$N_C(t+1) = N_C(t) - 1 , \quad (5.11)$$

$$N_D(t+1) = N_D(t) + 1 , \quad (5.12)$$

$$N_{aD}(t+1) = N_{aD}(t) + 1 , \quad (5.13)$$

$$N_{aC}(t+1) = N_{aC}(t) + n_{iaC}(t) - 1 . \quad (5.14)$$

As the $n_{iaC}(t)$ inactive C nodes become active, they contribute to the values of both k_{aC} and ν_{aC} :

$$k_{aC}(t+1) = \frac{k_{aC}(t)[N_{aC}(t) - 1] + n_{iaC}(t)k_{ia}(t)}{N_{aC}(t+1)}, \quad (5.15)$$

and

$$\nu_{aC}(t+1) = \frac{\nu_{aC}(t)[N_{aC}(t) - 1] - n_{aC}(t) + n_{iaC}(t)[k_{ia}(t) - 1]}{N_{aC}(t+1)}. \quad (5.16)$$

Similarly, the changes of k_{aD} and ν_{aD} are

$$k_{aD}(t+1) = \frac{N_{aD}(t)k_{aD}(t) + k_{aC}(t)}{N_{aD}(t+1)}, \quad (5.17)$$

$$\nu_{aD}(t+1) = \frac{N_{aD}(t)\nu_{aD}(t) + [2\nu_{aC}(t) - k_{aC}(t)]}{N_{aD}(t+1)}. \quad (5.18)$$

After we obtained the mean degree of active C and D nodes of time step $t+1$, the mean degree k_{ia} of inactive nodes is calculated as

$$k_{ia}(t+1) = \frac{N\langle k \rangle - N_{aC}(t+1)k_{aC}(t+1) - N_{aD}(t+1)k_{aD}(t+1)}{N - N_{aC}(t+1) - N_{aD}(t+1)}. \quad (5.19)$$

The set of equations Eqs. (5.10)–(5.19) models the dynamics and they can be iterated.

Comparisons between the results obtained by the set of equations and simulation results for systems with initial condition $x_0 = 0.3, 0.5$ and 0.7 are shown in Fig. 5.4. A transition from an AllC phase to a mixed phase is observed for all x_0 values, in agreement with simulation results. However, the transition points deviate from the simulation results and discrepancies are also found in the $r > r_C$ regions. Since we have neglected many factors in the analytic approach, such as the degree distribution, the analytic results do not agree quantitatively with the simulation results. A better theory oughts to take the neglected element into account.

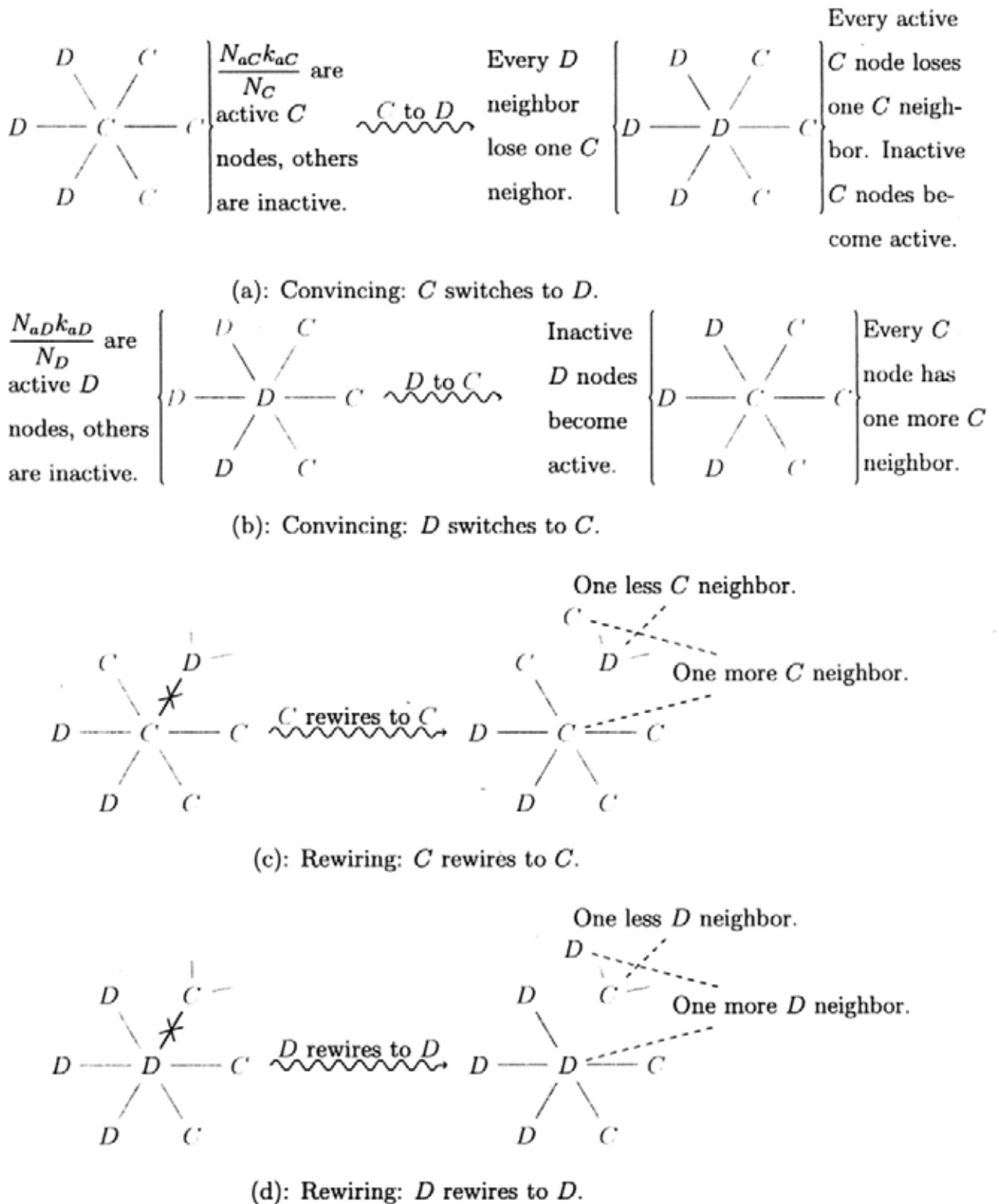


Figure 5.3: Schematic diagrams show the change of the key quantities of the four evolutionary processes.

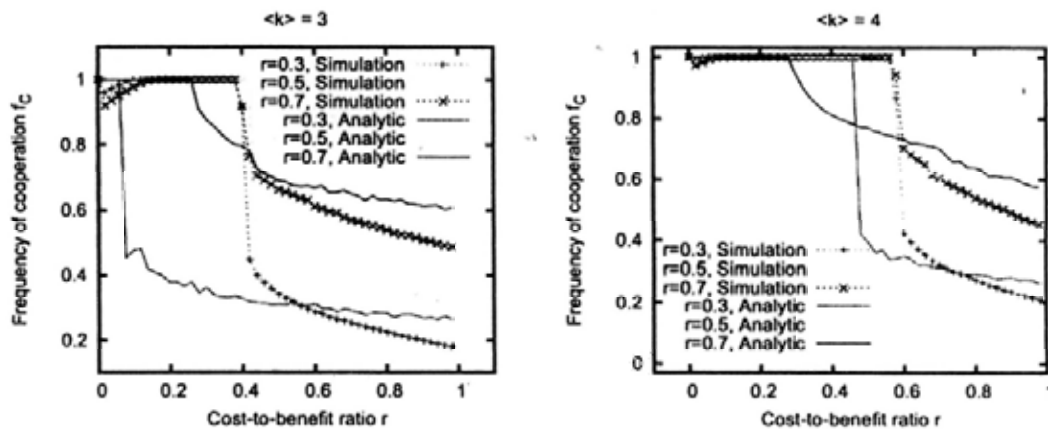


Figure 5.4: The analytic (lines) and simulation results (symbols) of the equilibrium frequency of cooperation f_C as a function of r , for both $\langle k \rangle = 3$ (Left) and 4 (Right) cases. The initial frequency of cooperation are taken to be $x_0 = 0.3, 0.5$ and 0.7 . The simulation parameters are $N = 10^4$ and 5×10^5 time steps. Each data point is an average over 100 realizations.

5.3 Conclusion

In this chapter, we studied the Snowdrift game on adaptive networks. Two rewiring mechanisms, the random rewiring and opinion rewiring, are imposed. By carrying out numerical simulations, it was found that the frequency of cooperation f_C is promoted in both cases. A phase transition takes place at the critical point r_C , where f_C drops suddenly. The network structure is examined for opinion rewiring. For $r < r_C$, the system is dominated by a large cluster of C nodes. When $r > r_C$, the system breaks into an AllC and an AllD cluster for most values of r . For some particular values of r , the system will not break. These values were explained by comparing the payoffs of adjacent C and D nodes. A semi-analytic approach was then proposed. The results are in qualitative agreement with simulation results. The theory, however, fails to predict the correct value of r_C and the detailed behavior of f_C for $r > r_C$.

As a preliminary study, our model emphasized on what a loser could do

when compared with a neighboring winner. In our model, an agent will try to rewire even if the difference between P_i and P_j is very small. The comparison between the payoffs of two agents to decide on the action also makes analytic treatment difficult. Our model has motivated a simpler model studied recently by Gräser et al. [68], which is based on the comparison between an agent's payoff and his own expectation. The modified model can be treated more readily by a mean-field approach with idea similar to the one presented here, but with results in good agreements with simulation results.

Chapter 6

Surface plasmon excitations

In this chapter, we first introduce some basic concepts that will be useful for our further discussions on surface plasmon excitations, including the Maxwell's equations, the TE and TM polarizations and the Drude model of the dielectric constant of metals. We then study the surface plasmon (SP) modes that localized on metal/dielectric interfaces. We derive the dispersion relation of SP modes in a semi-infinite metal/linear dielectric system, and in linear dielectric/metal/linear dielectric system. The SP dispersion relations of a nonlinear dielectric/metal/linear dielectric system is then studied analytically, by invoking a "first integral" technique. Our theory can treat arbitrary nonlinearity. The SP modes in a symmetric nonlinear dielectric/metal/nonlinear dielectric system are also discussed.

6.1 Basic concepts

6.1.1 Maxwell's Equations

The Maxwell's equations in matter can be written as

$$\nabla \times \mathbf{E} = -\frac{\partial \mathbf{B}}{\partial t}, \quad (6.1)$$

$$\nabla \times \mathbf{H} = \mathbf{J}_f + \frac{\partial \mathbf{D}}{\partial t}, \quad (6.2)$$

$$\nabla \cdot \mathbf{D} = \rho_f, \quad (6.3)$$

$$\nabla \cdot \mathbf{B} = 0, \quad (6.4)$$

where \mathbf{J}_f and ρ_f are the free current density and free charge density, respectively.

In this thesis, we will only consider non-magnetic material with no free current and charge, i.e.,

$$\mathbf{B} = \mu_0 \mathbf{H}, \quad (6.5)$$

$$\mathbf{J}_f = 0, \quad (6.6)$$

$$\rho_f = 0. \quad (6.7)$$

In this case, the Maxwell's equations become

$$\nabla \times \mathbf{E} = -\mu_0 \frac{\partial \mathbf{H}}{\partial t}, \quad (6.8)$$

$$\nabla \times \mathbf{H} = \frac{\partial \mathbf{D}}{\partial t}, \quad (6.9)$$

$$\nabla \cdot \mathbf{D} = 0, \quad (6.10)$$

$$\nabla \cdot \mathbf{H} = 0. \quad (6.11)$$

Consider the fields taking on the form of plane waves,

$$\mathbf{E}(\mathbf{r}, t) = \mathbf{E}(\mathbf{r})e^{-i\omega t}, \quad (6.12)$$

$$\mathbf{H}(\mathbf{r}, t) = \mathbf{H}(\mathbf{r})e^{-i\omega t}, \quad (6.13)$$

and the material to be a linear dielectric with

$$\mathbf{D} = \epsilon_0 \epsilon \mathbf{E} , \quad (6.14)$$

Eqs. (6.8) and (6.9) become

$$\nabla \times \mathbf{E} = i\omega\mu_0 \mathbf{H} , \quad (6.15)$$

$$\nabla \times \mathbf{H} = -i\omega\epsilon_0 \epsilon \mathbf{E} . \quad (6.16)$$

Taking the divergence of Eqs. (6.15) and (6.16) yield Eqs. (6.11) and (6.10). Thus Eqs. (6.10) and (6.11) are redundant under our assumptions, we only need to consider Eqs. (6.8) and (6.9).

6.1.2 TE and TM polarizations

In a homogeneous isotropic medium, if we restrict ourselves to an effectively two-dimensional problem, such that all quantities are independent of y , the \mathbf{E} and \mathbf{H} fields can be expressed as

$$\mathbf{E}(\mathbf{r}, t) = [E_x(x, z)\hat{x} + E_y(x, z)\hat{y} + E_z(x, z)\hat{z}]e^{-i\omega t} , \quad (6.17)$$

$$\mathbf{H}(\mathbf{r}, t) = [H_x(x, z)\hat{x} + H_y(x, z)\hat{y} + H_z(x, z)\hat{z}]e^{-i\omega t} . \quad (6.18)$$

Substituting Eqs. (6.17) and (6.18) into Eqs. (6.15) and (6.16), it can be shown that the set of equations for E_y, H_x, H_z are decoupled from that for H_y, E_x, E_z , thus revealing that there are two independent polarizations. One polarization has the electric field being perpendicular to the x - z plane, which is called Transverse Electric (TE) mode or s -polarization. The other polarization has the magnetic field being perpendicular to the x - z plane, which is called the Transverse Magnetic (TM) mode or p -polarization. These two polarizations obey different boundary conditions. For many situations, they can be treated separately.

6.1.3 Dielectric constants of metals

The Drude model [69] gives a convenient way to describe the dielectric constants of metal analytically.

In the Drude model, the electrons are treated as free electrons. The charge and mass of an electron are taken to be $-e$ and m , respectively. There are collisions between the electrons and impurities, phonons, etc., with the mean free time between collisions being τ . The damping constant $\Gamma = 1/\tau$. The motion of an electron in the presence of an external electric field $\mathbf{E}(\mathbf{r}, t) = \mathbf{E}(\mathbf{r})e^{-i\omega t}$ is described by

$$m\ddot{\mathbf{r}} + m\Gamma\dot{\mathbf{r}} = -e\mathbf{E}(\mathbf{r})e^{-i\omega t}. \quad (6.19)$$

The solution of Eq.(6.19) is $\mathbf{r}(t) = \mathbf{r}e^{-i\omega t}$ with

$$\mathbf{r} = \frac{e}{m\omega^2 + i\Gamma\omega}\mathbf{E}(\mathbf{r}). \quad (6.20)$$

The induced dipole moment has an amplitude

$$\mathbf{p} = -e\mathbf{r} = -\frac{e^2}{m\omega^2 + i\Gamma\omega}\mathbf{E}(\mathbf{r}). \quad (6.21)$$

Let N be the number of electrons per unit volume, the macroscopic polarization is

$$\mathbf{P} = N\mathbf{p} = \epsilon_0\chi\mathbf{E}. \quad (6.22)$$

Substituting Eq.(6.21) into Eq.(6.22), we obtain the electric susceptibility

$$\chi = -\frac{Ne^2}{m\epsilon_0}\frac{1}{\omega^2 + i\Gamma\omega}. \quad (6.23)$$

Thus the dielectric constant ϵ is

$$\epsilon = 1 + \chi = 1 - \frac{Ne^2}{m\epsilon_0}\frac{1}{\omega^2 + i\Gamma\omega}. \quad (6.24)$$

It is easily to see that ϵ is complex, with the real and the imaginary parts of ϵ given by

$$\epsilon_r = 1 - \frac{\omega_p^2}{\omega^2 + \Gamma^2} \quad (6.25)$$

and

$$\epsilon_i = \frac{\omega_p^2 \Gamma}{\omega^3 + \Gamma^2 \omega}, \quad (6.26)$$

respectively. Here ω_p is called the *plasma frequency*, given by

$$\omega_p^2 = \frac{Ne^2}{m\epsilon_0}. \quad (6.27)$$

For ω that satisfying $\omega^2 + \Gamma^2 < \omega_p^2$, ϵ_r is negative, while ϵ_i is always positive. For good conductors, Γ is much less than ω_p . Thus, we often neglect the Γ term and take the metal to be lossless. Under this approximation, the dielectric constant becomes real

$$\epsilon = \epsilon_r = 1 - \frac{\omega_p^2}{\omega^2}, \quad (6.28)$$

and ϵ is negative for $\omega < \omega_p$.

6.2 Surface plasmon at metal/linear dielectric interface

Surface plasmon (SP) is a surface electromagnetic wave that is localized and propagating along a metal/dielectric interface. SP is an old subject, with the pioneer work carried out by Ritchie in 1950s [70]. Later, the dispersion relations of SP in a number of metal/linear dielectric multilayer structures were studied by Economou in 1960s [71]. In recently years, researchers have been interested in the functionality of SP in manipulating light, including possible applications in optics, fabricating, biological sensors, and cloaking metamaterials [72, 73].

In this section, we review the SP modes in the following systems:

1. Semi-infinite metal/linear dielectric interface.
2. Metal film between two semi-infinite linear dielectrics.

The dispersion relation will be derived for these two systems and the main features will be discussed.

6.2.1 Semi-infinite metal/linear system

Here we consider a system of two semi-infinite media that are separated by an interface at $z = 0$. The dielectric constants of the medium above ($z > 0$) and below ($z < 0$) the interface are ϵ_1 and ϵ_2 , respectively.

For TM polarization, the \mathbf{H} field has a y -component only. The electric and magnetic fields at a location can in general be written as

$$\mathbf{E}(\mathbf{r}, t) = [E_x(z)\hat{x} + E_z(z)\hat{z}] e^{i(k_x x - \omega t)}, \quad (6.29)$$

$$\mathbf{H}(\mathbf{r}, t) = H_y(z)\hat{y} e^{i(k_x x - \omega t)}, \quad (6.30)$$

where k_x is the x -component of the wavevector.

For the SP mode localized at the interface, the fields exponentially decay outward from $z = 0$ for both $z > 0$ and $z < 0$. $H(z)$ and $E(z)$ in each medium can then be written as

$$H_1(z) = H_{1y}(0^+)\hat{y} \exp(-q_1 z), \quad (6.31)$$

$$E_1(z) = [E_{1x}(0^+)\hat{x} + E_{1z}(0^+)\hat{z}] \exp(-q_1 z), \quad (6.32)$$

$$H_2(z) = H_{2y}(0^-)\hat{y} \exp(q_2 z), \quad (6.33)$$

$$E_2(z) = [E_{2x}(0^-)\hat{x} + E_{2z}(0^-)\hat{z}] \exp(q_2 z), \quad (6.34)$$

where both q_1 and q_2 are positive, and the amplitudes are those at the value of z specified inside the parentheses.

For TM mode, the Maxwell's equations Eqs. (6.15) and (6.16) can be simplified to

$$i\omega\mu_0 H_y = \partial_z E_x - \partial_x E_z, \quad (6.35)$$

$$i\omega\epsilon_0\epsilon E_x = \partial_z H_y, \quad (6.36)$$

$$-i\omega\epsilon_0\epsilon E_z = \partial_x H_y. \quad (6.37)$$

Substituting Eqs. (6.31)–(6.34) into Eqs. (6.36) and (6.37), the relations

between E_x , E_z and H_y are

$$E_{1x} = \frac{iq_1}{\epsilon_0\epsilon_1\omega} H_{1y}, \quad (6.38)$$

$$E_{1z} = -\frac{k_x}{\epsilon_0\epsilon_1\omega} H_{1y}, \quad (6.39)$$

$$E_{2x} = -\frac{iq_2}{\epsilon_0\epsilon_2\omega} H_{2y}, \quad (6.40)$$

$$E_{2z} = -\frac{k_x}{\epsilon_0\epsilon_2\omega} H_{2y}. \quad (6.41)$$

The boundary conditions require the tangential components H_y and E_x be continuous at the interface $z = 0$, leading to

$$\frac{q_1}{\epsilon_1} + \frac{q_2}{\epsilon_2} = 0. \quad (6.42)$$

Notice that both q_1 and q_2 are positive. For Eq.(6.42) to hold, ϵ_1 and ϵ_2 must be of opposite signs. This requirement can be satisfied if one medium is a metal.

For TE polarization, the fields can be written down in a similar way. Using the Maxwell's equations, the relations between H_x and E_y are found to be

$$H_{1x} = -i\frac{q_1}{\mu_0\omega} E_{1y}, \quad (6.43)$$

$$H_{2x} = i\frac{q_2}{\mu_0\omega} E_{2y}. \quad (6.44)$$

The tangential components H_x and E_y are continuous at the interface $z = 0$, leading to

$$q_1 + q_2 = 0. \quad (6.45)$$

The condition can never be satisfied for positive q_1 and q_2 . Thus the SP mode can *only* be of TM polarization.

Substituting Eqs. (6.38) and (6.39) into Eq.(6.35), q_1 can be expressed as a function of k_x and ω ,

$$q_1^2 = k_x^2 - \epsilon_1 \frac{\omega^2}{c^2}, \quad (6.46)$$

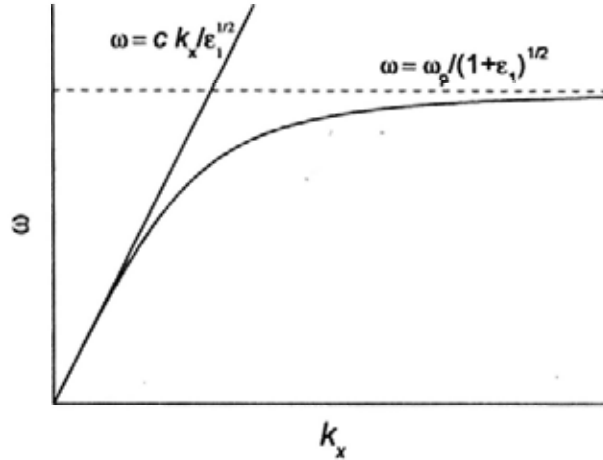


Figure 6.1: The SP dispersion relation at semi-infinite metal/linear interface. The metal is assumed to be lossless.

where $c = 1/\sqrt{\epsilon_0\mu_0}$ is the speed of light in vacuum. Similarly,

$$q_2^2 = k_x^2 - \epsilon_2 \frac{\omega^2}{c^2}. \quad (6.47)$$

The condition Eq.(6.42) can then be written as

$$k_x = \frac{\omega}{c} \sqrt{\frac{\epsilon_1 \epsilon_2}{\epsilon_1 + \epsilon_2}}. \quad (6.48)$$

This is the *dispersion relation* of surface plasmon at the interface in a semi-infinite linear dielectric/metal system.

Taking medium 1 ($z > 0$) to be a linear dielectric and medium 2 ($z < 0$) to be lossless metal with a dielectric constant given by Eq.(6.28), the SP dispersion relation is illustrated in Fig. 6.1. For $k_x \gg \omega_p/c$, ω tends to $\omega_{sp} = \omega_p/\sqrt{\epsilon_1 + 1}$. Notice that the SP dispersion relation curve always lies to the right of the light line $\omega = ck_x/\sqrt{\epsilon_1}$. Therefore, the SP mode cannot be directly excited by light incident from medium 1.

A common method to excite surface plasmons is to use a grating. When a light wave incident on a grating, a series of diffraction waves can be generated.

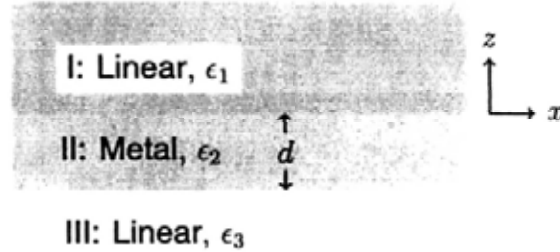


Figure 6.2: Schematic diagram shows the structure of a linear-metal-linear system.

The x -component of the wavevector of the n^{th} order diffraction wave k_{xn} is

$$k_{xn} = k_{x0} + n \frac{2\pi}{L}, \quad (6.49)$$

where L is the period of the grating. Surface plasmon can be excited if k_{xn} satisfies the dispersion relation:

$$k_{x0} + n \frac{2\pi}{L} = k_{xn} = \frac{\omega}{c} \sqrt{\frac{\epsilon_1 \epsilon_2}{\epsilon_1 + \epsilon_2}}. \quad (6.50)$$

6.2.2 Metallic film between two linear dielectrics

Here we introduce the surface plasmon dispersion relation of a linear dielectric/metal/linear dielectric structure.

Consider a metallic film of dielectric constant ϵ_2 and thickness d separating two semi-infinite dielectrics at $z = 0$ and $z = -d$. The dielectric constants of the two dielectrics are ϵ_1 ($z > 0$) and ϵ_3 ($z < -d$), respectively. Figure 6.2 shows the system structure schematically.

The SP modes should be TM polarized. The fields in each medium can be written down. In medium 1, the fields decay away from the $z = 0$ interface, thus

$$H_1(z) = H_{1y}(0^+) e^{-q_1 z} \hat{y}, \quad (6.51)$$

$$E_1(z) = [E_{1x}(0^+) \hat{x} + E_{1z}(0^+) \hat{z}] e^{-q_1 z}. \quad (6.52)$$

In medium 2, the fields are superpositions of the waves decaying from the two interfaces,

$$H_2(z) = [H_{2y}^+(0^-)e^{-q_2z} + H_{2y}^-(0^-)e^{q_2z}]\hat{y}, \quad (6.53)$$

$$E_2(z) = [E_{2x}^+(0^-)e^{-q_2z} + E_{2x}^-(0^-)e^{q_2z}]\hat{x} + [E_{2z}^+(0^-)e^{-q_2z} + E_{2z}^-(0^-)e^{q_2z}]\hat{z}. \quad (6.54)$$

In medium 3, the fields decay as z decreases,

$$H_3(z) = H_{3y}(-d^-)e^{q_3(z+d)}\hat{y}, \quad (6.55)$$

$$E_3(z) = [E_{3x}(-d^-)\hat{x} + E_{3z}(-d^-)\hat{z}]e^{q_3(z+d)}. \quad (6.56)$$

The coefficients q_i ($i = 1, 2$ and 3) are obtained from the wave equations as

$$q_i^2 = k_x^2 - \epsilon_i \frac{\omega^2}{c^2}. \quad (6.57)$$

The relation between E_x and H_y in each medium can be obtained by substituting Eqs. (6.51)–(6.56) into Eq.(6.36),

$$E_{1x} = -\frac{q_1}{i\omega\epsilon_0\epsilon_1}H_{1y}, \quad (6.58)$$

$$E_{2x}^+ = -\frac{q_2}{i\omega\epsilon_0\epsilon_2}H_{2y}^+, \quad (6.59)$$

$$E_{2x}^- = \frac{q_2}{i\omega\epsilon_0\epsilon_2}H_{2y}^-, \quad (6.60)$$

$$E_{3x} = \frac{q_3}{i\omega\epsilon_0\epsilon_3}H_{3y}. \quad (6.61)$$

The boundary conditions are that the tangential components E_x and H_y are continuous at the two interfaces $z = 0$ and $z = -d$. By applying the boundary conditions at $z = 0$, $H_{2y}^+(0^-)$ and $H_{2y}^-(0^-)$ can be expressed as a function of $H_{1y}(0^+)$,

$$H_{2y}^+(0^-) = \frac{1}{2} \left(1 + \frac{q_1\epsilon_2}{q_2\epsilon_1} \right) H_{1y}(0^+), \quad (6.62)$$

$$H_{2y}^-(0^-) = \frac{1}{2} \left(1 - \frac{q_1\epsilon_2}{q_2\epsilon_1} \right) H_{1y}(0^+). \quad (6.63)$$

So are E_{2x}^+ and E_{2x}^- .

Similarly, at $z = -d$, we found

$$\begin{aligned} H_{3y}(-d^-) &= H_{2y}^+(0^-)e^{q_2d} + H_{2y}^-(0^-)e^{-q_2d} \\ &= \left[\cosh(q_2d) + \frac{q_1\epsilon_2}{q_2\epsilon_1} \sinh(q_2d) \right] H_{1y}(0^+) , \end{aligned} \quad (6.64)$$

and

$$\begin{aligned} E_{3x}(-d^-) &= E_{2x}^+(0^-)e^{q_2d} + E_{2x}^-(0^-)e^{-q_2d} \\ &= -\frac{q_2}{i\omega\epsilon_0\epsilon_2} \left[\sinh(q_2d) + \frac{q_1\epsilon_2}{q_2\epsilon_1} \cosh(q_2d) \right] H_{1y}(0^+) . \end{aligned} \quad (6.65)$$

Substituting Eqs. (6.64) and (6.65) into Eq.(6.61) and canceling the $H_{1y}(0^+)$ term, we obtain the *SP dispersion relation* of a linear-metal-linear structure:

$$(q_2^2\epsilon_1\epsilon_3 + q_1q_3\epsilon_2^2) \tanh(q_2d) + q_2\epsilon_2(q_1\epsilon_3 + q_3\epsilon_1) = 0 . \quad (6.66)$$

For $d \rightarrow \infty$, $\tanh(q_2d) \sim 1$, Eq.(6.66) becomes

$$(q_1\epsilon_2 + q_2\epsilon_1)(q_2\epsilon_3 + q_3\epsilon_2) = 0 , \quad (6.67)$$

which leads to

$$q_1\epsilon_2 + q_2\epsilon_1 = 0 \quad \text{and} \quad q_2\epsilon_3 + q_3\epsilon_2 = 0 ,$$

i.e., the dispersion relations of SP modes excited on semi-infinite ϵ_1 /metal and metal/ ϵ_3 interfaces. The SP modes at the two interfaces become decoupled for thick metallic film.

In what follows, we discuss the SP modes supported by symmetric and asymmetric structures. For convenience, the metal is assumed to be lossless with the dielectric constant given by Eq.(6.28).

SP modes supported by symmetric structures

For a metallic film embedded in a symmetric environment with $\epsilon_3 = \epsilon_1$, $q_3 = q_1$, Eq.(6.66) becomes

$$(q_2^2\epsilon_1^2 + q_1^2\epsilon_2^2) \tanh(q_2d) + 2q_1q_2\epsilon_1\epsilon_2 = 0 , \quad (6.68)$$

which can be rewritten as

$$\left[q_1 \epsilon_2 + q_2 \epsilon_1 \tanh\left(\frac{q_2 d}{2}\right) \right] \left[q_2 \epsilon_1 + q_1 \epsilon_2 \tanh\left(\frac{q_2 d}{2}\right) \right] = 0. \quad (6.69)$$

So there are always two bound modes [71, 74]: one high frequency mode (s_b) that has a symmetric H_y and has the form $[q_2 \epsilon_1 + q_1 \epsilon_2 \tanh(\frac{q_2 d}{2})] = 0$; and one low frequency mode (a_b) that has an antisymmetric H_y and has the form $[q_1 \epsilon_2 + q_2 \epsilon_1 \tanh(\frac{q_2 d}{2})] = 0$.

Figure 6.3 shows the SP dispersion relations and their dependence on the film thickness for a metallic film in air. The metal is taken to be silver, with plasma frequency $\omega_p = 1.36 \times 10^{16}$ rad s⁻¹. When the film is thin, due to the coupling of the SP modes at the two interfaces, the s_b mode becomes higher and the a_b mode becomes lower in frequency (see $d = 20$ nm results). As the film becomes thicker, the coupling effect becomes weaker, and the two modes become closer in frequency (see $d = 30$ nm results). For $d \rightarrow \infty$, the two modes are uncoupled and become degenerate (see $d = 100$ nm results). The H_y field distribution for the two modes at $k_x = 4.53 \times 10^7$ m⁻¹ and $d = 30$ nm are shown in Fig. 6.4. For the s_b mode, the H_y field is distributed symmetrically (corresponding to Point 1 in Fig. 6.4). For the a_b mode, the H_y field is distributed anti-symmetrically (corresponding to Point 2 in Fig. 6.4).

SP modes supported by asymmetric structures

For a metallic film embedded in asymmetric environment, due to the mismatch of the SP frequencies excited at the two interfaces, the situation becomes more complicated [75, 73]. For the convenience of our discussion, we assume $\epsilon_1 > \epsilon_3$. For bounded SP modes to exist, both q_1 and q_3 should be positive, which requires

$$k_x^2 - \epsilon_1 \frac{\omega^2}{c^2} > 0 \quad \text{and} \quad k_x^2 - \epsilon_3 \frac{\omega^2}{c^2} > 0. \quad (6.70)$$

For the SP mode excited at the metal/ ϵ_1 interface, both conditions can be satisfied, indicating that this mode is always a bound mode. However, for the SP

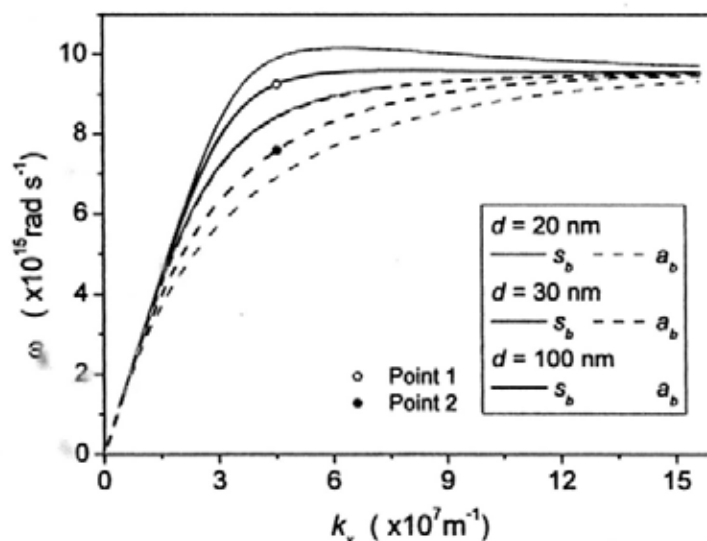
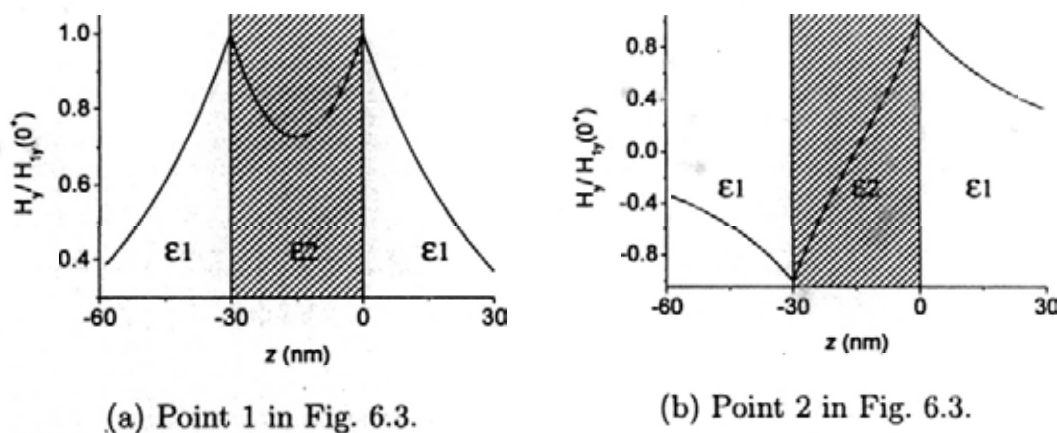


Figure 6.3: The SP dispersion relations for a metallic film in air. The thickness of the metallic film is taken to be $d = 20$ nm, 30 nm and 100 nm. Two points with the same k_x and d values are chosen for which the H_y field distributions are shown in Fig. 6.4.



(a) Point 1 in Fig. 6.3.

(b) Point 2 in Fig. 6.3.

Figure 6.4: The H_y field distribution for Points 1 and 2 in Fig. 6.3. Points 1 and 2 have the same k_x and thickness d , with $k_x = 4.53 \times 10^7 \text{ m}^{-1}$ and $d = 30$ nm.

mode at the metal/ ϵ_3 interface, the two conditions cannot be simultaneously satisfied for ω values less than $ck_x/\sqrt{\epsilon_1}$. When this happens, the SP mode is no longer bounded, the quantities q_1 , q_3 and k_x are all complex. The wave front is tilted towards the metal film in ϵ_3 , after propagating through the film, it grows exponentially in ϵ_1 . This mode is called *leaky* mode [75]. If ω can be larger than $ck_x/\sqrt{\epsilon_1}$, this mode will become a bound mode.

6.3 Surface plasmon of nonlinear/metal system

Besides the study of surface plasmon modes on metal/linear dielectric interfaces, researchers were interested in the SP dispersion relation at a metal/Kerr-type nonlinear interface. For a Kerr material, the **D-E** relation takes on the form $\mathbf{D} = \epsilon\mathbf{E} + \alpha|\mathbf{E}|^2\mathbf{E} = \epsilon_K\mathbf{E}$. The evanescent electric field into the Kerr medium gives a spatially-changing dielectric constant depending on the distance from the interface, provides an alternative way in modifying the SP dispersion relations. Recently, the surface plasmon mode in a semi-infinite Kerr/metal system has been studied independently by Huang [76] et al., and Xu [77] et al. Here, we study the SP dispersion relations of a nonlinear-metal-linear system and a symmetric nonlinear-metal-nonlinear system. Instead of considering Kerr dielectric only, we consider the general case where the **D-E** relation inside the nonlinear dielectric takes the form

$$\mathbf{D} = \epsilon\mathbf{E} + \alpha|\mathbf{E}|^\beta\mathbf{E} \equiv \epsilon_{nl}(E)\mathbf{E}, \quad (6.71)$$

where ϵ is the linear part of the response, α is a nonlinear susceptibility, and $E = |\mathbf{E}|$. This type of arbitrary nonlinearity has been studied in nonlinear random composite materials [78]. We will present exact analytic expressions of the SP dispersion relations.

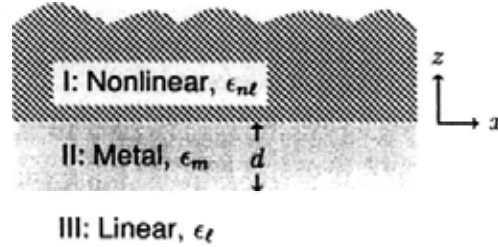


Figure 6.5: Schematic diagram showing the structure of a nonlinear-metal-linear system.

6.3.1 Nonlinear-metal-linear structure

This section is based on Ref. [79].

The system consists of a thin slab of metal of thickness d (Region 2 in Fig. 6.5) separating a nonlinear dielectric occupying the space of $z > 0$ (Region 1) and a linear dielectric occupying the space of $z < -d$ (Region 3). Let ϵ_m and ϵ_l be the dielectric constant of the metallic and linear dielectric regions, respectively. Consider a TM-polarized wave with the \mathbf{H} -field having y -component only. The electric field at a location in the system can in general be written as [80, 76]:

$$\mathbf{E}(\mathbf{r}, t) = \frac{1}{2} [iE_x(z)\hat{x} + E_z(z)\hat{z}] e^{i(k_x x - \omega t)} + c.c. \quad (6.72)$$

where k_x is the x -component of the wavevector. The relations between E_x , E_z and H_y are given by the Maxwell's equations Eqs. (6.8) and (6.9) as

$$H_y(z) = -\frac{\omega}{k_x} \epsilon_0 \epsilon_i E_z, \quad (6.73)$$

$$\frac{dE_x}{dz} = \left(k_x - \frac{\omega^2}{k_x c^2} \epsilon_i \right) E_z, \quad (6.74)$$

$$\frac{d(\epsilon_i E_z)}{dz} = k_x \epsilon_i E_x. \quad (6.75)$$

Here, $\epsilon_i = \epsilon_{nl}, \epsilon_m, \epsilon_l$, depending on the location. Since ϵ_m and ϵ_l do not depend on z , Eq.(6.75) reduces to $dE_z/dz = k_x E_x$ in Regions 2 and 3. In the nonlinear Region 1, however, $\epsilon_{nl}(E(z))$ cannot be canceled in Eq.(6.75).

The linear regions can be treated readily by writing down the general form of the \mathbf{E} -field. In Region 2, we have

$$\begin{aligned} E_{x2}(z) &= E_{x2}^-(0^-)e^{q_m z} + E_{x2}^+(0^-)e^{-q_m z} \\ E_{z2}(z) &= E_{z2}^-(0^-)e^{q_m z} + E_{z2}^+(0^-)e^{-q_m z} \quad (-d < z < 0), \end{aligned} \quad (6.76)$$

where $q_m = \sqrt{k_x^2 - \epsilon_m \frac{\omega^2}{c^2}}$ and the amplitudes are those at the value of z specified inside the parentheses. Similarly, in Region 3 ($z < -d$), we have

$$\begin{aligned} E_{x3}(z) &= E_{x3}^-(-d^-)e^{q_t(z+d)}, \\ E_{z3}(z) &= E_{z3}^-(-d^-)e^{q_t(z+d)}, \end{aligned} \quad (6.77)$$

where $q_t = \sqrt{k_x^2 - \epsilon_t \frac{\omega^2}{c^2}}$. The relations between E_z and E_x in Region 2 and 3 can be obtained by following Eq.(6.74), with $E_{z2}^- = k_x E_{x2}^-/q_m$, $E_{z2}^+ = -k_x E_{x2}^+/q_m$, and $E_{z3} = k_x E_{x3}/q_t$.

A standard treatment of the nonlinear Region 1 invokes a "first integral" to get at an equation for dE_{x1}/dz [80]. Here, we generalize the technique to arbitrary value of β characterizing the nonlinearity. Taking the derivative of Eq.(6.74) with respect to z and multiplying through by dE_{x1}/dz , we get in Region 1

$$\frac{dE_{x1}}{dz} \frac{d^2 E_{x1}}{dz^2} = k_x \frac{dE_{x1}}{dz} \frac{dE_{z1}}{dz} - \frac{\omega^2}{c^2} \epsilon_{nl} E_{x1} \frac{dE_{x1}}{dz}. \quad (6.78)$$

An integration with respect to z gives

$$\begin{aligned} \frac{1}{2} \left(\frac{dE_{x1}}{dz} \right)^2 &= \frac{1}{2} \left(k_x^2 - \frac{\omega^2}{c^2} \epsilon \right) E_{z1}^2 - \frac{1}{2} \frac{\omega^2}{c^2} \epsilon E_{x1}^2 - \\ &\quad \alpha \frac{\omega^2}{c^2} \left[\int (E_{x1}^2 + E_{z1}^2)^{\beta/2} (E_{x1} dE_{x1} + E_{z1} dE_{z1}) \right] + C, \end{aligned} \quad (6.79)$$

where C is an integration constant. The key step is to recognize the identity

$$\int (E_x^2 + E_z^2)^{\beta/2} (E_x dE_x + E_z dE_z) = \frac{1}{\beta + 2} (E_x^2 + E_z^2)^{\beta/2+1}, \quad (6.80)$$

and rewrite Eq.(6.79) as

$$\left(\frac{dE_{x1}}{dz} \right)^2 = k_x^2 E_{z1}^2 - \frac{\omega^2}{c^2} \epsilon (E_{x1}^2 + E_{z1}^2) - \frac{2\alpha}{\beta + 2} \frac{\omega^2}{c^2} (E_{x1}^2 + E_{z1}^2)^{\beta/2+1}, \quad (6.81)$$

where we have set $C = 0$ as E_{x1} , E_{z1} and dE_{x1}/dz must vanish as $z \rightarrow \infty$. Equation (6.81) is valid for $z > 0$ and it generalizes the result in Ref. [80, 76] specific for $\beta = 2$. Applying Eq.(6.81) to $z = 0^+$ where $E_{x1}(0^+) \equiv E_{x0}$ and $E_{z1}(0^+) \equiv E_{z0}$, we get

$$\left(\frac{dE_{x1}}{dz}\right)_{z=0}^2 = k_x^2 E_{x0}^2 - \frac{\omega^2}{c^2} \epsilon E_0^2 - \frac{2\alpha}{\beta+2} \frac{\omega^2}{c^2} E_0^{\beta+2}, \quad (6.82)$$

where $E_0^2 = E_{x0}^2 + E_{z0}^2$ is the squared magnitude of the electric field at the interface between Regions 1 and 2. Requiring this result to be consistent with dE_{x1}/dz in Eq.(6.74) gives

$$\left(\frac{\omega^2 \epsilon_{nt}^2}{k_x^2 c^2} - 2\epsilon_{nt}\right) E_{z0}^2 + \epsilon E_0^2 + \frac{2\alpha}{\beta+2} E_0^{\beta+2} = 0. \quad (6.83)$$

Another relation between E_{z0} and E_0 can be found by imposing the boundary conditions that E_x and H_y are continuous at the $z = 0$ and $z = -d$ interfaces. It gives

$$k_x \epsilon_m Q E_{x0} = q_m \epsilon_{nt} P E_{z0}, \quad (6.84)$$

where $P = q_\ell \epsilon_m + q_m \epsilon_\ell \tanh(q_m d)$ and $Q = q_m \epsilon_\ell + q_\ell \epsilon_m \tanh(q_m d)$. Since $E_{x0}^2 = E_0^2 - E_{z0}^2$, E_{z0}^2 can be solved to give

$$E_{z0}^2 = \frac{k_x^2 \epsilon_m^2 Q^2}{k_x^2 \epsilon_m^2 Q^2 + q_m^2 \epsilon_{nt}^2 P^2} E_0^2. \quad (6.85)$$

Finally, substituting Eq.(6.85) into Eq.(6.83), we obtain

$$\left(\frac{\omega \epsilon_{nt} \epsilon_m}{c}\right)^2 Q^2 - 2\epsilon_{nt} \epsilon_m^2 k_x^2 Q^2 + \left(\epsilon + \frac{2}{\beta+2} \alpha E_0^\beta\right) (q_m^2 \epsilon_{nt}^2 P^2 + k_x^2 \epsilon_m^2 Q^2) = 0. \quad (6.86)$$

This is the equation that gives the SP dispersion relations. Due to the non-linear dielectric, the strength E_0 at the interface appears and it can alter the dispersion relations. It recovers previous results for $\alpha = 0$ (Eq.(6.66)) and generalizes the results for a Kerr medium [76, 77] to the case of a thin metallic film.

Figure 6.6 shows results of model calculations illustrating the dispersion relations and their dependence on the metallic film thickness. The metal has

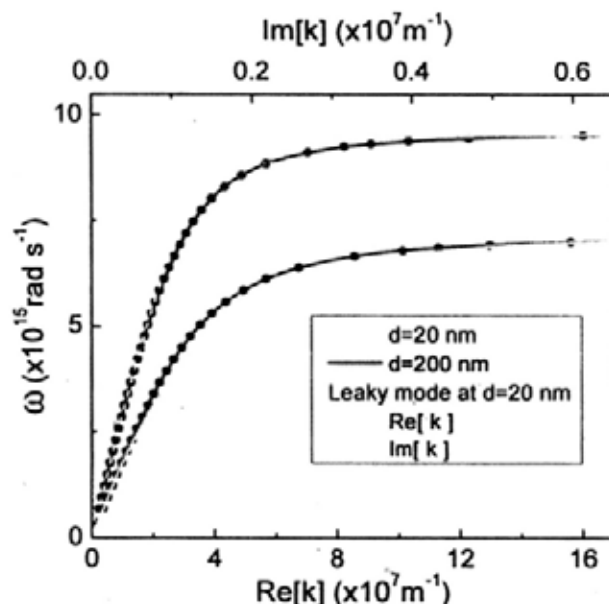


Figure 6.6: The dispersion relation of SP modes in a MBBA/silver/air system typical of thick ($d = 200 \text{ nm}$) and thin ($d = 20 \text{ nm}$) metallic films are shown.

a Drude form dielectric constant $\epsilon_m = 1 - \omega_p^2/\omega^2$, with ω_p takes the value for silver, $\omega_p = 1.36 \times 10^{16} \text{ rad s}^{-1}$. The nonlinear dielectric is the liquid crystal MBBA [80, 81] and the linear dielectric is air with $\epsilon_\ell = 1$. The parameters for MBBA are $\epsilon = 2.4025$, $\alpha = 6.379 \times 10^{-12} \text{ m}^2 \text{ V}^{-2}$ and $\beta = 2$, a field $E_0 = 2.5 \times 10^5 \text{ V/m}$ is used. The film thicknesses are taken to be 20 nm and 200 nm. For a given thickness, there are two branches. For thick films (see $d = 200 \text{ nm}$ results), the SP modes are uncoupled and the results coincide with the SP dispersion relations for a single interface between metal and each of the dielectrics, as indicated by the dots. These branches have a large k_x limit of $\omega_{sp}^{(m,\ell)} = \omega_p/\sqrt{1 + \epsilon_\ell}$ and $\omega_{sp}^{(m,n\ell)} = \omega_p/\sqrt{1 + \epsilon + \alpha E_0^2/2}$ [76], respectively. For thinner films (see $d = 20 \text{ nm}$ results), the upper (lower) branch becomes higher (lower) in frequency as a result of the mixing or hybridization of the SP modes in the thick-film limit, with the upper (lower) branch carries a heavier weight of the metal/nonlinear (metal/linear) dielectric SP mode. Due to the

mismatch between the two dielectrics, the upper branch contains two parts. When ω is small, it corresponds to a leaky mode with k_x being complex, as shown by the dotted line and dashed line in Fig. 6.6. For ω becomes large enough, the mode becomes bound and k_x becomes real (solid line).

Equation (6.86) contains the thick-film decoupled limits as a special case of $q_m d \rightarrow \infty$ so that $P = Q = q_\ell \epsilon_m + q_m \epsilon_\ell$. The equation reduces to

$$\left[\left(\frac{\omega \epsilon_{nl} \epsilon_m}{c} \right)^2 - 2\epsilon_{nl} \epsilon_m^2 k_x^2 + \left(\epsilon + \frac{2}{\beta + 2} \alpha E_0^\beta \right) (q_m^2 \epsilon_{nl}^2 + k_x^2 \epsilon_m^2) \right] P^2 = 0. \quad (6.87)$$

Setting $P^2 = 0$ recovers the standard SP modes at a metal/linear dielectric interface (Eq.(6.48)). Equating the first term to zero gives the uncoupled SP dispersion relations at an interface separating semi-infinite metal/nonlinear dielectric regions:

$$\omega = ck_x \left(\frac{2\epsilon_{nl}^3 + \beta\epsilon\epsilon_{nl}^2 - (2 + \beta)\epsilon_m^2\epsilon_{nl} - \beta\epsilon_m^2\alpha E_0^\beta}{\epsilon_m\epsilon_{nl}^2 (2\alpha E_0^\beta + (2 + \beta)(\epsilon - \epsilon_m))} \right)^{1/2}, \quad (6.88)$$

which is a generalization of the previous $\beta = 2$ results [76, 77] to arbitrary β .

The $k_x \rightarrow \infty$ limit gives $\omega_{sp}^{(m,n\ell)}$, which should be finite. It thus requires

$$\epsilon_m = -\sqrt{\frac{2\epsilon_{nl}^3 + \beta\epsilon\epsilon_{nl}^2}{(2 + \beta)\epsilon_{nl} + \beta\alpha E_0^\beta}}. \quad (6.89)$$

For Drude form of ϵ_m , it gives

$$\omega_{sp}^{(m,n\ell)} = \frac{\omega_p}{\sqrt{1 + \left(\frac{\epsilon_{nl}^2(2\epsilon_{nl} + \beta\epsilon)}{(2 + \beta)\epsilon_{nl} + \beta\alpha E_0^\beta} \right)^{1/2}}} \approx \frac{\omega_p}{\sqrt{1 + \epsilon + \frac{2}{2 + \beta} \alpha E_0^\beta}}, \quad (6.90)$$

where the last result corresponds to the weak field limit. The effects of different nonlinearity are shown in Fig. 6.7, which gives $\omega_{sp}^{(m,n\ell)}$ as a function of $|\alpha|E_0^\beta$ for different values of β . For $\alpha > 0$, $\omega_{sp}^{(m,n\ell)}$ decreases monotonically with E_0^β . For $\alpha < 0$, there is a cutoff value of $|\alpha|E_0^\beta = \frac{(2 + \beta)\epsilon}{(2 + 2\beta)}$ above which no real solution of $\omega_{sp}^{(m,n\ell)}$ exists. Figure 6.8 shows how the SP dispersion relation is modified by the nonlinear response in a nonlinear dielectric/metal interface by solving Eq.(6.88), as a result of the field-dependent dielectric constant in the nonlinear medium.

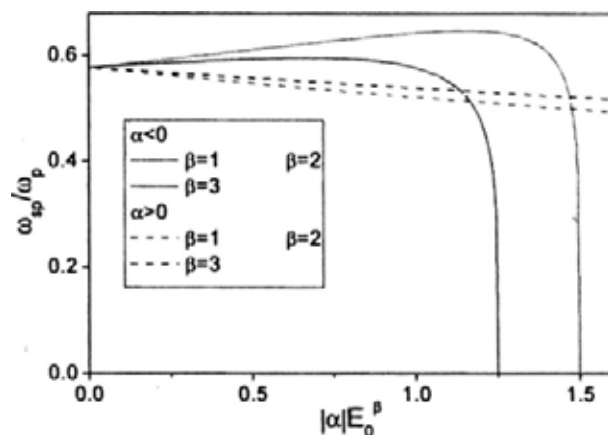


Figure 6.7: The limiting value $\omega_{sp}^{(m, n\ell)}$ as a function of $|\alpha|E_0^\beta$ for both $\alpha < 0$ and $\alpha > 0$ and different values of β in the thick film limit. The metal takes a Drude form dielectric constant ϵ_m and the linear part of the nonlinear medium takes on $\epsilon = 2$.

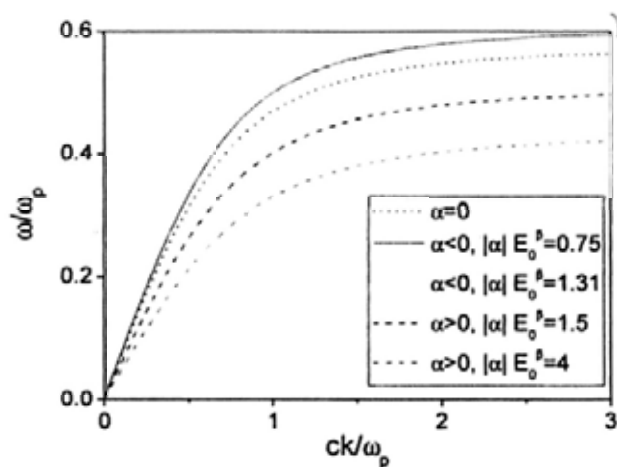


Figure 6.8: The dispersion relations at a metal/Kerr medium interface for different nonlinearities in the thick film limit. The metal takes a Drude form dielectric constant ϵ_m and the linear part of the nonlinear medium takes on $\epsilon = 2$.

6.3.2 Symmetric nonlinear/metal/nonlinear structure

Based on the results of nonlinear/metal/linear system, we are able to study the SP dispersion relation of a metallic film embedded in a symmetric nonlinear dielectric environment. The structure is similar to the previous structure in Fig. 6.5, with the linear dielectric in Region 3 replaced by a nonlinear material of dielectric constant ϵ_{nl} . For the structure to be symmetric, the strength of the \mathbf{E} fields at the two interfaces should have the same value E_0 . The x and z components of the \mathbf{E} field at $z = 0$ ($z = -d$) are E_{x0} (E_{xd}) and E_{z0} (E_{zd}), respectively.

Equation (6.83) still holds in Regions 1 and 3. By using this equation, E_{z0} can be expressed as a function of E_0 ,

$$E_{z0} = E_0 \sqrt{\frac{\left(\epsilon + \frac{2}{2+\beta} \alpha E_0^\beta\right) k_x^2 c^2}{2\epsilon_{nl} k_x^2 c^2 - w^2 \epsilon_{nl}^2}}. \quad (6.91)$$

Here we choose E_{z0} to be positive. For a decaying field in Region 1, $k_x - \frac{w^2}{c^2} \epsilon_{nl} > 0$. By using Eq.(6.74), $dE_x/dz > 0$, indicating that E_x should be negative. Similarly, we can prove that E_x and E_z share the same sign for $z \leq -d$.

By using Eq.(6.91) and $E_0^2 = E_x^2 + E_z^2$, E_{x0} can also be expressed as a function of E_0 ,

$$E_{x0} = -E_0 \sqrt{\frac{\left(\epsilon + \frac{2(1+\beta)}{2+\beta} \alpha E_0^\beta\right) k_x^2 c^2 - w^2 \epsilon_{nl}^2}{2\epsilon_{nl} k_x^2 c^2 - w^2 \epsilon_{nl}^2}}. \quad (6.92)$$

Similarly, we can write down E_{zd} and E_{xd} as a function of E_0 at $z = -d$. E_{zd} could have the same or opposite sign of E_{z0} , corresponding to the symmetric and anti-symmetric branches, respectively. E_{zd} and E_{xd} are

$$E_{zd} = \pm E_0 \sqrt{\frac{\left(\epsilon + \frac{2}{2+\beta} \alpha E_0^\beta\right) k_x^2 c^2}{2\epsilon_{nl} k_x^2 c^2 - w^2 \epsilon_{nl}^2}}, \quad (6.93)$$

$$E_{xd} = \pm \sqrt{\frac{\left(\epsilon + \frac{2(1+\beta)}{2+\beta} \alpha E_0^\beta\right) k_x^2 c^2 - w^2 \epsilon_{nl}^2}{2\epsilon_{nl} k_x^2 c^2 - w^2 \epsilon_{nl}^2}}. \quad (6.94)$$

The \mathbf{E} fields at the two interfaces can be related by matching boundary conditions at the two interfaces $z = 0$ and $z = -d$, giving

$$E_{zd} = E_{z0} \cosh(q_m d) - \frac{q_m \epsilon_{nl}}{k_x \epsilon_m} E_{z0} \sinh(q_m d), \quad (6.95)$$

$$\epsilon_{nl} E_{zd} = \frac{k_x \epsilon_m}{q_m} \left[-E_{z0} \sinh(q_m d) + \frac{q_m \epsilon_{nl}}{k_x \epsilon_m} E_{z0} \cosh(q_m d) \right]. \quad (6.96)$$

Due to symmetry, these two boundary conditions yield the same result. The dispersion relation can be obtained by substituting Eqs. (6.92)–(6.94) into either Eq.(6.95) or Eq.(6.96). For the symmetric branch s_b , the dispersion relation is

$$\frac{q_m \epsilon_{nl}}{k_x \epsilon_m} \sqrt{\left(\epsilon + \frac{2}{2 + \beta} \alpha E_0^\beta \right) k_x^2 c^2 / \left[\left(\epsilon + \frac{2(1 + \beta)}{2 + \beta} \alpha E_0^\beta \right) k_x^2 c^2 - w^2 \epsilon_{nl}^2 \right]} = -\tanh\left(\frac{q_m d}{2}\right), \quad (6.97)$$

and for the anti-symmetric branch a_b

$$\frac{q_m \epsilon_{nl}}{k_x \epsilon_m} \sqrt{\left(\epsilon + \frac{2}{2 + \beta} \alpha E_0^\beta \right) k_x^2 c^2 / \left[\left(\epsilon + \frac{2(1 + \beta)}{2 + \beta} \alpha E_0^\beta \right) k_x^2 c^2 - w^2 \epsilon_{nl}^2 \right]} = -\coth\left(\frac{q_m d}{2}\right). \quad (6.98)$$

When $\alpha = 0$, which corresponds to the case that Regions 1 and 3 are filled with the same linear dielectric, our results reduce to the well-known linear/metal/linear case, as given in Eq.(6.69). When $\alpha \neq 0$, our theory gives the SP dispersion relation for a metallic film in symmetric nonlinear materials of arbitrary nonlinearity.

Figure 6.9 shows the dispersion relations of a metallic film embedded in a symmetric MBBA environment. The metal is taken to be silver and the parameters of MBBA are the same as those we used in Sec. 6.3.1, a field $E_0 = 2.5 \times 10^5$ V/m is used. The results are similar to the SP dispersion relations of symmetric linear/metal/linear system. For thin film, the two branches are separated due to the hybridization of the SP modes in the thick film limit (see $d = 20$ nm results). As the film becomes thicker, this effect becomes weaker (see $d = 30$ nm results). For the thick film limit $d \rightarrow \infty$, $\tanh(q_m d/2) =$

$\coth(q_m d/2) = 1$, and the two branches become degenerate (see $d = 100$ nm results).

6.4 Conclusion

In this chapter, we reviewed several basic concepts, including the Maxwell's equations, the TE and TM polarizations, and the Drude dielectric constant of metals. These concepts will be used in our future discussions. The surface plasmon dispersion relations of a semi-infinite metal/linear dielectric system and linear/metal/linear structure are introduced. The bound and leaky SP modes are discussed. By invoking the "first integral" technique, the SP dispersion relations of a nonlinear-metal-linear system are derived, where the nonlinear medium can take on arbitrary nonlinearity. The effects of metallic film thickness and different nonlinearity on the SP dispersion relations are discussed. We derived the SP dispersions relation of a system with a slab of metal in a symmetric nonlinear dielectric environment. The dependence of the dispersion relations on film thickness is illustrated.

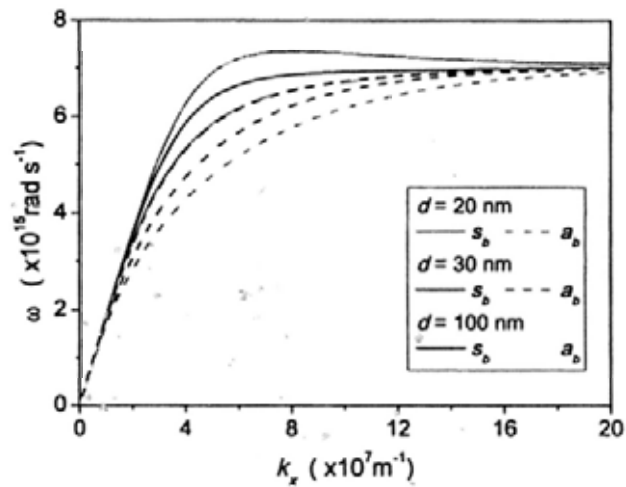


Figure 6.9: The dispersion relations of SP modes in a MBBA/metal/MBBA system. The thicknesses of the metallic film are taken to be $d = 20$ nm, 30 nm and 100 nm.

Chapter 7

The Rigorous Coupled-Wave Analysis

In this chapter, we introduce the Rigorous Coupled-Wave Analysis (RCWA), which is a grating theory commonly used to study the optical properties of periodic structures. The algorithms to treat one dimensional periodic structures are discussed. The Fourier factorization rule, and the scattering matrix technique are also introduced. Two simple examples are used to test the RCWA algorithm.

7.1 Introduction

The Rigorous Coupled-Wave Analysis (RCWA) is a numerical method for computing the diffraction fields of grating structures. It was first developed by Moharam and Gaylord [82, 83, 84]. Later, the idea of scattering matrix was introduced to improve the numerical stability [85], and the Fourier factorization rules were developed to speed up the convergence [86]. The RCWA method has been generalized to study arbitrary anisotropy [87] and geometric profiles [88, 89]. In this chapter, we present an introduction to the RCWA algorithm in handling one-dimensional periodic structures. The method will

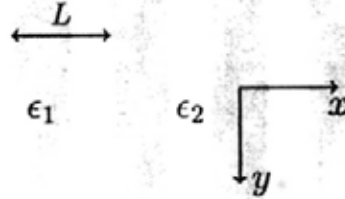


Figure 7.1: Schematic diagram showing a 1D structure with period L along the x direction.

then be used in the next two chapter.

7.2 RCWA for 1D periodic structures

From here on, we use \mathcal{H} to represent the \mathbf{H} field we used in Chapter 6, and redefine $\mathbf{H} = c\mathbf{B}$. By doing so, the \mathbf{H} field has the same dimension as the \mathbf{E} field, which is convenient for numerical treatment. The Maxwell's equations Eqs. (6.8) and (6.9) become

$$\nabla \times \mathbf{E} = -\frac{1}{c} \frac{\partial \mathbf{H}}{\partial t}, \quad (7.1)$$

$$\nabla \times \mathbf{H} = \frac{\epsilon}{c} \frac{\partial \mathbf{E}}{\partial t}. \quad (7.2)$$

Below we introduce the RCWA algorithm for TM and TE polarizations separately.

7.2.1 TM polarization

Consider EM fields taking on the form of plane waves

$$\mathbf{E}(\mathbf{r}, t) = \mathbf{E}(\mathbf{r})e^{-i\omega t}, \quad (7.3)$$

$$\mathbf{H}(\mathbf{r}, t) = \mathbf{H}(\mathbf{r})e^{-i\omega t}. \quad (7.4)$$

For TM polarization, the \mathbf{H} field has y -component only, Eqs. (7.1) and (7.2) can be rewritten as

$$ikH_y(x, z) = \partial_z E_x(x, z) - \partial_x E_z(x, z), \quad (7.5)$$

$$ik\epsilon E_x(x, z) = \partial_z H_y(x, z), \quad (7.6)$$

$$-ik\epsilon E_z(x, z) = \partial_x H_y(x, z), \quad (7.7)$$

where $k = \omega/c$ is the wavevector.

Here we consider a periodic structure that has periodicity along the x direction, with a period L . The dielectric constant $\epsilon(x)$ is a periodic function that takes on different values depending on the location. The structure is schematically illustrated in Fig. 7.1. For this system, both $\mathbf{E}(\mathbf{r})$ and $\mathbf{H}(\mathbf{r})$ can be expanded in Fourier series,

$$\begin{aligned} E_x(x, z) &= \sum_{n=-\infty}^{\infty} E_{xn}(z)e^{ik_{xn}x}, \\ E_z(x, z) &= \sum_{n=-\infty}^{\infty} E_{zn}(z)e^{ik_{xn}x}, \\ H_y(x, z) &= \sum_{n=-\infty}^{\infty} H_{yn}(z)e^{ik_{xn}x}, \end{aligned} \quad (7.8)$$

where k_{xn} is defined as

$$k_{xn} = k_x + \frac{2n\pi}{L}. \quad (7.9)$$

The dielectric constant $\epsilon(x)$ can also be expressed as a summation of Fourier components,

$$\epsilon(x) = \sum_{n=-\infty}^{\infty} \epsilon_n e^{i2n\pi x/L}. \quad (7.10)$$

Substituting Eqs. (7.8) and (7.10) into Eqs. (7.5)–(7.7), we obtain

$$ikH_{yn}(z) = E'_{zn}(z) - ik_{xn}E_{zn}(z), \quad (7.11)$$

$$ik \sum_m \epsilon_{n-m} E_{xm}(z) = H'_{yn}(z), \quad (7.12)$$

$$-k \sum_m \epsilon_{n-m} E_{zm}(z) = k_{xn} H_{yn}(z). \quad (7.13)$$

To numerically implement the algorithm, we should make a cutoff and use a finite number of Fourier orders to represent the H and E fields, as well as the dielectric constant ϵ . Here, we use N to denote the number of the remaining orders. Thus the summations in Eqs. (7.8) and (7.10) go from $-N$ to N , instead of from $-\infty$ to ∞ after the cutoff. For a function f that can be expanded in Fourier series, the $2N + 1$ Fourier coefficients can be represented in a vector form as $[f]$, with the n -th element of the vector $[f]_n = f_{n-N-1}$. Thus the Fourier coefficients of the H and E fields can all be written in vector forms. By doing so, Eqs. (7.11)–(7.13) can be rewritten as

$$ik|I|[H_y] = [E'_x] - i\|k_x\|[E_z], \quad (7.14)$$

$$ik|I|[\epsilon][E_x] = [H'_y], \quad (7.15)$$

$$-k|I|[\epsilon][E_z] = \|k_x\|[H_y], \quad (7.16)$$

where $|I|$ is an identity matrix, $\|s\|$ is a diagonal matrix with $\|s\|_{mn} = \delta_{mn}s_{n-N-1}$, $[[g]]$ is a toeplitz matrix with $[[g]]_{mn} = g_{m-n}$ [90]. The δ function is the Kronecker delta, $\delta_{mn} = 1$ if $m = n$, and 0 otherwise. Combining Eqs. (7.14)–(7.16), we have a second-order differential equation of H_y ,

$$[H''_y] = -[[\epsilon]](|I|k^2 - \|k_x\|[\epsilon]^{-1}\|k_x\|)[H_y] \equiv [M][H_y]. \quad (7.17)$$

Let $H_{yn}(z)$ take on the form $H_{yn}(z) = H_{yn}e^{-ik_z z}$. According to Eq.(7.17), k_z^2 should be an eigenvalue and $[H_y]$ be an eigenvector of the matrix $[M]$. The dimension of matrix $[M]$ is $2N + 1$, so there are $(2N + 1)$ sets of eigenvalues and eigenvectors in total. Denoting the p -th eigenvalue and eigenvector as k_{zp}^2 and H_{ynp}^{TM} , the general solution can be written as a linear combination of the eigenmodes,

$$H_y(x, z) = \sum_{n,p} H_{ynp}^{TM} (A_p^+ e^{ik_{zp}z} + A_p^- e^{-ik_{zp}z}) e^{ik_{zn}x}, \quad (7.18)$$

where A_p^+ and A_p^- are arbitrary constants. Here k_{zp} is chosen to have positive imaginary part, so that the A_p^+ term gives a forward decaying mode and the

A_p^- term gives a backward decaying field. We construct a $(2N + 1) \times (2N + 1)$ matrix $[H_y]$ by using the p -th eigenvector of the matrix $[M]$ to be the p -th column, and express the coefficients A_p^+ and A_p^- in vector forms, $[A^\pm]_p = A_p^\pm$. Thus, Eq.(7.18) becomes

$$[H_y(x, z)] = \|\exp(ik_x x)\| [H_y] (\|\exp(ik_z z)\| [A^+] + \|\exp(-ik_z z)\| [A^-]) . \quad (7.19)$$

Similarly, the general form of the E_x field is

$$[E_x(x, z)] = \|\exp(ik_x x)\| [E_x] (\|\exp(ik_z z)\| [A^+] - \|\exp(-ik_z z)\| [A^-]) , \quad (7.20)$$

where $[E_x] = \frac{1}{k} [\epsilon] \|k_z\| [H_y]$.

7.2.2 TE polarization

For TE polarization, the \mathbf{H} field has x and z components, while the \mathbf{E} field only has a y component. The Maxwell's equations Eqs. (7.1) and (7.2) for this case can be written as

$$ik\epsilon E_y(x, z) = \partial_x H_z(x, z) - \partial_z H_x(x, z) , \quad (7.21)$$

$$-ikH_x(x, z) = \partial_z E_y(x, z) , \quad (7.22)$$

$$ikH_z(x, z) = \partial_x E_y(x, z) . \quad (7.23)$$

By writing down the E and H fields, and $\epsilon(x)$ as Fourier series in a similar way as in Eqs. (7.8) and (7.10), Eqs. (7.21)–(7.23) become

$$ik \sum_m \epsilon_{n-m} E_{ym}(z) = ik_{zn} H_{zn}(z) - H'_{zn}(z) , \quad (7.24)$$

$$-ikH_{zn}(z) = E'_{ym}(z) , \quad (7.25)$$

$$kH_{zn}(z) = k_{zn} E_{ym}(z) . \quad (7.26)$$

A second order differential equation of E_y can be obtained by combining Eqs. (7.24) – (7.26), which can be expressed in matrix form as

$$[E_y''] = (\|k_x\|^2 - |I|k^2[\epsilon]) [E_y] \equiv [M] [E_y] . \quad (7.27)$$

Let $E_{yn}(z)$ take on the form $E_{yn}(z) = E_{yn}e^{-ik_z z}$, k_z^2 should be an eigenvalue and $[E_y]$ an eigenvector of the matrix $[M]$. Similar to the TM case, we denote the p -th eigenvalue and eigenvector as k_{zp}^2 and E_{ynp}^{TE} . The general solution can be written as

$$E_y(x, z) = \sum_{n,p} E_{ynp}^{TE} (A_p^+ e^{ik_{zp}z} + A_p^- e^{-ik_{zp}z}) e^{ik_{zn}x}, \quad (7.28)$$

where A_p^+ and A_p^- are arbitrary constants.

7.2.3 Fourier factorization rule

Previous researches have revealed that RCWA converges slowly in TM polarization [91]. Lalanne and Morris [92], and Granet and Guizal [93] improved the convergence rate by replacing $[\epsilon]$ with $[1/\epsilon]^{-1}$, without clarifying the reason. The mathematical proof of this replacement was given by Li [86]. Here we briefly introduce the idea. Our discussion here is based on Ref. [90, 94].

Consider three functions $f(x)$, $g(x)$, and $h(x)$ that have the same period L and have the following relation

$$f(x) = g(x)h(x). \quad (7.29)$$

The three functions can be expressed in Fourier series as

$$\begin{aligned} f(x) &= \sum_n f_n e^{i\frac{2n\pi x}{L}}, \\ g(x) &= \sum_n g_n e^{i\frac{2n\pi x}{L}}, \\ h(x) &= \sum_n h_n e^{i\frac{2n\pi x}{L}}. \end{aligned} \quad (7.30)$$

Thus, the n -th order Fourier coefficient of f can be written as

$$f_n = \sum_m g_{n-m} h_m, \quad (7.31)$$

which is called the Laurent's rule. If $g(x)$ and $h(x)$ do not have concurrent discontinuity, i.e., the discontinuities of $g(x)$ and $h(x)$ occur at different positions, the Laurent's rule Eq.(7.31) will give efficient convergence rate.

Another case is that $g(x)$ and $h(x)$ have concurrent discontinuity, but they are complementary, i.e., $g(x)$ and $h(x)$ are discontinuous at the same position x_d while their product $f(x) = g(x)h(x)$ is continuous at x_d . For this case, the *inverse rule* should be applied in order to achieve satisfactory convergence,

$$f_n = \sum_m \left[\left[\frac{1}{g} \right]_{mn} \right]^{-1} h_m . \quad (7.32)$$

For the case of TM polarization,

$$D(x) = \epsilon(x)E(x) . \quad (7.33)$$

$D(x)$ is continuous along x , while $\epsilon(x)$ and $E(x)$ have concurrent discontinuity, so the inverse rule should be applied. Equation (7.15) should be rewritten as

$$i|I|k \left[\left[\frac{1}{\epsilon} \right] \right]^{-1} [E_x] = [H'_y] , \quad (7.34)$$

and the $[M]$ matrix in Eq.(7.17) becomes

$$[M] = - \left[\left[\frac{1}{\epsilon} \right] \right]^{-1} (|I|k^2 - \|k_x\| \left[\left[\epsilon \right] \right]^{-1} \|k_x\|) . \quad (7.35)$$

7.2.4 Matching boundary conditions

Using the general solutions of the EM fields, the exact solutions can be obtained by matching boundary conditions. Here we use a three-layer system to illustrate the idea. Layers 1 and 3 are homogeneous media. Layer 2 is a periodic structure sandwiched between Layers 1 and 3 with the interfaces located at $z = 0$ and $z = d$, respectively. Light incident from Layer 1. Here, we only consider the TM polarization case. The TE polarization case can be derived in a similar way.

For TM polarization, the general forms of the H_y and E_x fields can be written in matrix form. For Layer 1,

$$\begin{aligned} [H_y^{(1)}] &= \|\exp(ik_x x)\| [H_{1y}] (\|\exp(ik_z^{(1)} z)\| [A_1^+] + \|\exp(-ik_z^{(1)} z)\| [A_1^-]), \\ [E_x^{(1)}] &= \|\exp(ik_x x)\| [E_{1x}] (\|\exp(ik_z^{(1)} z)\| [A_1^+] - \|\exp(-ik_z^{(1)} z)\| [A_1^-]). \end{aligned} \quad (7.36)$$

For Layer 2,

$$\begin{aligned} [H_y^{(2)}] &= \|\exp(ik_x x)\| [H_{2y}] (\|\exp(ik_z^{(2)} z)\| [A_2^+] + \|\exp(-ik_z^{(2)} z)\| [A_2^-]), \\ [E_x^{(2)}] &= \|\exp(ik_x x)\| [E_{2x}] (\|\exp(ik_z^{(2)} z)\| [A_2^+] - \|\exp(-ik_z^{(2)} z)\| [A_2^-]). \end{aligned} \quad (7.37)$$

For Layer 3,

$$\begin{aligned} [H_y^{(3)}] &= \|\exp(ik_x x)\| [H_{3y}] (\|\exp(ik_z^{(3)}(z-d))\| [A_3^+] + \|\exp(-ik_z^{(3)}(z-d))\| [A_3^-]), \\ [E_x^{(3)}] &= \|\exp(ik_x x)\| [E_{3x}] (\|\exp(ik_z^{(3)}(z-d))\| [A_3^+] - \|\exp(-ik_z^{(3)}(z-d))\| [A_3^-]). \end{aligned} \quad (7.38)$$

Matching boundary conditions at $z = 0$, the coefficients of the fields in Layers 1 and 2 are related through

$$\begin{pmatrix} [A_1^+] \\ [A_1^-] \end{pmatrix} = \begin{pmatrix} [T^{12+}] & [T^{12-}] \\ [T^{12-}] & [T^{12+}] \end{pmatrix} \begin{pmatrix} [A_2^+] \\ [A_2^-] \end{pmatrix}, \quad (7.39)$$

where

$$T^{\mu\nu\pm} = \frac{1}{2} (\| [H_y^{(\mu)}]^{-1} [H_y^{(\nu)}] \pm [E_x^{(\mu)}]^{-1} [E_x^{(\nu)}] \|). \quad (7.40)$$

Similarly, matching boundary conditions at $z = d$ lead to

$$\begin{pmatrix} [A_2^+] \\ [A_2^-] \end{pmatrix} = \begin{pmatrix} \|\exp(-ik_z^{(2)} d)\| & 0 \\ 0 & \|\exp(ik_z^{(2)} d)\| \end{pmatrix} \begin{pmatrix} [T^{23+}] & [T^{23-}] \\ [T^{23-}] & [T^{23+}] \end{pmatrix} \begin{pmatrix} [A_3^+] \\ [A_3^-] \end{pmatrix}. \quad (7.41)$$

In general, the transfer matrix that relates the coefficients of the fields of two adjacent layers takes on the following form

$$\begin{pmatrix} [A_j^+] \\ [A_j^-] \end{pmatrix} = \begin{pmatrix} \|\Phi^-\| & 0 \\ 0 & \|\Phi^+\| \end{pmatrix} \begin{pmatrix} [T_{11}^{jj+1}] & [T_{12}^{jj+1}] \\ [T_{21}^{jj+1}] & [T_{22}^{jj+1}] \end{pmatrix} \begin{pmatrix} [A_{j+1}^+] \\ [A_{j+1}^-] \end{pmatrix}. \quad (7.42)$$

Equation (7.39) is a special case that $\|\Phi^-\| = \|\Phi^+\| = |I|$.

Notice that $k_z^{(2)}$ has a positive imaginary part. Thus the $\exp(-ik_z^{(2)}d)$ term grows exponentially as the thickness d increases, which may lead to numerical instability for large d . To avoid the instability, an algorithm using the *scattering matrix* should be applied.

Scattering matrix

The idea of transfer matrix is to relate the coefficients of the fields in different regions, while the idea of scattering matrix is to relate the coefficients of the input and output fields. Take Layer 1 and Layer 3 of our three layer system as an example, A_1^+ and A_3^- are the coefficients of the fields moving towards the medium (input fields), and A_1^- and A_3^+ are the coefficients of the fields moving away from the medium (output fields). These two sets of coefficients are related by the scattering matrix as

$$\begin{pmatrix} [A_3^+] \\ [A_1^-] \end{pmatrix} = \begin{pmatrix} [S_{11}^{1,3}] & [S_{12}^{1,3}] \\ [S_{21}^{1,3}] & [S_{22}^{1,3}] \end{pmatrix} \begin{pmatrix} [A_1^+] \\ [A_3^-] \end{pmatrix}. \quad (7.43)$$

The scattering matrix that relates the fields of Layer 1 and an arbitrary layer can be obtained iteratively. Let us assume that the scattering matrix that relates the fields of Layer 1 and Layer j is known, i.e.,

$$\begin{pmatrix} [A_j^+] \\ [A_1^-] \end{pmatrix} = \begin{pmatrix} [S_{11}^{1,j}] & [S_{12}^{1,j}] \\ [S_{21}^{1,j}] & [S_{22}^{1,j}] \end{pmatrix} \begin{pmatrix} [A_1^+] \\ [A_j^-] \end{pmatrix}. \quad (7.44)$$

We want to find the scattering matrix that relates the fields in Layer 1 and Layer $j + 1$, i.e.,

$$\begin{pmatrix} [A_{j+1}^+] \\ [A_1^-] \end{pmatrix} = \begin{pmatrix} [S_{11}^{1,j+1}] & [S_{12}^{1,j+1}] \\ [S_{21}^{1,j+1}] & [S_{22}^{1,j+1}] \end{pmatrix} \begin{pmatrix} [A_1^+] \\ [A_{j+1}^-] \end{pmatrix}. \quad (7.45)$$

Notice that the coefficients of the fields in Layers j and $j + 1$ are related by the transfer matrix given by Eq.(7.42). Combining Eqs. (7.42) and (7.44), the

unknown elements in Eq.(7.45) can be solved:

$$\begin{aligned}
 [S_{11}^{1,j+1}] &= ([T_{11}^{j,j+1}] - |\Phi^-|^{-1}[S_{12}^{1,j}]|\Phi^+|[T_{21}^{j,j+1}])^{-1}|\Phi^-|^{-1}[S_{11}^{1,j}], \\
 [S_{12}^{1,j+1}] &= ([T_{11}^{j,j+1}] - |\Phi^-|^{-1}[S_{12}^{1,j}]|\Phi^+|[T_{21}^{j,j+1}])^{-1}(|\Phi^-|^{-1}[S_{12}^{1,j}]|\Phi^+|[T_{22}^{j,j+1}] - [T_{12}^{j,j+1}]), \\
 [S_{21}^{1,j+1}] &= [S_{21}^{1,j}] + [S_{22}^{1,j}]|\Phi^+|[T_{21}^{j,j+1}][S_{11}^{1,j+1}], \\
 [S_{22}^{1,j+1}] &= [S_{22}^{1,j}]|\Phi^+|[T_{22}^{j,j+1}] + [S_{22}^{1,j}]|\Phi^+|[T_{21}^{j,j+1}][S_{12}^{1,j+1}].
 \end{aligned} \tag{7.46}$$

In Eq.(7.46), only the $|\Phi^-|^{-1}$ term appears, thus the exponentially growth terms $\exp(-ik_{zn}d)$ are avoided. For multiple layered structures, by starting from the scattering matrix that relates Layer 1 with itself, i.e.,

$$\begin{pmatrix} [A_1^+] \\ [A_1^-] \end{pmatrix} = \begin{pmatrix} |I| & 0 \\ 0 & |I| \end{pmatrix} \begin{pmatrix} [A_1^+] \\ [A_1^-] \end{pmatrix}, \tag{7.47}$$

and applying Eq.(7.46) iteratively, we can find the scattering matrix that relates Layer 1 and the far end.

For the three layer system under consideration, the incident wave has the zeroth order only in Layer 1. Thus, the amplitude of the input field is $A_{1n}^+ = \delta_{n0}$. In Layer 3, there is no incoming wave, thus $[A_3^-] = 0$. By Eq.(7.43), the transmission and reflection coefficients can be obtained as

$$A_{3n}^+ = [S_{11}^{1,3}]_{n,N+1}, \tag{7.48}$$

$$A_{1n}^- = [S_{12}^{1,3}]_{n,N+1}. \tag{7.49}$$

The n -th order transmittance and reflectance are given by

$$T_n = \begin{cases} \operatorname{Re} \left(\frac{\epsilon_1 k_{zn}^{(3)}}{\epsilon_3 k_{z0}^{(1)}} \right) |A_{3n}^+|^2, & \text{for TM case,} \\ \operatorname{Re} \left(\frac{k_{zn}^{(3)}}{k_{z0}^{(1)}} \right) |A_{3n}^+|^2, & \text{for TE case,} \end{cases} \tag{7.50}$$

$$R_n = \operatorname{Re} \left(\frac{k_{zn}^{(1)}}{k_{z0}^{(1)}} \right) |A_{1n}^-|^2. \tag{7.51}$$

7.3 Sample calculations

In this section, we apply the RCWA method to two simple examples.

7.3.1 Total internal reflection at glass-air interface

We implemented RCWA by setting up our own computer codes. To test the validity of our code, we use RCWA to study the reflection and transmission at a glass-air interface. The dielectric constants of glass and air are $\epsilon_g = 2.25$ and $\epsilon_a = 1$, respectively. Consider a beam of TE polarized light incident from glass to the glass-air interface with incident angle θ_I . The transmittance and reflectance of this system can be analytically solved. The solutions

$$\begin{aligned} T_0 &= \frac{\sqrt{\epsilon_a} \cos \theta_T}{\sqrt{\epsilon_g} \cos \theta_I} \left(\frac{2 \cos \theta_I \sin \theta_T}{\sin(\theta_I + \theta_T)} \right)^2, \\ R_0 &= \left(\frac{\sin(\theta_I - \theta_T)}{\sin(\theta_I + \theta_T)} \right)^2, \end{aligned} \quad (7.52)$$

can be found in textbooks (e.g., Ref. [95]). Here, θ_T is the angle of refraction, which is related to θ_I by the Snell's Law

$$\frac{\sin \theta_T}{\sin \theta_I} = \frac{\sqrt{\epsilon_g}}{\sqrt{\epsilon_a}}. \quad (7.53)$$

Figure 7.2 shows T_0 and R_0 as a function of the incident angle θ_I (solid lines), based on Eq.(7.52). The RCWA results are also shown (symbols), which coincide with the analytic results. According to Eq.(7.52), the transmittance T_0 becomes 0 when $\theta_T = 90^\circ$. When this occurs, the reflectance becomes 1. This phenomenon is called total internal reflection. For our system, it occurs at $\theta_I = 42.8^\circ$, as shown in Fig. 7.2.

7.3.2 Enhanced transmission in a silver grating

In 1998, Ebbesen et al. studied the optical transmission through an optically thick silver film patterned with an array of sub-wavelength holes. They observed that the transmission efficiencies are orders of magnitude greater than

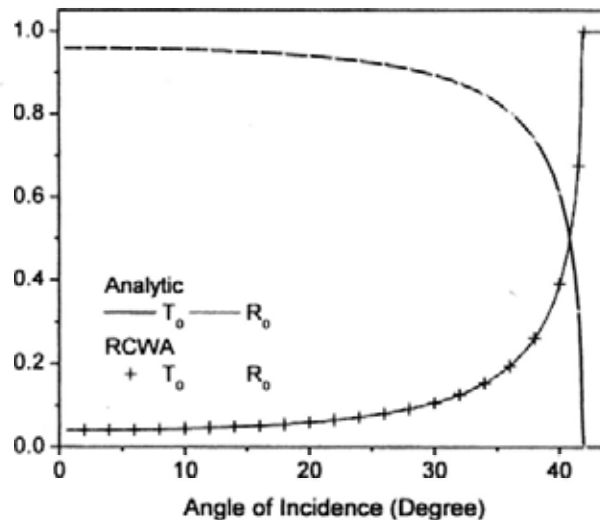


Figure 7.2: The transmittance T_0 and reflectance R_0 as a function of the incident angle θ_I , for a TE polarized EM wave incident from glass to air. Analytic results (solid lines) and results by RCWA (symbols) are shown.

predicted by classical theory at some frequencies [15]. This phenomenon is often referred to as the enhanced transmission or extraordinary transmission. The underlying mechanism is generally regarded to be related to the excitation of surface plasmon modes. Later, Schröter and Heitmann performed numerical calculations on the transmission through a one-dimensional silver grating [96]. Their results are in qualitative agreement with Ebbesen's measurements. They also verified that the transmission maxima indeed correspond to the excitation of surface plasmons. Here, we use RCWA to perform a similar calculation.

The system consists of a one dimensional silver grating of period $L = 900$ nm, with slit width $w = 36$ nm and thickness $d = 60$ nm. One side of the grating is air and inside the slits are filled with air. Another side is glass with dielectric constant $\epsilon_g = 2$. A beam of TM polarized light is incident upon the grating with angle θ . The system is schematically shown in Fig. 7.3. Our system is the same as in Ref. [90].

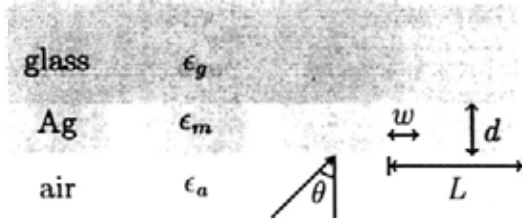


Figure 7.3: Schematic diagram showing a silver grating of period $L = 900$ nm, thickness $d = 60$ nm, and slit width $w = 36$ nm. One side of the grating is air and the slits are filled with air of dielectric constant $\epsilon_a = 1$, and another side of the grating is glass with dielectric constant $\epsilon_g = 2$. A TM polarized wave is incident upon the grating from air with an angle θ .

Figure 7.4(a) shows the zeroth order transmission T_0 as a function of incident frequency at normal incidence. For the frequency range of concern, there are three peaks. The slit takes on 4% of the period, but at the transmission peaks, more than 20% of the light can penetrate through. So the transmission is largely enhanced at these peaks. Now we show that these peaks are related to SP excitations. We change the incident angle θ and thus the value of k_x . The frequency of the transmission peaks are plotted versus k_x in Fig. 7.4(b) (symbols). As discussed in Chapter 6, k_x should satisfy the relation (Eq.(6.50)),

$$k_x + n \frac{2\pi}{L} = k_{xsp} = \frac{\omega}{c} \sqrt{\frac{\epsilon_i \epsilon_m}{\epsilon_i + \epsilon_m}} \quad (7.54)$$

for a SP mode to be excited. Here ϵ_i can be ϵ_a or ϵ_g , depending on the location. For any k_{xsp} , there is always a k_{x0} within $[0, 2\pi/L]$ that satisfies the following relation

$$k_{xsp} = k_{x0} + m \frac{2\pi}{L}, \quad (7.55)$$

where m is an integer, which can be positive or negative. Thus, by finding out k_{x0} , the SP dispersion relation can be folded into the region $0 < k_{x0} < 2\pi/L$, which is called the *Brillouin Zone*. Figure 7.4(b) shows the folded dispersion curves for SP modes excited at the metal-air interface (dashed lines) and metal-glass interface (solid lines), respectively. The peak values will agree

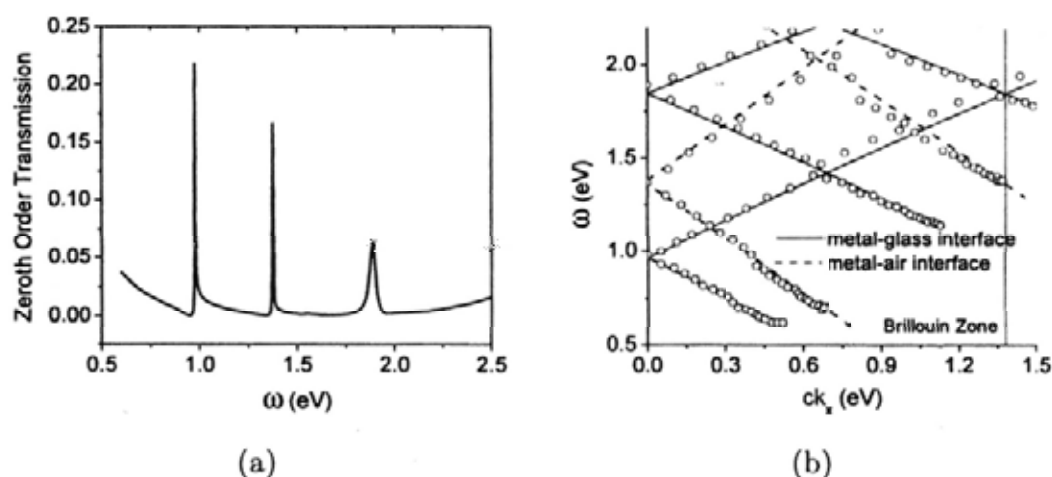


Figure 7.4: (a) The zeroth order transmission at normal incidence for the system shown in Fig. 7.3. (b) Symbols show the positions of the transmission peaks. Lines show the folded dispersion curves of SP modes excited at metal-air interface (dashed lines) and metal-glass interface (solid lines), respectively.

with the dispersion relation curves, showing that the transmission peaks are related to the excitation of SP modes at both interfaces.

7.4 Summary

In this chapter, we introduced the RCWA algorithm for one-dimensional periodic structures. We presented the formalisms, and introduced the scattering matrix and Fourier factorization rules, which are techniques to improve the numerical stabilities and the convergence rate. Two sample calculations were carried out, in which RCWA is used to study the total internal reflection at a glass-air interface and the surface plasmon excitations in a silver grating. The method and computer codes developed will be used in the next two chapters.

Chapter 8

Optical properties of metallic reflection gratings

In this chapter, we study two samples of one-dimensional metallic reflection gratings that are fabricated at CUHK and their measured reflectance. We carry out numerical calculations based on the Rigorous Coupled-Wave Analysis and compare the results with measured results. The phenomenon of Wood's anomaly is studied by measuring and computing the diffraction efficiency of different orders. We show numerical results of the near field patterns, which indicate that there is a coupling between waveguide modes and surface plasmon modes.

8.1 Sample preparation

Researchers have been mainly interested in studying the optical properties of transmission gratings since the discovery of enhanced transmission through patterned metallic films with subwavelength holes [15]. In contrast, studies on reflection grating are relatively few. The metallic reflection grating can support surface plasmon excitations at the surface and waveguide mode inside the

slits. They have possible applications including high efficiency surface-emitting organic light emitting diode (OLED)[17], surface-enhanced Raman scattering [16], etc. Here, we study the optical properties of one-dimensional gold reflection gratings. This chapter is based on a collaboration work with an experimental group. The experiments were mainly carried out by Mr. Luk Wai Chun, under the supervision of Prof. Daniel Ong [97]. We did the numerical calculations and theoretical analysis. Results in this chapter were reported in a conference (Ref. [98]).

In this section, we give a brief account on the preparation of the one-dimensional metallic reflection gratings and the geometry structure of the samples. The preparation process consists of two steps:

1. Use interference lithography to prepare a one-dimensional dielectric grating on a substrate.
2. Use sputtering to deposit a layer of gold on to the dielectric grating to form a one-dimensional metallic grating.

The preparation process is schematically shown in Fig. 8.1. Now we discuss the process in detail.

The interference lithography is a fabrication technique for preparing patterned structures on a substrate. The basic principle is as follows: First, a layer of photoresist is deposited onto the substrate. A patterned laser light is then incident upon the photoresist. The areas under the light become exposed and the other areas remain unexposed. After exposure, the unexposed photoresist is washed away by organic solvents. The remaining parts form a patterned structure.

The patterned incident laser is produced by using Lloyd mirror. The interference between the directly incident light and the light reflected by the mirror forms the periodic pattern. Glass is used as the substrate. The photoresist that we used is SU-8, which is a negative photoresist. The refraction

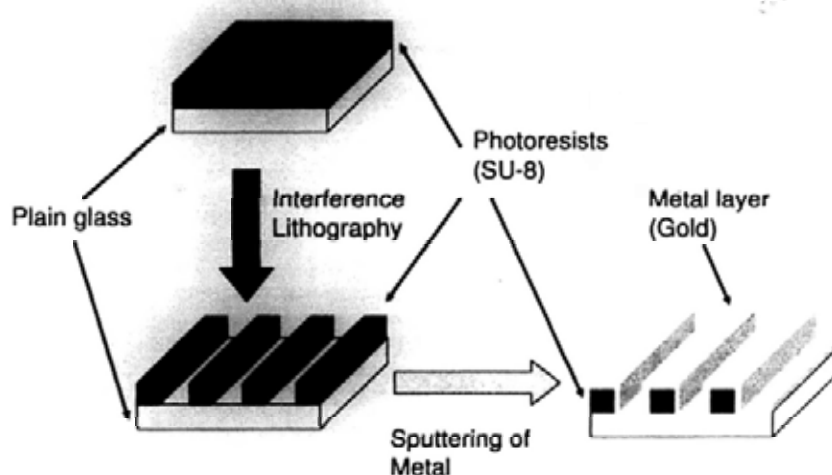


Figure 8.1: Schematic diagram showing the sample preparation process.

index of SU-8 is 1.59.

The parameters of the dielectric grating can be tuned [94]. The period of the grating can be changed by altering the incident angle. The slit width can be tuned by changing the exposure time. The grating height can be tuned by using different combinations of SU-8 concentration and spin coating speed.

After the dielectric grating is prepared, a layer of gold is deposited onto it to form a metallic grating by using sputtering. The idea of sputtering is as follows: The dielectric grating and a gold target are put in a chamber filled with argon gas. Due to the interaction with argon ions, gold atoms can be detached from the target. Some of these atoms fly to the substrate and deposit onto it.

Two samples are prepared, which are labelled Sample 1 and Sample 2. Figure 8.2 shows the pictures of the two samples, which are obtained by using scanning electron microscope (SEM). Both samples are very regular and periodic. The results are shown in Fig. 8.3. The period L of both samples is about 760 nm. The slit widths are $w = 140$ nm for Sample 1 and $w = 177$ nm for Sample 2, and they are quite similar. The main difference between the two samples is in their depth d , with $d = 390$ nm for Sample 1 and $d = 580$ nm for Sample 2.

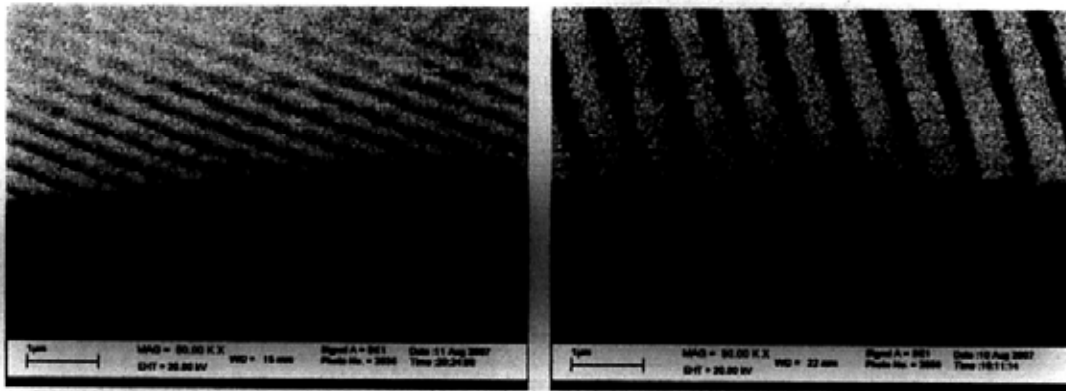


Figure 8.2: The SEM pictures of Sample 1 (left panel) and Sample 2 (right panel).

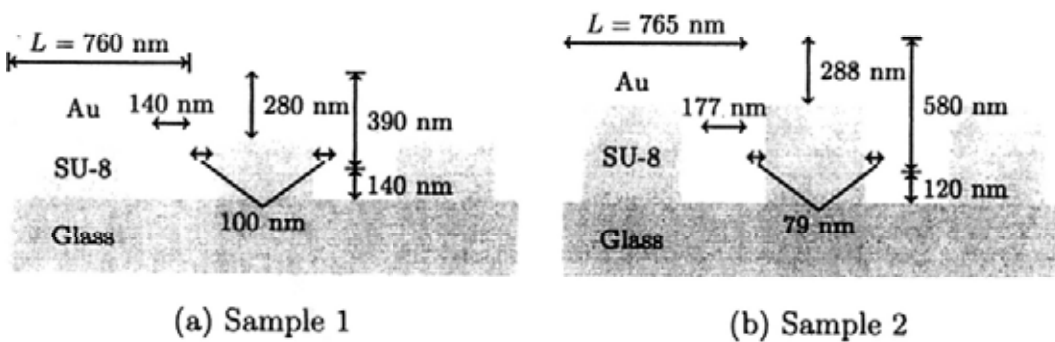


Figure 8.3: Schematic diagram showing the topological structures of Sample 1 (left panel) and Sample 2 (right panel). The parameters are measured by SEM.

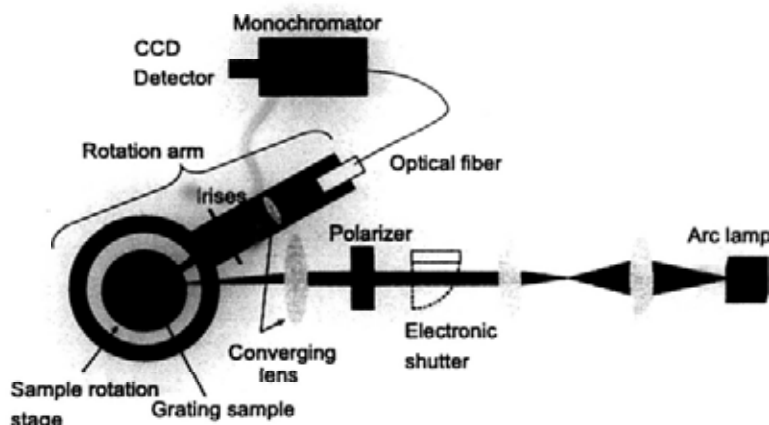


Figure 8.4: Schematic diagram showing the experimental set up for measuring the zeroth order reflectance.

8.2 The zeroth order reflectance

In this section, we study the zeroth order reflectance of the two samples. The experimental set up for measuring the zeroth order reflectance is shown in Fig. 8.4 [97]. A white arc lamp is used as the light source. The light beam becomes collimated after passing through the two objects. We are only interested in the TM polarization here, so a polarizer is used to produce TM polarized light beam. The polarized beam is focused on the sample surface. The grating can be rotated so as to change the incident angle, and the rotation arm can be rotated to right angle so that the reflected light can pass through. The reflected light is split into different wavelengths, and the intensities are recorded by the CCD detector.

Figures 8.5(a) and 8.6(a) show the measured zeroth order reflectance of Samples 1 and 2, respectively. The x axis is the incident angle θ and the y axis is the wavelength λ . The values of the reflectance are indicated by colors, greener for larger reflectance and bluer for smaller reflectance. The main features of the zeroth order reflectance are:

- There are nearly flat bands with very low reflectance (color in deep blue).

For Sample 1, there is one such flat band, located at around $\lambda \sim 750$ nm. For Sample 2, there are two such bands, one at around 650 nm and another at around 950 nm.

- For each sample, there are three oblique crossed bright lines.

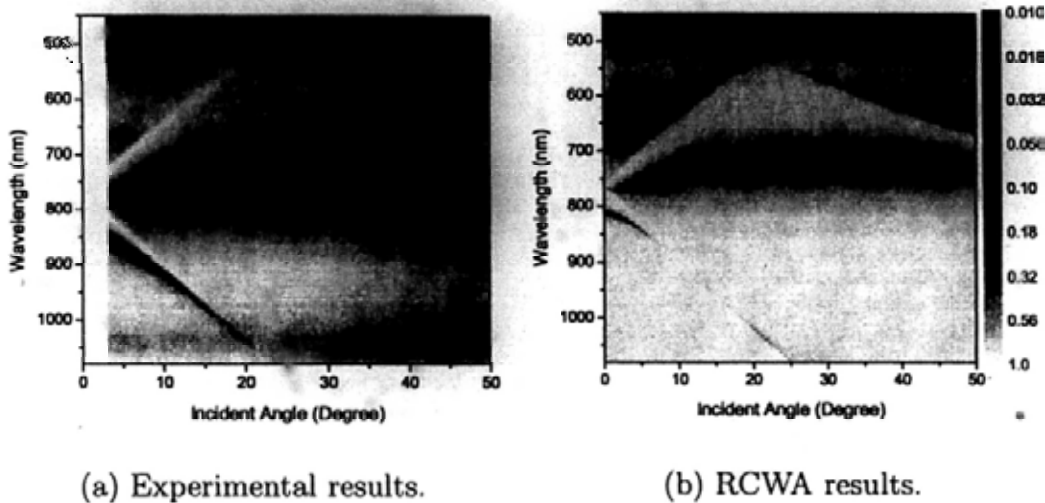
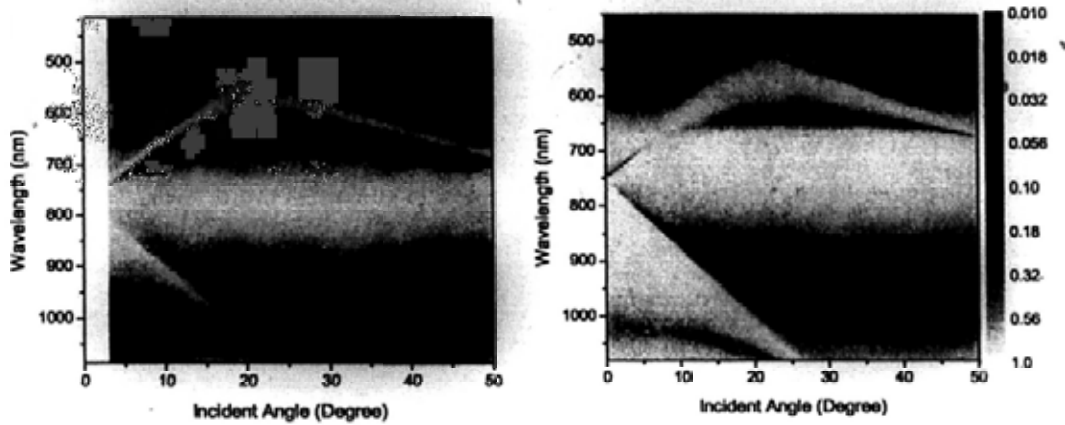


Figure 8.5: The zeroth order reflectance of Sample 1. Both experimental results (left panel) and results by RCWA (right panel) are shown.

We use RCWA to calculate numerically the zeroth order reflectance of the two samples, under TM polarization. The topological structures shown in Fig. 8.3 are used to model the two samples. The dielectric constant of gold is taken from Ref. [99]. The numerical results of the zeroth order reflectance are shown in Fig. 8.5(b) and 8.6(b) for Samples 1 and 2, respectively. The same color scale is used. The RCWA results are in good agreement with the experimental results. All main features of the experimental results are also found in the numerical results. Encouraged by the agreement, we proceed to study the optical properties of the two samples in greater detail. Our focus will be mainly on Sample 2, but results on Sample 1 will also be mentioned.

To look closer at the zeroth order reflectance of Sample 2, we re-plot Fig. 8.6 (b) in a more colorful way, as shown in Fig. 8.7, red for large reflectance



(a) Experimental results.

(b) RCWA results.

Figure 8.6: The zeroth order reflectance of Sample 2. Both experimental results (left panel) and results by RCWA (right panel) are shown.

and blue for low reflectance. The dispersion relations of the Wood's anomaly (dashed lines) and surface plasmon (solid lines) are drawn, after folding them into the first Brillouin Zone. The dispersion relation of the Wood's anomaly will be given in Sec. 8.3. To draw the SP dispersion relation, we take the grating surface as a semi-infinite metal surface. Thus, the dispersion relation is given by Eq.(6.50), i.e.,

$$k_{x0} + n \frac{2\pi}{L} = \frac{\omega}{c} \sqrt{\frac{\epsilon_m}{1 + \epsilon_m}}, \quad (8.1)$$

where k_{x0} is the x -component of the wavevector of the incident wave, n is an integer, and ϵ_m is the dielectric constant of gold. A set of four points, namely Point 1 – Point 4, are also indicated on Fig. 8.7. They are located on the low reflectance flat bands. In the following part, we will study the effect of Wood's anomaly, the surface plasmon, and the low reflectance flat bands.

8.3 Effects of the Wood's anomaly

When light of wavelength λ incident upon a reflection grating of period L at an angle θ , the light will be diffracted. Let k_{xn} be the x -component of the

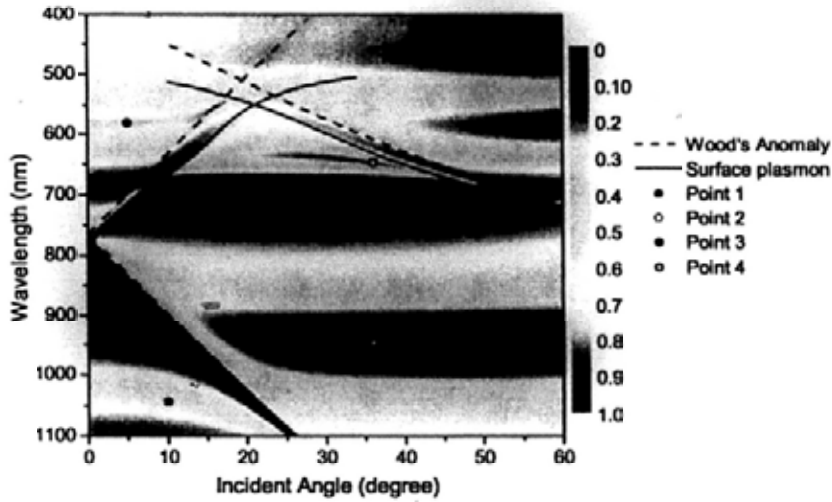


Figure 8.7: RCWA results of the zeroth order reflectance of Sample 2. The x axis is the incident angle and the y axis is the wavelength. Colors indicate the reflectance, with red for large reflectance and blue for low reflectance. The folded dispersion relations of the Wood's anomaly (dashed lines) and SP (solid lines) are shown. Four points, Point 1 – Point 4, are marked for studying the low reflectance flat bands.

wavevector of the n -th order diffracted wave, k_{zn} and k_{z0} are related by

$$k_{zn} = k_{z0} + n \frac{2\pi}{L} . \quad (8.2)$$

Notice that $k_{z0} = \frac{2\pi}{\lambda} \sin \theta$, and $k_{zn} = \frac{2\pi}{\lambda} \sin \theta'_n$, where θ'_n is the angle of reflection of the n -th order diffracted wave. Equation (8.2) can be rewritten as

$$\sin \theta'_n = \sin \theta + n \frac{\lambda}{L} . \quad (8.3)$$

When the condition

$$\sin \theta + n \frac{\lambda}{L} = \pm 1 \quad (8.4)$$

is satisfied, $\theta'_n = \pm 90^\circ$ and the diffracted wave becomes parallel to the grating surface. The energy carried by this order will be redistributed to other allowed diffraction orders. The redistribution of energy gives rise to a sudden

change in the diffraction efficiency of the other orders. This effect is called the Wood's anomaly [100]. Equation 8.4 gives the dispersion relation of the Wood's anomaly.

In Fig. 8.7, we observed that in most cases, the Wood's anomaly lines mark the boundaries between two different colors, meaning that there is a sudden change in the zeroth order reflectance when the Wood's anomaly occurs. Here, the diffraction efficiency of all allowed diffraction orders is measured so as to study the Wood's anomaly. Experimentally, a beam of Helium-Neon laser of wavelength 633 nm is used to measure the efficiency of the diffraction orders. The experimental set up is almost the same as that in Fig. 8.4. The main difference is that here a He-Ne laser is used as the light source. To measure the n -th order diffraction efficiency, the angle θ'_n is first calculated by using Eq.(8.3), and the rotating arm is then turned to the right angle, thus the efficiency can be measured.

The experimental results are shown in Fig. 8.8(a). The +1 order vanishes at about $\theta = 10^\circ$. The -2 order appears at about $\theta = 40^\circ$. These are the incident angles at which Wood's anomaly occurs. When Wood's anomaly occurs, the efficiencies of the 0th and -1 order change suddenly.

Numerically, the efficiency of the n -th diffraction order R_n can be calculated by RCWA,

$$R_n = \text{Re} \left(\frac{k_{zn}}{k_{z0}} \right) r_n^2, \quad (8.5)$$

where $k_{zn} = \sqrt{k^2 - k_{xn}^2}$ and r_n is the amplitude of the n -th order diffracted wave. Wood's anomaly occurs at $k_{zn} = 0$, thus $R_n = 0$. The RCWA results of Sample 2 are shown in Fig. 8.8(b), using the same wavelength as in the experimental results. Although the calculated magnitudes are not very close to the experimental results, the main features are almost the same. The disappearance of the +1 order and the appearance of the -2 order occur at the same incident angles as the experimental results. The occurrence of Wood's

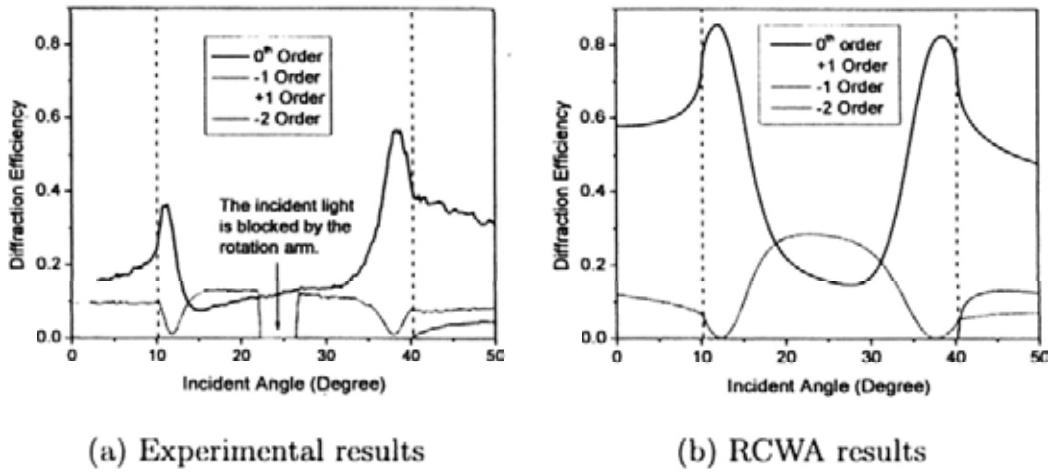


Figure 8.8: The efficiency of the 0th, +1, -1, and -2 diffraction orders for Sample 2, as a function of the incident angle. The incident wave has a wavelength of 633 nm, corresponding to a He-Ne laser. The left panel shows the experimental results, and the right panel shows the numerical results obtained by RCWA. The occurrences of the Wood's anomaly are marked by dashed vertical lines.

anomaly leads to a shoulder or kink in the efficiency of other orders.

8.4 Coupling between waveguide mode and SP mode

In this section, we carry out numerical studies on the low reflectance flat bands.

The algorithm of RCWA was introduced in Chapter 7. To use RCWA, we cut the system into layers, and solve the eigen modes of H_y in each layer. We can then write down the general solutions of the H and E fields in each layer. The coefficients are obtained by matching boundary conditions at the interfaces.

For our previous studies on the zeroth order reflectance and the Wood's anomaly, we only make use of the coefficients of the incoming and the diffracted fields in the space outside the grating (the first layer). Here, we make use of the coefficients in all layers, and obtain the near field map to show the field

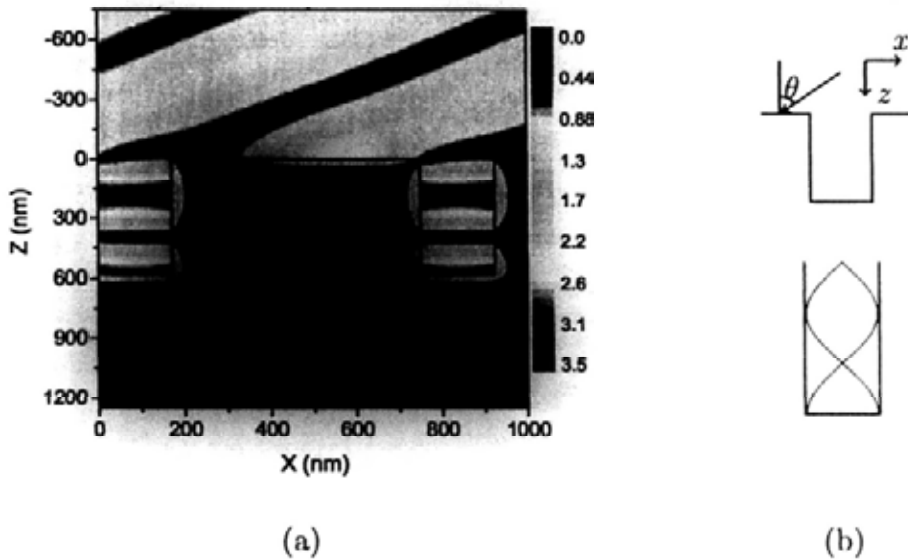


Figure 8.9: (a) The near field pattern of H_y at Point 2 in Fig. 8.7. (b) The upper panel shows the direction of the incident wave. The lower panel illustrates the sinusoidal pattern of the field inside the slit.

distribution inside and at the surface of the grating. For a given incident angle and wavelength, we divide the whole space into $5 \text{ nm} \times 5 \text{ nm}$ grids and compute the intensity of the H_y field at the centre of each grid. By plotting the intensity of H_y for all grids, we can obtain the near field pattern of H_y .

Let us first examine the near field pattern at Point 2 in Fig. 8.7, which has an incident angle of 36° and a wavelength of 947.5 nm . The near field map of H_y for Point 2 is shown in Fig. 8.9(a). In computing the near field pattern, we replaced the photoresist SU-8 by gold, since the gold layer is thicker than the skin depth. The intensity of the field is indicated by different colors, with red for large intensity and blue for small intensity. The black lines outline the structure of the grating. We are interested in the field distribution inside the slit. The field has a very large intensity at the bottom. As z increases, the intensity gradually decreases to zero and then increases again. At the open end, the intensity is small. This intensity distribution shows a sinusoidal

pattern of the field, which is characteristic of a standing wave. The wavelength is about $4/3$ of the slit depth, as illustrated in the lower panel of Fig. 8.9(b). The standing wave inside the slit can be understood as follows:

There is a dominating eigen mode inside the slit. Consider this mode propagating forward, and being reflected at the bottom. The superposition of the forward and backward propagating waves results in a standing wave. When the incident wave is in resonance with this eigen mode inside the slit, the energy is highly localized inside the slit, and the reflectance is low. We call the standing wave inside the slit a waveguide mode.

The above discussion is verified by the RCWA results. The RCWA results indicate that there is only one mode that can propagate along the z direction without significant loss, which is the dominating mode. For the H_y field inside the slit, the bottom is an antinode and the open end is a node, as illustrated in the lower panel of Fig. 8.9(b).

If the dominating eigen mode of the slit does not interact with the outside environment, the waveguide mode is independent of the incident angle, which results in a low reflectance flat band in the contour plot of the zeroth order reflectance. However, in both experimental and RCWA results (see Fig. 8.6), the low reflectance bands are not flat and are often separated by the SP dispersion relation lines. Here, we prove that the warp and separation are due to the interaction with SP modes.

Figure 8.10 shows the near field pattern of H_y at Point 1 in Fig. 8.7. Point 1 has an incident angle of 10° and a wavelength of 1044 nm. The wavelengths of Points 1 and 2 differ by about 100 nm, however, the intensity distribution of H_y inside the slit are quite similar. For both cases, the fields inside the slit show the character of a standing wave, with the wavelengths roughly equal $4/3$ of the slit depth. Thus, we can conclude that Points 1 and 2 belong to the same waveguide mode. The regions where these two points lie are related to the mixing of a flat waveguide mode and a dispersive SP mode. After mixing, these

two dispersion relations repel each other, resulting in a wavelength difference between Points 1 and 2.

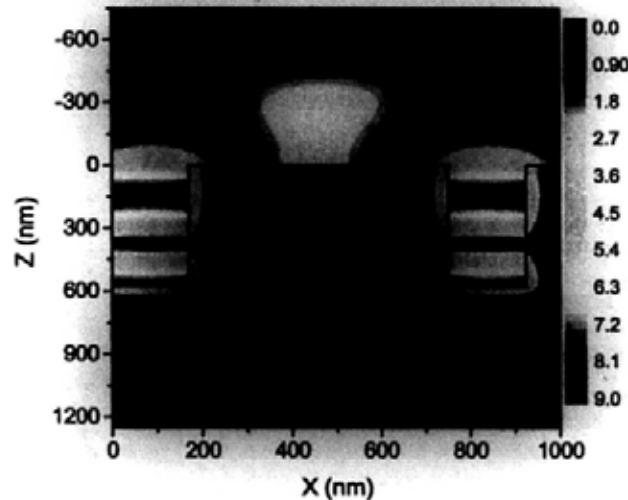


Figure 8.10: Near field pattern of H_y at Point 1 in Fig. 8.7.

Besides the waveguide mode for Points 1 and 2, there are three segments of flat band located at around $\lambda = 600$ nm, and they are separated by the SP dispersion relation lines. Points 3 and 4 in Fig. 8.7 are two points located on these segments. The coordinates of Points 3 and 4 are $(\theta = 5^\circ, \lambda = 580$ nm) and $(\theta = 36^\circ, \lambda = 646$ nm), respectively. Their wavelengths differ by 66 nm. The near field pattern of H_y at Points 3 and 4 are shown in Fig. 8.11. Similar to the previous results of Points 1 and 2, the standing waves inside the slits belong to the same waveguide mode, with the wavelength being roughly $4/5$ of the depth of the slit. Due to the mixing with the SP mode, this waveguide mode is separated into three parts and is no longer flat.

Sample 1 has a smaller slit depth as Sample 2. For the wavelength range under consideration, there is only one waveguide mode. We take a point with incident angle 38° and wavelength 721 nm to show the near field pattern. The intensity of the H_y field inside and at the surface of the grating is shown in Fig. 8.12. A standing wave with wavelength of about $4/3$ of the slit depth

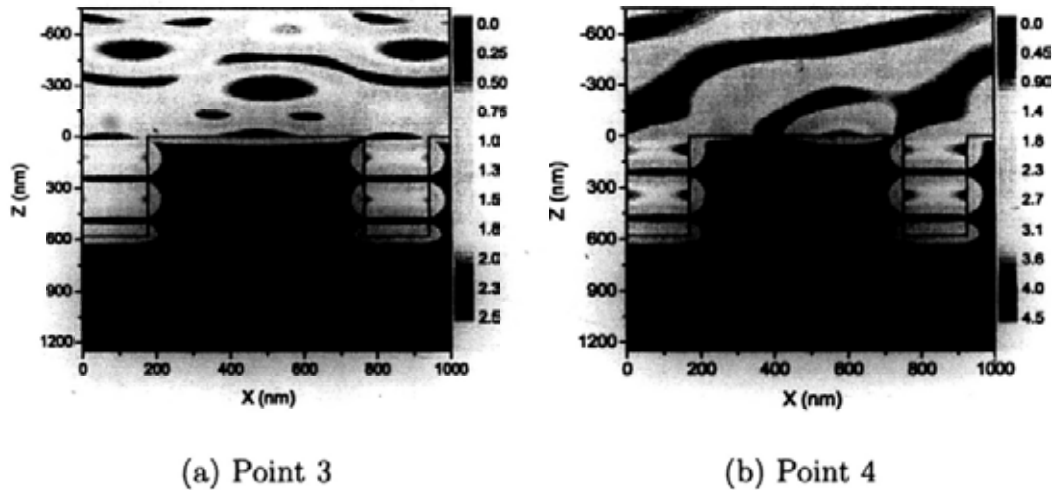


Figure 8.11: Near field pattern of H_y at Point 3 (left panel) and Point 4 (right panel) in Fig. 8.7.

is observed inside the slits. The waveguide mode also couples with the SP mode, and it shifts to the longer wavelength side at small incident angles (see Fig. 8.5).

8.5 Summary

In this chapter, we introduced the fabrication of one-dimensional metallic grating by using interference lithograph and sputtering techniques. We studied and measured the zeroth order reflectance of two samples. Results of numerical calculations are in good agreement with experimental data. The phenomena related to the Wood's anomaly are shown by measuring and calculating the efficiencies of all allowed diffraction orders. The near field pattern shows that the low reflectance flat bands are related to the excitation of waveguide modes. Both experimental and numerical results indicate a coupling between the waveguide mode and SP mode.

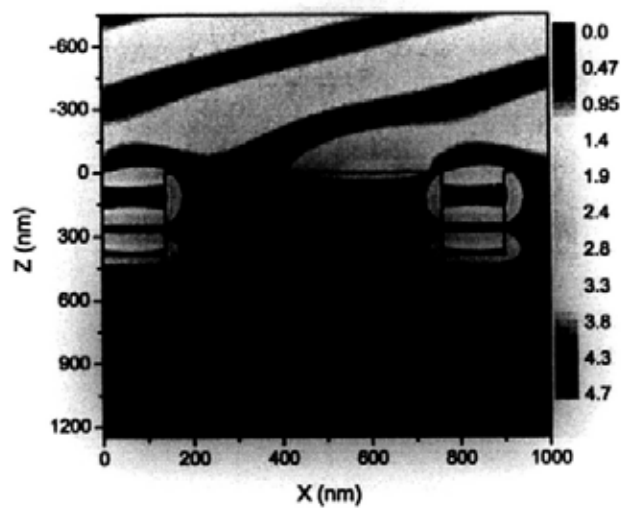


Figure 8.12: Near field pattern of H_y for Sample 1, at an incident angle of 38° and a wavelength of 721 nm.

Chapter 9

Controlling enhanced transmission through semiconductor gratings with subwavelength slits by a magnetic field

In this chapter, we exploit the change in the dielectric constant tensor of a conductor by a static magnetic field as a handle to control enhanced transmission in a semiconductor grating. Numerically, results of Rigorous Coupled-Wave Analysis (RCWA) incorporating the tensorial dielectric constant reveal that the zeroth-order transmission peaks at normal incidence can be shifted by about 15% to longer wavelengths and the peak values of transmission readily doubled when a moderate magnetic field is applied. Analytically, a single-mode theory incorporating anisotropy is developed and results are in quantitative agreement with RCWA, indicating that the tunability in the transmission stems from the waveguide mode. This chapter is based on Ref. [101].

9.1 Introduction

The phenomenon of enhanced transmission through patterned metallic films with subwavelength holes has triggered intensive research interest since its discovery [15]. The physical mechanism is generally regarded to be related to surface plasmon (SP) excitations [102], and the new area called plasmonics [19, 103] has flourished. The advancement has opened up exciting possibilities such as enhanced spectroscopy, high-resolution microscopy and sensing, and better light sources, just to name a few [19, 103, 104, 18]. Metallic gratings with subwavelength slits, in which the slits show periodicity in one dimension, show similar phenomena in transmission [96, 105, 106]. In addition to SP resonance, the one-dimensional structure allows waveguide resonance to play a crucial role in transmission through a thick metallic grating [105, 106, 107]. In this mechanism, the slits behave as open Fabry-Pérot resonant cavities that channel the incident electromagnetic (EM) waves through the grating [108, 109]. This mechanism is particularly important in metallic gratings in that there exists propagating waveguide mode with a vanishing cutoff frequency, while such a mode is absent in metallic films patterned with an array of holes. To make use of the enhanced transmission, it will be very useful if one can control the transmission through a grating *and* the frequencies at which the transmission peaks, without having to fabricate another grating using different slit widths, thicknesses, and/or different materials. There have been many attempts, and the main idea is to try to manipulate the dielectric constants in the system. For example, one could put an anisotropic material such as a liquid crystal into the slits [110] and tune the anisotropy and thus the dielectric constant tensor by aligning the directors by an external field [110, 111]. Enhanced transmission in the THz frequency range has also been observed in semiconductors patterned with an array of subwavelength holes [112, 113]. The dielectric constant of semiconductors depends on the carrier concentration through the bulk plasma

frequency and the transmission can be varied thermally [114, 113]. Similarly, in metallic gratings fabricated on a substrate of n -type GaAs, one can change the dielectric constant and thus the transmission by varying the doping in the substrate [115] and/or by varying a bias voltage [116, 117].

Here, we study the transmission of TM polarized EM wave through a semiconducting grating in the presence of a static magnetic field applied parallel to the slits. While most previous works introduce an anisotropic material into the slits, we exploit the anisotropy in the material forming the grating in the presence of a static magnetic field as a handle in controlling transmission. The physics is that the dielectric constant of a conductor becomes a *tensor* and thus anisotropic when a magnetic field is applied. For metals, the change in the dielectric constant by a magnetic field is tiny due to the dominance of the bulk plasma frequency over the cyclotron frequency. For semiconductors, the carrier concentration and the bulk plasma frequency are much lower than that in metals and a moderate magnetic field could lead to an appreciable change in the elements of the dielectric constant tensor. Accompanying with the use of semiconductor in the grating is that the frequency range of interest is shifted towards THz or lower, depending on the temperature and doping. Interestingly, this range is of great interest for civilian applications as well as those related to national security [118]. While the shift of the transmission peaks by a magnetic field in a semiconductor grating has recently been studied numerically by Hu *et al.* [119], these authors ignored the effects of damping and did not take full account of the tensorial nature of the dielectric constant, and thus they missed the effects of the magnetic field on the magnitude of transmission. In this chapter, we study the transmission both numerically and analytically. Using the method of Rigorous Coupled-wave Analysis (RCWA) generalized to treat media of tensorial dielectric constants, we show that both the transmission and the wavelengths at which the transmission peaks can be tuned over an appreciable range by a magnetic field of strength that is readily

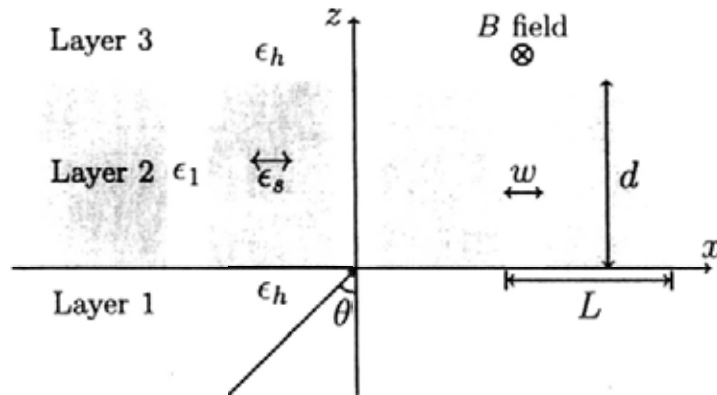


Figure 9.1: Schematic diagram showing a semiconductor grating of period L , thickness d , and slit width w . The tensorial dielectric constant is due to an external magnetic field $B_0\hat{y}$ applied in the direction parallel to the slits. The slits are filled with a medium with a scalar dielectric constant ϵ_1 and the media on both sides have scalar dielectric constants ϵ_h . Here, θ is the angle of incidence of a TM polarized electromagnetic wave.

attainable in a laboratory. Analytically, we explain the tunability in the transmission by developing a single-mode theory based on waveguide resonance and accounted for anisotropy.

9.2 The system and numerical results

Figure 9.1 shows schematically the system we propose to study. It consists of a semiconductor grating of thickness d , period L , and slit width w . The separation between adjacent slits is much larger than the skin depth in the relevant frequency range and the grating is thick in the sense that EM waves in the frequency range of interest cannot penetrate through. A static magnetic field $\mathbf{B} = B_0\hat{y}$ is applied to the grating in the direction parallel to the slits (see Fig. 9.1). The dielectric constants on both sides of the grating are assumed to be identical and taken to be a scalar ϵ_h and that inside the slit is a scalar

ϵ_{\perp} , both independent of B_0 . For a semiconductor, the charge carriers lead to a dielectric constant of the Drude form in the absence of a magnetic field [120]

$$\epsilon_{\parallel}(\omega) = \epsilon_{\infty} - \frac{\omega_p^2}{\omega(\omega + i\Gamma)}, \quad (9.1)$$

where ϵ_{∞} is the dielectric constant at high frequencies, ω_p is the plasma frequency and Γ is a damping constant. For $B_0 \neq 0$, the semiconductor develops a tensorial dielectric constant $\overleftrightarrow{\epsilon}_s$ given by [121, 90]:

$$\overleftrightarrow{\epsilon}_s(\omega) = \begin{pmatrix} \epsilon_{\infty} - \frac{\omega_p^2}{\omega^2 + i\Gamma\omega} \frac{1}{1-f^2} & 0 & -\frac{\omega_p^2}{\omega^2 + i\Gamma\omega} \frac{if}{1-f^2} \\ 0 & \epsilon_{\infty} - \frac{\omega_p^2}{\omega^2 + i\Gamma\omega} & 0 \\ \frac{\omega_p^2}{\omega^2 + i\Gamma\omega} \frac{if}{1-f^2} & 0 & \epsilon_{\infty} - \frac{\omega_p^2}{\omega^2 + i\Gamma\omega} \frac{1}{1-f^2} \end{pmatrix} \equiv \begin{pmatrix} \epsilon_{\perp} & 0 & -i\delta \\ 0 & \epsilon_{\parallel} & 0 \\ i\delta & 0 & \epsilon_{\perp} \end{pmatrix}, \quad (9.2)$$

where $f = \omega_c/(\omega + i\Gamma)$ with $\omega_c \equiv eB_0/m^*$ being the cyclotron frequency. Here, $-e$ and m^* are the electron charge and carrier effective mass, respectively. For tensorial dielectric constant takes on the form of $\overleftrightarrow{\epsilon}_s$, the independence of the TE and TM polarizations preserves. Here we are interested in the transmission of TM polarized EM waves. For a semiconductor, $\hbar\omega_p$ is typically 10^{-4} that of a metal and its value depends on the carrier concentrations and thus on doping and the temperature. This has the important consequence that a readily attainable B_0 (e.g., < 1 T) is sufficient to cause significant deviations of ϵ_{\perp} from ϵ_{\parallel} and δ from zero. This sensitivity of $\overleftrightarrow{\epsilon}_s$ on B_0 leads to a tunable transmission.

To illustrate the tunability and the enhancement in transmission in the presence of a moderate magnetic field, we calculate the transmission in an InSb grating using the exact method of RCWA generalized to treat anisotropic media [87, 90]. As a model system, we take $L = 2$ mm, $w = 0.2$ mm, and thickness $d = 4$ mm. The dielectric constant tensor of undoped InSb can be evaluated by the reported parameters [122]: $\epsilon_{\infty} = 15.68$, $\hbar\omega_p = 5.525 \times 10^{-3}$ eV, $\hbar\Gamma = 2.235 \times 10^{-4}$ eV. These values were obtained by detailed experiments

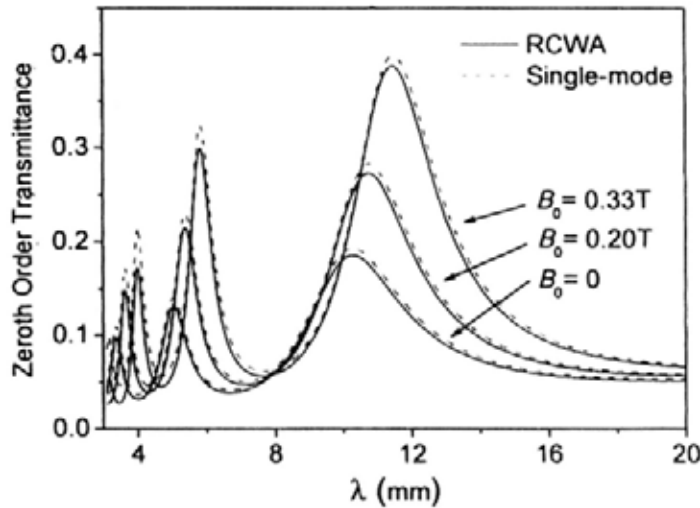


Figure 9.2: The zeroth order transmission at normal incidence as a function of incident wavelength for three different values of the magnetic field $B_0 = 0$, 0.20 T and 0.33 T. Results obtained by RCWA (solid lines) and single-mode theory (Eq.(9.45)) (dashed lines) are shown for comparison.

at a temperature of 80 K. We assume the media on the two sides of the grating and in the slit are identical with $\epsilon_h = \epsilon_l = 1$. For incident wavelengths in vacuum that range from $\lambda = 3$ mm to 20 mm, which are larger than the slit width, the corresponding frequencies are slightly below the THz range. Figure 9.2 shows the zeroth order transmission T_0 at normal incidence as a function of the wavelength, for $B_0 = 0$ T, 0.20 T and 0.33 T. The key features are:

- There are three transmission peaks in the range of λ considered.
- As B_0 increases, each peak shifts to longer wavelength and the peak value of T_0 increases.
- The shifts and enhancements are both substantial with $\Delta\lambda \sim 11\%$ to 19% of the wavelength that T_0 peaks at $B_0 = 0$ and the peak values of T_0 could readily be doubled by a moderate B_0 .

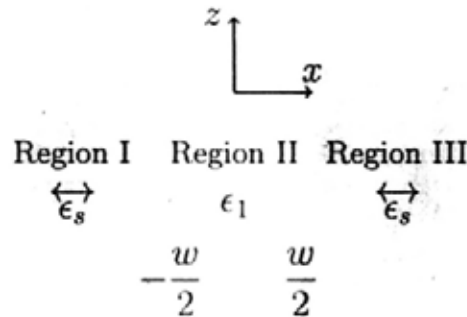


Figure 9.3: A zoom-in picture of a slit. Regions I and III are semiconductor. The two regions are separated by a slit (Region II) that occupies $-w/2 < x < w/2$.

Our system thus provides a simple way to control both the magnitude and wavelength of peak transmissions. We have checked that at room temperature, for which the dielectric constant tensor of InSb can be estimated [113], these key features persist and the frequency range shifts into the THz range.

9.3 Single mode approximation

The features of the RCWA results are tractable analytically, by developing a single-mode theory. The single-mode theory assumes that the field inside the slit is sufficiently well described by the fundamental mode. This assumption is valid if there is only one nonevanescant propagating mode in the slit [123]. We will show the analytic approach in this section.

9.3.1 The propagating mode inside the slits

To find the eigen mode of the propagation mode in the slit, we only need to consider one period of the grating with the slit centered at $x = 0$. The two adjacent semiconductor blocks (Regions I and III) are separated by a slit (Region II) that occupies $-w/2 < x < w/2$. Figure 9.3 shows the pattern

schematically.

For TM polarized wave, the \mathbf{H} and \mathbf{E} fields in each region can in general be written as

$$\begin{aligned} \mathbf{H}^{(j)}(\mathbf{r}, t) &= H_y^{(j)} \hat{y} \exp[i(k\alpha_j x + k\gamma_j z) - i\omega t], \\ \mathbf{E}^{(j)}(\mathbf{r}, t) &= (E_x^{(j)} \hat{x} + E_z^{(j)} \hat{z}) \exp[i(k\alpha_j x + k\gamma_j z) - i\omega t], \end{aligned} \quad (9.3)$$

with $j = 1, 2$, and 3 denoting Regions I, II and III. $k = 2\pi/\lambda$ is the wavevector in vacuum, $k\alpha_j$ and $k\gamma_j$ are the x and z components of k in Region j . The H_y field should be continuous at the two interfaces for any z , which requires the z -component of the wavevector to be the same in the three regions, $\gamma_j = \gamma$ for $j = 1, 2$, and 3 .

In Regions I and III, by substituting Eqs. (9.2) and (9.3) into the Maxwell's equations Eqs. (7.1) and (7.2), the relations between H_y , E_x , and E_z can be written in a matrix form

$$\begin{pmatrix} \gamma & -\epsilon_{\perp} & i\delta \\ \alpha & i\delta & \epsilon_{\perp} \\ 1 & -\gamma & \alpha \end{pmatrix} \begin{pmatrix} H_y \\ E_x \\ E_z \end{pmatrix} = 0. \quad (9.4)$$

To get a non-trivial solution, the determinant of the above matrix should be zero, thus

$$\alpha_{1,3}^{\pm} = \pm \sqrt{\frac{\epsilon_{\perp}(\epsilon_{\perp} - \gamma^2) - \delta^2}{\epsilon_{\perp}}}. \quad (9.5)$$

Following a similarly procedure, for Region II,

$$\alpha_2^{\pm} = \pm \sqrt{\epsilon_{\perp} - \gamma^2}. \quad (9.6)$$

The square roots of Eqs. (9.5) and (9.6) are chosen to give a positive imaginary part.

The relation between E_z and H_y in Regions I and III can be extracted from Eq.(9.4) as

$$\begin{pmatrix} \epsilon_{\perp} & -i\delta \\ i\delta & \epsilon_{\perp} \end{pmatrix} \begin{pmatrix} E_x \\ E_z \end{pmatrix} = \begin{pmatrix} \gamma H_y \\ -\alpha_{1,3}^{\pm} H_y \end{pmatrix}. \quad (9.7)$$

Thus for Regions I and III

$$\begin{aligned} E_z &= -\frac{i\delta\gamma \pm \sqrt{\epsilon_1^2(\epsilon_\perp - \gamma^2) - \epsilon_\perp\delta^2}}{\epsilon_1^2 - \delta^2} H_y \\ &= (Z_1 \pm Z_2)H_y, \end{aligned} \quad (9.8)$$

where $Z_1 = -\frac{i\delta\gamma}{\epsilon_1^2 - \delta^2}$, and $Z_2 = -\frac{\sqrt{\epsilon_1^2(\epsilon_\perp - \gamma^2) - \epsilon_\perp\delta^2}}{\epsilon_1^2 - \delta^2}$. Similarly, for Region II,

$$\begin{aligned} E_z &= -\frac{\alpha_2^\pm}{\epsilon_1} H_y \\ &= \pm Z_3 H_y, \end{aligned} \quad (9.9)$$

where $Z_3 = -\frac{\sqrt{\epsilon_1 - \gamma^2}}{\epsilon_1}$.

Now we can write down the general forms of the H_y and E_z fields in each region. In Region II,

$$H_y^{(2)}(x, z) = [Ce^{i\alpha_2^+ x} + De^{i\alpha_2^- x}]e^{ik\gamma z}. \quad (9.10)$$

$$E_z^{(2)}(x, z) = Z_3[Ce^{i\alpha_2^+ x} - De^{i\alpha_2^- x}]e^{ik\gamma z}. \quad (9.11)$$

In Regions I and III, the fields decay into the semiconductor from the interfaces.

For Region I with $x < -w/2$,

$$H_y^{(1)}(x, z) = Ae^{i\alpha_1^-(x+w/2)}e^{ik\gamma z}, \quad (9.12)$$

$$E_z^{(1)}(x, z) = (Z_1 - Z_2)Ae^{i\alpha_1^-(x+w/2)}e^{ik\gamma z}. \quad (9.13)$$

For Region III with $x > w/2$,

$$H_y^{(3)}(x, z) = Fe^{i\alpha_3^+(x-w/2)}e^{ik\gamma z}, \quad (9.14)$$

$$E_z^{(3)}(x, z) = (Z_1 + Z_2)Fe^{i\alpha_3^+(x-w/2)}e^{ik\gamma z}. \quad (9.15)$$

The boundary conditions require that the tangential components H_y and E_z be continuous at the interfaces. Matching boundary conditions at $x = -w/2$ gives

$$A = Ce^{-i\alpha_2^+ w/2} + De^{-i\alpha_2^- w/2}, \quad (9.16)$$

$$(Z_1 - Z_2)A = Z_3(Ce^{-i\alpha_2^+ w/2} - De^{-i\alpha_2^- w/2}). \quad (9.17)$$

At $x = w/2$, we have

$$F = Ce^{ik\alpha_2^+ w/2} + De^{ik\alpha_2^- w/2}, \quad (9.18)$$

$$(Z_1 + Z_2)F = Z_3(Ce^{ik\alpha_2^+ w/2} - De^{ik\alpha_2^- w/2}). \quad (9.19)$$

Combining Eqs. (9.16)–(9.19) and using the fact that $\alpha_2^- = -\alpha_2^+$ we get

$$(Z_1 - Z_2 - Z_3)\Phi^- C = -(Z_1 - Z_2 + Z_3)\Phi^+ D, \quad (9.20)$$

$$(Z_1 + Z_2 - Z_3)\Phi^+ C = -(Z_1 + Z_2 + Z_3)\Phi^- D, \quad (9.21)$$

where $\Phi^\pm = e^{ik\alpha_2^\pm w/2}$. By eliminating C and D , we obtain a transcendental equation for the propagation constant γ ,

$$i \tan(k\alpha_2^+ w) = \frac{\Phi^{+2} - \Phi^{-2}}{\Phi^{+2} + \Phi^{-2}} = \frac{2Z_2Z_3}{Z_1^2 - Z_2^2 - Z_3^2}. \quad (9.22)$$

The exact form is

$$i \tan(k\sqrt{\epsilon_\perp - \gamma^2} w) = \frac{2\epsilon_\perp \sqrt{\epsilon_\perp - \gamma^2} \sqrt{\epsilon_\perp [\epsilon_\perp (\epsilon_\perp - \gamma^2) - \delta^2]}}{\gamma^2 (\epsilon_\perp^2 + \epsilon_\perp - \delta^2) - \epsilon_\perp (\epsilon_\perp^2 + \epsilon_\perp \epsilon_\perp - \delta^2)}. \quad (9.23)$$

Note that ϵ_\perp and δ depend on B_0 through ω_c , and γ can thus be tuned by B_0 . To test our single-mode approach, we compare the complex γ obtained by numerically solving Eq.(9.23) (dotted lines) and by the exact RCWA (solid lines) for a range of λ and three values of B_0 in Fig. 9.4. The results are in excellent agreement, implying that our single-mode theory captures the essential physics.

9.3.2 The zeroth order transmittance

We proceed to obtain an analytic expression for the transmittance.

The general solutions of the \mathbf{H} field in Layers 1 and 3 (see Fig. 9.1) can be expressed as Rayleigh expansions,

$$\begin{aligned} H_y^{(1)}(x, z) &= \sum_n [\delta_{n0} \exp(ik_{zn}x + ik_{zn}z) + r_n \exp(ik_{zn}x - ik_{zn}z)], \\ H_y^{(3)}(x, z) &= \sum_n t_n \exp[ik_{zn}x + ik_{zn}(z - d)], \end{aligned} \quad (9.24)$$

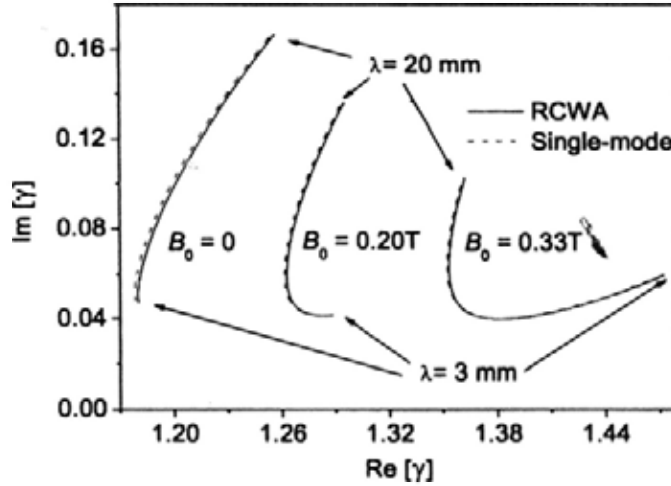


Figure 9.4: Real and imaginary parts of the propagation constant γ for incident wavelengths from 3 mm to 20 mm and $B_0 = 0, 0.20$ T and 0.33 T. Results obtained by RCWA (solid lines) and single-mode theory (Eq.(9.23)) (dashed lines) are shown for comparison.

where r_n (t_n) is the n -th order reflectance (transmittance) coefficient. The n -th order x and z components of the wavevector are $k_{xn} = k\sqrt{\epsilon_h} \sin \theta + \frac{2\pi n}{L}$, and $k_{zn} = \sqrt{k^2 \epsilon_h - k_{xn}^2} = k\sqrt{\epsilon_h - (\sqrt{\epsilon_h} \sin \theta + \frac{n\lambda}{L})^2}$.

For Layer 2, we consider the fundamental mode only. The z -component of the wavevector $k'_z = k\gamma$, with the coefficient γ solved from Eq.(9.23). The x -component of the wavevector is $k'_x = \sqrt{\epsilon_1 - k_z'^2}$. The general form of the **H**-field inside the slit is

$$H_y^{(2)}(x, z) = A^+ \exp(ik'_x x + ik'_z z) + A^- \exp[-ik'_x x - ik'_z(z - d)] . \quad (9.25)$$

The general form of the E_x field in each layer can also be written down

$$E_x^{(1)}(x, z) = \sum_n \frac{k_{zn}}{k\epsilon_h} [\delta_{n0} \exp(ik_{zn}x + ik_{zn}z) - r_n \exp(ik_{zn}x - ik_{zn}z)] ,$$

$$E_x^{(2)}(x, z) = \frac{k'_z}{k\epsilon_1} [A^+ \exp(ik'_x x + ik'_z z) - A^- \exp(-ik'_x x - ik'_z(z - d))] , \quad (9.26)$$

$$E_x^{(3)}(x, z) = \sum_n \frac{k_{zn}}{k\epsilon_h} t_n \exp[ik_{zn}x + ik_{zn}(z - d)] .$$

The transmittance and reflectance can be obtained by matching boundary conditions. The procedure is quite standard, here we mainly follow Ref. [90].

The boundary conditions are that E_x and H_y are continuous at the $z = 0$ and $z = d$ interfaces. The semiconductor surface can be treated as perfect conductor, thus E_x should be zero at the semiconductor surface.

Let the E_x field be continuous at $z = 0$, which leads to

$$\sum_n \frac{k_{zn}}{k\epsilon_h} (\delta_{n0} - r_n) e^{ik_{zn}x} = \begin{cases} \frac{k'_z}{k\epsilon_1} (A^+ e^{ik'_z x} - \Phi A^- e^{-ik'_z x}), & |x| < \frac{w}{2}, \\ 0, & \frac{w}{2} \leq |x| < \frac{L}{2}, \end{cases} \quad (9.27)$$

where $\Phi = \exp(ik'_z d)$. Multiplying both sides by $\exp(-ik_{zm}x)$ and integrating over a period from $x = -L/2$ to $L/2$, the equation becomes

$$\delta_{m0} - r_m = Z_m [A^+ S(-k_{zm} + k'_z) - \Phi A^- S(-k_{zm} - k'_z)], \quad (9.28)$$

where

$$Z_m = \frac{w}{L} \frac{k'_z \epsilon_h}{k_{zm} \epsilon_1}, \quad (9.29)$$

and

$$S(s) = \frac{1}{w} \int_{-\frac{w}{2}}^{\frac{w}{2}} e^{isx} dx = \frac{2}{sw} \sin\left(\frac{sw}{2}\right). \quad (9.30)$$

Following a similar procedure, the continuity of E_x at the upper interface $z = d$ leads to

$$t_m = Z_m [\Phi A^+ S(-k_{zm} + k'_z) - A^- S(-k_{zm} - k'_z)]. \quad (9.31)$$

If the summations in Eqs. (9.24) and (9.26) are taken to sum over a finite range $n = -N, \dots, 0, \dots, N$, then there are a total of $4N + 4$ unknowns: A^+ , A^- , and $2N + 1$ for each of t_n and r_n . Equations (9.28) and (9.31) represent $4N + 2$ conditions. To solve the problem, we need two more conditions, which can be obtained by considering the continuity of H_y at the two interfaces. At $z = 0$ and $-w/2 < x < w/2$,

$$\sum_n (\delta_{n0} + r_n) e^{ik_{zn}x} = A^+ e^{ik'_z x} + \Phi A^- e^{-ik'_z x}. \quad (9.32)$$

By expressing the functions at both sides in Fourier series over the domain $-w/2 < x < w/2$, and requiring each of the components of the two functions to be matched, we get

$$\begin{aligned} \frac{1}{w} \int_{-\frac{w}{2}}^{\frac{w}{2}} dx e^{-im2\pi x/w} \sum_n (\delta_{n0} + r_n) e^{ik_{xn}x} \\ = \frac{1}{w} \int_{-\frac{w}{2}}^{\frac{w}{2}} dx e^{-im2\pi x/w} \left[A^+ e^{ik'_x x} + \Phi A^- e^{-ik'_x x} \right]. \end{aligned} \quad (9.33)$$

We only need one condition for this interface, so we take the $m = 0$ component only, i.e.,

$$\sum_n (\delta_{n0} + r_n) S(k_{xn}) = A^+ S(k'_x) + \Phi A^- S(-k'_x). \quad (9.34)$$

Applying the same argument on the $z = d$ interface, the continuity of H_y leads to

$$\sum_n t_n S(k_{xn}) = \Phi A^+ S(k'_x) + A^- S(-k'_x). \quad (9.35)$$

Equations (9.28), (9.31), (9.34), and (9.35) provide all the conditions required to solve the $4N + 4$ unknowns.

For convenience, we define

$$q_n^\pm = Z_n S(k_{xn}) S(-k_{xn} \pm k'_x) / S(\pm k'_x), \quad (9.36)$$

and

$$p^\pm = \sum_n q_n^\pm. \quad (9.37)$$

Summing of both sides of Eq.(9.28) over m , we get

$$\sum_m (\delta_{m0} - r_m) S(k_{xm}) = A^+ S(k'_x) p^+ - \Phi A^- S(-k'_x) p^-. \quad (9.38)$$

Comparing this equation with Eq.(9.34), the r_m term can be eliminated, i.e.,

$$A^+ S(k'_x) (1 + p^+) + \Phi A^- S(-k'_x) (1 - p^-) = 2S(k_{x0}). \quad (9.39)$$

Similarly, by combining Eqs. (9.31) and (9.35), we have

$$\Phi A^+ S(k'_x) (1 - p^+) + A^- S(-k'_x) (1 + p^-) = 0. \quad (9.40)$$

The coefficients A^+ and A^- can be solved by using Eqs. (9.39) and (9.40),

$$A^+ = \frac{2(1+p^-)S(k_{x0})}{[(1+p^+)(1+p^-) - (1-p^+)(1-p^-)\Phi^2]S(k'_x)}, \quad (9.41)$$

$$A^- = \frac{2(p^+ - 1)S(k_{x0})\Phi}{[(1+p^+)(1+p^-) - (1-p^+)(1-p^-)\Phi^2]S(-k'_x)}. \quad (9.42)$$

Using Eq.(9.31), the zeroth order transmission coefficient t_0 is found to be

$$t_0 = \frac{2\Phi[q_0^+(1+p^-) + q_0^-(1-p^+)]}{(1+p^+)(1+p^-) - (1-p^+)(1-p^-)\Phi^2}, \quad (9.43)$$

For the system we concerned, $w \ll \lambda$, thus it is reasonable to make the approximation that $k'_x w \sim 0$. Under this approximation, $q_n^+ = q_n^- = q_n$ and $p^+ = p^- = p$, Eq.(9.43) becomes

$$t_0 = \frac{4q_0 \exp(ik\gamma d)}{(1+p)^2 - (1-p)^2 \exp(2ik\gamma d)}, \quad (9.44)$$

where $p = \sum_n q_n$ and $q_n = \frac{\epsilon_h w \gamma \operatorname{sinc}^2[kw(\sqrt{\epsilon_h} \sin \theta + n\frac{\lambda}{L})/2]}{\epsilon_1 L \sqrt{\epsilon_h - (\sqrt{\epsilon_h} \sin \theta + n\frac{\lambda}{L})^2}}$, with $\operatorname{sinc}(x) = \sin(x)/x$.

The zeroth order transmission efficiency is

$$T_0 = \left| \frac{4q_0 \exp(ik\gamma d)}{(1+p)^2 - (1-p)^2 \exp(2ik\gamma d)} \right|^2. \quad (9.45)$$

The results of $T_0(\lambda)$ calculated from Eq.(9.45) are also shown in Fig. 9.2. They agree very well with RCWA results, except for a slight overestimation at short wavelengths. The theory captures both the shifts and enhancements in the transmittance peaks. From Eq.(9.45), the positions (wavelengths) of the peaks can be estimated by the Fabry-Pérot condition

$$2\operatorname{Arg} \left(\frac{1-p}{1+p} \right) + 2k\operatorname{Re}[\gamma]d = 2n\pi, \quad (9.46)$$

where n is an integer. As B_0 increases, p and γ vary and the peaks shift. By numerical calculations using Eq.(9.45) on our model system for B_0 increases from 0 to 0.33 T, the values of T_0 are found to enhance by 92% to 132% for the three peaks and the shifts in the wavelength of the peaks $\Delta\lambda/\lambda$ range

from 11% to 19%. These values agree well with RCWA results and show that the transmittance can be significantly controlled by varying B_0 over a range accessible in laboratories.

9.4 Summary

In summary, we studied a semiconductor grating with a static magnetic field applied parallel to the slits both numerically and analytically. Incorporating the tensorial dielectric constant of the grating material and damping in RCWA calculations, the transmission and the wavelengths at which the transmission peaks show significant changes when a moderate magnetic field is applied. A single-mode theory that incorporates the anisotropy in the grating material was developed and results on the propagation constant and transmittance were in good agreement with RCWA results, indicating that the tunability in transmission stems from the waveguide mode. The properties of tunability and analytically tractable make the system useful for designing devices that rely on controlling EM wave transmission near the THz range.

Chapter 10

Summary

This thesis contains two independent parts. The first part (Chapters 1–5) focuses on the emergence of cooperative behavior in networked entities. The second part (Chapters 6–9) focuses on the optical properties of one-dimensional metallic gratings.

To provide the necessary backgrounds for the first part, we reviewed the basic properties of evolutionary games and networks. We introduced the general properties of two-strategy games, including fitness, Nash equilibrium, and evolutionarily stable strategy. We then reviewed the two most studied two-strategy games — the prisoner’s dilemma (PD) and the snowdrift game (SG). For networks, we introduced the concepts of several important properties, including the degree distribution, the clustering coefficient and the shortest path length. The random graph and the Barabási-Albert scale-free network are then reviewed.

We studied the infinitely iterative prisoner’s dilemmas in the full payoff space. It was found that the existence of a Tit-for-tat-like strategy E_{TFT} and an Always-defecting-like strategy E_{AUD} are crucial for the system to evolve to a state that is dominated by generous strategies at equilibrium. By carrying out detailed numerical and analytical investigations, the roles played by E_{TFT} and E_{AUD} were examined. The strategy E_{AUD} could replace many strategies

for any payoff value. However, for a large range of payoff values, it can be easily taken over by E_{TFT} . This process leads to the dominance of generous strategies at these payoff values.

We then studied the snowdrift game, which is regarded as an important alternative to PD. Previous studies found that there are phase transitions in the spatial snowdrift game. We explained the phase transitions by invoking the idea of comparing the payoffs to C and D players in the last surviving patterns. We should notice that phase transitions are common for SG-like games played on network structures. Thus, the idea we developed here can be extended to future studies on the emergent behavior in other games.

Previous studies on the evolutionary games were mainly focus on two-strategy games. However, examples of multi-agent interactions are abundant in reality. To model these interactions, we proposed the N -person snowdrift game (NPSG), which is a multi-person version of the classical two-person SG. The NPSG played in a well-mixed population was studied both analytically and numerically. We then studied NPSG on lattices numerically. Compared with the well-mixed case, the cooperation frequency is suppressed when NPSG is played on lattices. We developed an analytic theory by focusing on the local configurations consisting of a central site and its nearest neighbors. The theory works well for 1D chain, and discrepancies are found in higher dimensions, suggesting that a theory that includes larger spatial correlation is needed.

Until here, the games are played on static networks, i.e., the network structure remains unchanged as the game dynamics evolves. In many real systems, the relation between agents often co-evolves with the interactions between them. Inspired by this fact, we used the snowdrift game as a tool to study the co-evolving of networks and game dynamics. A model was proposed. By carrying out numerical simulations, it was found that the frequency of cooperation is promoted, compared with SG played on static networks with the same mean degree. A semi-analytic approach was then proposed, with the

results in qualitative agreement with simulation results.

The second part focuses mainly on studying the optical properties of metallic and semiconducting gratings. We first studied the surface plasmon (SP) dispersion relations in a system consisting of a thin metallic film sandwiched between a linear dielectric and a nonlinear dielectric. Exact expressions were derived, and the dependence of the SP dispersion relations on film thicknesses and nonlinearity were discussed. The main idea here is that we can change the dielectric constant of a nonlinear medium, and thus the SP dispersion relations, by tuning the strength of the electric field at the metal/nonlinear dielectric interface. We also studied the SP dispersion relations in a system consists of a thin metallic film in a symmetric nonlinear dielectric environment.

The Wood's anomaly, surface plasmon excitation and waveguide modes are characteristic features of one-dimensional reflection gratings under TM polarization. These effects were studied on two grating samples, using the Rigorous Coupled-Wave Analysis (RCWA) method. The phenomenon of Wood's anomaly was studied by measuring and computing the diffraction efficiency of different orders. The factors related to the existence of waveguide modes were studied by near-field patterns. Coupling between waveguide modes and SP excitations was also observed.

We also carried out numerical and theoretical studies on controllable enhanced transmission in semiconductor gratings. Incorporating the tensorial dielectric constant of a semiconductor in the presence of a magnetic field into RCWA calculations, we found that the transmission peaks can shift to longer wavelengths and the peak values of transmission can be largely enhanced when a moderate magnetic field is applied parallel to the slits. Moreover, this effect can be analytically studied by developing a single-mode theory. The properties of tunability and analytically tractable make the system useful for designing devices that rely on controlling EM wave transmission near the THz range.

Appendix A

Development of Friendship Network Among Young Scientists in an International Summer School

A total of 49 students, about half of them male, from various countries and 4 student helpers attended the 2008 China Complex Systems Summer School organized by the Santa Fe Institute and the Chinese Academy of Sciences held in Beijing. We studied the development of the social network among these participants during the School, which lasted for 4 weeks, by carrying out surveys at different times of the School. The students got to know each other through various activities, including being roommates, eating together everyday, attending lectures, doing group projects, sight-seeing visits, etc. The topological structures and various properties of the network are discussed. The results indicate how the participants became friends as time went by. By considering the correlations between reciprocal evaluations via the Pearson's correlation coefficient, it is found that the ethnicity and gender are important factors in establishing personal relationships and in getting mutually consistent perceptions on the relationships. We also study the clique components and community structures

in the networks. This work has been published in Ref. [124].

A.1 Introduction

There has been much interest in studying the formation and development of social networks in the real world [1, 23]. As early as the 1920's and 30's, Moreno studied the formation of acquaintance groups [125]. Other studies on various kinds of social networks then followed, among them the most well-known is probably the experiment revealing the "Six Degrees of Separation" carried out by Milgram in 1965 [5]. In this pioneering study in experimental social sciences, the participants were asked to pass a letter to an assigned targeted person in Boston by forwarding it to one of their acquaintances whom they thought would be closer to the addressee. One should, however, note that in the early days, information regarding social networks was usually gathered by surveys. With the availability of large databases in recent years, studies on large social networks have been carried out without doing surveys, e.g., the network on collaborations among scientists [126] and among workers in the film industry [26], and friendship networks in schools [127, 128, 129]. Alongside the studies on social networks are the extensive works on the nonsocial networks revealed in the contexts of information science [130, 4, 131, 8], and in biological systems [7]. The degree correlation of these two types of networks has been discussed [132]. These works have led to the developments in techniques in analyzing complex networks. For example, algorithms [133, 134, 135, 136] were developed to look for the communities or sub-structures in social and biological networks.

In the present work, we study the formation and development of the friendship network among the student participants and student helpers in the Santa

Fe Complex Systems Summer School 2008 held in Beijing, China. They comprise a group of young students in science and engineering from different countries, and they have different mother tongues. They got to know each other through various activities during the school. In three surveys carried out at different times in the school, participants were asked to indicate how well they knew each other. From the data, we study the change in the friendship network as time proceeds, the correlation of the evaluations between two participants, and the community structures. It is found that the ethnicity, probably due to convenience in communications in terms of languages, and gender are important factors in friendship network formation among the participants. We also use the data to explore the community structure in the network and how it changes with time.

A.2 The surveyed group in Santa Fe CSSS2008

The 2008 China Complex Systems Summer School (CSSS2008) was co-sponsored by the Santa Fe Institute and the Institute of Theoretical Physics at the Chinese Academy of Sciences. It was held in Beijing between 30 June and 25 July 2008. The School enrolled 49 students, among them 26 students are of Chinese nationality (14 males, 12 females) and 23 are “foreign” students (11 males, 12 females). The word “foreign” is used here with reference to the venue of the School and thus participants with non-Chinese nationality are counted as “foreign”. Most Chinese students attended a one-week English training course prior to the commencement of the school. Thus, those who attended the English training course met each other slightly earlier than they met the other participants. Among the 23 foreign students, about half of them came from the USA and the others were from Argentina, South Korea, India, Singapore and countries in the European Union. During the school, two students were assigned to one dormitory room, with one student from mainland

China and one from overseas. In addition, there were four student helpers from the Institute of Theoretical Physics at the Chinese Academy of Sciences. They lived and studied together with the participants during the workshop. The participants and the student helpers attended 5 hours of lectures per day and had meals together. The participants were required to carry out project work in groups of 3 to 7 students, and a group was designed to include both students from mainland China and elsewhere. Members in the same group had dinner together off-campus twice a week. Participants could also take part in various social activities in spare time, e.g., dancing and traveling. Most participants did not know each other before the school. Their personal relations were developed during the four weeks in the School. It makes the Summer School a well defined system for investigating the development and evolution of friendship among a group of young science and engineering students.

We collected the data on friendship among the participants and student helpers by carrying out three surveys at different times of the workshop. The first survey was conducted in the second week (6-11 July), the second survey during 13-18 July, and the third survey on the last day (25 July) of the School. Since one student was ill in the first week, the student was excluded from the survey. This left us with 52 names, 48 students and 4 student helpers, on the questionnaire. Each of the 52 informants was asked to evaluate how well he/she got to know the other participants, by using a 5-level ranking from "very unfamiliar" (1) to "very familiar" (5). We intentionally did not define a descriptor of each level, both because it is difficult to give a precise definition and friendship is most likely something of personal judgment. For each survey, we were able to receive 40-50 completed questionnaires. For someone who did not respond, the response on him/her by other participants was used as his/her response. For simplicity in displaying the network, we convert the data into undirected unweighted networks in the following discussion. It should be noted that the data actually allows us to construct networks with directed

links. Here, we will use the data to study the correlation between reciprocal evaluations, i.e., how close two participants rank each other's friendship.

A.3 Basic properties of the networks

To construct a network from the data, we use vertices (nodes) to represent the participants and links to represent an established friendship between two participants. Consider two nodes i and j . We define the establishment of a link as follows. A link is established when participant i (j) chose "very familiar" in his/her response towards participant j (i) and at the same time the participant j (i) chose either "very familiar" or "familiar" in his/her response towards i (j). In this way, a network is constructed from the data of each survey. The networks so formed in the three surveys are called Network 1, 2, and 3, respectively. Figure A.1 shows the topology of the three networks. The nodes are fixed in space in order to show the development of the three networks clearly. From the data, we have also calculated the average degree, the clustering coefficient, the average shortest path length and the diameter of the networks at different times. Results for these basic network properties are shown in Table A.1. These properties of the randomized version of the three networks are also listed for comparison. The randomized networks are constructed by keeping the degree of each node fixed while reshuffling the links [137, 138].

The degree of a node is the number of edges stemming from the node. In the friendship network, the degree k gives the number of friends of a node. Thus, $\langle k \rangle$ is the average number of friends per participant. Figure A.2 shows the degree distributions $P(k)$ of the three networks. The distribution, giving the fraction of nodes with degree k , shows the spread in the degrees among the nodes. As the school proceeded, the participants got to know each other better. This is reflected in the evolution of both $\langle k \rangle$ and $P(k)$. The average

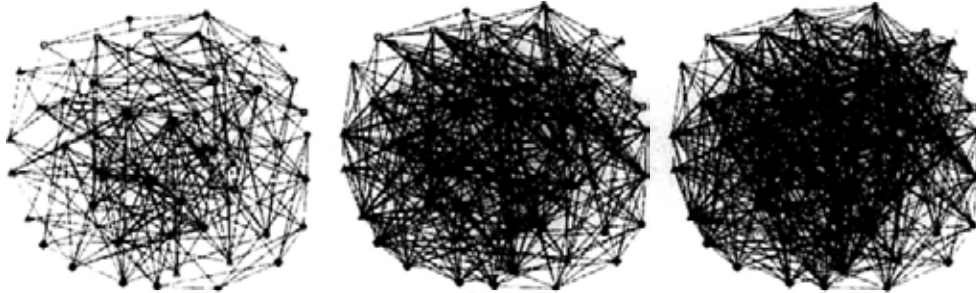


Figure A.1: Topology of the friendship networks, Network 1, 2 and 3 (from left to right), formed at different times of the workshop. ●: Non-Chinese females, ○: Non-Chinese males, ◆: Chinese females and ▲: Chinese males. Pajek is used to create the visualizations.

number of friends increased from 9 in Network 1 (early in the School) to 18 in Network 3 (last day of School); and $P(k)$ extended to the side of larger values of k , indicating the portion of participants with a large number of friends also increased with time.

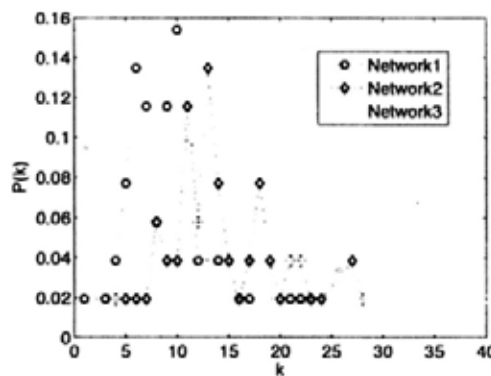


Figure A.2: Degree distributions $P(k)$ of the friendship networks, Network 1, 2 and 3, obtained at different times. The lines are just drawn to guide the eye.

In social networks, it is likely that your friend's friends are also your friends. This property is characterized by the clustering coefficient C [27]. A local clustering coefficient of the node i can be defined as $C_i = \frac{2N_i^{\Delta}}{k_i(k_i - 1)}$,

Table A.1: Basic properties of friendship networks and randomized networks at different times of the workshop. These properties include the clustering coefficient C , the average shortest path length L , the diameter D , the modularity Q and the average degree $\langle k \rangle$. Properties of randomized networks are averaged over 10 realizations.

	Network 1		Network 2		Network 3	
	Real	Randomized	Real	Randomized	Real	Randomized
C	0.34	0.25	0.45	0.36	0.51	0.45
L	2.08	1.99	1.76	1.74	1.66	1.64
D	4	4	3	3	3	2.9
Q	0.34	0.28	0.27	0.19	0.25	0.15
$\langle k \rangle$	9.23		14.58		18.31	

where k_i is the degree of the node i and thus the number of its nearest neighbors, and N_{Δ}^i is the number of triangles formed by the node i and its k_i neighbors. Thus, C_i measures the closeness of i 's nearest neighbors or friends. The clustering coefficient C of the network is the average of C_i over all nodes, i.e., $C = \frac{\sum_i C_i}{N}$. The values of C for the friendship networks are given in Table A.1. It is found that the values of the clustering coefficient C increased as the school proceeded. This is reasonable as the participants became friends of each other. This effect is also reflected in the average length of the shortest path [27] and the diameter [23], which dropped as the School proceeded.

A.4 Correlation between reciprocal evaluations

The data allow us to study the reciprocal evaluations, i.e., how close the evaluations of a participant i on others (or a group of other participants) are, when compared with the evaluations of the other participants on the participant i . Friendship is hard to quantify and very often it is a matter of perception. For

example, you may not be the best friend of whom you regarded to be your best friend. Here, we study the correlation between reciprocal evaluations. In simple terms, consider the mutual evaluations between two participants i and j . If the evaluation of i on j is identical to that of j on i , then the correlation of reciprocal evaluations is perfect. However, if i evaluated j as "very familiar" (or 5) and j evaluated i as "very unfamiliar" (or 1), then the correlation is opposite. To fully display the correlations of two-person reciprocal evaluations among all the 52 participants, we need a 52×52 matrix for each survey. It is thus more convenient to measure the correlations of evaluations between a participant i and a group G of participants, using the idea of the Pearson's correlation coefficient. The group may consist of all the other participants or a sub-group of participants. Let \mathcal{N} be the number of participants in the group G . A participant i evaluates each of the members in group G and thus the evaluations form an array (a vector) $\mathbf{x}^{i,G} = \{x_j^{i,G}\}$, where $j = 1, \dots, \mathcal{N}$ and $x_j^{i,G}$ is the evaluation on a member j in group G by participant i . Similarly, each of the \mathcal{N} members in group G evaluates the participant i and the evaluations also form an array (a vector) $\mathbf{x}^{G,i} = \{x_j^{G,i}\}$, where $j = 1, \dots, \mathcal{N}$ and $x_j^{G,i}$ is the evaluation on the participant i by the member j in group G . The Pearson's correlation coefficient (PCC) that measures the correlation between a participant i and a group G of participants is given by

$$r(i, \text{group } G) = \frac{\langle x_j^{i,G} x_j^{G,i} \rangle - \langle x_j^{i,G} \rangle \langle x_j^{G,i} \rangle}{\sqrt{(\langle (x_j^{i,G})^2 \rangle - \langle x_j^{i,G} \rangle^2) (\langle (x_j^{G,i})^2 \rangle - \langle x_j^{G,i} \rangle^2)}}, \quad (\text{A.1})$$

where $\langle \dots \rangle = \sum_{j=1}^{\mathcal{N}} (\dots) / \mathcal{N}$. The PCC so-defined falls into the range $-1 \leq r \leq 1$, with $r = 1$ stands for perfect correlation and $r = 0$ stands for no correlation.

Figure A.3 shows the values of the PCC of each participant against the group G consisting of all other participants, from the data of the second survey. Two students did not respond in this survey, which left us 50 participants. To

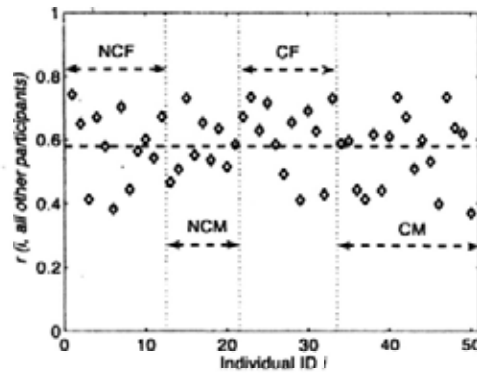


Figure A.3: The Pearson's correlation coefficient of all informants in the second survey. The participants are labeled by a number and grouped as NCF (Non-Chinese female), NCM (Non-Chinese male), CF (Chinese female), and CM (Chinese male). The dash line shows the average value of the correlation coefficient over all participants.

display the results, we assigned a number (characterizing the identity) to each of the 50 participants. In doing the assignment, we intentionally grouped the participants into four groups: Non-Chinese females (NCF), Non-Chinese males (NCM), Chinese females (CF), and Chinese males (CM). This grouping will be useful for later discussion. From Fig. A.3, the PCC values are all positive, with a mean (dashed line) of about 0.6. The mean PCC in the survey carried out on the last day of the school is slightly higher. This positive correlation in the responses of the participants also justifies the construction of an undirected network as shown in Fig. A.1.

During the School, we observed that participants in every sub-group (NCF, NCM, CF, CM) tended to know each other better. To quantify this observation, we define

$$\Delta r(i, \text{group } G') = r(i, \text{group } G') - r(i, \text{group } G). \quad (\text{A.2})$$

Here the group $G' = \text{NCF, NCM, CF, CM}$. If the participant i happens to belong to the group G' , he/she is excluded from the group in evaluating r and

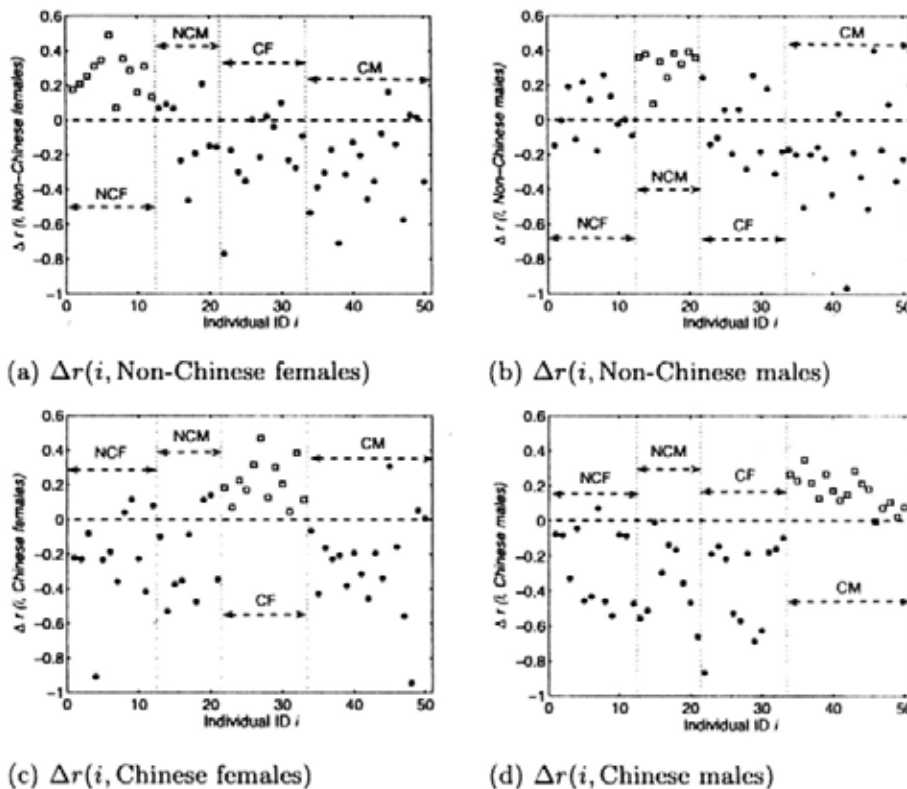


Figure A.4: Values of $\Delta r(i, \text{group } G')$ as defined in Eq.(A.2) for every participant i against different groups $G' =$ (a) Non-Chinese females, (b) Non-Chinese males, (c) Chinese females, and (d) Chinese males. The values are shown for data collected in the second survey. The values for G' in the own group of the participant i are shown in red (squares), which are always positive.

Δr . The group G consists of all the 49 participants, i.e., all participants except the participant i , and thus $r(i, \text{group } G)$ is the quantity shown in Fig. A.3. If the value of $\Delta r(i, \text{group } G')$ is positive (negative), it indicates that the correlation in mutual evaluations between the participant i and members in the group G' is better (worse) than the correlation between the participant i and all the other participants.

Figure A.4 shows the results of $\Delta r(i, \text{group } G')$ for all participants i against the four sub-groups G' , as obtained in the second survey. We have carried out

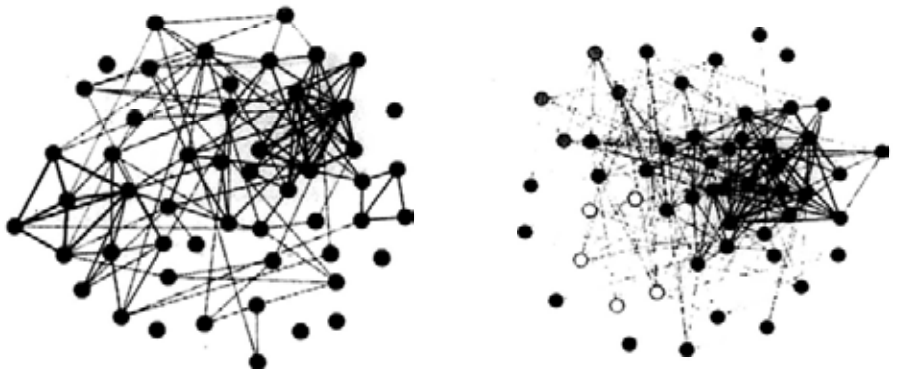
similar analyses for the other two surveys. From Fig. A.4, it is clear that $\Delta r(i, \text{own group})$ is always positive, and it is the case for all three surveys. The results show that participants belonging to the same ethnic group and the same sex can better evaluate the friendship among them. In contrast, there are consistently negative values of Δr in some cases. For example, Fig. A.4(d) indicates that the correlation between nearly all non-Chinese-male participants and the Chinese-male participants is worse than the correlation of the same participant between all other participants. The results indicate that, given the short time frame of the Summer School, the group of Chinese-male participants did not do very well in making new friends outside their group. The same feature is observed for the Non-Chinese-female and Chinese-female participants, but they did slightly better than the Chinese-male participants.

A.5 Community-like structures in friendship networks

A general property of social networks is that they contain compact sub-graphs [1]. The connections are dense within these sub-graphs, and the connections between the sub-graphs are less dense. This is related to the possible community structure of the network. In Table A.1, compared with the randomized networks, the real networks have larger clustering coefficient and average shortest path length, indicating the existence of compact sub-graphs. To reveal these compact structures, we study the k -clique components [139, 140] and the community structures of social networks of CSSS2008.

In graph-theoretical language, a k -clique is a complete sub-graph consisting of k vertices in a graph. Two k -cliques are said to be adjacent if they share $(k - 1)$ vertices. For example, four nodes forming two triangles gives two adjacent 3-cliques. The social structure of a population is reflected in the maximal sub-graph consisting of adjacent k -cliques. Such maximal sub-graph

is referred to as the k -clique percolation component. Finding the clique percolation components (CPC) in a network thus reveals how compact the groups of members are and the overlapping vertices. Since the links in the social networks we discussed so far are too dense for finding the k -clique components, we increase the threshold for the establishment of links so as to construct a network with fewer links. For studying k -cliques, we establish a link between two participants only if they chose “very familiar” towards each other. Figure A.5(a) shows the 3-clique and 4-clique components in the social network constructed from data in the first survey (VF Network 1), and Fig. A.5(b) shows the 4-clique and 5-clique components in the social network constructed from the second survey (VF Network 2).



(a) The 3-clique (thin lines) and 4-clique (thick lines) components based on data in the first survey (VF Network 1).

(b) The 4-clique (thin lines) and 5-clique (thick lines) components based on data in the second survey (VF Network 2).

Figure A.5: The k -clique components in networks constructed from data in the (a) first and (b) second survey. A link is drawn between two participants only when they ranked each other “very familiar”. Vertices connected by links with the same color (grey scale) belong to the same clique percolation component. Red vertices are shared by two CPCs or above.

There are interesting community structures in the results. The largest

cluster in Fig. A.5(a) (colored purple) is a group of Chinese students who received the English training course together prior to the School. They lived together for one more week, and the result was that they established a closer relationship among themselves. There were some project groups formed early in the school and prior to the first survey, and they formed the other clusters in Fig. A.5(a). In Fig. A.5(b) from the second survey, the largest cluster still constitutes the Chinese students, and there are more clusters formed by project groups. In addition to these two types of cluster, a Spanish-speaking cluster (colored in green) can also be seen clearly. Thus, our analysis on k -clique components reveals that clusters of participants were formed as a result of languages (Chinese and Spanish speaking) and activities such as group projects.

Participants in the school interacted through various activities. Among them, the most effective ones were the roommates and members in the same project group. In a way, participants were forced to interact under these two situations. Thus, they tended to establish a stronger friendship. This is indeed the case from the survey data. In Network 2, about 80% of the participants established connections with other members in their project group, and over 90% established links with their roommates. Besides interactions between roommates and project group members, there were other on-campus and off-campus activities that were meant to promote inter-personal relationships among the participants. These activities included having lunches and dinners together, visits to the Forbidden Palace and Olympic parks, and karaoke. By removing the links between roommates and members in a project group in Networks 1, 2 and 3, we obtain the social networks driven by these activities. We labeled these networks as Activity Network 1, 2 and 3. Figure A.6 shows the community structures of Activity Networks 2 and 3, respectively, after an analysis on the modularity Q . The hierarchical agglomeration algorithm [135, 136] is used to detect community structures in these activity networks by calculating

the values of the modularity Q until Q reaches a maximum. For a community inside the population, the value of Q is the difference between the actual fraction of edges inside the community and the expected fraction of edges that would fall inside the community if the links are randomly placed. By iteratively calculating Q for different partitions of the system, a maximum Q is reached when the underlying community structure is selected. Upon reaching a maximum, we identify the participants who formed the communities and the results are shown in Fig. A.6. A higher value of Q indicates a stronger community structure in the network. The values of the modularity Q of the Activity Networks 1, 2 and 3 and their randomized versions are listed in Table A.1.

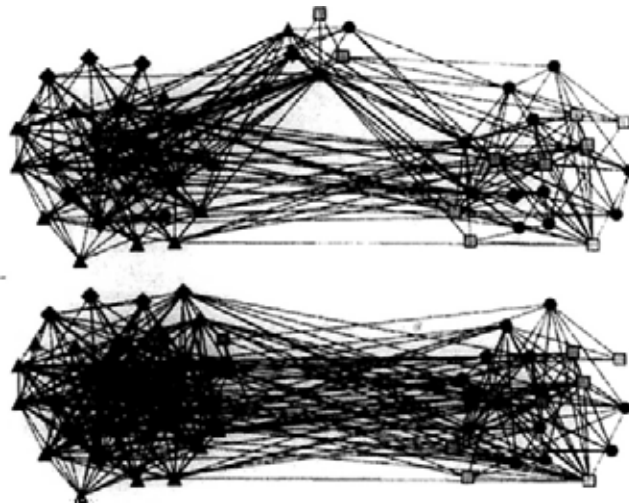


Figure A.6: The community structures in Activity Network 2 (upper) and 3 (lower). Symbols of different shapes (colors) are the nodes belonging to different groups. ●: Non-Chinese females, □: Non-Chinese males, ◆: Chinese females and ▲: Chinese males. Pajek is used to create the visualizations.

The Activity Network 2 (see Fig. A.6) contains three communities – one that is dominated by Chinese, one by Non-Chinese, with a small community that serves as a bridge between the two bigger communities. In this bridging

community, there are three Chinese students. Among them, one is a student helper, another two are participants who are very willing to help both the Chinese and non-Chinese participants. There are another three non-Chinese participants in this bridging group. One is an America-born Chinese and the other two are non-US and non-Europe participants. They served as a cultural bridge between the two bigger groups. As time went by, the bridging community disappeared in the data of the third survey. The members merged into the two bigger communities, as shown in Activity Network 3. Together with this change are many more inter-community links, indicating that more members in the two bigger communities have become known to each other at the end of the School. The modularity Q was not too large for all the three activity networks, indicating the strength of the community structure was weak. The value of Q decreased as the School proceeded, and thus the community structure decayed with time.

A.6 Summary

In summary, we studied the development of friendships among the participants in a recent Santa Fe Complex Systems Summer School held in Beijing. Three surveys were carried out at different times of the School. The data thus revealed the evolution of the friendship network as the participants got to know each other through various activities. The topological structures and the basic properties were discussed. We quantified the correlation between reciprocal evaluations by the Pearson's correlation coefficient. By grouping the participants based on their ethnicity and sex, the results indicated that participants within the same group were able to give very close mutual evaluations, while mutual evaluations for members in different groups were usually not very consistent. This may be a result of the different cultural backgrounds, social skills, and possibly language barriers among the participants in different groups. We

also studied the clique components and community structures in the networks. It was found that there was a small community of participants who served as a cultural bridge between two big communities of different ethnic groups at the early part of the School. As time went by, there were more connections between the two big communities and the bridging group disappeared. As the success of a school or an international event hinges much on how well the participants mix, our results indicate that it is crucial to have a group of helpers who can communicate with the participants of different backgrounds.

Acknowledgements

This work was initiated at the 2008 China Complex Systems Summer School, co-sponsored by the Santa Fe Institute (SFI) and the Institute of Theoretical Physics of the Chinese Academy of Sciences. The research and education programs of SFI are supported by core funding from the U.S. National Science Foundation and by gifts and grants from individuals, corporations, other foundations, and members of the Institute's Business Network for Complex Systems Research. SFI received direct support for the 2008 China CSSS from the US NSF under award OSIE-0623953. The work was completed at the Chinese University of Hong Kong. One of us (H.P.Y) was supported in part by a grant from the Research Grants Council of the Hong Kong SAR Government under grant No. CUHK-401005. We thank Professor Pak Ming Hui for a critical reading of an earlier draft and for suggestions on revising the manuscript.

Bibliography

- [1] M. E. Newman. The structure and function of complex networks. *SIAM Review*, 45:167–256, 2003.
- [2] http://nobelprize.org/nobel_prizes/physics/laureates/2009/index.html.
- [3] http://nobelprize.org/nobel_prizes/physics/laureates/2009/kao-lecture.pdf.
- [4] L. A. Adamic and B. A. Huberman. Power-law distribution of the World Wide Web. *Science*, 287(5461):2115, 2000.
- [5] S. Milgram. The small world. *Psychology Today*, 2:60–67, 1967.
- [6] S. Redner. How popular is your paper? An empirical study of the citation distribution. *European Physical Journal B*, 4:131–134, 1998.
- [7] H. Jeong, S. P. Mason, A. L. Barabási, and Z. N. Oltvai. Lethality and centrality in protein networks. *Nature*, 411:41–42, 2001.
- [8] J. P. Onnela, J. Saramäki, J. Hyvönen, G. Szabó, D. Lazer, K. Kaski, J. Kertész, and A. L. Barabási. Structure and tie strengths in mobile communication networks. *Proceedings of the National Academy of Sciences*, 104(18):7332, 2007.
- [9] P. P. Li, D. F. Zheng, and P. M. Hui. Dynamics of opinion formation in a small-world network. *Physical Review E*, 73(5):56128, 2006.

- [10] Q. Guo, J. G. Liu, B. H. Wang, T. Zhou, X. W. Chen, and Y. H. Yao. Opinion Spreading with Mobility on Scale-Free Networks. *Chinese Physics Letters*, 25:773–775, 2008.
- [11] T. S. Lo, K. P. Chan, P. M. Hui, and N. F. Johnson. Theory of enhanced performance emerging in a sparsely connected competitive population. *Physical Review E*, 71(5):50101, 2005.
- [12] R. Pastor-Satorras and A. Vespignani. Epidemic dynamics and endemic states in complex networks. *Physical Review E*, 63(6):66117, 2001.
- [13] Z. Tao, Fu Z. Q., and B. H. Wang. Epidemic dynamics on complex networks*. *Progress in Natural Science*, 16:452–457, 2006.
- [14] H. A. Atwater. The promise of plasmonics. *Scientific American*, 17(3):56–63, 2007.
- [15] T. W. Ebbesen, H. J. Lezec, H. F. Ghaemi, T. Thio, and P. A. Wolff. Extraordinary optical transmission through sub-wavelength hole arrays. *Nature*, 391(6668):667–669, 1998.
- [16] K. Kneipp, M. Moskovits, and H. Kneipp, editors. *Surface-enhanced Raman scattering: physics and applications*. Springer Verlag, 2006.
- [17] S. Wedge, I. R. Hooper, I. Sage, and W. L. Barnes. Light emission through a corrugated metal film: The role of cross-coupled surface plasmon polaritons. *Physical Review B*, 69(24):245418, 2004.
- [18] K. A. Willets and R. P. Van Duyne. Localized surface plasmon resonance spectroscopy and sensing. 58:267, 2007.
- [19] S. A. Maier. *Plasmonics: fundamentals and applications*. Springer, New York, 2007.

- [20] M. A. Nowak. *Evolutionary Dynamics: Exploring the Equations of Life*. Harvard University Press, Cambridge, Massachusetts, 2006.
- [21] J. von Neumann and O. Morgenstern. *Theory of games and economic behavior*. Princeton University Press, Princeton, New Jersey, 1944.
- [22] http://en.wikipedia.org/wiki/evolutionarily_stable_strategy.
- [23] R. Albert and A. L. Barabási. Statistical mechanics of complex networks. *Reviews of Modern physics*, 74(1):47–96, 2002.
- [24] P. Erdős and A. Rényi. On random graphs. *Publicationes Mathematicae*, 6:290–297, 1959.
- [25] A. L. Barabási and R. Albert. Emergence of scaling in random networks. *Science*, 286(5439):509, 1999.
- [26] L. A. N. Amaral, A. Scala, M. Barthélémy, and H. E. Stanley. Classes of small-world networks. *Proceedings of the National Academy of Sciences*, 97:11149, 2000.
- [27] D. J. Watts and S. H. Strogatz. Collective dynamics of small world networks. *Nature*, 393:440–442, 1998.
- [28] A. Broder, R. Kumar, F. Maghoul, P. Raghavan, S. Rajagopalan, R. Stata, A. Tomkins, and J. Wiener. Graph structure in the web. *Computer Networks*, 33:309–320, 2000.
- [29] G. Siganos, M. Faloutsos, P. Faloutsos, and C. Faloutsos. Power laws and the AS-level internet topology. *IEEE/ACM Transactions on Networking*, 11:514–524, 2003.
- [30] Q. Chen, H. Chang, R. Govindan, S. Jamin, S. J. Shenker, and W. Willinger. The origin of power-laws in internet topologies revisited. In *IEEE*

- INFOCOM*, volume 2, pages 608–617. INSTITUTE OF ELECTRICAL ENGINEERS INC (IEEE), 2002.
- [31] H. Jeong, B. Tombor, R. Albert, Z. N. Oltvai, and A. L. Barabási. The large-scale organization of metabolic networks. *Nature*, 407:651–654, 2000.
- [32] S. N. Dorogovtsev, J. F. F. Mendes, and A. N. Samukhin. Structure of growing networks with preferential linking. *Physical Review Letters*, 85(21):4633–4636, 2000.
- [33] P. L. Krapivsky, S. Redner, and F. Leyvraz. Connectivity of growing random networks. *Physical Review Letters*, 85(21):4629–4632, 2000.
- [34] A. Fronczak, P. Fronczak, and J. A. Holyst. Mean-field theory for clustering coefficients in Barabási-Albert networks. *Physical Review E*, 68(4):046126, 2003.
- [35] B. Bollobás and O. Riordan. The diameter of a scale-free random graph. *Combinatorica*, 24(1):5–34, 2004.
- [36] M. A. Nowak. Five rules for the evolution of cooperation. *Science*, 314:1560, 2006.
- [37] Robert Axelrod. *The evolution of cooperation*. BasicBooks, New York, 1984.
- [38] Martin Nowak and Karl Sigmund. Tit for tat in heterogeneous populations. *Nature*, 355(6357):250–253, 1992.
- [39] J. Z. Wu and R. Axelrod. How to cope with noise in the iterated prisoner's dilemma. *Journal of Conflict Resolution*, 39(1):183–189, 1995.
- [40] Martin Nowak and Karl Sigmund. Tit for tat in heterogeneous populations. *Nature*, 364(6432):56–58, 1992.

- [41] J. Hofbauer and K. Sigmund. *Evolutionary games and population dynamics*. Cambridge University Press, Cambridge; New York, 1998.
- [42] P. Li. Structural Properties and Dynamical Processes in Networks. Master's thesis, The Chinese University of Hong Kong, Hong Kong, August 2006.
- [43] C.-H. Chan, C. Xu, H. Yin, P. Li, and P. M. Hui. unpublished.
- [44] C.-H. Chan. Topics in the Emergence of Cooperation in Competing Games. Master's thesis, The Chinese University of Hong Kong, Hong Kong, August 2008.
- [45] M. Doebeli and C. Hauert. Models of cooperation based on the Prisoner's Dilemma and the Snowdrift game. *Ecology Letters*, 8:748--766, 2005.
- [46] C. L. Tang, W. X. Wang, X. Wu, and B. H. Wang. Effects of average degree on cooperation in networked evolutionary game. *The European Physical Journal B*, 53:411--415, 2006.
- [47] M. A. Nowak and R. M. May. Evolutionary games and spatial chaos. *Nature*, 359:826--829, 1992.
- [48] B. A. Huberman and N. S. Glance. Evolutionary games and computer simulations. *Proceedings of the National Academy of Sciences*, 90:7716--7718, 1993.
- [49] M. A. Nowak, S. Bonhoeffer, and R. M. May. Spatial games and the maintenance of cooperation. *Proceedings of the National Academy of Sciences*, 91:4877--4881, 1994.
- [50] H. X. Yang, Wang B. H., Wang W. X., and Rong Z. H. Spatial games based on pursuing the highest average payoff. *Chinese Physics Letters*, 25:3504--3506, 2008.

- [51] C. Hauert and M. Doebeli. Spatial structure often inhibits the evolution of cooperation in the snowdrift game. *Nature*, 428:643–646, 2004.
- [52] H. Matsuda, N. Ogita, A. Sasaki, and K. Satō. Statistical Mechanics of Population. *Progress of Theoretical Physics*, 88:1035–1049, 1992.
- [53] S. H. Y. Chan, T. S. Lo, P. M. Hui, and N. F. Johnson. Transitions in collective response in multi-agent models of competing populations driven by resource level. *Arxiv preprint cond-mat/0505575*, 2005.
- [54] L. X. Zhong, D. F. Zheng, B. Zheng, X. Chen, and P. M. Hui. Networking effects on cooperation in evolutionary snowdrift game. *Europhysics Letters*, 76:724–730, 2006.
- [55] W. X. Wang, J. Ren, G. R. Chen, and B. H. Wang. Memory-based snowdrift game on networks. *Physical Review E*, 74:56113, 2006.
- [56] J. H. Kagel, A. E. Roth, and J. D. Hey. *The handbook of experimental economics*. Princeton University Press, Princeton, New Jersey, 1995.
- [57] D. F. Zheng, H. P. Yin, C. H. Chan, and P. M. Hui. Cooperative behavior in a model of N -person evolutionary snowdrift games. *Europhysics Letters*, 80:18002, 2007.
- [58] C. H. Chan, H. P. Yin, P. M. Hui, and D. F. Zheng. Evolution of cooperation in well-mixed N -person snowdrift games. *Physica A*, 387:2919–2925, 2008.
- [59] D. G. Rand, A. Dreber, T. Ellingsen, D. Fudenberg, and M. A. Nowak. Positive Interactions Promote Public Cooperation. *Science*, 325:1272, 2009.

- [60] H. Brandt, C. Hauert, and K. Sigmund. Punishment and reputation in spatial public goods games. *Proceedings of the Royal Society B*, 270:1099–1104, 2003.
- [61] D. M. Shi, H. X. Yang, M. B. Hu, W. B. Du, B. H. Wang, and X. B. Cao. Preferential selection promotes cooperation in a spatial public goods game. *Physica A*, 388(21):4646–4650, 2009.
- [62] W. O. Kermack and A. G. McKendrick. A Contribution to the Mathematical Theory of Epidemics. *Proceedings of the Royal Society of London. Series A*, 115:700–721, 1927.
- [63] T. Gross, C. J. D. D’Lima, and B. Blasius. Epidemic dynamics on an adaptive network. *Physical Review Letters*, 96:208701, 2006.
- [64] R. A. Holley and T. M. Liggett. Ergodic theorems for weakly interacting infinite systems and the voter model. *The annals of probability*, 3:643–663, 1975.
- [65] F. Vazquez, V. M. Eguíluz, and M. S. Miguel. Generic absorbing transition in coevolution dynamics. *Physical Review Letters*, 100:108702, 2008.
- [66] C. Nardini, B. Kozma, and A. Barrat. Who’s talking first? Consensus or lack thereof in coevolving opinion formation models. *Physical Review Letters*, 100:158701, 2008.
- [67] M. G. Zimmermann, V. M. Eguíluz, and M. San Miguel. Coevolution of dynamical states and interactions in dynamic networks. *Physical Review E*, 69:65102, 2004.
- [68] O. Gräser, C. Xu, and P. M. Hui. Disconnected-connected network transitions and phase separation driven by co-evolving dynamics. *Europhysics Letters*, 87:38003, 2009.

- [69] P. Drude. Electronic theory of metals I. *Annales de Physique*, 1:566--613, 1900.
- [70] R. H. Ritchie. Plasma losses by fast electrons in thin films. *Physical Review*, 106(5):874--881, 1957.
- [71] E. N. Economou. Surface plasmons in thin films. *Physical review*, 182(2):539--554, 1969.
- [72] W. L. Barnes, A. Dereux, and T. W. Ebbesen. Surface plasmon sub-wavelength optics. *Nature*, 424(6950):824--830, 2003.
- [73] S. A. Maier and H. A. Atwater. Plasmonics: Localization and guiding of electromagnetic energy in metal/dielectric structures. *Journal of Applied Physics*, 98:011101, 2005.
- [74] F.-Z. Yang, J. R. Sambles, and G. W. Bradberry. Long-range surface modes supported by thin films. *Physical Review B*, 44(11):5855--5872, 1991.
- [75] J. J. Burke, G. I. Stegeman, and T. Tamir. Surface-polariton-like waves guided by thin, lossy metal films. *Physical Review B*, 33(8):5186--5201, 1986.
- [76] J. H. Huang, R. Chang, P. T. Leung, and D. P. Tsai. Nonlinear dispersion relation for surface plasmon at a metal-Kerr medium interface. *Optics Communications*, 282(7):1412--1415, 2009.
- [77] G.-D. Xu, T. Pan, T.-C. Zang, and J. Sun. Nonlinear surface polaritons in anisotropic Kerr-type metamaterials. *Journal of Physics D: Applied Physics*, 42:045303, 2009.

- [78] O. Levy and D. J. Bergman. Clausius-Mossotti approximation for a family of nonlinear composites. *Physical Review B*, 46(11):7189–7192, 1992.
- [79] Haiping Yin, C. Xu, and P. M. Hui. Exact surface plasmon dispersion relations in a linear-metal-nonlinear dielectric structure of arbitrary nonlinearity. *Applied Physics Letters*, 94:221102, 2009.
- [80] D. Mihalache, G. I. Stegeman, C. T. Seaton, E. M. Wright, R. Zaroni, A. D. Boardman, and T. Twardowski. Exact dispersion relations for transverse magnetic polarized guided waves at a nonlinear interface. *Optics Letters*, 12(3):187–189, 1987.
- [81] A. D. Boardman and T. Twardowski. Transverse-electric and transverse-magnetic waves in nonlinear isotropic waveguides. *Physical Review A*, 39(5):2481–2492, 1989.
- [82] M. G. Moharam and T. K. Gaylord. Rigorous coupled-wave analysis of planar-grating diffraction. *Journal of the Optical Society of America*, 71(7):811–818, 1981.
- [83] M. G. Moharam and T. K. Gaylord. Diffraction analysis of dielectric surface-relief gratings. *Journal of the Optical Society of America*, 72(10):1385–1392, 1982.
- [84] M. G. Moharam and T. K. Gaylord. Rigorous coupled-wave analysis of metallic surface-relief gratings. *Journal of the Optical Society of America A*, 3(11):1780–1787, 1986.
- [85] L. Li. Formulation and comparison of two recursive matrix algorithms for modeling layered diffraction gratings. *Journal of the Optical Society of America A*, 13:1024–1035, 1996.

- [86] L. Li. Use of Fourier series in the analysis of discontinuous periodic structures. *Journal of the Optical Society of America A*, 13(9):1870–1876, 1996.
- [87] L. Li. Reformulation of the Fourier modal method for surface-relief gratings made with anisotropic materials. *Journal of Modern Optics*, 45(7):1313–1334, 1998.
- [88] L. Li. New formulation of the Fourier modal method for crossed surface-relief gratings. *Journal of the Optical Society of America A*, 14(10):2758–2767, 1997.
- [89] E. Noponen and J. Turunen. Eigenmode method for electromagnetic synthesis of diffractive elements with three-dimensional profiles. *Journal of the Optical Society of America A*, 11(9):2494–2502, 1994.
- [90] K.-Y. Fong. Theoretical Studies on Grating Diffraction and Enhanced Optical Transmission Through Patterned Metallic Films. Master's thesis, The Chinese University of Hong Kong, Hong Kong, September 2006.
- [91] L. Li and C. W. Haggans. Convergence of the coupled-wave method for metallic lamellar diffraction gratings. *Journal of the Optical Society of America A*, 10(6):1184–1189, 1993.
- [92] P. Lalanne and G. M. Morris. Highly improved convergence of the coupled-wave method for TM polarization. *Journal of the Optical Society of America A*, 13(4):779–784, 1996.
- [93] G. Granet and B. Guizal. Efficient implementation of the coupled-wave method for metallic lamellar gratings in TM polarization. *Journal of the Optical Society of America A*, 13(5):1019–1023, 1996.

- [94] C.-H. Sham. Experimental and Theoretical Studies on Metallic Gratings. Master's thesis, The Chinese University of Hong Kong, Hong Kong, August 2009.
- [95] J. D. Jackson. *Classical Electrodynamics*, chapter 7. John Wiley & Sons, New York, third edition, 1999.
- [96] U. Schröter and D. Heitmann. Surface-plasmon-enhanced transmission through metallic gratings. *Physical Review B*, 58(23):15419–15421, 1998.
- [97] W.-C. Luk. Study of the Optical Properties of One Dimensional Metallic Gratings. Master's thesis, The Chinese University of Hong Kong, Hong Kong, January 2010.
- [98] W.-C. Luk, H.-P. Yin, J. Li, P. M. Hui, and H. C. Ong. Theoretical and experimental studies of the optical properties of one-dimensional metallic gratings. In *Progress In Electromagnetics Research Symposium*, Hangzhou, China, March 2008.
- [99] D. W. Lynch and W. R. Hunter. Comments on the optical constants of metals and an introduction to the data for several metals. In E. D. Palik and G. Ghosh, editors, *Handbook of Optical Constants of Solids*, pages 275–367. Academic press, 1985.
- [100] R. W. Wood. On a remarkable case of uneven distribution of light in a diffraction grating spectrum. *Proceedings of the Physical Society of London*, 18:269–275, 1902.
- [101] Haiping Yin and P. M. Hui. Controlling enhanced transmission through semiconductor gratings with subwavelength slits by a magnetic field: Numerical and analytical results. *Applied Physics Letters*, 95:011115, 2009.

- [102] L. Martín-Moreno, F. J. García-Vidal, H. J. Lezec, K. M. Pellerin, T. Thio, J. B. Pendry, and T. W. Ebbesen. Theory of extraordinary optical transmission through subwavelength hole arrays. *Physical Review Letters*, 86(6):1114–1117, 2001.
- [103] E. Ozbay. Plasmonics: Merging photonics and electronics at nanoscale dimensions. *Science*, 311(5758):189, 2006.
- [104] M. Righini, C. Girard, and R. Quidant. Light-induced manipulation with surface plasmons. *Journal of Optics A: Pure and Applied Optics*, 10:093001, 2008.
- [105] J. A. Porto, F. J. García-Vidal, and J. B. Pendry. Transmission resonances on metallic gratings with very narrow slits. *Physical Review Letters*, 83(14):2845–2848, 1999.
- [106] E. Popov, M. Nevière, S. Enoch, and R. Reinisch. Theory of light transmission through subwavelength periodic hole arrays. *Physical Review B*, 62(23):16100–16108, 2000.
- [107] Q. Cao and P. Lalanne. Negative role of surface plasmons in the transmission of metallic gratings with very narrow slits. *Physical review letters*, 88(5):57403, 2002.
- [108] S. Astilean, P. Lalanne, and M. Palamaru. Light transmission through metallic channels much smaller than the wavelength. *Optics Communications*, 175(4-6):265–273, 2000.
- [109] K.-Y. Fong and P. M. Hui. Coupling of waveguide and surface modes in enhanced transmission through stacking gratings. *Applied Physics Letters*, 89:091101, 2006.
- [110] F. Yang and J. R. Sambles. Microwave liquid crystal wavelength selector. *Applied Physics Letters*, 79:3717, 2001.

- [111] K.-Y. Fong and P. M. Hui. Controlling enhanced transmission through metallic gratings with subwavelength slits by anisotropic waveguide resonance. *Applied Physics Letters*, 91:171101, 2007.
- [112] J. Gómez Rivas, C. Schotsch, P. Haring Bolivar, and H. Kurz. Enhanced transmission of THz radiation through subwavelength holes. *Physical Review B*, 68(20):201306, 2003.
- [113] J. Gómez Rivas, C. Janke, P. Haring Bolivar, and H. Kurz. Transmission of THz radiation through InSb gratings of subwavelength apertures. *Optics Express*, 13(3):847--859, 2005.
- [114] J. Gómez Rivas, P. Haring Bolivar, and H. Kurz. Thermal switching of the enhanced transmission of terahertz radiation through subwavelength apertures. *Optics letters*, 29(14):1680--1682, 2004.
- [115] D. Wasserman, EA Shaner, and JG Cederberg. Midinfrared doping-tunable extraordinary transmission from sub-wavelength gratings. *Applied Physics Letters*, 90:191102, 2007.
- [116] E. A. Shaner, J. G. Cederberg, and D. Wasserman. Electrically tunable extraordinary optical transmission gratings. *Applied Physics Letters*, 91:181110, 2007.
- [117] H.-T. Chen, H. Lu, A. K. Azad, R. D. Averitt, A. C. Gossard, S. A. Trugman, J. F. O'Hara, and A. J. Taylor. Electronic control of extraordinary terahertz transmission through subwavelength metal hole arrays. *Optics Express*, 16(11):7641--7648, 2008.
- [118] B. Ferguson and X. C. Zhang. Materials for terahertz science and technology. *Nature materials*, 1(1):26--33, 2002.

- [119] B. Hu, B.-Y. Gu, Y. Zhang, and M. Liu. Transmission interference tuned by an external static magnetic field in a two-slit structure. *Applied Physics Letters*, 95:121103, 2009.
- [120] M. Balkanski and R. F. Wallis. *Semiconductor physics and applications*. Oxford University Press, oxford, 2000.
- [121] R. F. Wallis, J. J. Brion, E. Burstein, and A. Hartstein. Theory of surface polaritons in anisotropic dielectric media with application to surface magnetoplasmons in semiconductors. *Physical Review B*, 9(8):3424–3437, 1974.
- [122] S. C. Howells and L. A. Schlie. Transient terahertz reflection spectroscopy of undoped InSb from 0.1 to 1.1 THz. *Applied Physics Letters*, 69:550, 1996.
- [123] P. Lalanne, J. P. Hugonin, S. Astilean, M. Palamaru, and K. D. Moller. One-mode model and Airy-like formulae for one-dimensional metallic gratings. *Journal of Optics A: Pure and Applied Optics*, 2:48, 2000.
- [124] Haiping Yin, Z. H. Rong, and G. Yan. Development of friendship network among young scientists in an international Summer School. *Physica A*, 388:3636–3642, 2009.
- [125] J. L. Moreno and H. H. Jennings. *Who shall survive?* Nervous and Mental Disease Publishing co., Washington, D.C., USA, 1934.
- [126] M. E. J. Newman. Scientific collaboration networks. I. Network construction and fundamental results. *Physical Review E*, 64(1):16131, 2001.
- [127] P. S. Bearman, J. Moody, and K. Stovel. Chains of affection: the structure of adolescent romantic and sexual networks 1. *American Journal of Sociology*, 110(1):44–91, 2004.

- [128] S. M. Park, P. Holme, and B. J. Kim. Student network in Ajou University based on the course registration data. *Sae Mulli*, 49(5):339–405, 2004.
- [129] P. Holme, S. Min Park, B. J. Kim, and C. R. Edling. Korean university life in a network perspective: Dynamics of a large affiliation network. *Physica A*, 373:821–830, 2007.
- [130] M. Faloutsos, P. Faloutsos, and C. Faloutsos. On power-law relationships of the Internet topology. *SIGCOMM Computer Communication Review*, 29:251–263, 1999.
- [131] B. Wellman. Computers as Social Networks. *Science*, 293(5538):2031, 2001.
- [132] M. E. J. Newman. Mixing patterns in networks. *Physical Review E*, 67(2):26126, 2003.
- [133] M. Girvan and M. E. J. Newman. Community structure in social and biological networks. *Proceedings of the National Academy of Sciences*, 99(12):7821, 2002.
- [134] M. E. J. Newman. Modularity and community structure in networks. *Proceedings of the National Academy of Sciences*, 103(23):8577, 2006.
- [135] M. E. J. Newman. Fast algorithm for detecting community structure in networks. *Physics Review E*, 69:066133, 2004.
- [136] A. Clauset, M. E. J. Newman, and C. Moore. Finding community structure in very large networks. *Physical Review E*, 70(6):66111, 2004.
- [137] S. Maslov and K. Sneppen. Specificity and stability in topology of protein networks. *Science*, 296(5569):910, 2002.

- [138] S. S. Shen-Orr, R. Milo, S. Mangan, and U. Alon. Network motifs in the transcriptional regulation network of *Escherichia coli*. *Nature Genetics*, 31(1):64–68, 2002.
- [139] I. Derényi, G. Palla, and T. Vicsek. Clique percolation in random networks. *Physical Review Letters*, 94(16):160202, 2005.
- [140] G. Palla, I. Derényi, I. Farkas, and T. Vicsek. Uncovering the overlapping community structure of complex networks in nature and society. *Nature*, 435:814, 2005.